

ABSTRACT

Title of dissertation: COHERENT CONTROL OF
LOW ANHARMONICITY SYSTEMS
FOR SUPERCONDUCTING QUANTUM COMPUTING

Shavindra Premaratne, Doctor of Philosophy, 2018

Dissertation directed by: Professor Frederick C. Wellstood
Department of Physics

Dr. Benjamin S. Palmer
Laboratory for Physical Sciences

This dissertation describes research to coherently control quantum states of superconducting devices. In the first project, the state of an 8 GHz 3D superconducting Al cavity at 20 mK was manipulated to add a quantum of excitation. Preparing a harmonic resonator in a state with a well-defined number of excitations (Fock states) is not possible using one external classical drive. I generated Fock states by transferring a single excitation from a 5.5 GHz transmon qubit to a cavity using Stimulated Raman Adiabatic Passage (STIRAP). I also extended the STIRAP technique to put the cavity in higher Fock states, superpositions of Fock states, and Bell states between the qubit and the cavity. Master-equation simulations of the system's density matrix were in good agreement with the data, and I obtained estimated fidelities of 89%, 68% and 43% for the first three Fock states, respectively.

The second project involved implementing an entangling gate between two Al/AlO_x/Al transmon qubits that were mounted in an Al cavity and cooled to 20 mK. Pertinent

system frequencies were as follows: one qubit was at 6.0 GHz, the other qubit at 6.8 GHz, the cavity at 7.7 GHz, and the qubit-qubit dispersive shift was -1 MHz. By applying a specially-shaped pulse of duration $\tau_g = 907$ ns, I implemented a generalized CNOT gate using an all-microwave technique known as Speeding up Waveforms by Inducing Phases to Harmful Transitions (SWIPHT). Using quantum process tomography, I found that the gate fidelity was 80%–82%, close to the 87% fidelity expected from decoherence in the transmons during the gate time. Details of the device fabrication, device characterization, measurement techniques, and extensive modeling of device behavior are presented, along with χ -matrix characterization of single-qubit gates and SWIPHT gates.

COHERENT CONTROL OF LOW ANHARMONICITY SYSTEMS FOR
SUPERCONDUCTING QUANTUM COMPUTING

by
Shavindra Priyanath Premaratne

Dissertation submitted to the Faculty of the Graduate School of the
University of Maryland, College Park in partial fulfillment
of the requirements for the degree of
Doctor of Philosophy
2018

Advisory Committee:

Professor Frederick Wellstood, Chair/Co-Advisor
Dr. Benjamin Palmer, Co-Advisor
Professor Andrew Childs, Dean's Representative
Professor Christopher Jarzynski
Dr. Kevin Osborn
Professor James Williams

© Copyright by
Shavindra Priyanath Premaratne
2018

Dedicated to my father, my mother, my brother, my sister

and

my wife Kasuni

මගේ අම්මාට, මගේ අප්පච්චිට, මගේ මල්ලිට, මගේ නංගිට,

සහ

මගේ බිරිඳ කසුනිට පුදමි .

Acknowledgments

The past few years I spent at the University of Maryland and the Laboratory for Physical Sciences have been some of the best in my academic life. My achievements would not have been possible without the help I received from many people. I humbly take this opportunity to thank them.

First of all, I thank Benjamin Palmer and Frederick Wellstood, who are amazing physicists. It was my privilege to call them my advisors and mentors. Over the past four years, I learned innumerable things from Ben. Ben's persistence and perseverance is unparalleled among all the people I have worked with. He has an amazing ability to visualize a solution to a grand problem, and chip away at it until it is resolved. Working with him both in the lab, and when developing a theory, I was amazed at how much can be accomplished by steadily and methodically attacking a problem. Fred is an amazing scientist with a wealth of knowledge. His inquisitive nature into minute details led me to question many things that I sometimes took for granted, during the course of modeling and measurements. Some of the perspectives Fred had were awe-inspiring, and his ability to look at anything in multiple angles, is truly awesome.

I am grateful to Professors Chris Jarzynski, James Williams, and Kevin Osborn for agreeing to be members of my dissertation committee. I thank Andrew Childs for agreeing to serve as the Dean's representative for my committee and for the encouragement and support I received when he was the professor for CMSC858K.

Over the past four years, I received help from all of my labmates. Everything was built on teamwork and I am especially grateful to Sergey Novikov and Baladitya Suri, who helped me get started with my research work in Ben's lab. I thank Jen-Hao Yeh who arrived at Ben's lab at about the same time I did. He was the lead postdoc

in Ben's lab, and I am glad we were able to collaborate on projects, and chat about everyday things. I am grateful to Jay Lefebvre and Raymond Jachja, who were two undergraduate students that helped me out in various ways, including getting me acquainted with Autodesk Inventor and programming the Tektronix AWG. I thank Rui Zhang and Tamin Tai for the many useful discussions we had over the past few years.

I thank Rangga Budoyo, who was the only person to send a warm reply to my email, when I was still trying to decide if UMD would be my graduate school. After I came to College Park, he was kind enough to show me his lab and his dilution refrigerator, which was inoperable at the time. At that time, I thought I would never get into research requiring low-temperature operations. It was a stroke of fate and serendipity that I came to work in Ben's superconducting quantum computing lab, with Fred (who happened to be Rangga's advisor) as my co-advisor. This was truly a fortuitous series of events, that allowed me to work in one of the best labs, with some of the greatest people around.

I thank my friends from LPS — Luke Robertson, Wan-Ting Liao, Joyce Coppock, Yaniv Rosen, Nathan Siwak, Pavel Nagornykh, Neda Forouzani and Tim Kohler — for discussions regarding important research matters, as well as trivial day-to-day things. I appreciate the advice and support I received from Bruce Kane and Chris Richardson.

I thank the LPS cleanroom, research, and administrative staff members who were always helpful with whatever issue I brought to them. I should particularly mention Toby Olver, Steve Brown, Curt Walsh, Jim Fogleboch, Paul Hannah, Dan Hinkel, David Gutierrez, Doug Ketchum, Warren Berk, Debtanu Basu, Dave Bowen, Jonas Wood, Niquinn Fowler, Althia Kirlew, and Cynthia Evans who were simply amazing people to work with. I consider myself lucky, to have had the opportunity to interact with people who had such an amazing work ethic. The machinists in the LPS machine shop were always ready to help out with any project we were working on. I thank Donald Crouse, Ruben Brun, John Sugrue, and Bill Donaldson who fabricated many different parts for

us. I am grateful to Greg Latini and Mark Thornton, for helping out whenever we had issues with electronics or computers. Over the past few years, Greg and Mark probably saved me several days of work and frustration by finding solutions to the problems that I encountered.

I thank the members of our lunchtime group, Victor Yun, Donghun Park, Charlie Krafft, Yongzhang Leng, and Mihaela Ballarotto with whom I had many interesting conversations. It was never a dull moment when they were around. Victor's enthusiasm was infectious, and sometimes he was the sole reason some of us would go for a jog, to be re-energized. Victor and Donghun invited me to accompany them on a skiing trip, which was an unforgettable experience. Charlie was kind enough to show me thistle sailing, though we didn't get a chance to sail on that day. I consider myself truly lucky to have worked at the Laboratory for Physical Sciences. The people I met here were amazing, and I am grateful for all the support I received.

I thank Sophia Economou, Frederick Strauch, Timothy Sweeney, Xiu-Hao Deng, and Edwin Barnes for useful discussions regarding my research projects.

I thank all my professors at University of Maryland, from whom I learned many things. In particular, I am grateful to Alexey Gorshkov and Steven Anlage who encouraged and helped my work in many ways. I extend my great appreciation to the UMD Physics department staff members — Pornshuda Rirksopa, Paulina Alejandro, Margaret Lukomska, Linda Ohara, Jane Hessing, Amy Streets, and Jessica Crosby — who ensured we had as little paperwork to deal with as possible. Their support enabled me to focus completely on the work I was doing, and worry very little about other matters.

It was an honor and a privilege to work at Laboratory for Physical Sciences and University of Maryland.

There were people outside of UMD and LPS who helped me in innumerable ways. Without them, the time I spent in the US as a graduate student would not have been

complete. These are the people who were our family away from home. Abeyratne Bandara, Chandrika Bandara, and Sanjay Bandara were such a welcoming family to us. Though we met only once or twice annually, we always enjoyed the little time we had to spend with them. Suresh Jayasekara, Aruna Ramanayaka, Sajini Randeniya, Shashikala Ratnayake, and Sameera Meegoda were our great friends, who helped us in time of need, and developed an incredible bond with us. I also want to thank my little buddies Nethuka Ramanayaka, Iruka Ramanayaka, and Dinith Jayasekara who with their antics, were a constant source of delight. I am grateful to Dulith Abeykoon, Vidumin Dahanayake, and Aishan Gonaduwa for their help in getting me set up in the US, which would have been arduous task without them.

I thank my parents-in-law and my brother-in-law Geemal for their constant support and encouragement.

I am grateful to my parents, my brother, and my sister for their immense love, care, support and encouragement. Without them, I would not be where I am today.

Finally, I thank my wife and best friend, Kasuni, who supported me throughout my time in the US. I am most fortunate to have met such a wonderful person, and for her to be my wife is bliss.

Table of Contents

Dedication	ii
Acknowledgements	iii
List of Tables	xi
List of Figures	xii
List of Abbreviations	xv
List of Publications	xvii
Chapter 1 Introduction	1
1.1 Superseding Classical Computation	1
1.2 Coherent Control of Quantum Systems	3
1.3 Overview of the Dissertation	6
Chapter 2 Theory	8
2.1 Theory of the Transmon	8
2.1.1 Physics of the Josephson Junction	8
2.1.2 Physics of the Transmon	10
2.2 Circuit Quantum Electrodynamics	12
2.2.1 The Quantum Harmonic Oscillator	13
2.2.2 The Transmon Hamiltonian	15
2.2.3 The Jaynes-Cummings Hamiltonian	16
2.2.4 Hamiltonian of the Driven System	19
2.3 Density Matrix and Master Equation Formalism	21
2.3.1 The Bloch Sphere Representation	21
2.3.2 The Density Matrix	22
2.3.3 The Lindblad-Kossakowski Master Equation	24
2.4 Quantum Tomography	26
2.4.1 Quantum State Tomography	26
2.4.2 Maximum Likelihood Estimation	28
2.4.3 Quantum Process Tomography	30
Chapter 3 Device Design and Fabrication	36
3.1 Transmon Design	37
3.2 Cavity Design	38
3.3 Microwave Simulations	40

3.4	Black Box Quantization	42
3.5	Transmon Fabrication	45
3.6	Cavity Fabrication	51
3.6.1	Cavity Cleaning and Preparation	52
3.6.2	Cavity Tuning and Packaging	54
3.6.3	Details of Fabricated Cavities	56
Chapter 4 Experimental Setup for Controlling and Measuring Qubits		58
4.1	The Dilution Refrigerator Setup	59
4.2	Vector Network Analyzer	63
4.3	Heterodyne Pulsed Measurement System	64
4.4	Microwave Signal Generators	67
4.4.1	Synthesized Signal Generators	67
4.4.2	Arbitrary Waveform Generators	68
4.5	Device Control and Measurement	69
Chapter 5 System Characterization		72
5.1	Cavity Spectroscopy	73
5.2	Transmon Readout	76
5.2.1	Dispersive Readout	76
5.2.2	The Non-linear High-power Readout	77
5.3	Transmon Spectroscopy	81
5.4	Rabi Oscillations	83
5.4.1	Qubit Population Calibration	87
5.4.2	Qubit Pulse Calibration	88
5.4.3	Off-resonant Rabi drives	90
5.4.4	The Rabi Coupling	91
5.5	Relaxation Time Measurements	92
5.6	Ramsey Oscillations	93
5.6.1	Precise Determination of Qubit Frequency	95
5.7	Spin-Echo Measurements	97
5.8	Photon Number Splitting	99
5.8.1	Determining the Cavity Coupling to the Input Drive	101
5.9	Summary of Measured Parameters of the Devices	103
Chapter 6 Fock State Generation using Stimulated Raman Adiabatic Pas-		
	sage	106
6.1	Introduction	106
6.2	The Device and the Experimental Setup	108
6.3	Modeling and Characterizing the System	110
6.4	Generating Fock States $n = 1, 2, 3$	113
6.5	Generating Fock State Superpositions	121
6.6	STIRAP Reversal	124
6.7	Fractional STIRAP	126
6.8	Summary	128

Chapter 7 A Generalized CNOT Gate	130
7.1 Introduction	130
7.2 The Device and the Experimental Setup	132
7.2.1 Details of the cQED System	132
7.2.2 The System Hamiltonian	133
7.2.3 Joint Qubit State Readout	135
7.3 The SWIPHT Gate	141
7.4 Quantum State Tomography	144
7.4.1 Constructing the Likelihood Function	145
7.4.2 QST During SWIPHT Evolution	147
7.4.3 Verification of Coherence and Phase Control	149
7.5 Quantum Process Tomography	150
7.6 Summary	156
Chapter 8 Conclusion	158
8.1 Summary of Main Results	158
8.1.1 Fock State Generation	158
8.1.2 A Generalized CNOT Gate	159
8.2 Possible Improvements	161
8.2.1 Improving Fock State Generation	161
8.2.2 Improving the SWIPHT gate	162
Chapter A Experimental Determination of Quality Factors for a Bandpass Cavity	163
A.1 Modeling the Cavity	163
A.2 ABCD Matrix Analysis for the Model	164
A.3 Obtaining the S-parameters	165
A.4 Approximations for Calculation of Quality Factors	166
A.4.1 $Q_{\text{out}} = Q_{\text{in}} = 2Q_E$	166
A.4.2 $\omega = \omega_0$	167
Appendix B Rabi Oscillations after FSG	168
Appendix C MATLAB Code for STIRAP Master Equation Simulations	173
C.1 The Main Program for Simulating FSG upto $n = 3$	173
C.2 Subprogram for the Lindblad Master Equation	177
Appendix D Code for Quantum Tomography	179
D.1 Mathematica Program for Performing Quantum State Tomography	179
D.2 MATLAB Programs for Constructing the Likelihood Function	185
D.2.1 MATLAB Function to Import the Raw Data Files	185
D.2.2 MATLAB Function to Obtain the Density Matrix of a Ket	185
D.2.3 MATLAB Function to Construct a Single Term of the Likelihood Function	186
D.2.4 MATLAB Program for Parallel Construction of All the Terms of the Likelihood Function	191

D.2.5	MATLAB Program to Construct the Expression for the Completeness Relation	192
D.3	Mathematica Program to Perform Quantum State Tomography	195
D.4	Mathematica Program to Generate the Simulation Data for QPT	199
Appendix E	QPT Process Matrices for Implementing SWIPHT	200
E.1	QPT Process Matrices for SWIPHT Gates	200
E.2	QPT Process Matrices for Single-Qubit Gates	203
Bibliography		207

List of Tables

Table 2.1	Complete set of orthogonal tomography operators	31
Table 3.1	List of fabricated cavities	57
Table 5.1	Summary of parameters for the devices	105
Table 6.1	Parameter values used in STIRAP pulses	116
Table 6.2	Optimized cavity and qubit pulse parameters used in simulating Fock state generation	119
Table 6.3	Sensitivity of process fidelity to STIRAP parameters	121
Table 7.1	Device parameters for the two qubits coupled to the cavity	134
Table 7.2	Parameters for joint-qubit readout	139
Table 7.3	List of tomographic maps	145
Table 7.4	QPT performance metrics for gates	154

List of Figures

Fig. 2.1	Schematic of a Josephson junction	9
Fig. 2.2	Eigenenergies of a charge qubit for various E_J/E_C	12
Fig. 2.3	Dispersive shift of the resonator	18
Fig. 2.4	The Bloch sphere	23
Fig. 2.5	Illustration of quantum process tomography	32
Fig. 3.1	The qubit chip design for microwave simulations	38
Fig. 3.2	The cavity design for microwave simulations	39
Fig. 3.3	Mesh for the substrate and capacitor pads	41
Fig. 3.4	Waveports in HFSS	42
Fig. 3.5	Blackbox quantization results	44
Fig. 3.6	The transmon design for electron beam writing	46
Fig. 3.7	Photomicrographs of the transmon after ZEP development	48
Fig. 3.8	Photomicrographs of the transmon after MMA development	49
Fig. 3.9	Summary of the transmon fabrication process	51
Fig. 3.10	The cavity design for machining	52
Fig. 3.11	Photograph of cavity 6D	57
Fig. 4.1	Photograph of the CF-450 Dilution refrigerator	60
Fig. 4.2	Input/Output microwave lines in the dilution refrigerator	61
Fig. 4.3	Heterodyne measurement setup	66
Fig. 4.4	Schematic of circuit for controlling and measuring transmon qubits	71
Fig. 5.1	High-power and low-power cavity spectroscopy	73
Fig. 5.2	Cavity spectroscopy versus drive power with transmon in $ g\rangle$	75
Fig. 5.3	Cavity spectroscopy versus drive power with transmon in $ e\rangle$	76
Fig. 5.4	Pulse sequence to obtain cavity switching curves	78
Fig. 5.5	Switching curves	80
Fig. 5.6	Pulses for transmon spectroscopy	82
Fig. 5.7	Transmon Spectroscopy	83
Fig. 5.8	Two-photon process between $ g\rangle$ and $ f\rangle$	84
Fig. 5.9	Pulse sequence for Rabi oscillations	85
Fig. 5.10	Rabi Oscillations	86
Fig. 5.11	The π -pulse and the $\pi/2$ -pulse	89
Fig. 5.12	Rabi Coupling Measurement	91
Fig. 5.13	Pulse sequence for T_1 measurement	92
Fig. 5.14	T_1 measurement	93
Fig. 5.15	Pulse sequence for Ramsey oscillation measurement	94
Fig. 5.16	Ramsey oscillations measurement	95

Fig. 5.17	Drive frequency versus Ramsey frequency	96
Fig. 5.18	Pulse sequence for T_2 measurement	97
Fig. 5.19	Spin-echo T_2 measurement	98
Fig. 5.20	Pulse sequence for photon number splitting	99
Fig. 5.21	Measurement of photon number splitting spectrum	100
Fig. 5.22	Photon number splitting spectrum versus drive power	102
Fig. 6.1	The transmon-cavity device	109
Fig. 6.2	STIRAP in a transmon-cavity system	111
Fig. 6.3	Generation of the first three Fock states	115
Fig. 6.4	Verification of $ g1\rangle$ Fock state	118
Fig. 6.5	Generation of Fock state superpositions with STIRAP	122
Fig. 6.6	Fock state superpositions' variations with STIRAP phases	123
Fig. 6.7	Reverse STIRAP and measurement of cavity decay rate	125
Fig. 6.8	Cavity-qubit entangled state preparation	127
Fig. 7.1	Computer generated model of the device	133
Fig. 7.2	Two-transmon S-curves	136
Fig. 7.3	Cavity powers chosen for joint qubit readout	138
Fig. 7.4	Pulse train for joint qubit readout	138
Fig. 7.5	SWIPHT pulse shape	144
Fig. 7.6	Pulse train used during QST	146
Fig. 7.7	Evolution of populations during SWIPHT gate	148
Fig. 7.8	Phase control of coherences	149
Fig. 7.9	Pulse train for QPT	150
Fig. 7.10	Process matrices from QPT	153
Fig. A.1	Simplified effective circuit model for a bandpass resonator.	163
Fig. B.1	Rabi oscillations performed after $ g1\rangle$ generation	169
Fig. B.2	Rabi oscillations performed after $ g1\rangle$ generation under $\omega_{g1 \rightarrow e1}$ drive	170
Fig. B.3	Rabi oscillations performed after $ g1\rangle$ generation under ω_q drive	171
Fig. B.4	Rabi oscillations performed after $ g2\rangle$ generation under $\omega_{g2 \rightarrow e2}$ drive	172
Fig. E.1	χ -matrix for SWIPHT $_L^{49\pi/36}$	201
Fig. E.2	χ -matrix for SWIPHT $_H^0$	201
Fig. E.3	χ -matrix for SWIPHT $_H^{7\pi/12}$	202
Fig. E.4	χ -matrix for $I \otimes I$	203
Fig. E.5	χ -matrix for $I \otimes R_x^\pi$	203
Fig. E.6	χ -matrix for $I \otimes R_y^\pi$	204
Fig. E.7	χ -matrix for $R_x^\pi \otimes I$	204
Fig. E.8	χ -matrix for $R_y^\pi \otimes I$	204
Fig. E.9	χ -matrix for $I \otimes R_x^{\pi/2}$	204
Fig. E.10	χ -matrix for $I \otimes R_x^{-\pi/2}$	205

Fig. E.11	χ -matrix for $I \otimes R_y^{\pi/2}$	205
Fig. E.12	χ -matrix for $I \otimes R_y^{-\pi/2}$	205
Fig. E.13	χ -matrix for $R_x^{\pi/2} \otimes I$	205
Fig. E.14	χ -matrix for $R_x^{-\pi/2} \otimes I$	206
Fig. E.15	χ -matrix for $R_y^{\pi/2} \otimes I$	206
Fig. E.16	χ -matrix for $R_y^{-\pi/2} \otimes I$	206

List of Abbreviations

AMO	Atomic-Molecular-Optical
AWG	Arbitrary Waveform Generator
BBQ	Black Box Quantization
BNC	Bayonet Neill-Concelman
CAD	Computer Aided Design
CNOT	Controlled NOT
CPB	Cooper Pair Box
cQED	Circuit Quantum Electrodynamics
CR	Cross Resonance
DC	Direct Current
DI	De-ionized (water)
DUT	Device Under Test
FSG	Fock State Generation
f-STIRAP	fractional Stimulated Raman Adiabatic Passage
HEMT	High Electron Mobility Transistor
HFSS	High Frequency Structure Simulator
HPF	High Pass Filter
I/Q	In-phase/Quadrature
IF	Intermediate Frequency
IPA	Iso-propyl Alcohol
IVC	Inner Vacuum Chamber
JJ	Josephson Junction
LO	Local Oscillator
LPF	Low Pass Filter
LPS	Laboratory for Physical Sciences
OVC	Outer Vacuum Chamber
QED	Quantum Electrodynamics
QPT	Quantum Process Tomography
QST	Quantum State Tomography
RF	Radio Frequency
RIP	Resonator Induced Phase
rms	root-mean-square
RO	Read out
SEM	Scanning Electron Microscope
SET	Single Electron Transistor
SHO	Simple Harmonic Oscillator
SMA	SubMiniature version A

SNAP	Selective Number dependent Arbitrary Phase
SPAM	State Preparation And Measurement
SQUID	Superconducting Quantum Interference Device
SSG	Synthesized Signal Generator
STIRAP	Stimulated Raman Adiabatic Passage
SWIPHT	Speeding up Waveforms by Inducing Phases to Harmful Transitions
TE	Transverse Electric
TLS	Two Level System
VNA	Vector Network Analyzer

List of Publications

- [1] **S. P. Premaratne**, F. C. Wellstood, and B. S. Palmer, “Microwave photon Fock state generation by stimulated Raman adiabatic passage,” [Nat. Commun. **8**, 14148 \(2017\)](#).
- [2] **S. P. Premaratne**, F. C. Wellstood, and B. S. Palmer, “Characterization of coherent population-trapped states in a circuit-QED Λ system,” [Phys. Rev. A **96**, 043858 \(2017\)](#).
- [3] **S. P. Premaratne**, J.-H. Yeh, F. C. Wellstood, and B. S. Palmer, “Implementation of a generalized CNOT gate between fixed-frequency transmons,” In review, 2018.
- [4] S. Novikov, T. Sweeney, J. E. Robinson, **S. P. Premaratne**, B. Suri, F. C. Wellstood, and B. S. Palmer, “Raman coherence in a circuit quantum electrodynamics lambda system,” [Nat. Phys. **12**, 75 \(2016\)](#).
- [5] J.-H. Yeh, J. LeFebvre, **S. Premaratne**, F. C. Wellstood, and B. S. Palmer, “Microwave attenuators for use with quantum devices below 100 mK,” [J. Appl. Phys. **121**, 224501 \(2017\)](#).

CHAPTER 1

Introduction

1.1 Superseding Classical Computation

In 1936–1937, Church [1] and Turing [2] independently formalized the notion of computability. These ideas laid the foundation for the subsequent development of classical computers in the twentieth century. The Strong Church–Turing Thesis captures the essence of using an algorithm to compute a function [3, 4]: *Every finitely realizable physical system can be perfectly simulated by a universal Turing machine by finite means.* However, this definition was incompatible with the paradigm of classical computation upon which virtually all modern computers are currently built.

Classical computing relies on an inherently discrete digital system. Since many physical systems are continuous, and governed by quantum mechanics rather than classical physics, it is not possible to efficiently simulate all realizable physical systems with classical computation. *Quantum computation* offers a potential solution. *Universal Quantum Computing* is compatible with the Strong Church–Turing thesis and also had properties not reproducible by any Turing machine [4]. Following the

initial ideas of Feynman [5], Benioff [6], and Albert [7] in the 1980s, Deutsch [4] introduced the concept of a fully quantum model for computation. This model had the potential to supersede classical computation when solving certain classical and many quantum problems. In principle, a quantum computer \mathcal{Q} would be capable of efficiently simulating every finite realizable physical system. With arbitrarily high accuracy, it could simulate zero temperature systems, all instances of quantum computers, and quantum simulators. Furthermore, unlike a Universal Turing machine \mathcal{T} , Deutsch's machine \mathcal{Q} could simulate any finite classical discrete stochastic process (*i.e.* randomized algorithms) also efficiently [4].

In 1994, Shor [8] described a quantum algorithm that was vastly superior to any known classical algorithm for resolving a composite number into its prime factors. This caused a burst of excitement and stimulated activity that continues to this day to realize actual working quantum computers. Following demonstrations of primitive quantum computing systems, DiVincenzo [9] put forth a set of criteria that a universal quantum computer needed to satisfy,

- A scalable physical system with well-characterized qubits
- Ability to initialize the state of the qubits to a simple fiducial state
- Qubit coherence times that are much longer than gate operation times
- A universal set of quantum gates
- A reliable technique to measure the state of the qubits with high fidelity

Since Shor's proposal, researchers worldwide have pursued building quantum

computers using many different types of quantum systems. Initially, well-understood naturally occurring systems such as atoms [10], ions [11], and nuclear spins [12] showed the most promise as qubits. However, as interest in quantum computing spread, more sophisticated, carefully engineered, and unconventional solid-state quantum systems such as quantum dots [13] and superconducting devices [14] were pursued. In addition to these examples, so many other systems have been used to demonstrate quantum coherence and quantum operations over the past 20 years, that a comprehensive review would be far too long for this dissertation.

1.2 Coherent Control of Quantum Systems

A formidable difficulty in building a functioning and useful quantum computer is the problem of *decoherence*. Universal Quantum computation requires quantum entanglement and the use of superpositions of different states. However, excited states eventually relax back to the ground state and superposition states dephase; both effects can be described as a loss of information to the environment. While decoherence can be suppressed by reducing the coupling of a quantum system to the environment, it is impossible to completely isolate a system and eliminate decoherence. In particular, any deliberate operations we perform on the system will necessitate some type of interaction with the system, and this will result in the introduction of decay channels [15]. Imperfections in carrying out quantum operations is another difficulty in building quantum computers. In general, quantum operations span a continuous space (e.g.

rotations by arbitrary angles on the Bloch sphere). In the real world, carrying out operations to arbitrary precision is impossible – and operations will inevitably have errors associated with them [15]. These are serious issues and a major breakthrough was the development of quantum error correcting codes and related techniques [16].

Much of the foundation for superconducting quantum computing was actually developed in the 1980s. Key work included discovery of macroscopic quantum tunneling [17, 18] and quantum energy levels in Josephson devices [19], as well as the development of single-electron devices [20], the Cooper-pair box [21], and the search for macroscopic quantum coherent oscillations in the rf superconducting quantum interference device (SQUID) [22, 23]. The field of superconducting quantum computing truly began with the seminal work by Nakamura *et al.* [14] in which a Cooper-pair-box (CPB) [24] was found to undergo coherent quantum oscillations. A CPB works on the principle that the excess number of Cooper pairs on a tiny superconducting island is a sensitive function of the reduced gate charge [24]. The state of the device can be measured using a sensitive single electron transistor (SET) or by coupling the device to a resonator. Unfortunately, charge qubits are sensitive to quasiparticles and $1/f$ charge noise [25], and severely limited the coherence time of the quantum states [26].

The direct susceptibility of a CPB to charge noise was “remedied” by Koch *et al.* [27], by making the electrostatic charging energy $E_C = e^2/2C_\Sigma$ much smaller than the Josephson energy E_J . This remedy also removed the sensitivity of the device to applied gate voltage, and pushed it out of the charge qubit limit and into the phase qubit limit. The reduction in E_C was accomplished by adding a shunting capacitance across the junction to increase the total capacitance to C_Σ . The new device was christened a

“transmon,” which stood for transmission line plasma oscillation qubit [27]; it was not quite a phase qubit, since it lacks a bias current and required a specific range of E_C to achieve a useful anharmonicity.

At present, superconducting qubits are leading candidates for building scalable quantum computers. They now have reasonably high coherence times, fast gate times, and are relatively easy to fabricate in large numbers using fairly standard lithographic techniques. However, fabricating qubits with precisely chosen frequencies is still a major challenge for scaling up to systems with a large number of superconducting qubits. The largest superconducting quantum computer at present appears to be a 20-qubit system at IBM [28]. Ongoing work to develop systems with 50 or more qubits has also been reported [29–31]. As many government and private entities continue to invest in building a useful quantum computer, I expect many more systems will be reported that satisfy all five of DiVincenzo’s criteria. A major goal of such efforts in the next few years is the demonstration of *quantum supremacy* [32], *i.e.* showing a quantum computer can outperform the fastest classical computer, for some specific computation.

Quantum computing is a computing paradigm that has some significant potential advantages over classical computing for certain problems. While the power and advantages of quantum computing have been proven theoretically, realizing an efficient, accurate, and large quantum computer remains a daunting challenge. Many difficulties must be overcome and novel techniques developed before efficient quantum computation becomes a practical alternative to classical computers.

1.3 Overview of the Dissertation

In this dissertation, I discuss how I used superconducting qubits to realize coherent control over a three-dimensional microwave resonator by generating Fock states, and to generate entanglement between two qubits using a generalized CNOT gate. The qubits I fabricated and measured were fixed-frequency transmons. The transmons were mounted in three-dimensional superconducting cavities to allow measurement of the qubit state and to provide isolation of the qubit from the surrounding environment.

In [Chapter 2](#), I describe the theory behind the transmon and circuit quantum-electrodynamics (cQED), which paved the way for many key developments in superconducting quantum computing. I also describe the master equation formalism that I used to simulate quantum interactions and model the behavior of my devices. In [Chapter 3](#), I discuss the design and fabrication of the cavities and transmons. This chapter explains how I went from a set of experimental design parameters to an actual device.

[Chapter 4](#) describes the experimental setup I used to acquire data. I discuss the instruments I used and present circuit schematics for the different measurement setups. In [Chapter 5](#), I discuss the process I used to systematically determine the cavity and qubit characteristics. I also elaborate on why the qubit calibration is not a sequential process, but rather an iterative process that required multiple runs to fine-tune the parameters.

[Chapter 6](#) describes my work on using Stimulated Raman Adiabatic Passage (STI-

RAP) to transfer an excitation from a transmon to a superconducting microwave cavity [33]. I found good agreement between my results and simulations for the generation of the first three Fock states, and I verified the generation of the first two Fock states using Rabi oscillations. The coherence of the technique was also demonstrated by performing STIRAP on various prepared superposition states. I discuss the distinct interference patterns I observed and compare them to master equation simulations.

In [Chapter 7](#), I describe my implementation of a generalized CNOT gate between two superconducting qubits using a technique known as Speeding up Waveforms by Inducing Phases to Harmful Transitions (SWIPHT). For this project, I repackaged two transmons into a single cavity to create a two-qubit device that was suitable for implementing SWIPHT. My gating results were in good agreement with master-equation simulations. I also verified the performance of the gate by using quantum process tomography, which I describe in detail. I conclude the dissertation in [Chapter 8](#), where I summarize the main results from my research and discuss possible avenues for further investigation.

CHAPTER 2

Theory

2.1 Theory of the Transmon

2.1.1 Physics of the Josephson Junction

The Josephson effect is one of the most remarkable phenomena associated with superconductors [34]. In a seminal article, Josephson [35] predicted that two superconductors separated by a sufficiently thin barrier (insulator or a superconducting weak link) would permit a current to flow with a zero voltage difference between the two superconducting electrodes (see Fig. 2.1). This “supercurrent” is due to the quantum tunneling of Cooper pairs [36]. Furthermore, if a constant voltage difference V is maintained between the two electrodes, the difference in the phases of the two order parameters associated with the two superconducting regions was predicted to oscillate at a well-defined frequency $f = 2eV/h$ [34, 35, 37].

The phenomenon of a supercurrent I_s at zero voltage bias is called the DC Josephson effect, and the phenomenon of an alternating superconductor phase resulting from

a fixed voltage bias is called the AC Josephson effect. The equations describing the effect are

$$I_s = I_c \sin \Delta\phi \quad (2.1)$$

$$\frac{d(\Delta\phi)}{dt} = \frac{2eV_J}{\hbar} \quad (2.2)$$

where I_c is the “critical current” or the maximum supercurrent that can flow through the junction, $\Delta\phi$ and V_J are the difference in the superconducting phase and voltage, between the superconducting electrodes, respectively [34, 37]. Combining the two Josephson relations (Eq. (2.1) and Eq. (2.2)), one finds that a Josephson junction consisting of two superconducting electrodes separated by a thin insulating barrier obeys:

$$V_J = \pm \left(\frac{\hbar}{2e} \frac{1}{\sqrt{I_c^2 - I_s^2}} \right) \frac{dI_s}{dt}. \quad (2.3)$$

For an inductor, the voltage drop across the inductor is related to the rate of change of the current by $V_J = L_J \frac{dI_s}{dt}$. Comparing this to Eq. (2.3) one sees that a Josephson

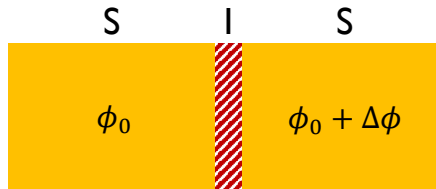


Fig. 2.1 Schematic of a Josephson junction. Two superconducting electrodes (yellow) are separated by a thin insulating barrier (striped red). The superconducting phase difference between the two electrodes is $\Delta\phi$.

junction behaves as a non-linear inductor with the Josephson inductance L_J given by,

$$L_J = \pm \frac{\hbar}{2e} \frac{1}{\sqrt{I_c^2 - I_s^2}} = \frac{\Phi_0}{2\pi I_c \cos \Delta\phi} \quad (2.4)$$

where $\Phi_0 = h/2e$ is the flux quantum. By integrating $I_s V_J$ with respect to time, the total work done on the junction U can be shown to be

$$U = -E_J \cos \phi, \quad (2.5)$$

where the Josephson energy E_J is,

$$E_J \equiv \frac{I_c \Phi_0}{2\pi}. \quad (2.6)$$

2.1.2 Physics of the Transmon

The Hamiltonian for the transmon is the same as that for an un-biased phase qubit, and can be obtained from that of a charge qubit as

$$\mathcal{H}_{\text{CPB}} = 4E_C (\hat{n} - n_g)^2 - E_J \cos \hat{\phi}, \quad (2.7)$$

where \hat{n} is the operator for the excess number of Cooper pairs that tunnels onto the CPB island, $\hat{\phi}$ is the operator for the Josephson phase difference across the junction, $n_g = C_g V_g / e$ is the reduced gate charge, and V_g is the gate voltage applied across the gate capacitor C_g to the island [26]. Since \hat{n} and $\hat{\phi}$ are conjugate operators, Eq. (2.7)

can be written [26] in either the charge basis as

$$\mathcal{H}_{\text{cq}} = \sum_n \left[4E_C (\hat{n} - n_g)^2 |n\rangle \langle n| - \frac{E_J}{2} (|n\rangle \langle n+1| + |n+1\rangle \langle n|) \right], \quad (2.8)$$

or in the phase basis as

$$\mathcal{H}_{\text{cq}} = 4E_C \left(\frac{1}{i} \frac{\partial}{\partial \hat{\phi}} - n_g \right)^2 - E_J \cos \hat{\phi}. \quad (2.9)$$

In the phase basis, the Hamiltonian (Eq. (2.9)) has exact solutions [38] that can be written in terms of the Mathieu functions [27], and the eigenenergies are given by

$$E_m(n_g) = E_C a_{2[n_g + k(m, n_g)]} \left(-\frac{E_J}{2E_C} \right), \quad (2.10)$$

where $a_\nu(q)$ is the characteristic value for the ν^{th} Mathieu cosine function and $k(m, n_g)$ is a sorting function for eigenvalues. The sorting function k is given by,

$$k(m, n_g) = \sum_{l=\pm 1} \left[\text{int} \left(2n_g + \frac{l}{2} \right) \bmod 2 \right] \{ \text{int}(n_g) + l(-1)^m [(m+1) \text{div} 2] \} \quad (2.11)$$

where $\text{int}(x)$ is a function rounding x to the nearest integer, and $(x \text{ div } y)$ gives the integer quotient of x and y [27].

By solving Eq. (2.10) for various E_J/E_C ratios, we can see that higher values of E_J/E_C flatten the energy levels as a function of n_g , at the expense of reduced anharmonicity (see Fig. 2.2). Nevertheless, one finds that for $E_J > E_C$, the anharmonicity only decreases as a weak power law of E_J/E_C , while the charge dispersion (variation in E_m

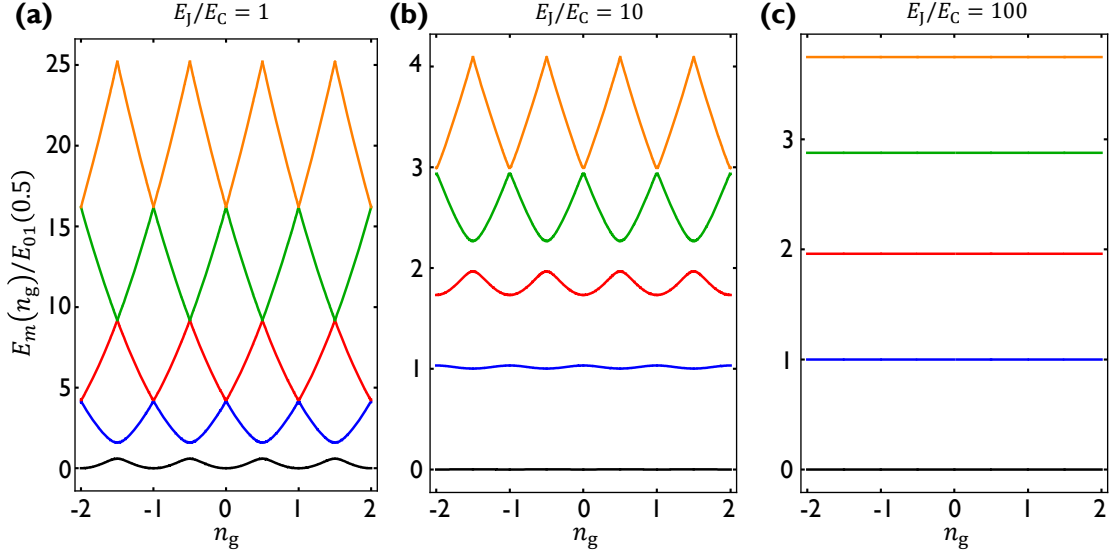


Fig. 2.2 (a) Eigenenergies of a charge qubit versus reduced gate charge n_g for energy levels $m = 0$ (black), $m = 1$ (blue), $m = 2$ (red), $m = 3$ (green), and $m = 4$ (orange) with $E_J/E_C = 1$ (the Cooper-pair-box regime), (b) $E_J/E_C = 10$, and (c) $E_J/E_C = 100$ (the transmon regime). For all the plots, the zero of energy has been defined as the value for $E_0(0)$. Furthermore, the level structure has been normalized with the quantity $E_{01} = E_1(0.5) - E_0(0.5)$ for ease in comparison.

with n_g) is suppressed exponentially with E_J/E_C [27], as expected for a device that is in the phase regime. By setting $E_J/E_C \sim 100$ excellent charge noise suppression is obtained, along with an anharmonicity equal to $\sim E_C$, which can be made sufficiently large to allow for reasonably-fast qubit operations, without driving upper levels of the system.

2.2 Circuit Quantum Electrodynamics

Cavity quantum electrodynamics (QED) involves the interaction between atoms and photons in high-quality-factor cavities, often in the few photon limit where quantum

effects prevail [39]. Cavity QED studies have long been carried out in both the optical regime and the microwave regime, and many striking results have been obtained [39–41].

Both the ideas of cavity QED and the work in the field of microwave kinetic inductance detectors (MKIDs) eventually led to circuit quantum electrodynamics (cQED) [42–45]. In cQED, superconducting devices are coupled to a microwave resonator. This simple arrangement produces several benefits [42],

- The resonator can be used to isolate the qubit from the external electromagnetic environment
- The resonator enables a quantum non-demolition readout method for the state of the qubit
- Coupling to the qubit enables techniques for manipulating the microwave cavity states
- The resonator can act as a quantum bus [46] for entangling qubits

In this section, I describe the theory for the components in my cQED experiments and the Hamiltonian for the combined qubit-cavity system.

2.2.1 The Quantum Harmonic Oscillator

The simple harmonic oscillator (SHO) is one of the most well understood quantum systems in physics. Some physicists even still claim that the SHO might be the only

thing that is understood, or that most of the physical world can be constructed from approximations that are based on the SHO. Although both claims are incorrect, understanding the harmonic oscillator is critical for understanding cQED and many other systems [47].

The classical equation of motion for an undriven LC SHO is given by $C\ddot{\Phi} + \Phi/L = 0$, where Φ is the flux, C is the capacitance, and L is the inductance [48]. Comparing this equation to that of a SHO, one can see the Φ will oscillate freely at resonance frequency $\omega_r = 1/\sqrt{LC}$. The Hamiltonian for the system can then be written as

$$H = \frac{Q^2}{2C} + \frac{\Phi^2}{2L}, \quad (2.12)$$

where Q is the charge on one plate of the capacitor. This equation from classical physics can be directly converted to the Hamiltonian for a quantum harmonic oscillator (QHO),

$$\hat{H} = \frac{\hat{Q}^2}{2C} + \frac{\hat{\Phi}^2}{2L} \quad (2.13)$$

where \hat{Q} and $\hat{\Phi}$ are Hermitian operators. The non-Hermitian raising and lowering operators can be constructed as

$$\hat{a} = \sqrt{\frac{C\omega_r}{2\hbar}} \left(\hat{\Phi} + \frac{i\hat{Q}}{C\omega_r} \right) \quad (2.14)$$

$$\hat{a}^\dagger = \sqrt{\frac{C\omega_r}{2\hbar}} \left(\hat{\Phi} - \frac{i\hat{Q}}{C\omega_r} \right), \quad (2.15)$$

where \hat{a} is the “annihilation” operator and \hat{a}^\dagger is the “creation” operator. The Hamilto-

nian for the harmonic oscillator (or resonator) can then be written as

$$\mathcal{H}_{\text{res}} = \hbar\omega_r \left(\hat{a}^\dagger \hat{a} + \frac{1}{2} \right) = \hbar\omega_r \left(\hat{\mathcal{N}} + \frac{1}{2} \right), \quad (2.16)$$

where $\hat{\mathcal{N}} = \hat{a}^\dagger \hat{a}$ is the photon number operator [47].

2.2.2 The Transmon Hamiltonian

In [Sec. 2.1.2](#) I gave exact expressions for the energy of the n^{th} transmon level in terms of characteristic values of the Mathieu functions. These expressions are not transparent. Instead, perturbation theory can be used to find simpler approximate results when $E_C/E_J \ll 1$. The general asymptotic expressions for transmon eigenenergies E_m , absolute anharmonicity $\alpha_{\text{abs}} = (E_{m+2} - E_{m+1}) - (E_{m+1} - E_m)$, and relative anharmonicity $\alpha_{\text{rel}} = \alpha_{\text{abs}}/E_0$ can then be obtained as [27, 49],

$$E_m = -E_J + \sqrt{8E_J E_C} \left(m + \frac{1}{2} \right) - \frac{E_C}{4} (2m^2 + 2m + 1) \quad (2.17)$$

$$\alpha_{\text{abs}} = -E_C \quad (2.18)$$

$$\alpha_{\text{rel}} = -\sqrt{\frac{E_C}{8E_J}}. \quad (2.19)$$

In the limit $E_J \gg E_C$, the transmon Hamiltonian reduces to a slightly anharmonic oscillator,

$$\mathcal{H}_{\text{trans}} = \hbar\omega_p \left(b^\dagger b + \frac{1}{2} \right) - \frac{E_C}{4} (2b^\dagger b b^\dagger b + 2b^\dagger b + 1) - E_J, \quad (2.20)$$

where $\omega_p = \sqrt{8E_J E_C}/\hbar$ is the plasma frequency of the transmon, while b and b^\dagger are annihilation and creation operators for the transmon, analogous to those of a resonator. Alternatively, if we define the transition frequency for the m^{th} level as $\omega_m = E_m/\hbar$ (see Eq. (2.17)), then the transmon Hamiltonian can be written simply in terms of the eigenkets $|m\rangle$ as,

$$\mathcal{H}_{\text{trans}} = \sum_{m=0}^{\infty} \hbar\omega_m |m\rangle \langle m|. \quad (2.21)$$

2.2.3 The Jaynes-Cummings Hamiltonian

When a qubit or a two-level system (TLS) with transition frequency ω_q is coupled to a single-mode cavity, the total system may be described by the Jaynes-Cummings Hamiltonian [48–50],

$$\mathcal{H}_{\text{JC}} = \hbar\omega_r \left(a^\dagger a + \frac{1}{2} \right) + \frac{1}{2} \hbar\omega_q \sigma_z + \hbar g (a\sigma^+ + a^\dagger\sigma^-). \quad (2.22)$$

Here, $\hbar g$ quantifies the coupling strength between the qubit and the resonator. In particular, if $\omega_q = \omega_r$ and one excitation is placed in the system, then the excitation will be exchanged between the qubit and the cavity at a rate g .

Equation (2.22) can be extended to describe a resonator interacting with a multi-level system. The resulting generalized Jaynes-Cummings Hamiltonian can be written

as

$$\mathcal{H}_{\text{JC}}^{(\text{gen})} = \hbar\omega_r a^\dagger a + \sum_j \hbar\omega_j |j\rangle \langle j| + \hbar g_{\text{ge}} (ab^\dagger + a^\dagger b) \quad (2.23)$$

$$= \hbar\omega_r a^\dagger a + \sum_j \hbar\omega_j |j\rangle \langle j| + \sum_j \hbar g_{j,j+1} (a|j+1\rangle \langle j| + a^\dagger |j\rangle \langle j+1|), \quad (2.24)$$

where $j \geq 2$. Here, I use the notation of Bishop [49] and define $g_{n,n+1} \simeq g_{\text{ge}} \sqrt{n}$ as the coupling strength for the n -photon manifold in the transmon-cavity system. In Eq. (2.23) and Eq. (2.24), the zero-point energy for the cavity and multi-level system was eliminated. To clearly distinguish the cavity levels from the levels of the transmon, throughout the dissertation, I will use $\{g, e, f, h, \dots\}$ to indicate transmon levels.

When the transition frequency $\omega_{\text{ge}} = \omega_e - \omega_g$ is far detuned from the resonance of the cavity ω_r compared to the coupling strength g_{ge} , *i.e.* $g_{\text{ge}} \ll |\omega_r - \omega_{\text{ge}}|$, the system is said to be in the “dispersive regime”. In this regime, Eq. (2.24) can be approximately diagonalized and the transmon truncated to the lowest two levels (qubit levels) [48, 49]. For convenience, I can define the transition frequencies $\omega_{j,j+1}$, detunings $\Delta_{j,j+1}$, and dispersive shifts $\chi_{j,j+1}$ as

$$\omega_{j,j+1} \equiv \omega_{j+1} - \omega_j \quad (2.25)$$

$$\Delta_{j,j+1} \equiv \omega_{j,j+1} - \omega_r \quad (2.26)$$

$$\chi_{j,j+1} \equiv \frac{g_{j,j+1}^2}{\Delta_{j,j+1}}. \quad (2.27)$$

Truncating Eq. (2.24) to the two lowest transmon levels ($|g\rangle$ and $|e\rangle$) and taking the dispersive limit then yields a Jaynes-Cummings Hamiltonian with the following

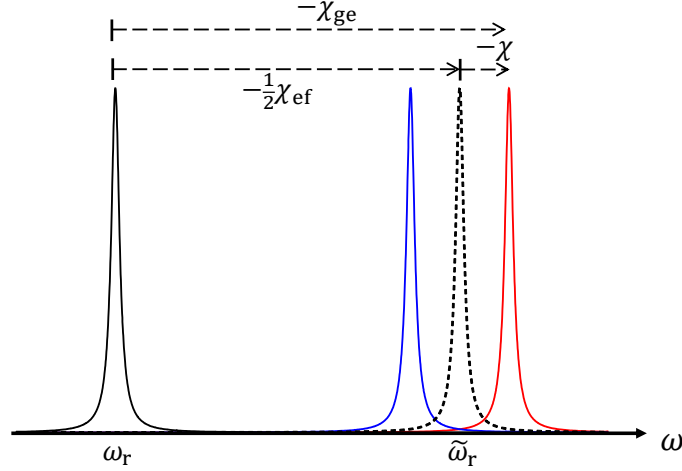


Fig. 2.3 Dispersive shift of the resonator.

convenient form [49, 51],

$$\mathcal{H}_{\text{JC}}^{(\text{disp})} = \hbar \tilde{\omega}_r a^\dagger a + \frac{1}{2} \hbar \tilde{\omega}_{\text{ge}} \sigma_z + \hbar \chi a^\dagger a \sigma_z, \quad (2.28)$$

where $\chi = \chi_{\text{ge}} - \chi_{\text{ef}}/2$, $\tilde{\omega}_{\text{ge}} = \omega_{\text{ge}} + \chi_{\text{ge}}$, $\tilde{\omega}_r = \omega_r - \chi_{\text{ef}}/2$, and χ_{ge} , χ_{ef} are as defined by Eq. (2.27) (see Table 5.1 for detailed device parameters).

If we assume $\omega_{\text{ge}} < \omega_r$ it is easy to see that $\chi_{\text{ge}} < 0$ and $\chi_{\text{ef}} < 0$. Then for typical couplings and detunings between the resonator and the transmon, the dispersive shifts of the resonator are qualitatively shown in Fig. 2.3. In particular, when the qubit is in the ground state, the bare cavity frequency ω_r (solid black) shifts higher to the dressed frequency $\tilde{\omega}_r$ (dashed black). When the transmon is occupying $|g\rangle$, the resonator is shifted to $\tilde{\omega}_r^{(g)} = \tilde{\omega}_r - \chi = \omega_r - \chi_{\text{ge}}$ (red), and when the transmon is occupying $|e\rangle$, the resonator is shifted to $\tilde{\omega}_r^{(e)} = \tilde{\omega}_r + \chi = \omega_r + \chi_{\text{ge}} - \chi_{\text{ef}}$ (blue).

2.2.4 Hamiltonian of the Driven System

Using Eq. (2.28) to describe the undriven Hamiltonian for the dressed cavity qubit system, I next consider adding a term to the Hamiltonian to describe the microwave drive. Following the method of Steck [52], I consider the interaction term between a microwave electric field and a charged TLS. The electric field is given by

$$\vec{E}(t) = \vec{\epsilon} E_0 \cos \omega_d t \equiv \frac{1}{2} \vec{\epsilon} E_0 (e^{i\omega_d t} + e^{-i\omega_d t}), \quad (2.29)$$

where $\vec{\epsilon}$ is the polarization vector for the field, E_0 is the amplitude of the electric field of the drive, and ω_d is the drive frequency.

I now assume that the TLS has an electric dipole moment operator \vec{d} , which can be rewritten in the following form [52],

$$\hat{d} = \langle g | \vec{d} | e \rangle (|g\rangle \langle e| + |e\rangle \langle g|) \equiv \langle g | \vec{d} | e \rangle (\sigma^- + \sigma^+). \quad (2.30)$$

The drive Hamiltonian can then be written as

$$\mathcal{H}_{\text{int}} = -\hat{d} \cdot \vec{E} \quad (2.31)$$

$$= \frac{E_0}{2} \langle g | \vec{\epsilon} \cdot \vec{d} | e \rangle (\sigma^- + \sigma^+) (e^{i\omega_d t} + e^{-i\omega_d t}) \quad (2.32)$$

$$\simeq \frac{E_0}{2} \langle g | \vec{\epsilon} \cdot \vec{d} | e \rangle (\sigma^- e^{i\omega_d t} + \sigma^+ e^{-i\omega_d t}), \quad (2.33)$$

where in going from Eq. (2.32) to Eq. (2.33) the rotating wave approximation (RWA) has been applied, allowing the fast, counter-rotating, terms to be eliminated [52]. The

Rabi frequency for the atom interacting with the field can then be defined as

$$\Omega_q = -\frac{E_0}{\hbar} \langle g | \vec{\epsilon} \cdot \vec{d} | e \rangle. \quad (2.34)$$

With this definition, the interaction Hamiltonian for a charged TLS interacting with a classical electromagnetic drive can be written as,

$$\mathcal{H}_{\text{int}} = \frac{\hbar\Omega_q}{2} (\sigma^- e^{i\omega_d t} + \sigma^+ e^{-i\omega_d t}). \quad (2.35)$$

The drive Hamiltonian for a resonator can be obtained by replacing the qubit operators in Eq. (2.35) with the corresponding ladder operators for a resonator [49]:

$$\mathcal{H}_{\text{int}}^{(\text{res})} = \frac{\hbar\Omega_r}{2} (a e^{i\omega_d t} + a^\dagger e^{-i\omega_d t}), \quad (2.36)$$

where Ω_r is the effective Rabi drive frequency for the resonator. The driven dispersive Jaynes-Cummings Hamiltonian $\mathcal{H} = \mathcal{H}_{\text{JC}}^{(\text{disp})} + \mathcal{H}_{\text{int}}$ can then be written as,

$$\begin{aligned} \tilde{\mathcal{H}} &= \hbar\tilde{\omega}_r a^\dagger a + \frac{\hbar}{2} (\tilde{\omega}_{\text{ge}} + 2\chi a^\dagger a) \sigma_z \\ &+ \frac{\hbar\Omega_q}{2} (\sigma^- e^{i\omega_d t} + \sigma^+ e^{-i\omega_d t}) + \frac{\hbar\Omega_r}{2} (a e^{i\omega_d t} + a^\dagger e^{-i\omega_d t}). \end{aligned} \quad (2.37)$$

Following the method of Bishop [49], one can apply an appropriate unitary transformation to remove the time dependence in Eq. (2.37) and move into the rotating frame of the drive. This yields the following time-independent driven Jaynes-Cummings

Hamiltonian [48, 49],

$$\mathcal{H} = \hbar\Delta_r a^\dagger a + \frac{\hbar}{2}(\Delta_{ge} + 2\chi a^\dagger a)\sigma_z + \frac{\hbar\Omega_q}{2}(\sigma^- + \sigma^+) + \frac{\hbar\Omega_r}{2}(a + a^\dagger), \quad (2.38)$$

where $\Delta_r = \tilde{\omega}_r - \omega_d$ and $\Delta_{ge} = \tilde{\omega}_{ge} - \omega_d$.

2.3 Density Matrix and Master Equation Formalism

2.3.1 The Bloch Sphere Representation

Using Dirac notation, any physically distinct pure quantum state of a qubit can be written in the form

$$|\psi\rangle = \cos\frac{\theta}{2}|g\rangle + e^{i\phi}\sin\frac{\theta}{2}|e\rangle. \quad (2.39)$$

One implication of Eq. (2.39) is that any superposition state of a single qubit can be specified using two independent variables θ and ϕ .

As I discuss next in Sec. 2.3.2 on the density operator formalism, one needs three independent parameters to describe the mixed states of an ensemble of qubits. One way to visualize the state of a qubit ensemble is by using the three expectation values $\langle\hat{\sigma}_x\rangle$, $\langle\hat{\sigma}_y\rangle$, and $\langle\hat{\sigma}_z\rangle$ to specify the components of a vector. The resulting ‘‘Bloch vector’’

can be written as [52]

$$\boldsymbol{\sigma}_{\text{Bloch}} = \langle \hat{\sigma}_x \rangle \hat{\mathbf{i}} + \langle \hat{\sigma}_y \rangle \hat{\mathbf{j}} + \langle \hat{\sigma}_z \rangle \hat{\mathbf{k}}. \quad (2.40)$$

If the ensemble is in a pure state, the density matrix will be represented by $|\psi\rangle\langle\psi|$ and only two parameters are needed to fully specify the state of the ensemble; in this case, $\boldsymbol{\sigma}_{\text{Bloch}}$ will be a unit vector. When the ensemble is in a mixed state, the length of the vector is less than 1, and it will be proportional to the degree of purity. In all cases, $\boldsymbol{\sigma}_{\text{Bloch}}$ will lie within a unit sphere, which is known as the “Bloch sphere” (see Fig. 2.4). The angles θ and ϕ in Eq. (2.39) represent the angular spherical coordinates of the qubit state on the Bloch sphere.

2.3.2 The Density Matrix

The density operator $\hat{\rho}$ is very useful for understanding quantum mechanical behavior of real systems [47]. The density operator naturally allows one to treat a statistical ensemble of quantum systems that may be in different states – a so-called “mixed ensemble”, with the “density matrix” representing the “mixed state” of the system. A simple example is when we have an ensemble of systems each in a pure state $|\alpha_i\rangle$ with a fractional population p_i such that $\sum_i p_i = 1$. In this case, the density operator $\hat{\rho}$ can be defined as

$$\hat{\rho} \equiv \sum_i p_i |\alpha_i\rangle\langle\alpha_i|. \quad (2.41)$$

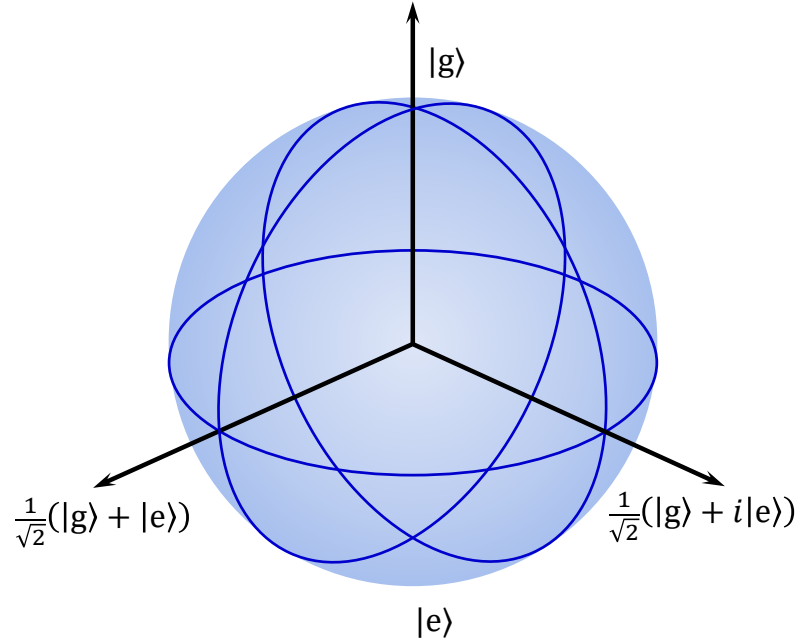


Fig. 2.4 The Bloch sphere with different states labelled. Points on the equator correspond to equal superpositions between $|g\rangle$ and $|e\rangle$ with different phases. Points on the surface of the sphere correspond to pure states of the qubit, while points within the sphere indicate mixed states of the qubit.

If the operator $\hat{\theta}$ is an observable of the system, then the “ensemble average” of $\hat{\theta}$ is,

$$\langle \hat{\theta} \rangle = \text{tr}(\hat{\rho} \hat{\theta}). \quad (2.42)$$

In general, the density operator $\hat{\rho}$ must satisfy the following properties:

- $\rho = \rho^\dagger$ (Hermiticity)
- $\rho_{jj} \geq 0$ (non-negative diagonal elements)
- $\text{tr}(\rho) = 1$ (unit trace)

Given that the elements of an ensemble are not interacting with each other, it is possible to obtain an equation of motion for the density matrix. For an isolated system,

the state will evolve in time according to the Schrödinger equation [47], and one can show that the evolution of ρ is then given by

$$i\hbar \frac{\partial \rho}{\partial t} = -[\rho, \mathcal{H}] = \mathcal{H} \rho - \rho \mathcal{H} \quad (2.43)$$

where $[\rho, \mathcal{H}]$ is the commutator of the density matrix ρ and the Hamiltonian \mathcal{H} .

2.3.3 The Lindblad-Kossakowski Master Equation

Equation (2.43) describes the evolution of the density matrix of an isolated system under a unitary operation. However, real systems are not completely isolated from their environment. Dissipation and decoherence are inevitable in non-isolated systems and these processes must be included for realistic simulations of a quantum system. The quantum master equation approach involves modifying Eq. (2.43) to include terms corresponding to decoherence channels, which cause non-unitary evolution of the states. The idea is to treat the system of interest as a “small system” that is coupled to a “large reservoir”. If the reservoir is sufficiently large, it should undergo little change due to its interaction with the small system and can be assumed to remain in thermal equilibrium.

To formulate a master equation for our cQED system, I will assume that the reservoir is Markovian – *i.e.* the reservoir has no memory of its interactions with the small system. In this case, the reservoir component of the density matrix can be traced out to obtain the reduced density matrix for the small system [53]. Since I am only interested in the

evolution of the small system, and not the reservoir, this master equation approach is appropriate.

The above set of assumptions lead to the Lindblad-Kossakowski master equation [54, 55]:

$$i\hbar \frac{\partial \rho}{\partial t} = -[\rho, \mathcal{H}] + \mathcal{L}[\rho], \quad (2.44)$$

where $\mathcal{L}[\rho]$ is the Liouvillian describing the non-Hermitian evolution of the small system [53]. The Liouvillian is given by

$$\mathcal{L}[\rho] = \sum_i \Gamma_i \mathcal{D}[\mathcal{A}_i]\rho = \sum_i \Gamma_i \left(\mathcal{A}_i \rho \mathcal{A}_i^\dagger - \frac{1}{2} \mathcal{A}_i^\dagger \mathcal{A}_i \rho - \frac{1}{2} \rho \mathcal{A}_i^\dagger \mathcal{A}_i \right) \quad (2.45)$$

where \mathcal{D} are dissipators, Γ_i is the decoherence rate, and \mathcal{A}_i is the ‘Lindblad operator’ or ‘jump operator’ corresponding to the i^{th} decoherence channel [49, 53].

The master equation for the coupled transmon-cavity system is thus,

$$i\hbar \frac{\partial \rho}{\partial t} = -[\rho, \mathcal{H}] + \kappa \mathcal{D}[a]\rho + \Gamma \mathcal{D}[\sigma^-]\rho + \frac{\gamma}{2} \mathcal{D}[\sigma_z]\rho \quad (2.46)$$

where \mathcal{H} is the driven transmon-cavity Hamiltonian (Eq. (2.38)), κ is the total relaxation rate of the cavity, Γ is the relaxation rate of the transmon and γ is the pure dephasing rate of the transmon [49]. Here, I have only included three well-known decoherence channels: relaxation of the cavity, relaxation of the resonator, and dephasing of the transmon. On the other hand, I have assumed that the system is at temperature $T = 0$ K, so there is not rate for thermal excitations to be generated in the

qubit or the cavity [56, 57].

2.4 Quantum Tomography

2.4.1 Quantum State Tomography

The cQED readout method I used yields $\langle \hat{\sigma}_z \rangle$ for a qubit state (see [Sec. 5.2.1](#) and [Sec. 5.2.2](#)). However, as I discussed in [Sec. 2.3.1](#), three quantities need to be determined to fully characterize a qubit that is in a mixed state. It should be emphasized that is not possible to completely determine the state of a qubit when given just a single copy [3, 58, 59]. However, when multiple copies of the same unknown qubit state can be generated, it is possible to reconstruct the density matrix for the system [3, 58, 59]. This method is referred to as Quantum State Tomography (QST). *Tomos* is Greek for “to cut” or “slice”, and the method involves reconstructing the qubit state from multiple slices or projections. In some sense, the purpose of quantum state tomography (QST) is to determine $\langle \hat{\sigma}_x \rangle$ and $\langle \hat{\sigma}_y \rangle$, which can then be used with $\langle \hat{\sigma}_z \rangle$ to construct the density matrix for the qubit [60].

At this point, it is helpful to understand the precise relationship between ρ and $\{\langle \hat{\sigma}_x \rangle, \langle \hat{\sigma}_y \rangle, \langle \hat{\sigma}_z \rangle\}$. The relationship is closely related to orthographic projections. Orthographic projection is commonly used in engineering drawings to render a 3D object on a 2D surface. Typically three such orthogonal projections are used to represent a 3D object, corresponding to visualizing the object from three different viewpoints.

This is analogous to QST, in that the Bloch sphere is measured in three orthogonal directions. However, unlike in technical drawings, in QST the Bloch vector is rotated in three particular directions and the average result obtained from repeated application of the same projective measurement. This is equivalent to taking three orthogonal measurements with the Bloch vector held fixed. For single qubit tomography, the three measurements are [60],

- A projective measurement yielding the probability p_z for the system to be in the excited state $|e\rangle$,
- a $R_x^{\pi/2}$ operation on the qubit followed by a projection yielding a probability p_x that the system was in the state $\frac{|g\rangle+i|e\rangle}{\sqrt{2}}$,
- a $R_y^{\pi/2}$ operation on the qubit followed by a projection yielding a probability p_y that the system was in the state $\frac{|g\rangle+|e\rangle}{\sqrt{2}}$.

These three measurements can be inverted to obtain the Stokes parameters [61], which are the $\{x, y, z\}$ components of the Bloch vector [60]:

$$\langle \hat{\sigma}_x \rangle = 2p_y - 1 \quad (2.47)$$

$$\langle \hat{\sigma}_y \rangle = 2p_x - 1 \quad (2.48)$$

$$\langle \hat{\sigma}_z \rangle = 1 - 2p_z, \quad (2.49)$$

and the density matrix for the qubit [60],

$$\rho = \begin{pmatrix} \rho_{g,g} & \rho_{g,e} \\ \rho_{e,g} & \rho_{e,e} \end{pmatrix} = \begin{pmatrix} 1 - p_z & p_y - ip_x - \frac{1}{2}(1 - i) \\ p_y + ip_x - \frac{1}{2}(1 + i) & p_z \end{pmatrix}. \quad (2.50)$$

2.4.2 Maximum Likelihood Estimation

The method described in [Sec. 2.4.1](#) for reconstructing the density matrix is convenient and relatively straightforward. However, it is prone to errors when applied to real data, *i.e.* results obtained from experimental measurements. In particular, errors associated with the measurements or state preparation, including rotations of the Bloch vector during QST, will induce errors in the values of p_x , p_y , and p_z . The resulting density matrix can even be unphysical, as manifested by the loss of one or more of the density matrix properties listed in [Sec. 2.3.2](#). To prevent the reconstruction of an unphysical density matrix, I used a Maximum Likelihood Estimation (MLE) technique restricted to physically constrained matrices [62].

The method I describe below is based on the method described by James *et al.* [63], and I adapt it to perform quantum state tomography on our two-qubit system. I start with an explicitly “physical” matrix which will be constrained to have unit trace, be Hermitian and have positive eigenvalues. It can be proven that any matrix $\hat{\rho}$ of the form

$$\hat{\rho} = \frac{\hat{T}^\dagger \hat{T}}{\text{Tr}(\hat{T}^\dagger \hat{T})} \quad (2.51)$$

will satisfy all the requirements for a density matrix [63]. Since an arbitrary density matrix for a two-qubit system will have 15 independent parameters, it is convenient to choose a tridiagonal form for \hat{T} [63],

$$\hat{T} = \begin{pmatrix} t_1 & 0 & 0 & 0 \\ t_5 + it_6 & t_2 & 0 & 0 \\ t_{11} + it_{12} & t_7 + it_8 & t_3 & 0 \\ t_{15} + it_{16} & t_{13} + it_{14} & t_9 + it_{10} & t_4 \end{pmatrix}. \quad (2.52)$$

Using this form for \hat{T} , I write the density matrix using Eq. (2.51) and parameterize it with the 16 real variables t_i (the unit trace condition will set the number of independent variables to 15).

For clarity, I assume that this system is measured using a joint-qubit readout scheme (see Chapter 7). In such a scheme, the measurement signal m_i will have weighted contributions from populations from all four eigenstates of the two-qubit system. If the system's density matrix is given by ρ , then the outcome of the measurement is

$$m = \sum_{i=1}^4 c_i \rho_{ii} \quad (2.53)$$

where c_i indicates the output if the system was in the i^{th} eigenstate. Each measurement will have an associated uncertainty which can be written in terms of the uncertainties ϵ_i in a corresponding measurement of c_i . Now, following James *et al.* [63], I define the

likelihood function

$$\mathcal{L}(t_1, t_2, \dots, t_{16}) = \sum_{j=1}^N \frac{[m_j - \sum_{i=1}^4 c_i (\hat{G}_j \hat{\rho} \hat{G}_j^\dagger)_{ii}]^2}{\sum_{i=1}^4 [\epsilon_i (\hat{G}_j \hat{\rho} \hat{G}_j^\dagger)_{ii}]^2} \quad (2.54)$$

where the \hat{G}_j are two-qubit operators which form a complete set of orthogonal tomographic operations when $N = 15$. The numerator of each term in \mathcal{L} quantifies the closeness of the matrix $\hat{\rho}$ to the measurements. The sum in the denominator is the estimated uncertainty in the measurement m_j . For $N > 15$, one has an overcomplete set of tomographic operations, and this allows the optimization routine to find the most likely physical state with higher precision. An example of a complete set of tomographic operations for two-qubit state tomography is given in [Table 2.1](#) [64].

By simultaneously minimizing the likelihood function \mathcal{L} with respect to all the parameters t_k , it is possible to determine the best estimate for $\{t_1, t_2, \dots, t_{16}\}$. These values can then be used to reconstruct the most likely density matrix for the system, by substituting into [Eq. \(2.51\)](#). In practice, to expedite the search for the minimum, it can be helpful to initialize the variables with the expected ideal values for t_k . The ideal values for t_k can be obtained by performing a Cholesky decomposition on the ideal density matrix, expected from either theory or simulations.

2.4.3 Quantum Process Tomography

The QST analysis I discussed in [Sec. 2.4.1](#) can be used for the reconstruction of a density matrix for an unknown state. Although this gives the most likely density

Table 2.1 A complete set of orthogonal tomography operators [65, 66] used for two-qubit QST.

Operator	Two-qubit gate representation
\hat{G}_1	$I \otimes I$
\hat{G}_2	$I \otimes R_x^{\pi/2}$
\hat{G}_3	$I \otimes R_y^{\pi/2}$
\hat{G}_4	$I \otimes R_x^\pi$
\hat{G}_5	$R_x^{\pi/2} \otimes I$
\hat{G}_6	$R_x^{\pi/2} \otimes R_x^{\pi/2}$
\hat{G}_7	$R_x^{\pi/2} \otimes R_y^{\pi/2}$
\hat{G}_8	$R_x^{\pi/2} \otimes R_x^\pi$
\hat{G}_9	$R_y^{\pi/2} \otimes I$
\hat{G}_{10}	$R_y^{\pi/2} \otimes R_x^{\pi/2}$
\hat{G}_{11}	$R_y^{\pi/2} \otimes R_y^{\pi/2}$
\hat{G}_{12}	$R_y^{\pi/2} \otimes R_x^\pi$
\hat{G}_{13}	$R_x^\pi \otimes I$
\hat{G}_{14}	$R_x^\pi \otimes R_x^{\pi/2}$
\hat{G}_{15}	$R_x^\pi \otimes R_y^{\pi/2}$

matrix for a specific quantum operation on a specific starting state, it does not provide complete information regarding the operation itself. To fully characterize the operation, we need to perform the same operation on a complete set of initial states [3], and then perform QST on the resulting output states. This technique for characterizing a quantum operation or process is known as quantum process tomography (QPT). The essence of QPT is to prepare a complete set [66] of initial states, perform the desired operation on each state, and then do QST on all the resulting states to quantify the performance of the gate [3] (see Fig. 2.5).

A quantum operation or quantum process can be thought of as a mapping between input and output density matrices. Given an input state described by ρ_{in} , and a quantum

process \mathcal{E} , the density matrix ρ_{out} for the output state is

$$\rho_{\text{out}} = \mathcal{E}(\rho_{\text{in}}). \quad (2.55)$$

Given a set of ρ_{in} and ρ_{out} , the goal is to find an explicit form for \mathcal{E} . Thus, the objective

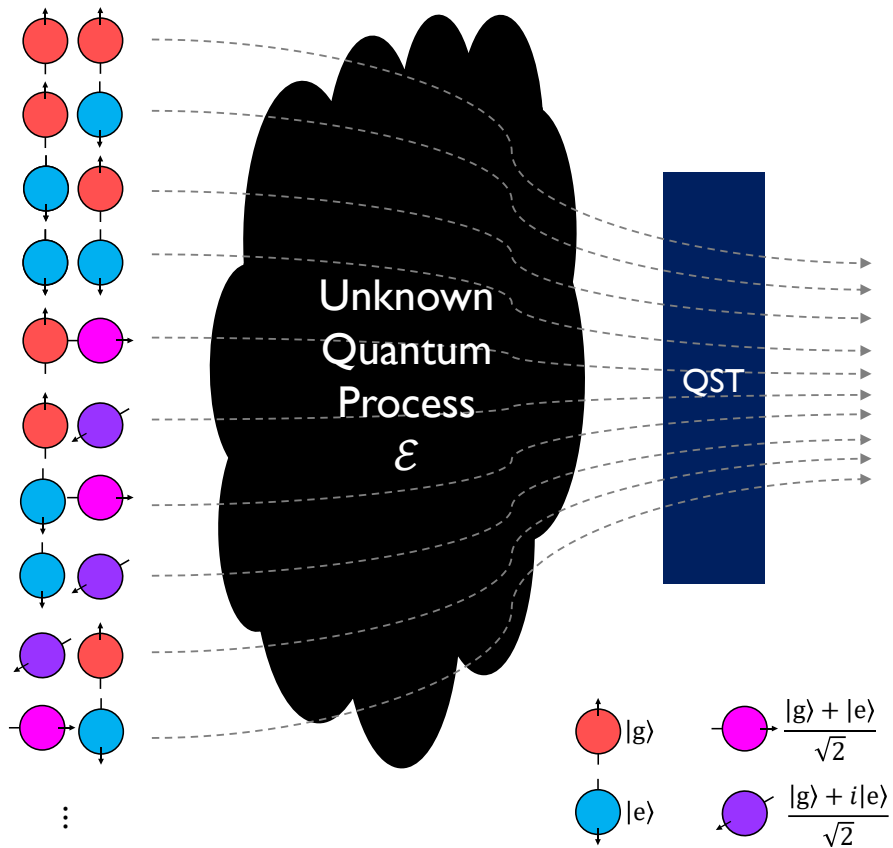


Fig. 2.5 Illustration of quantum process tomography (QPT). The quantum operation is represented as a black box. A complete set of initial states for a two-qubit system are sent in, one at a time. Each output state is then analyzed with QST. By studying the input state to output state transformation, a complete description of the operation (\mathcal{E}) can be determined.

is to find a set of operators \hat{O}_i , such that

$$\rho_{\text{out}} = \mathcal{E}(\rho_{\text{in}}) = \sum_i \hat{O}_i \rho_{\text{in}} \hat{O}_i^\dagger \quad (2.56)$$

is satisfied for an every possible input density matrix ρ_{in} [3].

To proceed, we write the constituent operators \hat{O}_i in terms of the chosen basis operators \hat{A}_j as

$$\hat{O}_i = \sum_j q_{ij} \hat{A}_j, \quad (2.57)$$

where q_{ij} are complex numbers representing the relative weights of basis operators.

We can then write Eq. (2.56) using the basis operators as

$$\mathcal{E}(\rho_{\text{in}}) = \sum_{j,k} \chi_{jk} \hat{A}_j \rho_{\text{in}} \hat{A}_k^\dagger, \quad (2.58)$$

where $\chi_{jk} = \sum_m q_{mj} q_{mk}^*$ are matrix elements of the “process matrix” or “ χ -matrix” which completely and uniquely describes the quantum operation \mathcal{E} [3]. The dimensionality of the process matrix will be $d^4 \times d^4$ where d is the number of qubits. Since the χ -matrix needs to satisfy positivity and Hermiticity [3, 67], I can use Cholesky decomposition as described in Sec. 2.4.1 and Sec. 2.4.2 to constrain the matrix and write:

$$\chi = \hat{T}^\dagger \hat{T}, \quad (2.59)$$

where \hat{T} has the appropriate tridiagonal form with a dimensionality of d^4 . In addition,

any real process has to be trace-preserving [3, 67], and this implies:

$$\hat{I} = \sum_i \hat{O}_i \hat{O}_i^\dagger = \sum_{j,k} \chi_{jk} \hat{A}_j \hat{A}_k^\dagger. \quad (2.60)$$

I enforce this completeness condition by introducing a cost function

$$\Xi = \sum_{j,k} \left\{ [\operatorname{Re}(\mathcal{Z}_{jk}) - I_{jk}]^2 + [\operatorname{Im}(\mathcal{Z}_{jk})]^2 \right\}, \quad (2.61)$$

where $\mathcal{Z} = \sum_{j,k} \chi_{jk} \hat{A}_j \hat{A}_k^\dagger$.

To apply this method to measurement, I follow O'Brien *et al.* [67], and implicitly define the quantum process as

$$\rho_{\text{out}}^{(\sigma)} = \sum_{j,k} \chi_{jk} \hat{A}_j \rho_{\text{in}}^{(\sigma)} \hat{A}_k^\dagger, \quad (2.62)$$

where $\rho_{\text{in}}^{(\sigma)}$ is the input density matrix and $\rho_{\text{out}}^{(\sigma)}$ is the output density matrix corresponding to the initial state σ . By using a complete set of initial states, one can use a maximum likelihood estimation technique to extract the best estimation for χ . For QPT, I used the following likelihood function:

$$\mathcal{L}(t_i, \lambda) = \sum_{\sigma} \sum_{\tau} \frac{[m_{\sigma,\tau} - \sum_{i=1}^4 c_i (\hat{G}_{\tau} \rho_{\text{out}}^{(\sigma)} \hat{G}_{\tau}^\dagger)_{ii}]^2}{\sum_{i=1}^4 [\epsilon_i (\hat{G}_{\tau} \rho_{\text{out}}^{(\sigma)} \hat{G}_{\tau}^\dagger)_{ii}]^2} + \lambda \Xi, \quad (2.63)$$

where τ is the index for the tomographic operators \hat{G}_{τ} , λ is a Lagrange multiplier [67], and the final term in Eq. (2.63) is used to enforce the completeness relation in Eq. (2.61). By minimizing the likelihood function with respect to the variables t_i

and λ , the most likely quantum process matrix χ giving rise to the mapping will be determined.

As in QST, by using an overcomplete set of tomographic operations and initial states, the accuracy of this technique can be improved. For example, in [Chapter 7](#) I describe QPT on a two-qubit system where I used an overcomplete set of 36 initial states.

CHAPTER 3

Device Design and Fabrication

Proper design of the quantum system is essential to obtain reliable and repeatable results in many solid state quantum computing experiments. The original proposal for a circuit quantum electrodynamics (cQED) platform was based on planar resonators and Cooper-pair box qubits [42, 43, 68]. Using 3D cavities instead of lumped-element or distributed-element resonators decreased the electric field energy stored in the interfaces of the materials [69]. The first use of such cavities in superconducting quantum computing resulted in significantly longer transmon lifetimes and larger internal quality factors of resonators. Since then, fabrication methods and designs for planar geometries have improved and lifetimes for 2D and 3D structures are now comparable [70, 71]. Nevertheless, I chose to use a 3D cavity for its simplicity and ease of use, which allowed me to focus on improving the control of the qubit and cavity.

In this chapter I will discuss how I designed the transmon and the cavity following the groundwork laid by Dr. Sergey Novikov [72] in our research group. I will then explain how I used finite-element-method microwave simulations in conjunction with Black Box Quantization to determine suitable system parameters, depending on the

experimental requirements. I will conclude the chapter by explaining how the transmon and cavity were fabricated, and how the device was packaged and prepared for cooldown.

3.1 Transmon Design

The concept of the transmon [27] is quite simple – fabricate a small Josephson junction with an appropriate shunting capacitor. However, there are a few important design considerations when incorporating such a device in a 3D cavity so that it can perform quantum operations. In addition to decreasing the charging energy E_C , the pads of the capacitor also serve as an antenna and set the transmon-cavity coupling. Wang *et al.* [73] examined different physical designs to obtain optimal performance for the 3D transmons and studied the effect of various interfaces. They found that certain interfaces resulting from processing and fabrication contributed the most to dissipation.

My design for the transmon was largely based on a design by Novikov [72], which is very similar to the original 3D transmon design of Paik *et al.* [69]. In my transmon design (see Fig. 3.1), the shunting capacitor had two $650\ \mu\text{m} \times 500\ \mu\text{m}$ pads on a sapphire substrate. The two pads were adjacent to each other on their shorter side, with a separation of $150\ \mu\text{m}$. Although the electric field of the capacitor is dispersed in the substrate, vacuum, and interfaces, with this design most ($\sim 90\%$) of the energy stored in the electric field is in the substrate, which has low dielectric loss and relatively

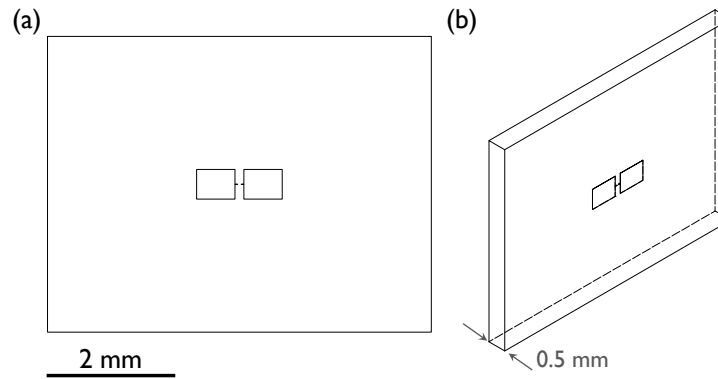


Fig. 3.1 (a) Front view and (b) 3D perspective wireframe view of the qubit chip for 3D microwave simulations. The capacitor was designed in Inventor along with the leads that contact the Josephson junction. The junction itself was not part of the 3D microwave simulations.

high permittivity.

3.2 Cavity Design

The cavities for my cQED experiments were also based on cavities used by Novikov [72]. All of my cavities were designed to have a TE_{101} mode frequency close to 8 GHz. The 1 GHz to 10 GHz frequency range is well suited for experiments due to the availability of compatible commercial instruments. This frequency range is also well suited for QC experiments since thermal populations can be suppressed at the milliKelvin temperatures achievable using a dilution refrigerator. In particular, this allowed me to initialize the system in a well-defined ground state by simply waiting long enough for the system to dissipate energy. I also chose the cavity resonance to be at a higher frequency than the qubit, as this enhances the lifetime of the qubit, by

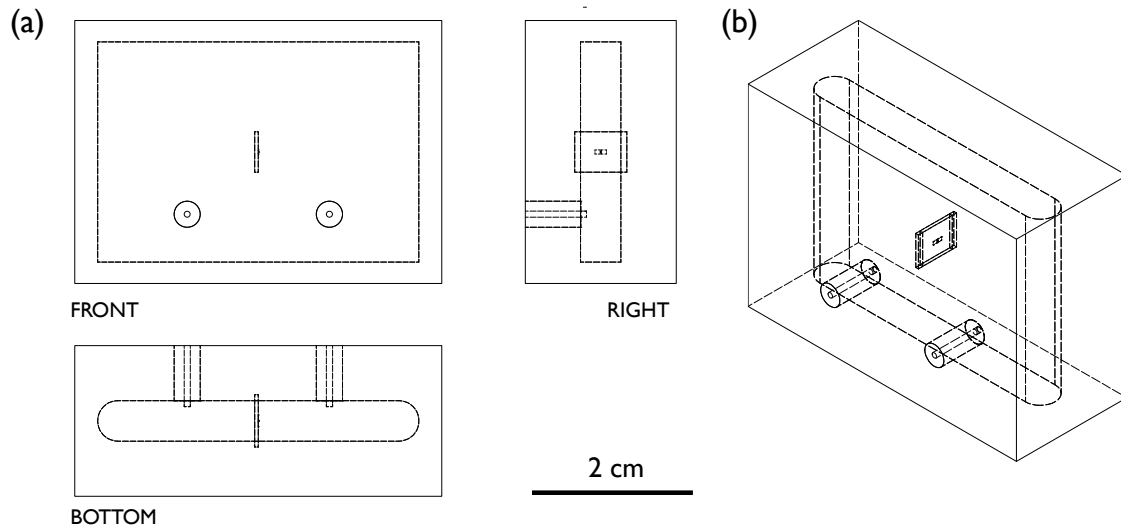


Fig. 3.2 The cavity design for microwave simulations. (a) Orthographic projections and (b) 3D perspective wireframe view of the designed cavity with the transmon shunting capacitor.

reducing contributions to loss from the Purcell effect from higher modes [74].

For microwave simulations, I drew a rectangular cavity within Autodesk Inventor, with length $l = 35$ mm, width $w = 20.5$ mm, and depth $h = 5$ mm (see Fig. 3.2 for a schematic and Fig. 3.11 for a photograph). I also included a $5 \text{ mm} \times 6.5 \text{ mm} \times 450 \mu\text{m}$ sapphire chip and the transmon shunting capacitor (see Fig. 3.1) to mimic a transmon. The sapphire chip decreases the fundamental mode frequency of the cavity to just below 8 GHz. The input and output coupling ports were included as perfectly conducting pins that protruded into the cavity. I then imported the CAD design into the microwave simulation software Ansys HFSS (High Frequency Structure Simulator) as a SAT file [75]. Although HFSS has its own design capability, I preferred laying out the cavity geometry using Inventor because it was easier to use and had superior capabilities.

3.3 Microwave Simulations

After importing the CAD layout for the chip and cavity into HFSS, I next designated the materials for the different regions. The bulk of the cavity and the coupling pins were set to be perfect electrical conductors, the empty space was set as vacuum and the chip material was set to be sapphire with relative permittivity $\epsilon_r = 10$. The material for pads of the shunting capacitor and the leads to the capacitor pads were also set to be perfect electrical conductors.

Since HFSS is a finite-element solver [75], it is important to have sufficiently fine meshing on the surfaces in order to obtain accurate solutions. This means that I had to restrict the maximum length of meshing elements (see Fig. 3.3). For initial simulations, I usually set the maximum length to be 5–10% of the shortest non-zero dimension of the object. For example, the capacitor pads had an initial maximum meshing restriction of 50 μm . Of course this ignored the much smaller thickness ($\sim 80 \text{ nm}$) of the pads. Since my main interest was about the behavior of the transmon, I manually set the meshing for the leads to the capacitor pads, the capacitor pads, and the sapphire chip. The remaining regions used an automatically generated mesh.

To perform an HFSS microwave simulation in the “driven modal” method, I set up ports #1 and #2 to couple microwaves in to and out of the cavity. To represent the ports, I drew two circles each starting from the center of the coupling pin and ending on the surface of cavity, as shown in green and yellow in Fig. 3.4. I assigned each circle on the cavity wall as Waveports with an impedance of 50 Ω (see Fig. 3.4). The integration

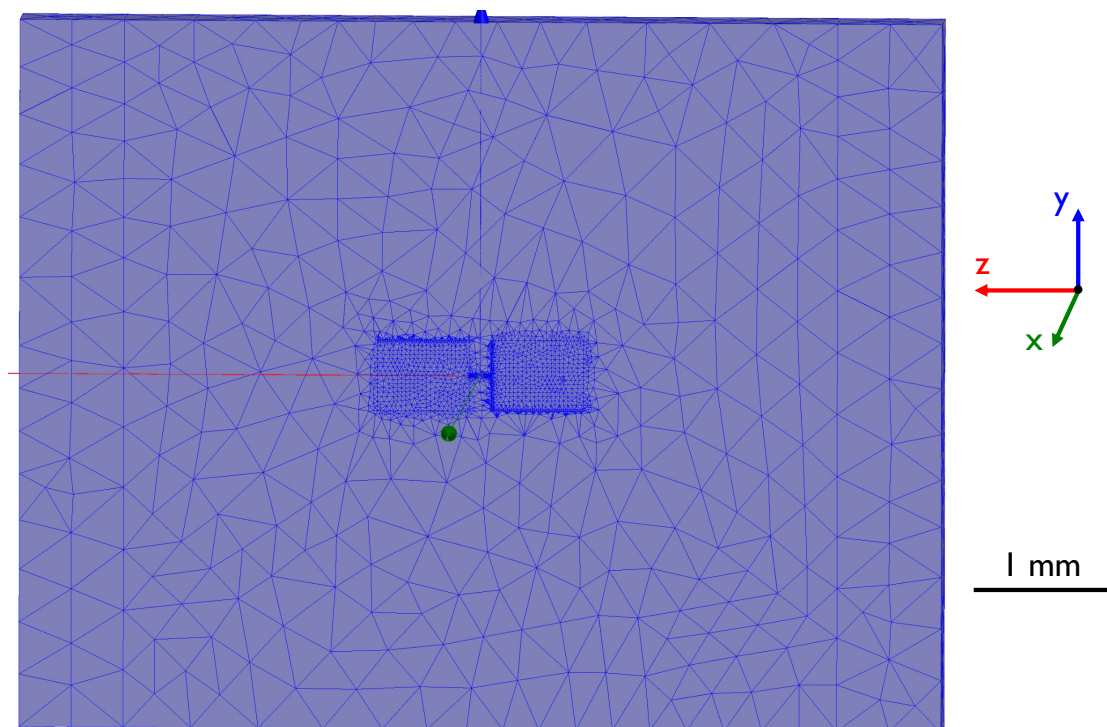


Fig. 3.3 Mesh for the substrate and capacitor pads after restricting the maximum length of elements. Picture taken from HFSS.

line for the excitation was radially directed from the center of the circle (the pin) to the edge of the circle (the cavity wall). This ensured that the ports were generating the microwave signals correctly. To represent the junction, I drew a rectangle between the two capacitor leads. This rectangle was designated as a lumped port (#3) with an impedance of $10\text{ G}\Omega$. I discuss how I used this lumped port in [Sec. 3.4](#), to extract the cavity transmission simulation results and to determine the required parameters for the junction. After setting up the ports, I set the frequency range for the sweep and ran HFSS to find the transmission S_{21} through the cavity to confirm that the resonance was close to 8 GHz and the waveports were set up correctly.

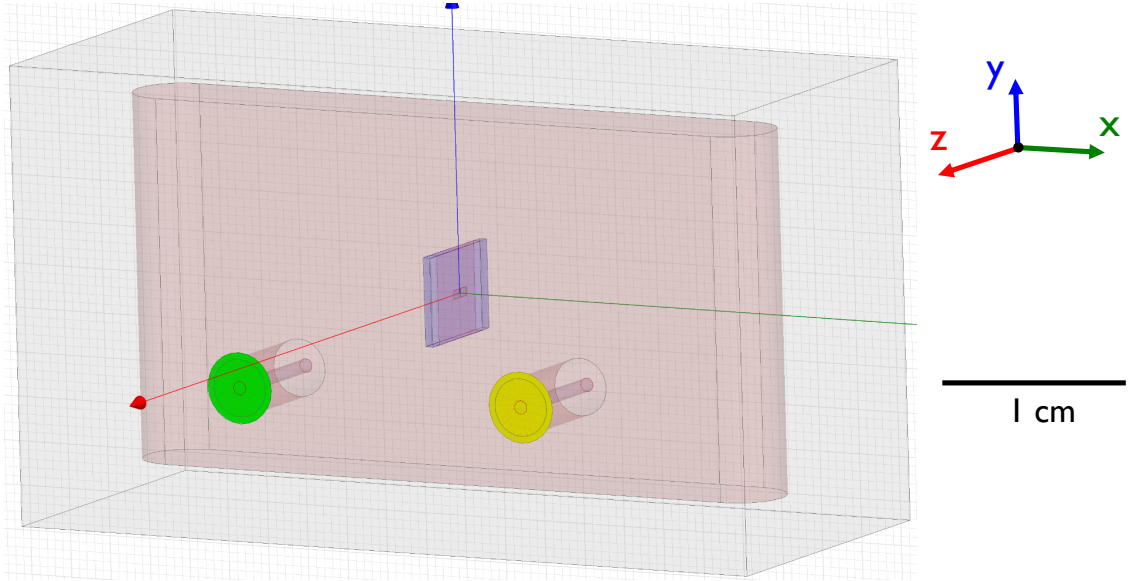


Fig. 3.4 Waveports for coupling microwaves in (green port) and out (yellow port) of the microwave cavity, as depicted in HFSS. Both waveports are set to have an impedance of $50\ \Omega$ and a radial excitation.

3.4 Black Box Quantization

Black Box Quantization (BBQ) is a semi-classical method that was developed to determine the approximate energy level structure of coupled transmon-cavity systems [76]. In this method, microwave simulations are used to model the electromagnetic environment around the JJ, including the capacitor pads, chip and cavity.

To perform BBQ analysis of my device, I extracted the self admittance versus frequency data $Y_{33}(\omega)$ for the lumped port (#3) from the HFSS output results (see [Sec. 3.3](#)). The discrete data of $Y_{33}(\omega)$ was interpolated using Mathematica to obtain a smooth analytic function [72]. From the $100\ \text{nm} \times 125\ \text{nm}$ area of the JJ, I estimated the capacitance of the junction by itself to be $C_j = 4\ \text{fF}$ [77]. Since C_j is much less than

the shunting capacitance from the pads, which dominates the charging energy E_C , this rough estimate for the junction capacitance is sufficient for design purposes. As part of the BBQ analysis, the JJ is treated as a simple linear inductor with inductance L_{J0} . Accordingly, I set L_{J0} between 3 nH to 15 nH depending on the target characteristic frequency for the transmon. I then analytically combined the admittance contribution from the JJ capacitance and inductance, with $Y_{33}(\omega)$ from the simulation to obtain the total admittance:

$$Y_{\text{tot}}(\omega) = Y_{33}(\omega) + \frac{1}{i\omega L_{J0}} + i\omega C_j. \quad (3.1)$$

From $\text{Im}[Y_{\text{tot}}(\omega)]$, I used BBQ to obtain the transmon characteristic frequency, the expected dispersive shifts, the anharmonicity in the system, and other pertinent parameters [76]. An example for BBQ analysis is shown in Fig. 3.5 where $Y_{33}(\omega)$ extracted from HFSS results and $Y_{\text{tot}}(\omega)$ calculated through Mathematica are shown. The two poles of Y_{tot} represent the characteristic frequencies of the qubit and cavity. When I set $L_{J0} = 4.5$ nH, the analysis predicted the qubit frequency to be at $\omega_q \approx 5.9$ GHz (see Fig. 3.5).

From $\text{Re}[Y(\omega)]$, I note that I also used the BBQ analysis to estimate the lifetimes of the transmons from Purcell coupling to the external 50Ω environment or bulk dielectric loss of the substrate. My simulations did not include lossy surface layers or lossy residue that could be left from the fabrication process, due to the very small meshing that would be required. BBQ also cannot incorporate other loss mechanisms such as non-equilibrium quasiparticles. Thus, it was only possible to obtain an upper

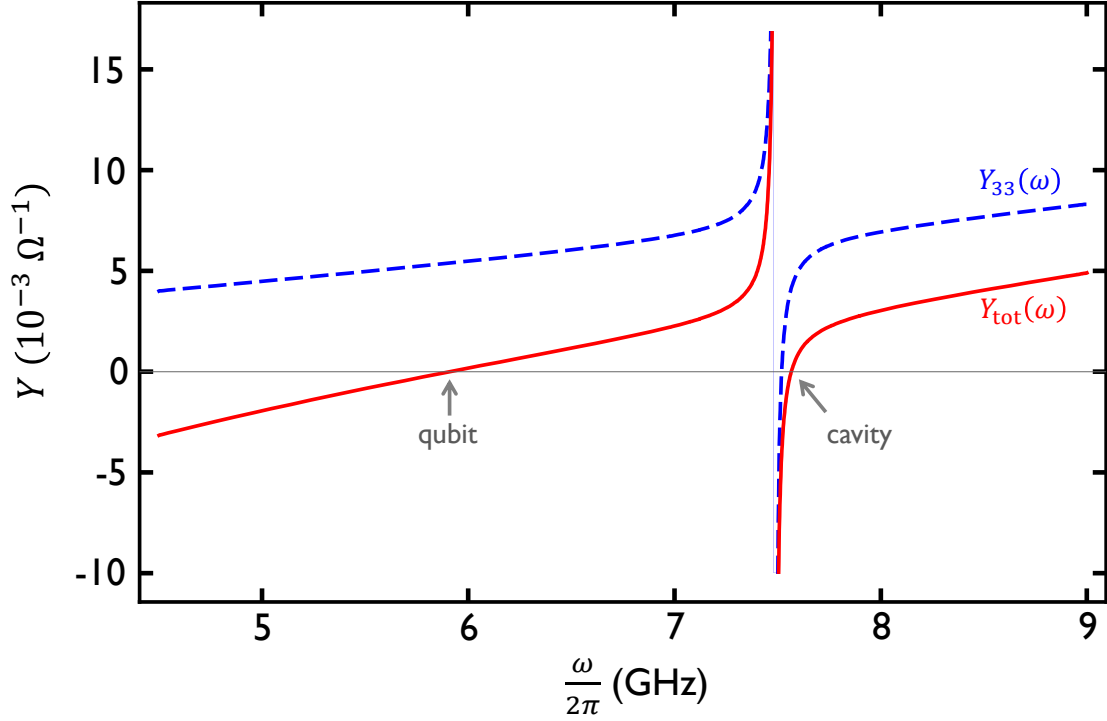


Fig. 3.5 Blackbox quantization results for simulating the transmon SPP-v1-Q7. I set $L_{J0} = 4.5$ nH to obtain the qubit frequency $\omega_q \approx 5.9$ GHz and the cavity frequency $\omega_r \approx 7.6$ GHz.

bound for the lifetime.

It should be noted that Solgun *et al.* [78] have developed a more advanced and accurate method to perform quantization of superconducting quantum circuits. However, the relative simplicity of BBQ makes it particularly useful for design work, and I found that the resulting simulated parameters for my single-transmon and two-transmon devices were accurate to within a few percent. For these reasons, I continued using the original BBQ method developed by Nigg *et al.* [76].

3.5 Transmon Fabrication

My transmons were fabricated in the LPS cleanroom using electron-beam lithography, and double-angle evaporation, with both the Josephson junction and the shunting capacitor pads deposited at the same time. I first cleaned a 3" c-plane oriented polished sapphire wafer [79] using acetone, methanol, and isopropyl alcohol (IPA). I then spun on a 900 nm layer of MMA(8.5)MAA EL11 [80] at 1000 rpm for 60 s, and baked the wafer in an oven for 5 min at 180 °C. After letting the wafer cool down, I spun a 100 nm layer of ZEP520A DR2.3 [81], and baked the wafer for the second time in an oven for 5 min at 180 °C. The wafer was then hard baked for 30 min at 180 °C. I then used a thermal evaporator to deposit a 10 nm thick Al layer over the ZEP, to act as an anti-charging layer during e-beam writing. Here, I used a thermal evaporator, to ensure that there was no stray ultraviolet or x-ray exposure of the e-beam resist layers, as one would get with an electron-beam evaporator. I next spun on a 5 μm thick coating of FSC-M resist [82] at 2000 rpm for 60 s, to protect the lower layers of the wafer during dicing. The wafer was finally baked at 120 °C for 3.5 min to evaporate any remaining solvents. After the protective layer was applied, I diced the wafer into 5 mm × 7 mm chips using a Dicing Blade Technology Type CA-010-270-080H blade [83] in a Disco DAD3220 dicing saw [84]. Individual chips were cleaned, patterned and processed when I had to fabricate a device. This completed the initial processing of the sapphire wafer, and I note that this process was nominally identical to that used by Suri [48] and Novikov [72].

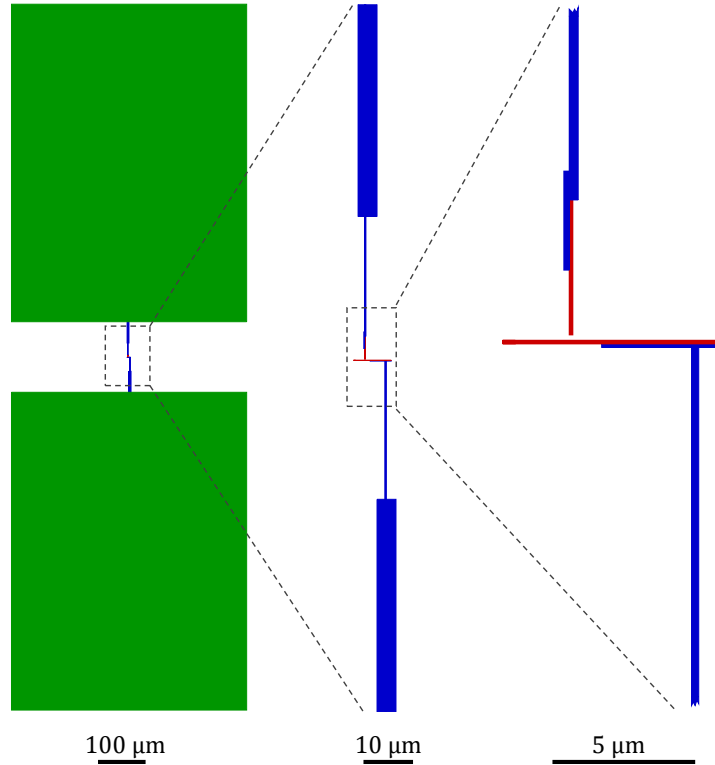


Fig. 3.6 The computer aided design (CAD) of the transmon for the electron beam writing. Three different magnifications are depicted to successively show the details from the shunting capacitor pads to the Josephson junction region.

Prior to e-beam patterning of a chip, I removed the protective FSC-M layer using successive 40 s dips in Acetone, Methanol and IPA. I then used a JEOL JSM-6500F scanning electron microscope (SEM) at LPS to write the pattern (see Fig. 3.6). The blue and red regions in Fig. 3.6 were written at a magnification of 500x while the green capacitor pads were written at a 70x magnification. For the fine red regions, I used a dosage of $175 \mu\text{C cm}^{-2}$, while the green/blue regions were written with a dosage of $100 \mu\text{C cm}^{-2}$. The horizontal red line had a pattern width of 100 nm and the vertical red line had a pattern width of 125 nm. The two red regions were separated by 200 nm to form the suspended bridge [85] for the double-angle evaporation of the JJ. I note

that the smaller features were written at a beam current of ~ 30 pA while the pads were written at a current of ~ 2.5 nA.

After the e-beam writing, I removed the anti-charging layer by first agitating the chip in a beaker of OPD 4262 [86] for 60 s, then agitating the chip in a beaker of de-ionized water for 60 s, followed by a quick 3 s dip in IPA, and finally blow drying with nitrogen.

I next developed the ZEP by agitating the chip in a beaker of Amyl Acetate [87] for 2 min, followed by a 1 min agitation in a beaker of IPA, and completed this step with blow drying using nitrogen. After developing the ZEP, I imaged the chip with a Keyence confocal laser microscope to obtain optical micrographs as shown in Fig. 3.7. After imaging the chip, I developed the MMA by first agitating the chip in a 5:1 volume ratio solution of IPA:DI for 260 s, followed by a 60 s agitation in de-ionized water, and finally blow drying. Following MMA development, I imaged the chip again with the Keyence microscope to obtain micrographs as shown in Fig. 3.8.

I performed the two imaging steps after development to ensure that there were no problems with the developed patterns. When the process was successful, the micrographs after ZEP development clearly showed the existence of the bridge region (see Fig. 3.7), and the micrographs obtained after MMA development allowed me to confirm that the undercut was as expected (see Fig. 3.8).

After development, the chip was placed in a thermal evaporator dedicated for Al deposition. The evaporator had a custom-built chamber with commercial vacuum components. This evaporator was pumped to $< 1 \times 10^{-6}$ torr over 12 h using a Varian turbomolecular pump. Aluminum was deposited at two angles from the normal to

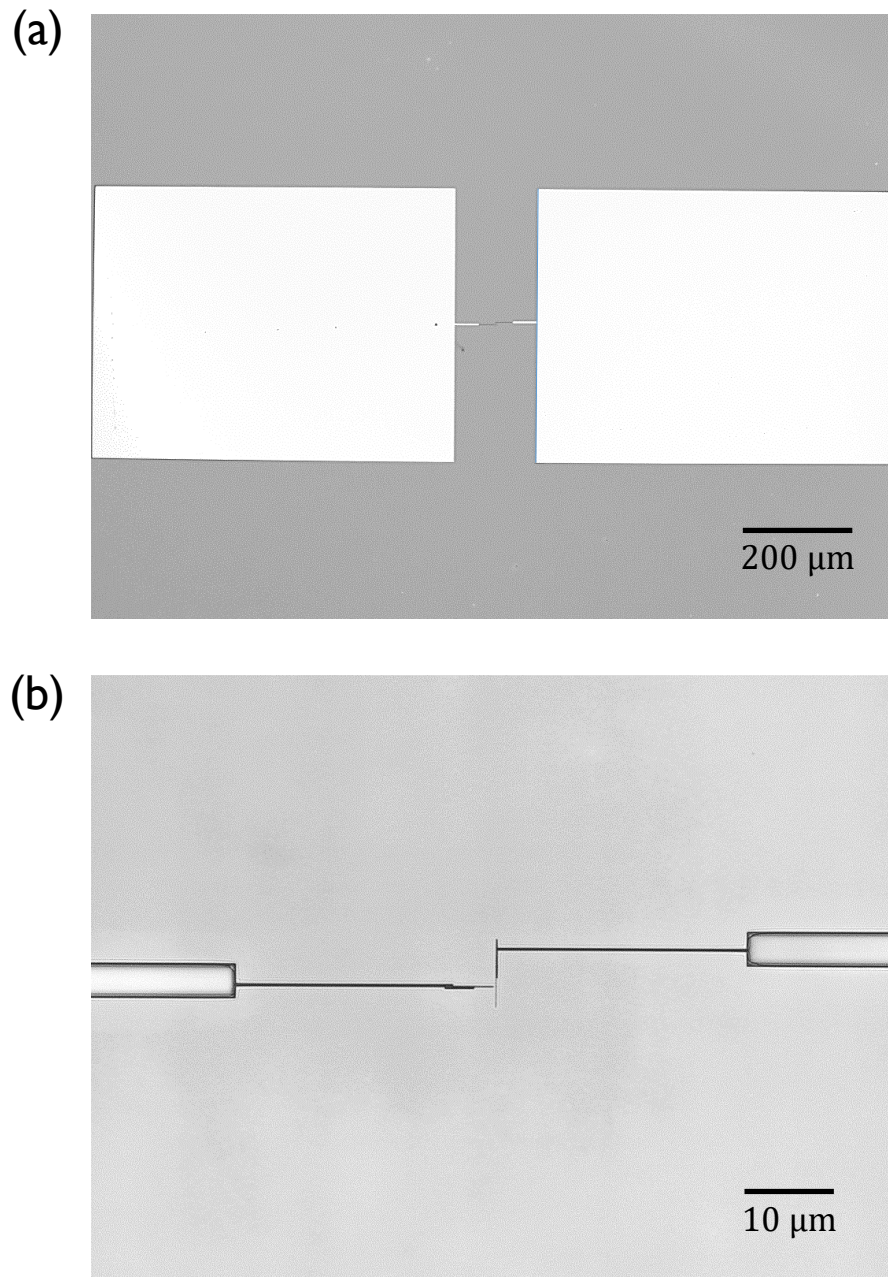


Fig. 3.7 (a) 10x and (b) 150x magnification photomicrographs of the resist layers after developing ZEP.

the chip, following the double-angle evaporation technique introduced by Dolan [85]. The first Al layer had a thickness of 30 nm and was deposited at an angle 12.5° to the normal. I then oxidized the Al surface to create the insulating barrier for the JJ;

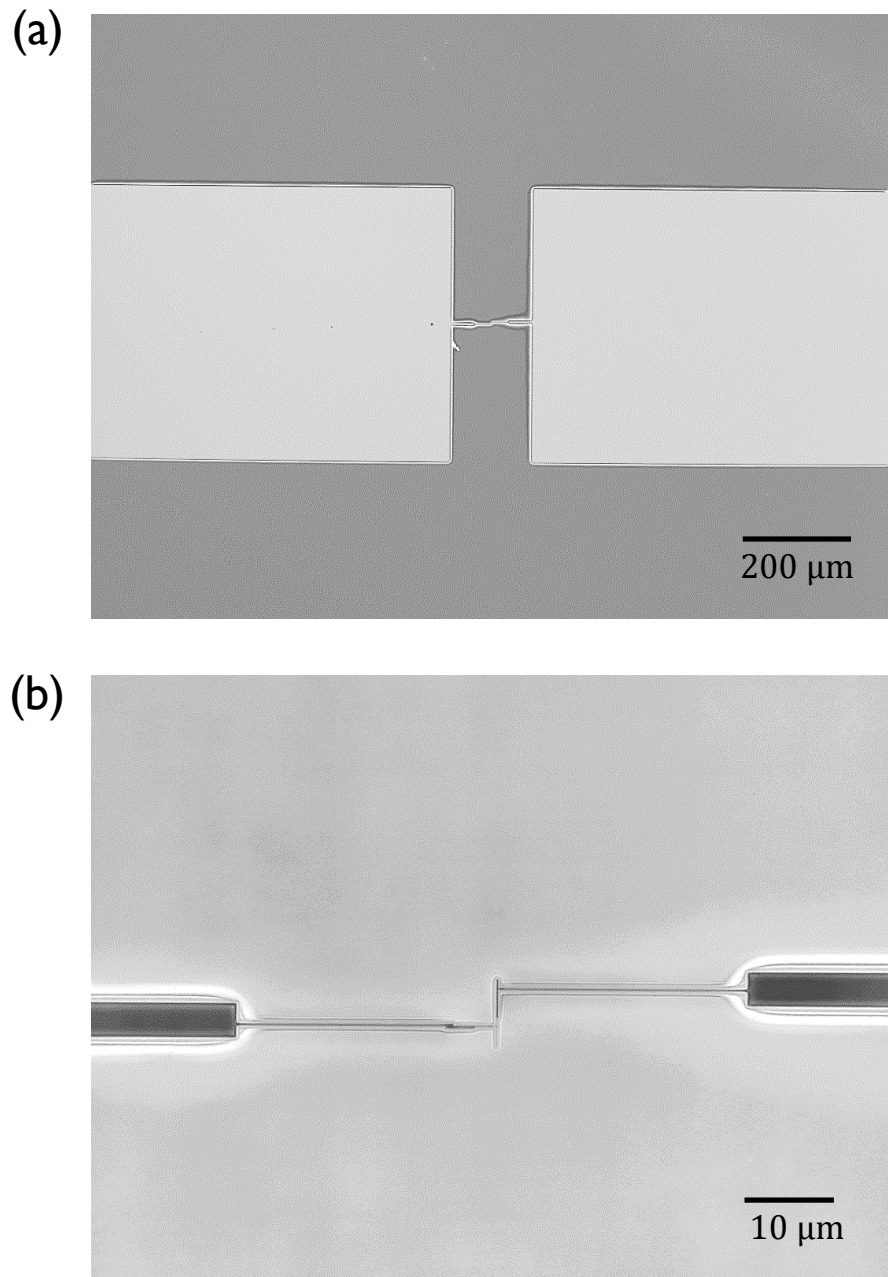


Fig. 3.8 (a) 10x and (b) 150x magnification photomicrographs of the resist layers after developing MMA.

typically at an O_2 pressure of ~ 16 Pa for ~ 5 min. The chamber was evacuated again, and I deposited the second Al layer with a thickness of 50 nm at an angle -12.5° . Finally a passivation step was performed by oxidizing the device for ~ 20 min at an O_2

pressure of ~ 33 Pa.

When fabricating the JJ, the duration of the oxidation was the primary factor I used to control the tunnel barrier thickness. To determine a good value for the duration, I built multiple test junctions simultaneously and measured their resistance, to obtain statistics for the JJ characteristics. These resistances were compared to the target value for R_J , that I found using my designed value for E_J (see [Sec. 3.4](#)) and the Ambegaokar-Baratoff formula [[34](#), [88](#)],

$$R_J = \frac{h}{e^2} \frac{\Delta_{\text{Al}}}{8E_J}. \quad (3.2)$$

I used $\Delta_{\text{Al}}/e \approx 210 \mu\text{eV}$ as the superconducting energy gap for thin-film Al. Bulk Al has a superconducting energy gap of $170 \mu\text{eV}$ [[89](#)], but the value used here is slightly larger because thin superconducting films of Al are well-known to have a larger gap [[89–94](#)]. Since I typically wanted $E_C/h \approx 200$ MHz and $E_J/h \approx 20$ GHz so that $E_J/E_C \approx 100$, [Eq. \(3.2\)](#) yielded a target value of $R_J \approx 8 \text{ k}\Omega$.

To complete the fabrication of a transmon, I had to lift-off the remaining unexposed resist. I used a modified version of the lift-off recipes developed by Novikov [[72](#)] and Suri [[48](#)]. First, I set a hotplate to 125°C , and used it to heat two crystallizing beakers each with 125 ml of Microposit-1165 for ~ 1 h; the liquids reached a steady-state temperature of $\approx 80^\circ\text{C}$. The processed chip was then placed in the first beaker for 60 min and agitated every 8 min. Next, I transferred the chip to the second beaker and agitated every 3 min. After 15 min, the chip was thoroughly cleaned using IPA and DI water, and blown dry. I placed completed chips in a plastic container which itself

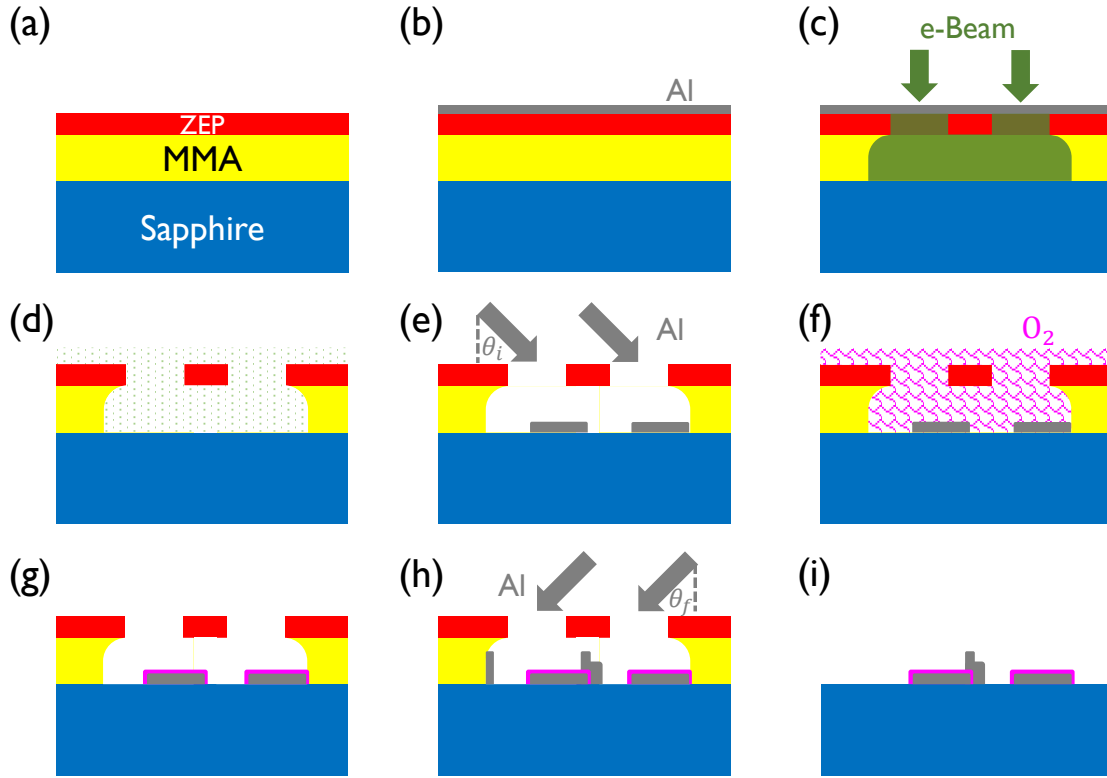


Fig. 3.9 Summary of the transmon fabrication process. (a) Spinning the dual-resist layer on sapphire, (b) depositing the Al anti-charging layer and dicing the wafer into chips, (c) electron-beam exposure in SEM, (d) development of the resists, (e) 30 nm deposition of Al at $\theta_i = 12.5^\circ$ to normal, (f) oxidation of Al, (g) completed oxidation (h) 50 nm deposition of Al at $\theta_f = -12.5^\circ$ to normal, and (i) lift-off for MMA resist.

was encased in a static shielding bag, to prevent destruction when handling. The full fabrication process is depicted in Fig. 3.9.

3.6 Cavity Fabrication

Using the electromagnetic simulations discussed in Sec. 3.3, I designed a cavity with suitable dimensions (see Fig. 3.10), and had the LPS machine shop build several

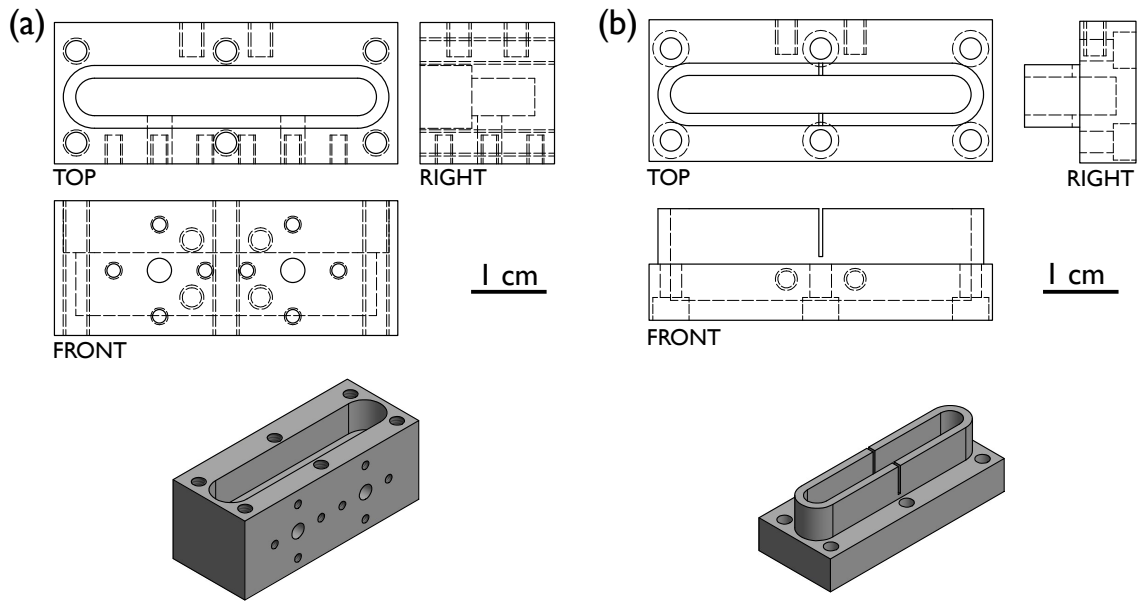


Fig. 3.10 (a) Orthographic projections and 3D perspective view for base and (b) lid of the microwave cavity.

from 6063 Al alloy. This is a corrosion-resistant, non-magnetic, hardened alloy. The cavities were made of superconducting Aluminum to minimize resistive losses from the cavity surfaces.

3.6.1 Cavity Cleaning and Preparation

After machining, I had to do some additional preparation work on the cavity to achieve a relatively high internal quality factor Q_i . First, it was necessary to clean debris from the small scratches and crevices that were created during machining. In particular, the blind tapped holes would tend to collect loose metal fragments and lubricants from the machining. I used dental picks and tweezers to dislodge, break apart, and extract the debris. Although the tools might seem unconventional in a

physics laboratory, their strength, reach, and maneuverability made them well-suited for my purpose. Of course these tools were designed to work with cavities, although not those made of Aluminum.

After the debris was removed, I thoroughly degreased, cleaned, and etched the two pieces of the cavity according to the following steps:

1. Degreasing by ultrasonication in successive baths of acetone, methanol, IPA, and de-ionized (DI) water for ≈ 10 min each.
2. Cleaning in a 50°C heated Alconox detergent bath for 10 min with a magnetic stirrer.
3. Etching in two successive baths of Avantor Aluminum Etch 80-15-3-2 at 50°C for 60 min each. A magnetic stirrer was used for agitation, along with periodic rotation of pieces to remove attached gas bubbles.
4. Thorough rinsing of pieces with DI water spray.
5. Cleaning in a 50°C heated Alconox detergent bath for 1.5 h with a magnetic stirrer to neutralize any remaining acid.
6. Thorough rinsing with DI water spray, followed by immediate drying with compressed nitrogen.
7. Drying the cavity pieces on a hotplate at 150°C for 1.5 min to evaporate residual chemicals.

Etching removes material, and makes holes and slots larger. This effect is more

pronounced for smaller features, and it is necessary to take this into account during the design phase.

3.6.2 Cavity Tuning and Packaging

I coupled microwaves into and out of the cavity using SubMiniature version A (SMA) feedthroughs. The flange of the connector was secured to the outer surface of the cavity and a pin connected to the inner conductor protruded into the cavity space. The coupling of the pin to a cavity mode will depend on the physical position of the pin, the length of the pin, and the mode. For example, with pins located as in [Fig. 3.2](#), we would expect the coupling to the TE_{101} mode to be lower than for the TE_{102} mode since the pins are further from the single anti-node of the electric field of the TE_{101} mode than they are from the antinodes of the TE_{102} mode; the proximity of the coupling pins to the anti-nodes of the electric field determine the strength of capacitive coupling to the pins. Conversely, the proximity of the coupling pins to the anti-nodes of the magnetic field would determine the strength of inductive coupling to a coil shaped termination of the line.

The strength of coupling between the coaxial line and the cavity for a given cavity mode is primarily adjusted by changing the length of the center conductor pin of the SMA jack. In general, as the pin protrudes further into the cavity the coupling will increase. However, it should be noted that beyond a certain critical length, the coupling decreases. This is due to the metal in the pin causing a large distortion of the cavity modes, which can essentially be shorted out by the pin. This critical length for

the protrusion of the pin was observed to be ≈ 1 mm when measured from the inner surface. My procedure for tuning the SMA port couplings of the cavity was as follows:

1. I placed a sapphire chip with a test device in the cavity lid slot for the qubit. Then, using an Indium gasket around the lip of the lid, sealed the cavity and secured it using screws.
2. I attached two identical unmodified non-magnetic EZ Form #705615-801 SMA feedthroughs to the cavity. Obtained the parameter $S_{21}(\omega)$ and fit it using the method described in [Appendix A](#). From this fit, I determined the coupling quality factors (Q_{in} and Q_{out}) for the input and output generic ports ($Q_{\text{in}} = Q_{\text{out}} \sim 10^6$).
3. I removed the generic SMA output feedthrough. The remaining input port had known coupling Q_{in} . To achieve the best results, I input the desired coupling values and calculate the target values for S_{22} and S_{21} at resonance as well as the total Q for the desired cavity mode.
4. I next made a modified output port by extending the center pin of another SMA connector. To do this, I used a short piece of Coax Company SC-219/50-SC low-loss semi-rigid coaxial cable with a silver-plated copper center conductor. I removed the outer conductor and the teflon jacket to obtain just the center conductor. After snipping off a ≈ 6 mm piece, I soldered it to the center conductor of a generic SMA feedthrough. This ensured that the pin was reaching well into the cavity. I obtained VNA measurements of S_{22} and S_{21} versus frequency and fit this data, to determine the coupling Q_{out} for the modified port. If the coupling

Q was too low, I removed the connector, trimmed the pin's length, reattached, and re-measured the coupling Q . The procedure was repeated until the desired coupling Q was obtained for the given port. Typically I wanted $Q_{\text{in}} \sim 10^5$ and $Q_{\text{out}} \sim 10^4$. The actual cavity Q values used in experiments are listed in [Sec. 5.9](#).

5. After the first pin was adjusted as desired, I replaced the connector with another SMA jack with an elongated center pin. The trimming and fitting process was repeated until that port was properly set up as well. This method was suitable for setting up couplers with $Q \sim 10^3$ – 10^6 . After both pins were set, I removed the control port and replaced it with the first modified port.
6. I unsealed the cavity, replaced the test chip with the actual transmon chip, placed In pieces between the chip and the slot, and secured the chip. I next applied a fresh In seal around the lip of the cavity lid, and sealed the cavity using McMaster-Carr non-magnetic Al screws. Finally, I note that I had to take proper precautions against electrostatic discharge while mounting the transmon chip in the cavity.

3.6.3 Details of Fabricated Cavities

For my experiments, I had the LPS machine shop build four nominally identical cavities based on my design, using 6063 Al from the supplier McMaster-Carr. After receiving the cavities, I prepared them as described in [Sec. 3.6.1](#). A few details on the cavities are given in [Table 3.1](#). [Figure 3.11](#) shows a photograph of the cavity 6D. A summary of parameters for microwave cavities used in experiments is listed in [Sec. 5.9](#).

Table 3.1 List of fabricated cavities

Fabrication date	Cavity Name	Note
7/1/2014	6C	Initial Machining
7/1/2014	6D	Initial Machining
4/8/2015	6F	Initial Machining
4/8/2015	6G	Initial Machining
9/26/2017	6G	Modification to have two chip slots

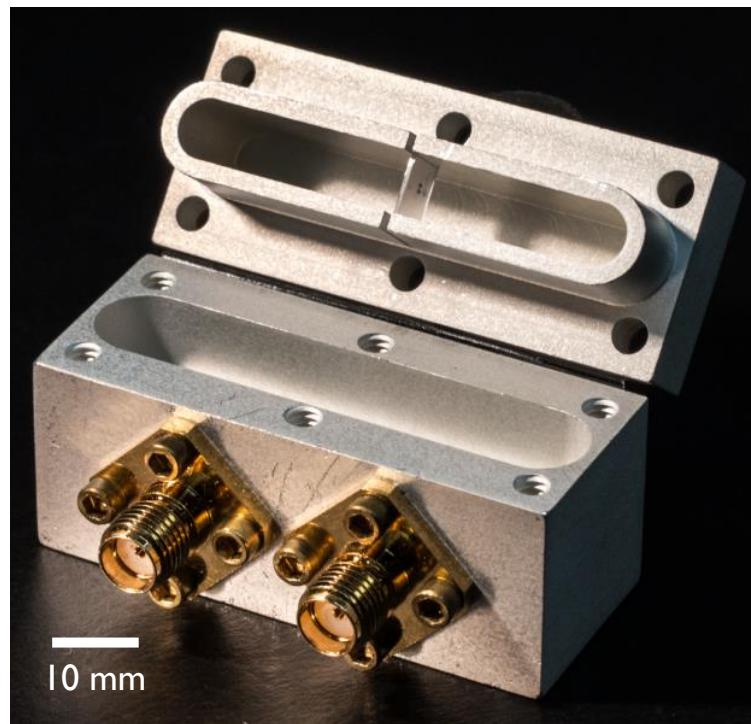


Fig. 3.11 Photograph of cavity 6D

CHAPTER 4

Experimental Setup for Controlling and Measuring

Qubits

Superconducting quantum integrated circuits are currently one of the leading candidates for building a scalable quantum computer. Given that superconducting circuits can be fabricated with a wide range of parameters, there is a very large phase space of possible device parameters. This space is greatly reduced due to technological and practical considerations [95]. For superconducting qubits, I will assume that we need to satisfy:

$$k_B T \ll \hbar \omega_q \ll 2\Delta \quad (4.1)$$

where T is the operating temperature of the environment that is coupled to the qubit, $\omega_q/2\pi$ is the qubit transition frequency, and Δ is the energy gap of the superconductor [95]. The first inequality in Eq. (4.1) allows a qubit to be initialized in its ground state by simply waiting much longer than the relaxation time T_1 , and it also minimizes thermal excitation. The second inequality in Eq. (4.1) must be satisfied to minimize

thermal generation of quasiparticles by breaking Cooper pairs. Both requirements can be satisfied by using a superconductor with $T_c > 1$ K and keeping characteristic transition frequencies in the 5 GHz to 10 GHz range [95]. The qubits I fabricated were made from thin films of Al ($T_c \simeq 1.2$ K) and had $\omega_q/2\pi$ in the range 5 GHz to 6 GHz, while the Al cavity had a resonance frequency $\omega_r/2\pi \approx 8$ GHz.

4.1 The Dilution Refrigerator Setup

Since I designed my devices to have characteristic frequencies between 5 GHz and 10 GHz, I needed to cool them down to well below 1 K. In practice, for thin film Al devices we find loss from thermally generated quasiparticles to be significant for $T \geq 150$ mK. Keeping $T \sim 20$ mK also ensures that the Boltzmann factor $e^{-\hbar\omega_q/kT} < 10^{-6}$, resulting in minimal thermal excitations of the qubit or cavity. The most popular method for cooling superconducting qubits is the ^3He - ^4He dilution refrigerator [96]. Dilution refrigerators offer continuous operation at temperatures as low as a few mK, which is ideal for satisfying Eq. (4.1) [97].

All my experiments were conducted in a Leiden CF-450 cryogen-free dilution refrigerator [98]. This apparatus had a nominal cooling power of $\sim 450 \mu\text{W}$ at a mixing chamber temperature of 120 mK. The first two stages of the Leiden refrigerator were cooled by a two-stage pulse tube cryocooler to 50 K and 3 K, respectively. The qubit or qubits were mounted in an Al cavity that was thermally anchored to the mixing chamber stage, which had a base temperature of 15 mK. The operation of this



Fig. 4.1 Photograph of the CF-450 Dilution refrigerator with two Cu mounting posts. The thermal shields and cryoperm shields have been removed.

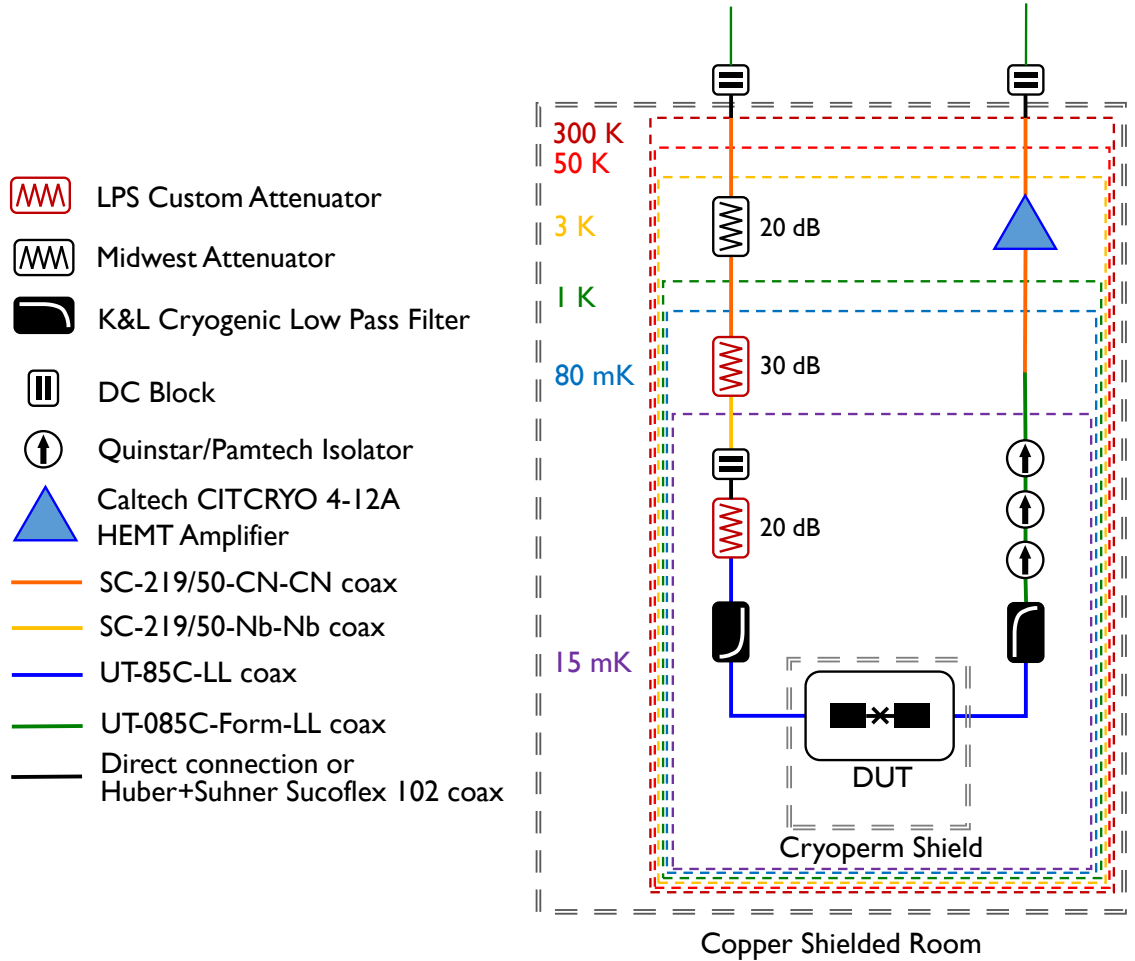


Fig. 4.2 Input/Output microwave lines in the dilution refrigerator.

refrigerator, and details of the apparatus, are described extensively by Novikov [72].

Figure 4.1 shows a photograph of our CF-450 dilution refrigerator.

While the refrigerator cools to 15 mK, it is very challenging to ensure that the microwave signals propagating to the device are well-thermalized to a low temperature. Thermal noise on the input or output lines can produce unwanted excitation of the qubit and cavity, and lead to relaxation and dephasing [56, 57, 99, 100]. To block external RF interference, and to ensure thermalization of noise on the input signal

line to the device-under-test (DUT), broadband attenuators are placed strategically at various cooling stages in the dilution refrigerator (see Fig. 4.2). Although these attenuators filter out high-frequency blackbody noise emanating from the 300 K stage electronics, they also generate blackbody radiation corresponding to their operating temperature. The refrigerator I used had an input line with 70 dB of attenuation from lumped element components and further attenuation contributed by cupro-nickel coaxial cables used for some sections (see Fig. 4.2). This yielded a noise temperature ≤ 50 mK for signals reaching the DUT [57]; this was significantly higher than the base temperature of the refrigerator, for reasons that are still not well-understood. The 30 dB and 20 dB attenuators at the cold plate and mixing chamber stages (see Fig. 4.2) were custom-made by Dr. Jen-Hao Yeh to have high cooling-power and low noise temperature at cryogenic temperatures [57].

The output line from the cavity had 60 dB of directional isolation provided by two Pamtech CWJ1015-K3 isolators and one Quinstar QCI-075900X000 isolator (see Fig. 4.2). The input and the output lines to the device also had K&L 11L250-12000/T20000 low-pass filters (LPFs) with a 12 GHz cutoff to block noise that could cause excitations of higher modes of the cavity. The output signal from the cavity was amplified at 3 K by a Caltech CITCRYO 4-12A high-electron-mobility-transistor (HEMT) amplifier which had a nominal noise temperature $T_n < 5$ K [101].

The DUT was enclosed in two Amuneral Manufacturing Amumetal 4K cryoperm shields [102] to protect the device from low-frequency magnetic fields. These shields were attached to the mixing chamber stage. The mixing chamber stage (at 15 mK) had no dedicated shield, but both the cold plate stage (at 80 mK) and the still stage

(at < 1 K) had Au-plated Cu shields. The 3 K, 50 K, and 300 K stages all had Al shields. The 3 K and 50 K shields were wrapped in blankets of Aluminized Mylar. The 300 K and 50 K stages composed the outer vacuum chamber (OVC), while the stages at 3 K and below composed the inner vacuum chamber (IVC). There were no other magnetic shields used at room temperature. The entire dilution refrigerator was housed in a grounded Cu shielded room to reduce electromagnetic interference.

4.2 Vector Network Analyzer

A vector network analyzer (VNA) is a powerful instrument for characterizing a microwave network based on its scattering parameters (S-parameters) [103]. The S-parameters are obtained by measuring the amplitude and the phase of reflected and transmitted signal components with respect to a DUT. The Agilent 5071C VNA I used has an internal microwave source that can sweep the frequency while simultaneously measuring the two-port S-parameters, making it very useful for microwave spectroscopy of qubits and cavities. I used the VNA to accurately measure the loaded quality factor of the cavity at 15 mK, and at room temperature to tune the cavity coupling ports as described in [Sec. 3.6.2](#).

I mainly used the Agilent E5071C VNA for preliminary characterization of our devices. After a device was cooled to 15 mK, I first measured transmission through the cavity as a function of frequency. Although the cavity was designed to have predetermined spectra, due to imperfections during machining, chemical processing and

variations in mounting the qubit chip, its frequency would inevitably vary slightly from the design value. Furthermore, due to thermal contraction and changes in the London penetration depth, the frequency changes when cooling the device from 300 K to 15 mK; the room temperature value was a good starting guess. This simple measurement also allowed me to determine if there was a serious problem with the qubit.

It is known that the cavity transmission at high power (average cavity photon number $\bar{n}_{\text{cav}} \sim 10^6$), is insensitive to the state of the qubit and the cavity resonance frequency will be at the bare frequency $\omega_r^{(\text{bare})}$ [104]. However, when a low power is used ($\bar{n}_{\text{cav}} \leq 10$), the dressed cavity resonance $\tilde{\omega}_r$ depends on the state of the qubit (see Fig. 2.3). By sweeping the output signal power from the VNA during spectroscopy, I examined these two regimes and checked that the qubit had a well-behaved response (see Fig. 5.2). Furthermore, measuring the shift $\chi_{\text{ge}} = \omega_r^{(\text{bare})} - \tilde{\omega}_r^{(|g\rangle)}$ allowed me to estimate the dispersive shift between the cavity and the transmon qubit.

4.3 Heterodyne Pulsed Measurement System

Most of the qubit gate operations I used were accomplished by applying one or more discrete microwave pulses. Since qubits have a limited lifetime, it was also necessary to perform qubit measurement using a pulsed measurement system. Most of my measurements and control operations were carried out using a pulsed control and measurement setup (see Chapter 5). Although the VNA offered exquisite measurement capability for continuous-wave applications, for gating and qubit state measurements,

I used the customized setup depicted in Fig. 4.3. The qubit state was interrogated by measuring the transmission of pulsed signals through the cavity. The apparatus was set up for signal detection at either the bare or dressed cavity frequency, depending on whether I used a high-power or low-power readout technique (see Sec. 5.2).

To perform digital signal processing on the data, an analog-to-digital converter was used to convert the high frequency microwave signals from the cavity output line to a digital record (see Fig. 4.3). The two most commonly used methods for radio-frequency (RF) signal down-conversion are “homodyne” and “heterodyne” [105]. Homodyne detection is also known as direct-conversion, since the original RF signal is mixed with a local oscillator (LO) signal which is operated at the same frequency, *i.e.* $\omega_{\text{LO}} = \omega_{\text{RF}}$, to yield a zero-frequency measurement signal. By using an IQ mixer which mixes the sine and cosine components separately, it is possible to perform a quadrature measurement of the RF signal. Although homodyne detection has fewer components such as synthesized signal generators, it can be difficult to correct and compensate for non-idealities present in the IQ mixer. These non-idealities can depend on the frequency and amplitude of the LO, harmonic distortions, as well as DC offsets [105].

As an alternative, heterodyne detection involves down-conversion to an intermediate frequency (IF) using a heterodyne receiver. With this type of receiver $\omega_{\text{IF}} = \omega_{\text{LO}} - \omega_{\text{RF}}$, and an IF frequency $\omega_{\text{IF}} \sim 1 \text{ MHz to } 10 \text{ MHz}$ was suitable for my cQED applications. The in-phase and quadrature (I/Q) components of the RF signal were extracted from the measured amplitude and phase of the IF signal. For high-performance detection, it is also possible to use a superheterodyne receiver which performs double

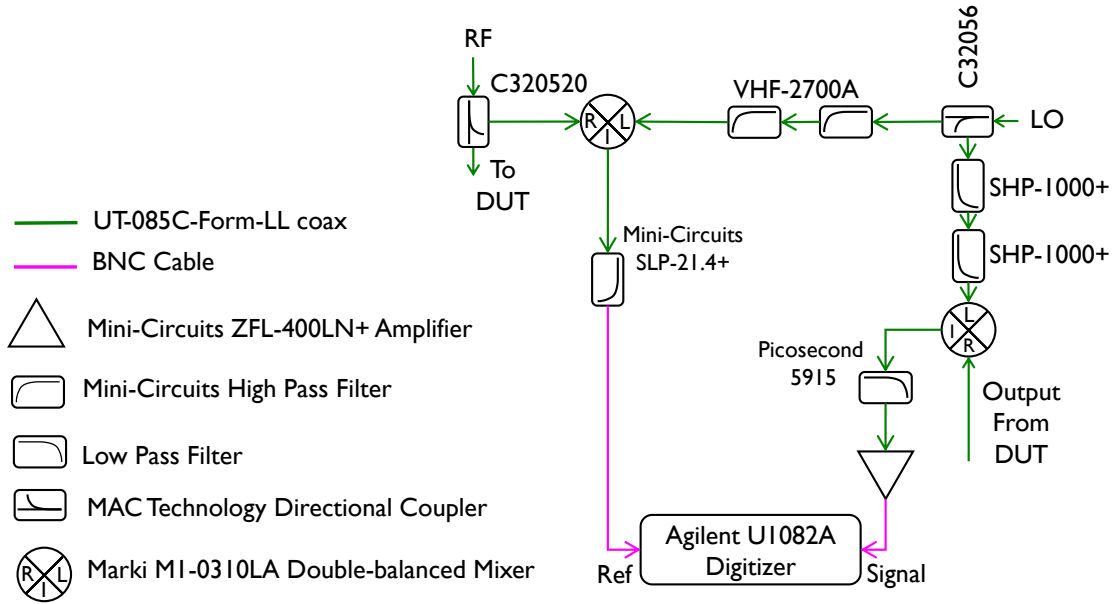


Fig. 4.3 Heterodyne setup for measuring reference signal and the output signal from the DUT.

down-conversion with two different LO and IF frequencies. Double-conversion or an image reject mixer can be used to prevent image noise fold-over [106, 107]. Although a heterodyne detection system has more complex circuitry and also requires a separate LO signal generator, it is insensitive to harmonic distortion and DC offsets, and does not require calibration for accurate I/Q measurements [105].

All my pulsed qubit measurements were performed with a single-conversion heterodyne detector shown schematically in Fig. 4.3. The input signal to the DUT was separated into two branches using a 20 dB directional coupler and the LO signal was separated into two branches using a 6 dB directional coupler. One branch of the input signal was mixed with the filtered LO signal and used as the reference waveform for the digitizer. The other branch of the input signal was sent to the DUT. The output signal from the DUT was mixed with the second branch of the LO signal, filtered, and

amplified, before being sent to the second input channel on the digitizer. The I/Q demodulation was performed using software in LabVIEW. In my measurements, I set $IF = 10$ MHz and used 1000 onboard averages of the voltage using the Agilent Acqiris 1082A digitizer board to perform measurements efficiently.

To ensure phase matching during acquisition and averaging, the RF signal generator and the digitizer were triggered by the same source, which was an Agilent 33250A arbitrary waveform generator locked to a Rb atomic clock (see [Fig. 4.4](#)).

4.4 Microwave Signal Generators

4.4.1 Synthesized Signal Generators

For signal generation, I used Agilent E8257D/E8267D synthesized signal generators (SSGs) that output a highly coherent continuous analog tone at a set frequency (300 kHz to 20 GHz). By triggering the SSG output signal, I generated pulsed wave trains with high accuracy and precision. The time between the trigger reception and pulse output had a minimum duration of 70 ns for the Agilent SSGs. When timing pulses from different SSGs with respect to each other, this delay had to be properly accounted for. Unfortunately, it is not possible to have in-phase and quadrature (I/Q) control solely using a triggered SSG. Hence, I used these instruments for preliminary qubit characterization, and to perform measurements which did not require I/Q control such as Rabi oscillations and Ramsey oscillations (see [Chapter 5](#)).

4.4.2 Arbitrary Waveform Generators

I used arbitrary waveform generators (AWGs) capable of digitally generating arbitrary waveforms, as signal sources for my experiments. With these complex instruments, a user can program any desired waveform as a series of voltage values versus time (waypoints), and the AWG will generate the specific waveform, within its bandwidth and voltage resolution limitations. The output of AWGs are limited in their frequency range by the sampling rate, in their voltage resolution, and the maximum length of pulses.

The Tektronix AWG70002A that I used for device control had a sampling rate of 25 GSa/s, while the microwave signals used in our experiments had frequencies in the range 4 GHz to 8 GHz. Based on the sampling theorem attributed to numerous scientists and engineers [108–110], real-world AWGs can faithfully generate analog signals up to 40% of its sampling rate [111]. Since the device frequencies in our system were < 10 GHz, the Tektronix AWG70002A had the capability to directly generate the required pulses for qubit and cavity control. For my experiments, I fixed the sampling rate at 25 GSa/s and made any change in signal frequency directly by adjusting the waypoints.

For all programmed waveforms, the instrument had a minimum waveform length of 2400 samples and a maximum waveform length of 8×10^9 samples per channel, limited by the AWG memory of 16 GB. At 25 GSa/s, the shortest pulse corresponded to a minimum length of 96 ns and the longest pulse corresponded to a maximum length of 320 ms. Although most of the waveforms I programmed into the AWG had

lengths > 96 ns, to simplify programming, all the waveforms I created had a 100 ns length zero-voltage buffer-zone at the beginning. Each pulse train was designed in LabVIEW and uploaded as a text file to the AWG via an ethernet connection. The text file consisted of a discrete set of voltage values at the maximum sampling rate of the instrument. Following upload, each text file was read using the AWG's internal software and stored in its native format in the AWG memory. The experiments were then carried out by loading the waveforms sequentially into the AWG70002A and using an Agilent 33250A AWG to trigger qubit or cavity pulses (see [Fig. 4.4](#)).

4.5 Device Control and Measurement

The essential components of the device control and measurement network have been described in previous sections. Here, I take a holistic approach and trace the path of microwave signals from generation to detection (see [Fig. 4.4](#)).

For preliminary characterization, all the signal generators shown in [Fig. 4.4](#) are disconnected, and the E5071C VNA is used both as the signal source and the detector. In this configuration, the output signal from the top of the refrigerator is amplified by a single MITEQ amplifier before being fed into the VNA input.

For pulsed qubit control and heterodyne measurements, the Agilent 33250A cavity AWG was set up with the proper timing, to trigger its counterpart Agilent 33250A qubit AWG, and the cavity SSG E8267D. The qubit AWG was in turn used to trigger the qubit signal generator (either Tektronix AWG70002A or Agilent E8257D). A third SSG

E8257D was used to apply a third tone, if necessary. The latter SSG could either be set in continuous mode or triggered mode. The signals from the three signal generators are routed through a Weinschel programmable attenuator and combined using two 6 dB MAC attenuators (see Fig. 4.4). The combined microwave drive signal passed through a DC block at the wall of the shielded enclosure and entered the input line at the top of the dilution refrigerator.

As the drive signal passed through the cold stages, it was progressively attenuated in the cupro-nickel cables (from 300 K to 0.08 K) and lumped element attenuators (70 dB total attenuation). A Nb cable was used at the 80 mK stage to limit the conduction of heat from higher temperature stages. The heavily attenuated signal was further filtered with a LPF at the mixing chamber stage before being fed to the input pin of the cavity.

The output signal from the DUT then passes through another LPF and three isolators. The isolators and the LPF work in conjunction to prevent thermal noise from propagating down the output line from the 3 K stage to the cavity output pin. The output signal was amplified at 3 K with a Caltech HEMT amplifier [101] and further amplified at room temperature with a MITEQ low-noise amplifier [112]. This signal was then mixed to a lower IF using the heterodyne system before being digitized by the Agilent 1082A digitizer. All the signal generators were synchronized with a single Stanford Research Systems FS725/2 Rubidium frequency standard, to prevent drift.

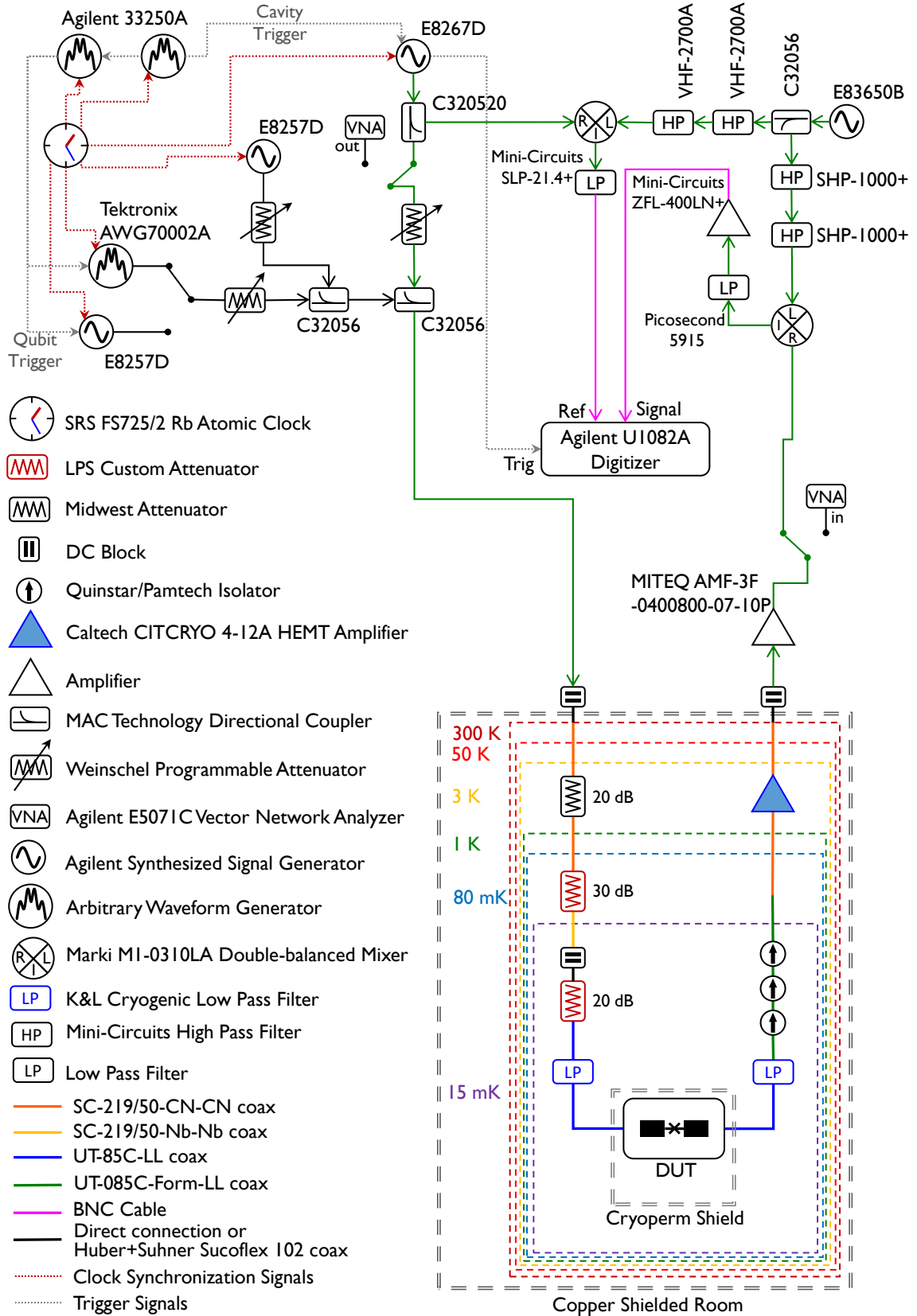


Fig. 4.4 Schematic of circuit for controlling and measuring transmon qubits.

CHAPTER 5

System Characterization

Device characterization is an essential component in quantum computing, especially so in superconducting qubits. Due to the propensity for the transition frequencies, couplings, and other qubit parameters to vary somewhat from one cooldown to the next, it is important to properly characterize the devices at the beginning of each experiment run. Parameters can also drift slightly during a run, and occasional calibration checks are a good idea. This helps to ensure that quantum gating operations are performed accurately. The basic physics of Rabi oscillations, relaxation time measurements, Ramsey oscillations (Ramsey fringes), and spin-echo measurements are described in detail by Meystre and Sargent III [53] and in many other places. In this chapter, I will focus on the experimental approach to characterize my transmons.

5.1 Cavity Spectroscopy

I began the characterization process by performing spectroscopy near the cavity frequency versus drive power. This revealed the quality factor of the cavity and let me determine a good pulse length for reading out the transmon state. The spectroscopic measurements also allowed me to determine a preliminary power bias point for the high-power qubit readout. As mentioned in [Sec. 4.2](#), it was particularly convenient to perform this spectroscopy using the VNA.

[Figure 5.1](#) shows an example where I did cavity spectroscopy at high power and low power. The two traces show $|S_{21}|$ versus frequency f for input powers of -67 dBm (black) and -117 dBm (red). The resonance at high-power occurs at the bare cavity resonance frequency, and the resonance at low-power occurs at the dressed cavity

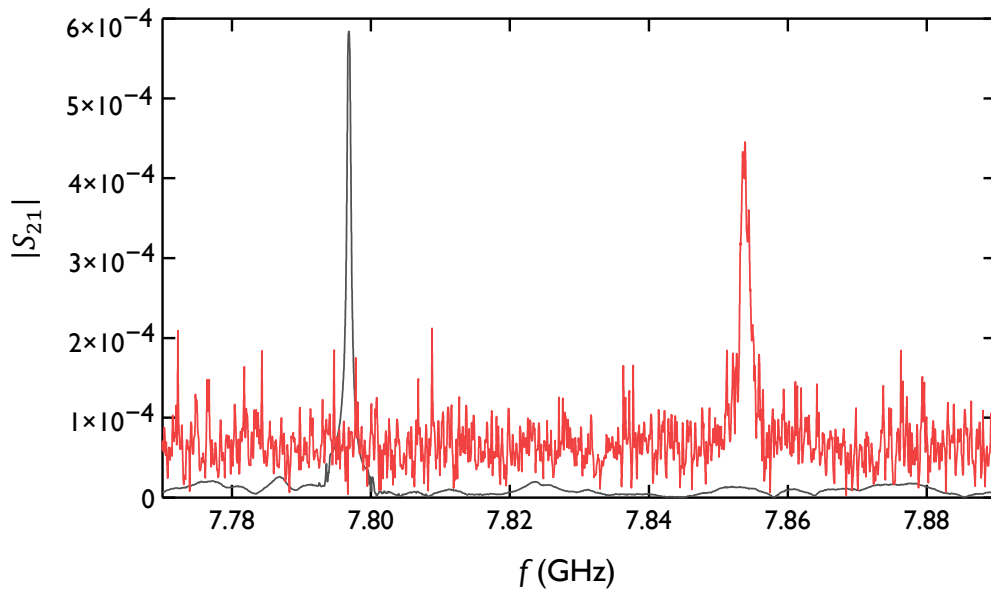


Fig. 5.1 High-power (-67 dBm, black) and low-power (-117 dBm, red) spectroscopy showing $|S_{21}|$ versus frequency f of cavity 6D during Measurement Run #1.

resonance frequency, where average stored photon number $\bar{n}_{\text{cav}} \sim 1$. It is the dressed cavity resonance frequency that depends on the state of the qubit (see [Sec. 2.2.3](#)). In this case, since the qubit was not excited, the resonance at $\omega_r/2\pi = 7.7968$ GHz is the bare resonance, while the dressed resonance is at $\tilde{\omega}_r^{(|g\rangle)}/2\pi = 7.8524$ GHz, and this yields a shift of $\chi_{ge}/2\pi = -56$ MHz. I note that the effective quality factor of the resonance also varied, as indicated by the different peak heights and widths.

Seeing the shift of the resonance as in [Fig. 5.1](#) gave me the confirmation that the qubit had survived the mounting and cooldown. I next completed a more comprehensive measurement of the spectrum as a function of power. An example of such a measurement is shown in [Fig. 5.2](#). This false color plot shows $|S_{21}|^2$ of the cavity resonance versus frequency f and drive power P . Note in particular the rich structure in the intermediate powers. Examination of this structure is beyond the scope of this work, but Mavrogordatos *et al.* [[113](#)] conducted an extensive analysis of the behavior.

[Figure 5.2](#) shows the steady-state measured $|S_{21}|^2$ versus applied frequency and power; that allowed me to pick an initial bias point for transmon readout as discussed next in [Sec. 5.2](#). Using this spectroscopy, I picked the initial bias point suitable for the non-linear high-power readout (see [Sec. 5.2.2](#)) at frequency $\omega_r/2\pi = 7.9227$ GHz with an applied power of $P = -57$ dBm. This was a good preliminary bias point since at powers > -57 dBm the cavity exhibits good transmission and at powers < -57 dBm the cavity exhibits low transmission. By biasing the cavity at -57 dBm I expected the cavity transmission to increase dramatically when the qubit was in an excited state (see [Sec. 5.2.2](#) for further details).

Following preliminary qubit characterization, I revisited cavity spectroscopy to

obtain the cavity transmission with the transmon in state $|e\rangle$ (see Fig. 5.3(a)). The difference in the cavity transmission between state $|e\rangle$ and $|g\rangle$ is shown in Fig. 5.3(b). The latter plot allowed me to verify the optimum position for biasing the cavity in order to read out the transmon state efficiently. As is evident from Fig. 5.3(b), the optimum bias point was at the bare cavity frequency with a bias power of -58 dBm.

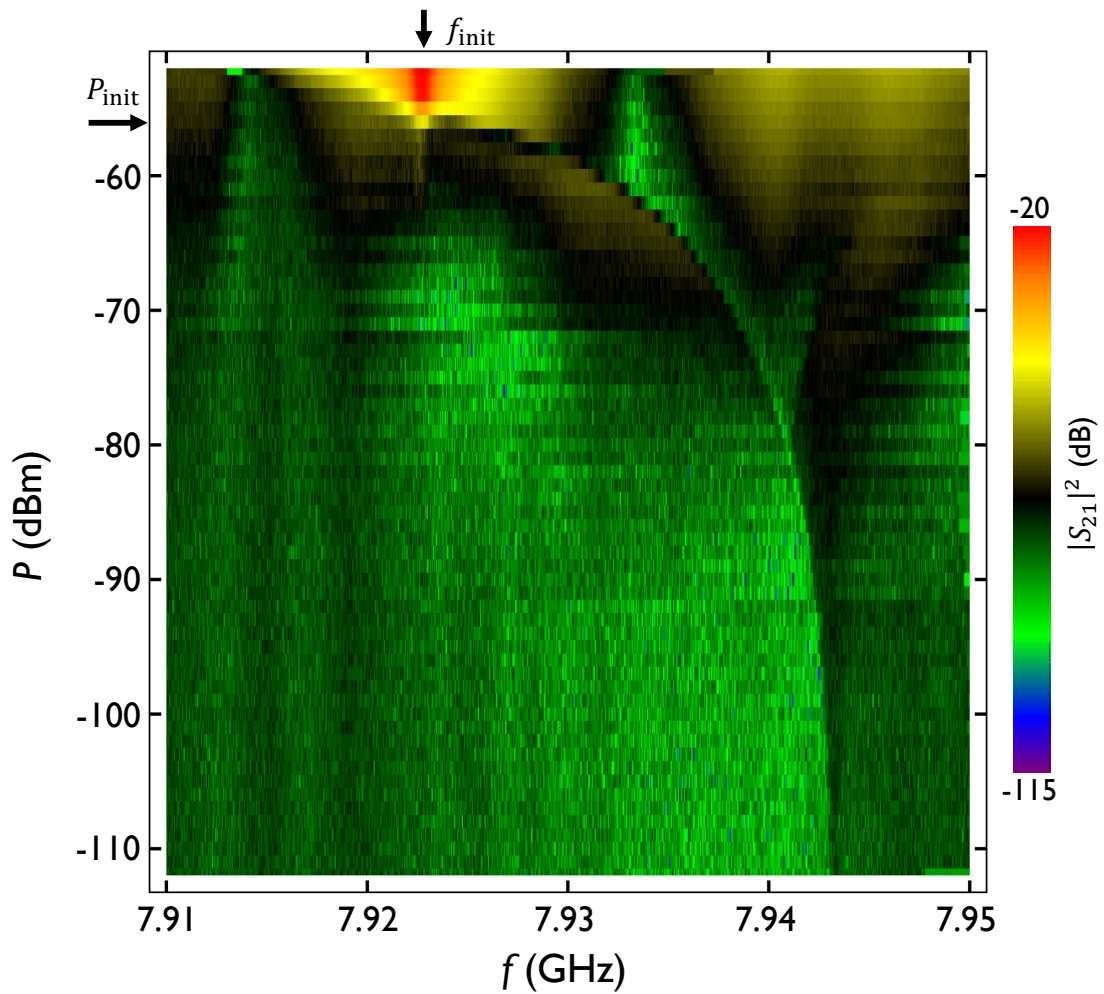


Fig. 5.2 $|S_{21}|^2$ versus frequency f and drive power P for the cavity 6D, during Measurement Run #5. Bare cavity resonance $\omega_r/2\pi = 7.9227$ GHz and the dressed cavity resonance with the transmon in $|g\rangle$ is at $\tilde{\omega}_r^{(g)}/2\pi = 7.9430$ GHz. The preliminary qubit readout point is depicted by $(f_{\text{init}}, P_{\text{init}})$

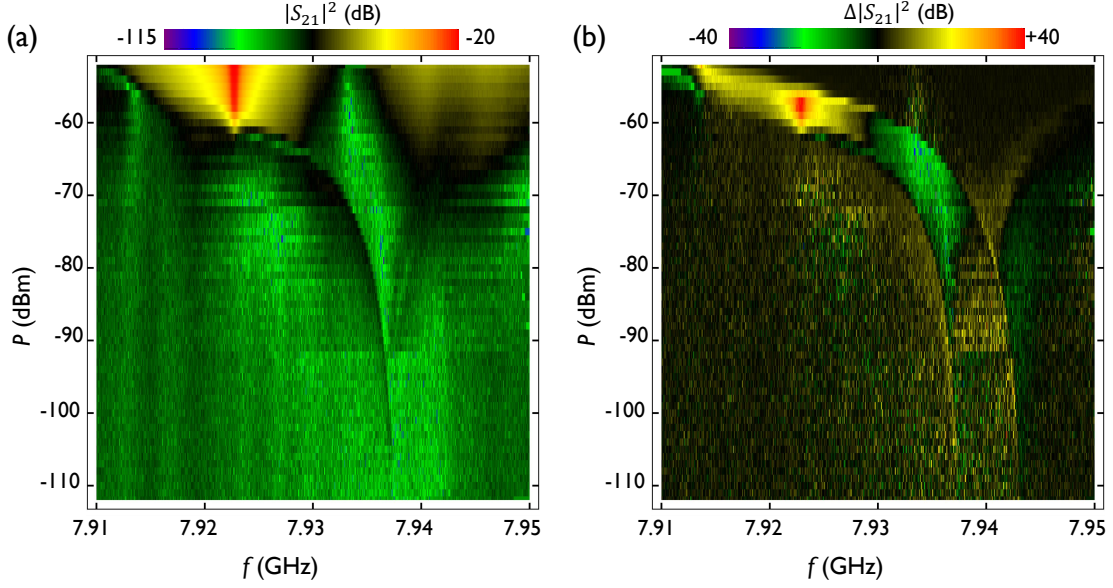


Fig. 5.3 (a) $|S_{21}|^2$ versus frequency f and drive power P of the cavity 6D, during Measurement Run #5. Color corresponds to the transmission $|S_{21}|^2$ in dB. The dressed cavity resonance with the transmon in $|e\rangle$ is at $\tilde{\omega}_r^{(|g\rangle)}/2\pi = 7.9373$ GHz. (b) The difference $\Delta|S_{21}|^2$ between transmission $|S_{21}|^2$ when the transmon state changes from $|e\rangle$ to $|g\rangle$.

5.2 Transmon Readout

5.2.1 Dispersive Readout

Dispersive readout was initially proposed by Blais *et al.* [42] and demonstrated by Wallraff *et al.* [43] for reading out Cooper-pair box qubits in a circuit QED architecture. The specific readout method they proposed involved probing the transmission properties of the cavity with a low-powered pulse, typically at the dressed cavity frequency $\tilde{\omega}_r^{(|g\rangle)} = \tilde{\omega}_r - \chi$ with the qubit in state $|g\rangle$. From Eq. (2.28), we see that high transmission of the microwave pulse is indicative that the transmon was in the ground state, and low transmission is indicative that the transmon was in an excited state. For example, the

dispersive readout could have been used in device SPP-v2-Q2 by probing the 6D cavity at a power of -117 dBm (see Fig. 5.1). A “low” $|S_{21}|^2$ signal would have indicated the transmon was in an excited state, while a “high” $|S_{21}|^2$ would indicate that the transmon was in an excited state.

This low-power method had the advantage of being a quantum non-demolition readout and being a weak measurement of the system [42]. However, due to the low power used during the measurement, the output signal was weak as well. Without the use of a quantum-limited amplifier, the signal must be averaged over many shots in order to obtain a good signal-to-noise ratio.

In fact, most of my devices showed a low-power resonance (see Fig. 5.2), that was somewhat distorted and weak in strength compared to the bare resonance at high-power. Hence, I chose to employ a high-power readout technique, as described in the next section.

5.2.2 The Non-linear High-power Readout

An alternative method of reading out the state of a transmon was demonstrated by Reed *et al.* [104]. This method realized a projective strong measurement by applying a high-power microwave pulse at the bare cavity frequency ω_r . By mapping the cavity transmission S_{21} as a function of the pulse power P and the transmon state, suitable bias powers can be found which give good discrimination between the transmon $|g\rangle$ and $|e\rangle$ states [104]. In general, occupying higher transmon levels will yield a higher transmission at a lower pulse power [33]. This non-linear high-power readout

technique was used exclusively in all my measurements since it showed better stability and signal-to-noise ratio, compared to the dispersive readout for my devices.

The non-linear high-power readout was calibrated by measuring the cavity transmission S_{21} at the bare cavity frequency as a function of pulse power P . I started this calibration process by choosing the length of the cavity transmission measurement pulse. Most of my cavities had lifetimes of 50 ns to 100 ns. For such cavities, I chose the length of the cavity pulse to be $1 \mu\text{s}$ so that the cavity had ample time to ring-up. For my Fock state measurements [33], the cavity had a lifetime of $\sim 2 \mu\text{s}$ and, in that case, I chose the pulse length to be $3 \mu\text{s}$.

After fixing the pulse length, I applied the pulse sequence shown in Fig. 5.4 1000 times repeatedly, and averaged the amplitude of the transmitted signal separately in two batches using the digitizer's onboard averaging capability. The first set of measurements (background) consisted of applying no operations for an idle time $t_{\text{idle}} \sim 100 \mu\text{s}$ to $400 \mu\text{s}$, followed by performing a cavity transmission S_{21} measurement with a pulse of duration $t_{\text{RO}} \sim 1 \mu\text{s}$ to $3 \mu\text{s}$. The second set of measurements (qubit) consisted of applying the desired set of transmon operations and then applying the cavity

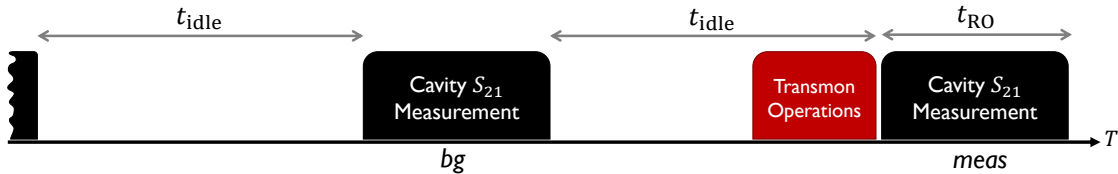


Fig. 5.4 Pulse sequence to obtain cavity switching curves. t_{idle} is the time between cavity measurement pulses, used to ensure the system returns to a ground state. t_{RO} is the length of the readout pulse, sufficiently long to calculate the relative transmission depending on the transmon state. The background measurement (bg) and signal measurement (meas) are obtained without and with transmon operations, respectively.

measurement pulse. I chose t_{idle} to be over five times the lifetime of the longest-lived component, to ensure the system always started in the ground state. The background and qubit measurement pulses were interleaved, to allow me to detect random variations in the system, or systematic effects such as heating; these would show up as variations in the background measurements. Given these measurement signals, I then constructed $(\Delta V/V)_{\text{meas}}$ and the background signal $(\Delta V/V)_{\text{bg}}$, where ΔV and V are the demodulated in-phase voltage components at the “Signal” and “Reference” inputs to the digitizer in Fig. 4.3, respectively. In most of my data plots, I actually report the fractional difference signal

$$\left(\frac{\Delta V}{V}\right) = \left(\frac{\Delta V}{V}\right)_{\text{meas}} - \left(\frac{\Delta V}{V}\right)_{\text{bg}}. \quad (5.1)$$

The phase of the reference pulse after digitization, was also adjusted through LabVIEW software, in order to report all the signal information in the in-phase (I) component for each Measurement Run. This meant that the information relating to the qubit state was strictly visible as a difference in the detected amplitude and not in phase.

I initialized the transmon in various states using microwave drives and performed the pulse sequence represented in Fig. 5.4 to obtain the “switching curves,” $(\Delta V/V)$ versus P , for the transmon-cavity system with the qubit prepared in different initial states. These switching curves served as the roadmap that I used to determine the optimum power P_0 for the cavity transmission measurement pulse for the high-power readout. Unfortunately, there were a few devices where the cavity measurement when the transmon state was in $|e\rangle$ was not easy to distinguish, from that produced when

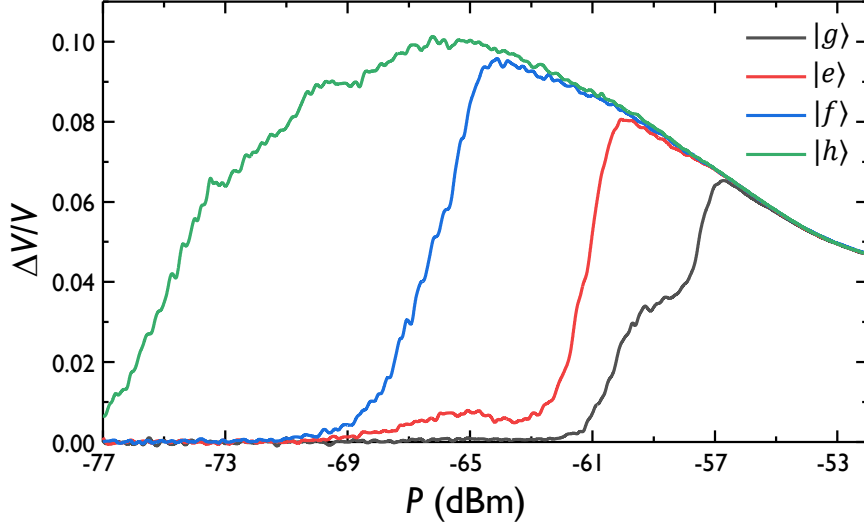


Fig. 5.5 Switching curves of the cavity δD during Measurement Run #2. The black curve was obtained using the background measurement for different input powers P of the cavity measurement pulse. The red, blue, and green curves were obtained in similar fashion after initializing the transmon in the states $|e\rangle$, $|f\rangle$, and $|h\rangle$ respectively.

the transmon was in the state $|g\rangle$.

For example, Fig. 5.5 shows switching curves I obtained for device SPP-v1-Q7 prepared in states $|g\rangle$, $|e\rangle$, $|f\rangle$, and $|h\rangle$. It is evident that there is relatively poor discrimination between the black ($|g\rangle$) and red ($|e\rangle$) curves for any power from -69 dBm to -56 dBm. In contrast, the maximum possible signal value of $\Delta V/V \approx 0.1$, is found at the peak of the green curve. The peak of the blue curve near -64 dBm also shows excellent contrast between the $|g\rangle$ state and $|f\rangle$ state signals. In a situation such as this, I found it highly advantageous to map the population $|e\rangle \Rightarrow |f\rangle$ to increase the contrast between the states during a measurement. This technique allowed me to efficiently measure the state of the transmon with fewer false counts. Of course there was a higher chance for the transmon state to decay during measurement, but this was a price that was worth paying. After determining a good cavity bias power for the

high-power readout, I proceeded with characterizing the transmon, as described in the next sections.

5.3 Transmon Spectroscopy

I used transmon spectroscopy to find the allowed transition frequencies of the transmon. In all the transmons I measured, I did not know the Josephson energy E_J prior to the cooldown. In fact, to minimize the possibility of destroying the junction through electrostatic discharge, I deliberately did not measure the room temperature resistance of live devices. Although I had a good idea of the transmon capacitance C_Σ , not knowing E_J meant I did not know the characteristic frequency of the transmon until I measured it through spectroscopy.

I performed transmon spectroscopy after first selecting a preliminary cavity bias power. For example, for the map shown in [Fig. 5.2](#), suitable preliminary bias points are at $\{7.9227 \text{ GHz}, -57 \text{ dBm}\}$, or at $\{7.9430 \text{ GHz}, -100 \text{ dBm}\}$.

After setting a preliminary cavity power bias point, I performed the pulsed measurement sequence depicted in [Fig. 5.4](#) using a long pulse to excite the transmon. The frequency of the pulse was incremented to perform spectroscopy, as shown in [Fig. 5.6](#). Since I was not initially sure of the power and length of a pulse required to excite the transmon (*i.e.* power and length of a π -pulse), I started by using a high-power, long saturation pulse to locate the transition frequency of the transmon. The saturation pulse was typically $\sim 100 \mu\text{s}$ for my transmons which had lifetimes $\sim 20 \mu\text{s}$.

Although the preliminary cavity power bias point found from visual inspection was not optimal, it usually had sufficient contrast to allow me to find the transmon's $g \leftrightarrow e$ transition frequency. After finding this frequency, I was able to find a better cavity power bias point and iteratively optimize the system for qubit measurements. [Figure 5.7](#) shows an example of a spectrum for device SPP-v1-Q6, after all measurement parameters have been optimized; I used a saturation pulse of power -111 dBm and length $t_{\text{sat}} = 200 \mu\text{s}$ to obtain the transmon spectrum.

A transmon transition spectrum such as [Fig. 5.7](#) reveals a wealth of information about the device. For example, the $|g\rangle \rightarrow |e\rangle$ transition frequency is $\omega_{ge}/2\pi = f_1 = 6.3312$ GHz. The peaks at f_2 and f_3 are due to two-photon and three-photon transitions, respectively, from the ground state to the second and third excited states; from there I obtain $\omega_{gf}/4\pi = f_2 = 6.2335$ GHz, and $\omega_{gh}/6\pi = f_3 = 6.1295$ GHz. From these frequencies of the higher excited states, I determined the charging energy using $E_C/h \approx 2(f_1 - f_2) = 195$ MHz. However, as the higher energy levels are prone to Stark shifting and power broadening, this value is close to but only approximately equal to E_C .

When there was a doubt regarding the identity of a transition, I was able to check that a spectral peak corresponded to single-photon, or multi-photon transitions by

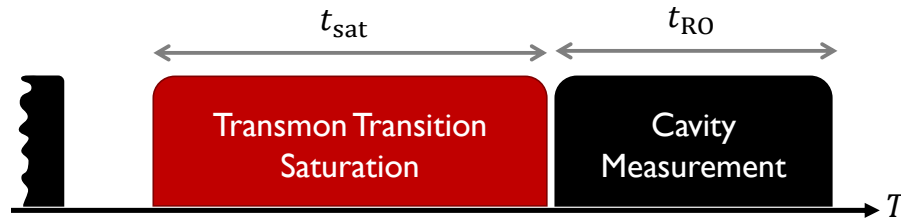


Fig. 5.6 Pulses for transmon spectroscopy.

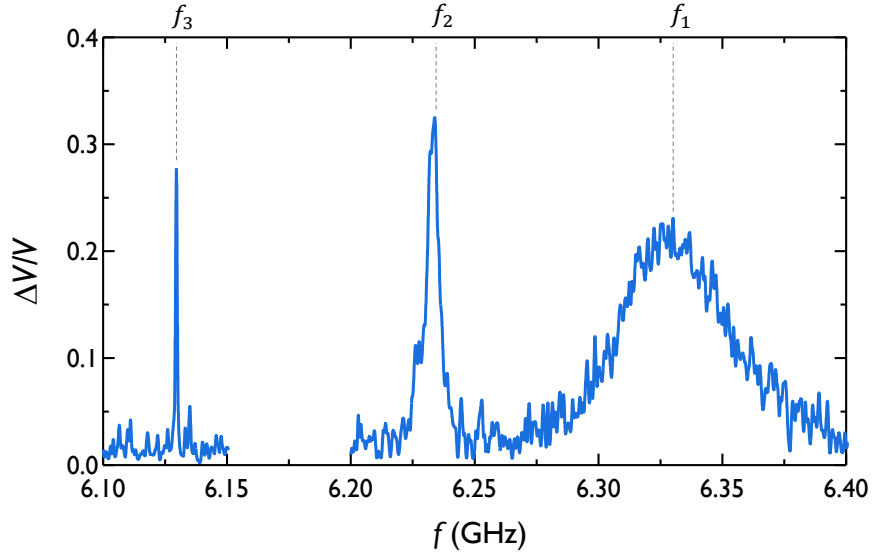


Fig. 5.7 Transmon spectroscopy for transmon SPP-v1-Q6 during Measurement Run #6. The three peaks have frequencies at $f_1 = 6.3312$ GHz, $f_2 = 6.2335$ GHz, and $f_3 = 6.1295$ GHz. The saturation pulses had length $t_{\text{sat}} = 200 \mu\text{s}$ and an input power of -111 dBm. The cavity measurement pulse had a power -81.5 dBm and a length $t_{\text{RO}} = 3 \mu\text{s}$.

measuring the width and amplitude of the spectroscopy versus power and examining the power broadening that occurs in systems with anharmonicity [114]. At each power, I fit the peak to a Lorentzian distribution and then plotted the widths versus power [115]. The power dependence of the widths reveals the order of the transition. Figure 5.8 shows an example for a two-photon transition between the $|g\rangle$ and $|f\rangle$ levels of the transmon.

5.4 Rabi Oscillations

Rabi oscillations are central to many implementations of gates in quantum computing. A Rabi oscillation describes the behavior of the state of a two-level system

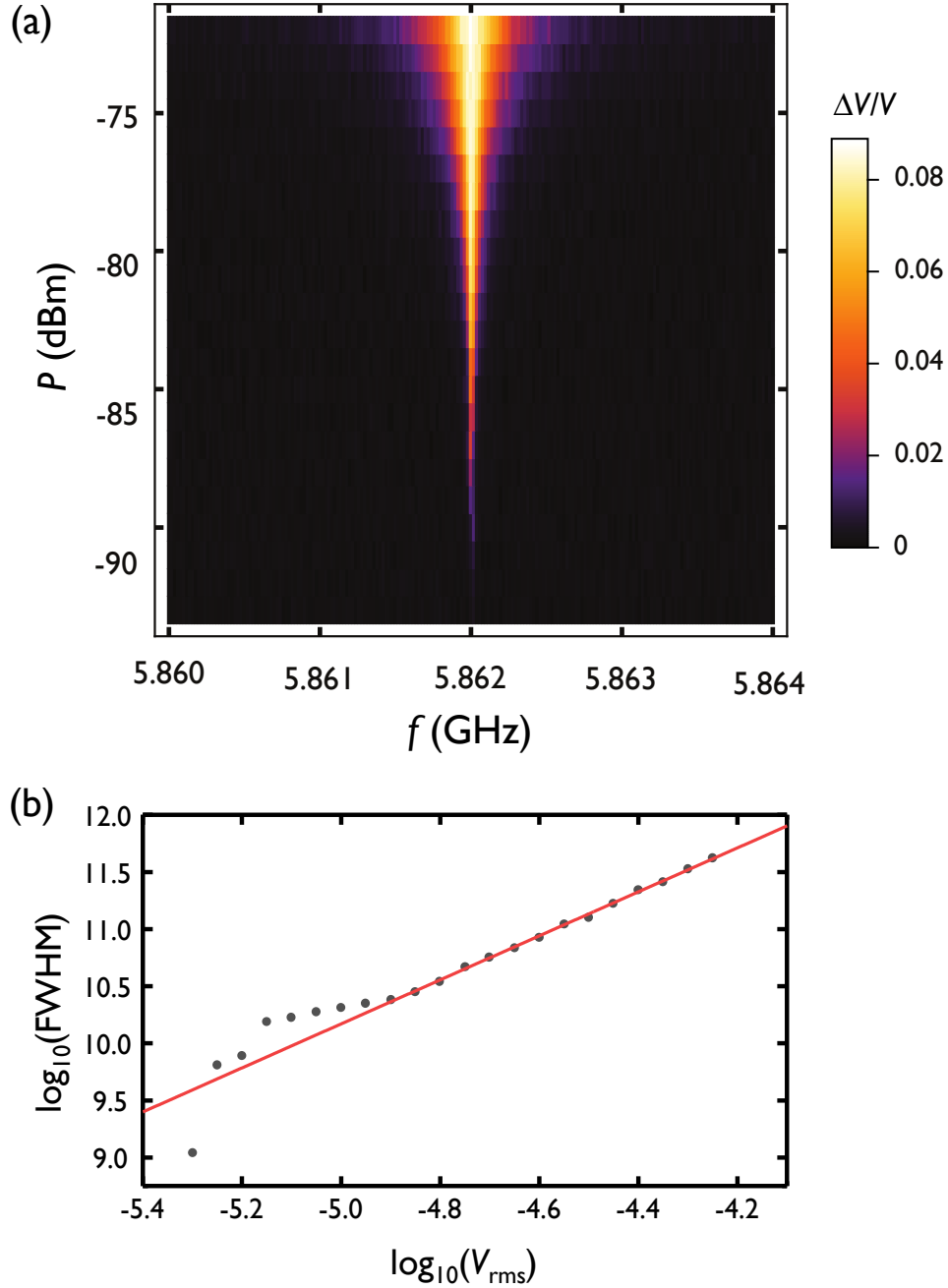


Fig. 5.8 (a) The $|g\rangle \leftrightarrow |f\rangle$ two-photon process spectroscopy for transmon SPP-v1-Q7 during Measurement Run #5. $\Delta V/V$ was measured versus frequency f and applied power P . (b) Plot of full-width at half-maximum $\log_{10}(\text{FWHM})$ versus rms applied voltage $\log_{10}(V_{\text{rms}})$. The fit (red line) to data (black points) has a gradient of 1.93 confirming that this is a two-photon process.

that is driven for a time t by a sinusoidal oscillating applied field [47, 53]. When the two-level system is driven on-resonance, it is possible to obtain a simple analytical solution using the rotating wave approximation. Ignoring dissipation and dephasing, driving a qubit at its $|g\rangle \leftrightarrow |e\rangle$ transition frequency will cause the state of the system to oscillate sinusoidally between the two levels [53]. These oscillations are known as Rabi oscillations after Isidor Rabi who studied them in the field of nuclear magnetic resonance [116].

In cQED, Rabi oscillations are generated by driving the transmon with a microwave signal on resonance at the $|g\rangle \rightarrow |e\rangle$ transition frequency (see Fig. 5.9). With the system passively cooled, the transmon starts in state $|g\rangle$. Applying a microwave drive at frequency ω_{ge} induces stimulated transition oscillations between levels $|g\rangle$ and $|e\rangle$. It is not possible to observe the full oscillation in a single experiment; instead these measurements were performed by applying a Rabi drive for a time t_{Rabi} , before measuring the qubit state using a high-powered cavity measurement. I typically repeated this procedure 1000 times to obtain a single averaged data point $\Delta V/V$, and used this to find the population at time t . I repeated this averaged measurement with different Rabi lengths t_{Rabi} . Figure 5.10 shows an example of a Rabi oscillation in

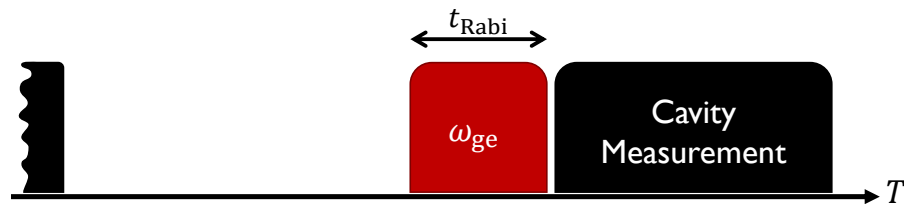


Fig. 5.9 Pulse sequence for Rabi oscillations. The time t_{Rabi} is varied for the measurement.

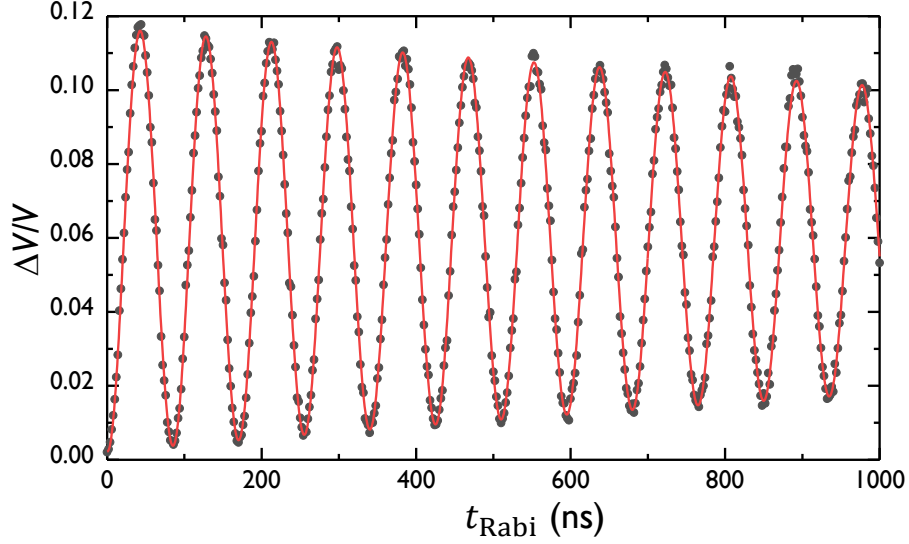


Fig. 5.10 Rabi Oscillations in transmon SPP-v1-Q7 during Measurement Run #5. Microwaves at 5.963 39 GHz were delivered to the cavity input with power -70 dBm to induce Rabi oscillations of frequency $f_{\text{Rabi}} \approx 11.7$ MHz. Data (black points) are overlaid with a decaying sinusoidal fit (red curve).

device SPP-v1-Q7.

In an ideal but unrealistic system, the Rabi oscillations would persist indefinitely, as long as the drive was applied. However, real qubits do not exist in isolation. Dissipation and dephasing are always present and will cause the amplitude of oscillations to decay, leaving the system in a mixed state between the $|g\rangle$ and $|e\rangle$ states. This condition is referred to as saturation. Assuming a frequency independent loss, the decay time of the Rabi envelope T' , is related to the relaxation time T_1 and the coherence time T_2 of the qubit by [48]

$$\frac{1}{T'} = \frac{1}{2T_1} + \frac{1}{2T_2}. \quad (5.2)$$

In the special case where there is no dephasing, it turns out that $T_2 = 2T_1$ and Eq. (5.2)

then gives $T' = 4T_1/3$. The experimental method that I used to determine T_1 and T_2 are discussed below.

5.4.1 Qubit Population Calibration

By measuring a complete Rabi oscillation (see [Fig. 5.10](#)) I was able to extract a few important parameters and calibrate the qubit drive. The fitting function I used for the Rabi oscillations was,

$$\left(\frac{\Delta V}{V}\right)_{\text{Rabi}} = Ae^{-t/T'} \sin(\Omega t + \phi) + B \quad (5.3)$$

where A is the amplitude, T' is the envelope decay time, $\Omega/2\pi$ is the Rabi frequency, $\phi \approx -\pi/2$ is the phase offset, and B is an overall offset. Note that this is not the correct functional form for a Rabi oscillation, but a convenient form that was similar enough at high drive power. Since a Rabi oscillation causes the state of the qubit to vary sinusoidally, and I assume the system starts in the ground state, I can now relate the maximum excited population to the detected signal. When the system is prepared in the ground state $|g\rangle$ at $t = 0$, [Eq. \(5.3\)](#) will give

$$\left(\frac{\Delta V}{V}\right)_g = A \sin \phi + B \simeq -A + B. \quad (5.4)$$

On the other hand, if the system is prepared in the excited state at time $t = 0$, then one finds

$$\left(\frac{\Delta V}{V}\right)_e = A \sin(\pi + \phi) + B \simeq A + B. \quad (5.5)$$

Thus the general expression for converting a detected signal to the corresponding qubit excited population \mathcal{P}_e is,

$$\mathcal{P}_e = \frac{\left(\frac{\Delta V}{V}\right)_e - \left(\frac{\Delta V}{V}\right)_g}{\left(\frac{\Delta V}{V}\right)_e - \left(\frac{\Delta V}{V}\right)_g}. \quad (5.6)$$

Note that this depends crucially on the assumption that the system was initialized in the ground state. In reality, this cannot be done perfectly, and application of [Eq. \(5.6\)](#) will yield some systematic errors.

5.4.2 Qubit Pulse Calibration

With the signal calibrated in terms of the qubit population, I can now find the pulse lengths corresponding to two basic operations: the bit-flip and the Hadamard gate.

When I program the AWG to apply the drive tone for a Rabi oscillation, I explicitly set the phase of the drive as $\phi_d = 0^\circ$. This sets the reference x -axis with respect to the Bloch sphere (see [Chapter 2](#)). The bit-flip operation which I perform is equivalent to the R_x^π gate, which yields a half-cycle-rotation of the Bloch vector around the x -axis. We refer to this pulse as a π -pulse or a X_π -pulse. I determine the duration t_π of this pulse by applying the microwave drive on resonance and finding the time which maximizes

the output signal $\Delta V/V$ (see Fig. 5.11). I note that this bit-flip operation can be written equivalently as

$$R_x^\pi \equiv \sigma_x = |0\rangle\langle 1| + |1\rangle\langle 0| = \begin{pmatrix} 0 & 1 \\ 1 & 0 \end{pmatrix} \quad (5.7)$$

The Hadamard gate can be described in terms of two rotations on the Bloch sphere: a π -rotation around the x -axis followed by a $\pi/2$ -rotation around the y -axis. The length for the $\pi/2$ rotation pulse is $t_{\pi/2}$, which is the time required to perform a quarter-cycle rotation on resonance. We refer to such a pulse as a $\pi/2$ -pulse. The

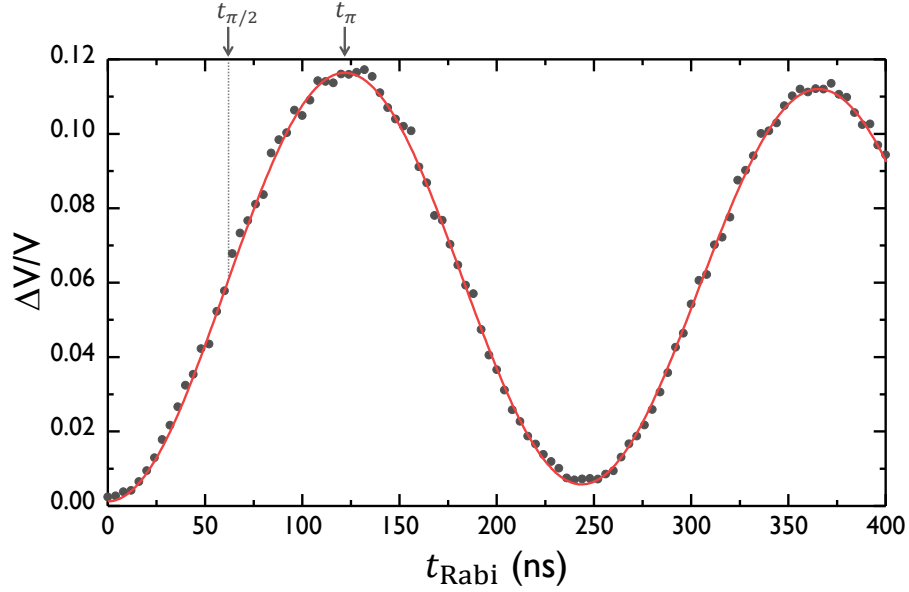


Fig. 5.11 Rabi Oscillations for the transmon SPP-v1-Q7 during Measurement Run #5. The π -pulse length was $t_\pi \simeq 122$ ns and the $\pi/2$ -pulse length was $t_{\pi/2} \simeq 61$ ns. The transmon $|g\rangle \rightarrow |e\rangle$ transition was driven on resonance with a power -79 dBm to obtain $f_{\text{Rabi}} = 4.1$ MHz.

Dirac representation of the Hadamard gate H is

$$H = \left(\frac{|0\rangle + |1\rangle}{\sqrt{2}} \right) \langle 0| + \left(\frac{|0\rangle - |1\rangle}{\sqrt{2}} \right) \langle 1| = \frac{1}{\sqrt{2}} \begin{pmatrix} 1 & 1 \\ 1 & -1 \end{pmatrix} \quad (5.8)$$

Figure 5.11 shows an example for transmon SPP-v1-Q7 when I extracted the t_π and $t_{\pi/2}$ times from a Rabi oscillation curve; with a microwave drive power giving $f_{\text{Rabi}} = 4.1$ MHz Rabi oscillations, I obtained $t_\pi \simeq 122$ ns and $t_{\pi/2} \simeq 61$ ns.

5.4.3 Off-resonant Rabi drives

If the microwave drive is applied with a frequency detuning Δ from the $|g\rangle \leftrightarrow |e\rangle$ transition frequency, the two-level system will still undergo oscillations with a smaller amplitude and larger Rabi frequency. These are known as generalized Rabi oscillations. In the presence of relaxation and dephasing, there is no analytical form for the resulting Rabi oscillations. Nevertheless, the generalized Rabi frequency and amplitude are approximately given by [52]

$$\Omega_{\text{gen}} \simeq \sqrt{\Omega^2 + \Delta^2} \quad (5.9)$$

$$A_{\text{gen}} \simeq \frac{\Omega^2}{\Omega^2 + \Delta^2}, \quad (5.10)$$

where Ω is the Rabi frequency observed on resonance. Note that A_{gen} is less than unity for $\Delta \neq 0$, indicating that it is not possible to fully excite the system with an off-resonant drive.

5.4.4 The Rabi Coupling

Figure 5.10 shows Rabi oscillations in a transmon using microwave power set to a single value. I repeated this measurement at different powers to obtain a series of Rabi oscillations with different Rabi frequencies. As I discussed in Chapter 2, the Rabi frequency $f_{\text{Rabi}} \equiv \Omega/2\pi$ at sufficiently high drive power is proportional to the amplitude of the drive. By measuring the variation of f_{Rabi} with the applied qubit drive voltage, I obtained the coupling strength Υ (in units HzV^{-1}) of the drive to the transmon.

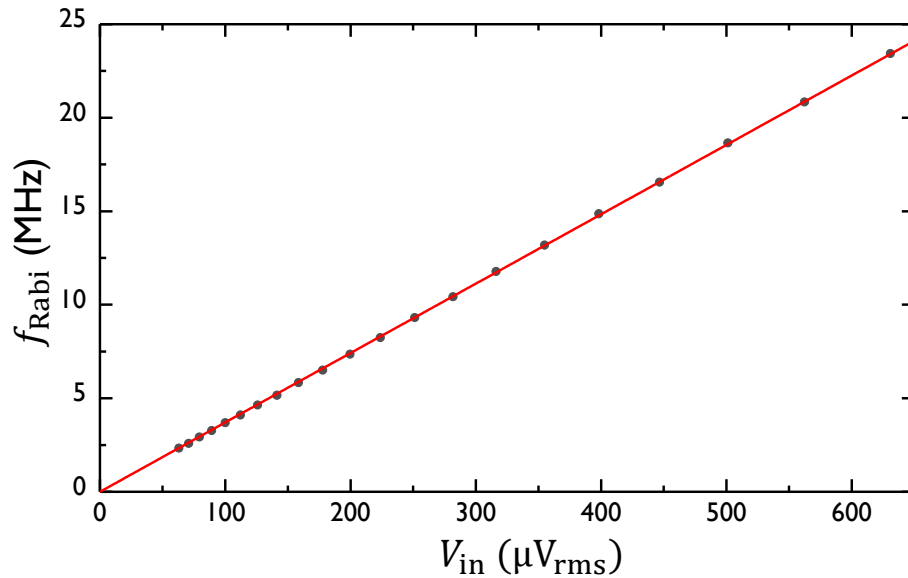


Fig. 5.12 Rabi coupling measurement for transmon SPP-v1-Q7 during Measurement Run #5. Microwaves at a frequency 5.963 39 GHz were delivered to the cavity input with power -84 dBm to -64 dBm to induce Rabi oscillations. The resulting data was fitted using Eq. (5.3) to extract f_{Rabi} for each input voltage V_{in} (black points), and plotted versus the input rms voltage. A linear fit to the data (red line) yields the slope or the Rabi coupling strength to be $\Upsilon = 37 \text{ kHz } \mu\text{V}^{-1}$ for the device.

5.5 Relaxation Time Measurements

The relaxation time T_1 determines the lifetime of the excited state $|e\rangle$ of the qubit. To measure T_1 , I applied a calibrated π -pulse as described in [Sec. 5.4.2](#). I then waited a time t_{rel} and performed a cavity measurement which I used to obtain the probability of being in the excited state \mathcal{P}_e at time t_{rel} . Averaging 1000 such measurements completed a single averaged measurement at time t_{rel} . These steps were repeated for varied t_{rel} , as illustrated by the pulse sequence in [Fig. 5.13](#). I fitted the obtained data to the formula

$$\mathcal{P}_e = Ae^{-t_{\text{rel}}/T_1} + B \quad (5.11)$$

where $A \simeq 1$ and $B \simeq 0$. [Figure 5.14](#) shows an example T_1 measurement in transmon SPP-v1-Q6. This device had a stable lifetime of $6.71 \mu\text{s}$ as verified by multiple measurements on successive days.

I note that it was important to know T_1 for many reasons. For example, for properly calibrated quantum operations and measurements, the reset time t_{idle} between

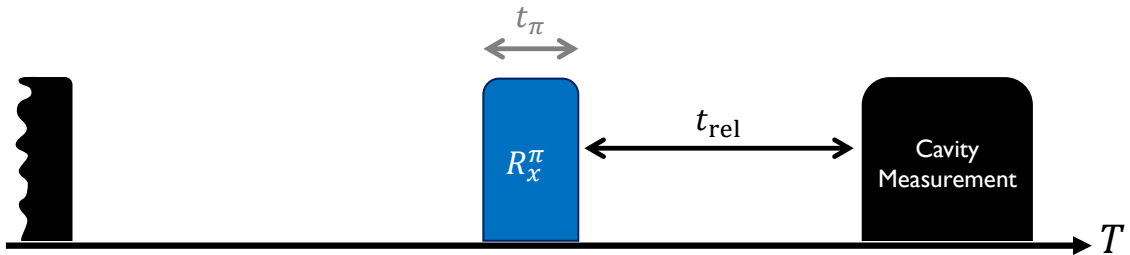


Fig. 5.13 Pulse sequence for T_1 measurement. The time t_{rel} is varied for the measurement.

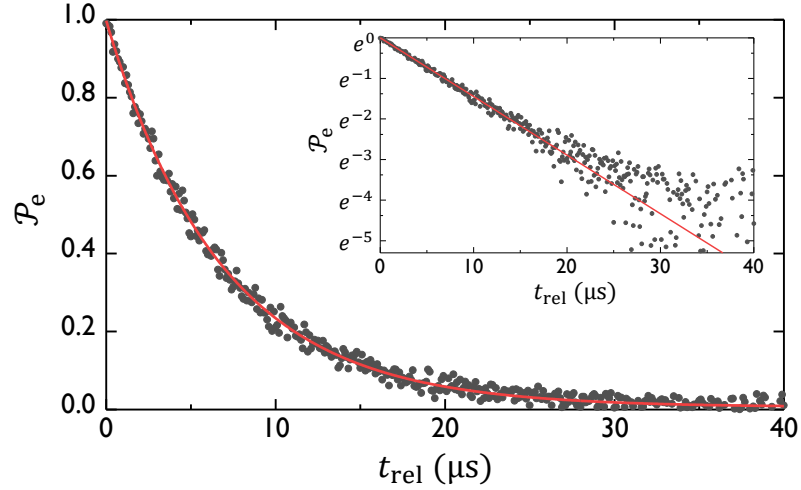


Fig. 5.14 Relaxation time measurement of transmon SPP-v1-Q6 during Measurement Run #6. Data (black points) are overlaid with an exponential decay fit (red curve). (inset) T_1 measurement on a semilog plot.

measurements must be long enough to ensure that the qubit has sufficient time to relax back to the ground state. I ensured this by setting $t_{\text{idle}} > 5T_1$, which will give $\mathcal{P}_e < 0.7\%$ if the qubit started in state $|e\rangle$. This step is one of many, required to optimize and fine-tune the measurement process described in [Sec. 5.2](#).

5.6 Ramsey Oscillations

The Ramsey method is a crucial technique in atomic timekeeping and provides interesting information about a qubit [52]. Norman Ramsey was a former student of Isidor Rabi who extended molecular beam methods to develop a highly accurate method of atomic interferometry [117]. Ramsey's method (see [Fig. 5.15](#)) involved first applying a $\pi/2$ -pulse to put an atom into an equal superposition of the $|g\rangle$ and

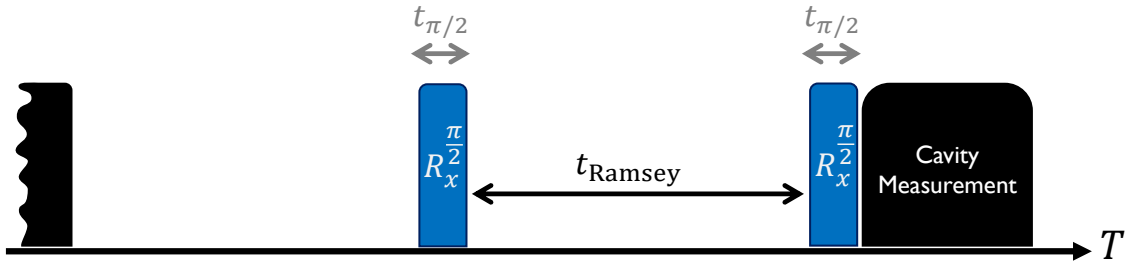


Fig. 5.15 Pulse sequence for Ramsey oscillation measurement. The time t_{Ramsey} is varied for the measurement.

$|e\rangle$ states. The atom was then allowed to evolve freely for a time t_{Ramsey} . Another $\pi/2$ -pulse was then applied and the state of the system measured.

Depending on the magnitude of the accumulated phase of the superposition state, the final measured population would differ. As t_{Ramsey} is varied in a given experiment, this accumulated phase can vary from 0 to π to 2π resulting in complete oscillations. For $\omega_d \neq \omega_{ge}$, the frequency of these Ramsey oscillations depends on the detuning Δ between the applied drive frequency ω_d and the qubit transition frequency ω_{ge} .

Steck [52] provides an informative analogy for the Ramsey interference fringes: the Ramsey method is similar to Young's double-slit experiment where the two $\pi/2$ -pulses act as two slits separated in the time domain, resulting in interference fringes which appear as a function of the frequency or detuning. Ramsey interferometry samples the integrated noise that impacts the transmon, and hence is a sensitive metric of the coherence.

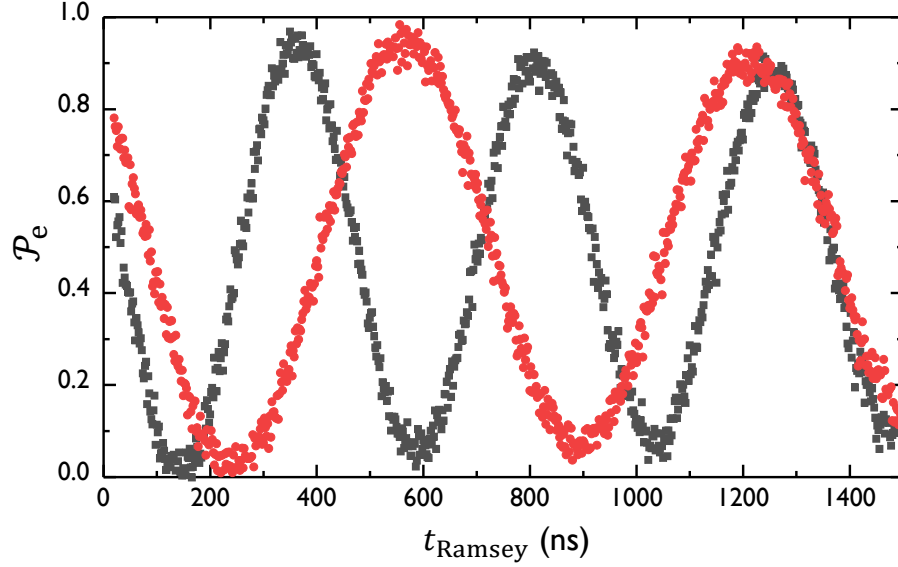


Fig. 5.16 Ramsey oscillations for transmon SPP-v1-Q6 during Measurement Run #7. I obtained the two Ramsey oscillation traces by applying the $\pi/2$ -pulses at frequencies of 6.7520 GHz (black), and 6.7527 GHz (red). The resulting Ramsey frequencies f_{Ramsey} were 2.247 MHz and 1.549 MHz, respectively.

5.6.1 Precise Determination of Qubit Frequency

Figure 5.16 shows two examples of Ramsey oscillations I observed in transmon SPP-v1-Q6. I fit those Ramsey oscillations to damped sinusoidal functions with an average decay time of $T_2^* = 6.1 \mu\text{s}$ and frequency which depends on the detuning. For a frequency independent loss mechanism, Ramsey decay time T_2^* obeys

$$\frac{1}{T_2^*} = \frac{1}{2T_1} + \frac{1}{T_\phi} + \frac{1}{T^\dagger} = \frac{1}{T_2} + \frac{1}{T^\dagger}, \quad (5.12)$$

where T_ϕ is the pure dephasing time and T^\dagger is a time constant characterizing inhomogeneous broadening (see next section).

During Measurement Run #3, I was able to obtain Ramsey oscillations with detun-

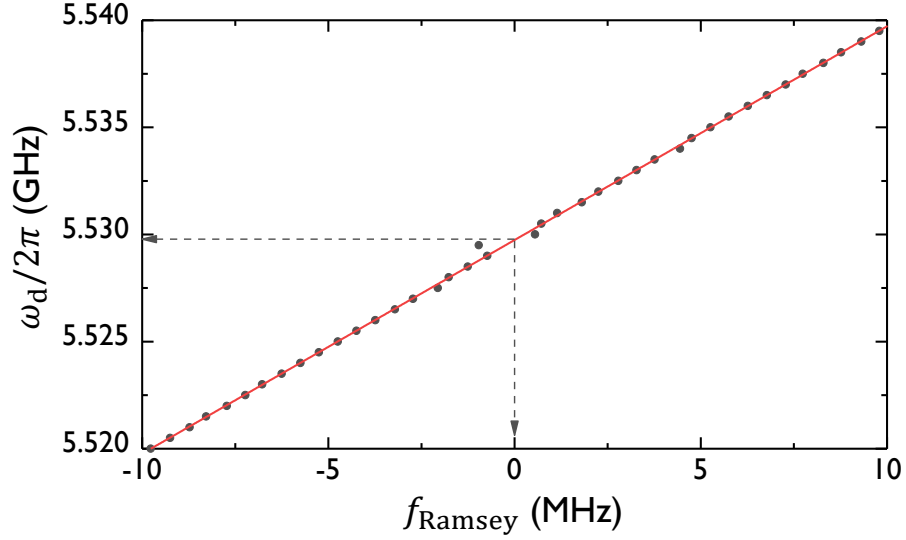


Fig. 5.17 Plot of drive frequency $\omega_d/2\pi$ versus Ramsey frequency f_{Ramsey} for transmon SPP-v1-Q7 during Measurement Run #3. The drive frequency of $\pi/2$ -pulses was varied from 5.52 GHz to 5.54 GHz. The data (black) are overlaid with the linear fit (red), and the y -intercept value from the fit is taken to be the precise qubit frequency.

ings Δ in the range -10 MHz to 10 MHz for transmon SPP-v1-Q7. By plotting the drive frequency ω_d versus the resulting Ramsey frequencies f_{Ramsey} , I obtained the $|g\rangle \rightarrow |e\rangle$ transition frequency with a high precision (see Fig. 5.17). By using the y -intercept of a linear fit to the data, I extracted the qubit frequency precisely to be 5.52972 GHz. It should be noted that when $\Delta \approx 0$, long traces have to be obtained to precisely determine the frequency. Given the relatively short coherence times this is often not possible, as was evident with the two data points for $\omega_d \approx 5.529$ GHz in Fig. 5.17.

5.7 Spin-Echo Measurements

The method of spin-echo was developed by Erwin Hahn [118] to decrease, to first order, effects of inhomogeneous broadening when studying the coherence of a spin ensemble. Inhomogeneous broadening means different atoms in an ensemble have slightly different transition frequencies due to local effects such as variations in the local magnetic field, or a spread in velocities for a train of atoms/ions [52]. When a Ramsey experiment is performed on such an ensemble, some atoms will be accumulating phases faster than others, after the first $\pi/2$ -pulse. When the second $\pi/2$ -pulse is applied and the ensemble is measured, this differential phase accumulation will reduce the resulting coherent signal, much like pure dephasing. A spin-echo measurement (Hahn echo) involves applying a π -pulse around an orthogonal axis, halfway between the two $\pi/2$ -pulses as illustrated in Fig. 5.18. The π -pulse causes the spins to evolve in a time-reversed fashion, allowing the slow parts and fast parts to refocus. The spin-echo technique has become commonplace in other applications as well, and can be used to

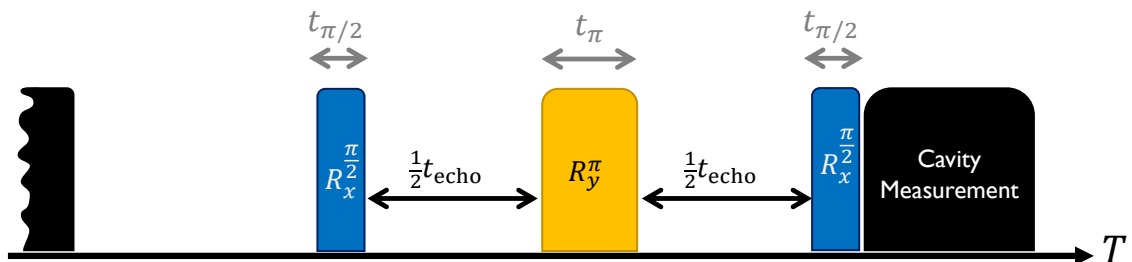


Fig. 5.18 Pulse sequence for spin-echo measurement. The time t_{echo} is varied for the measurement.

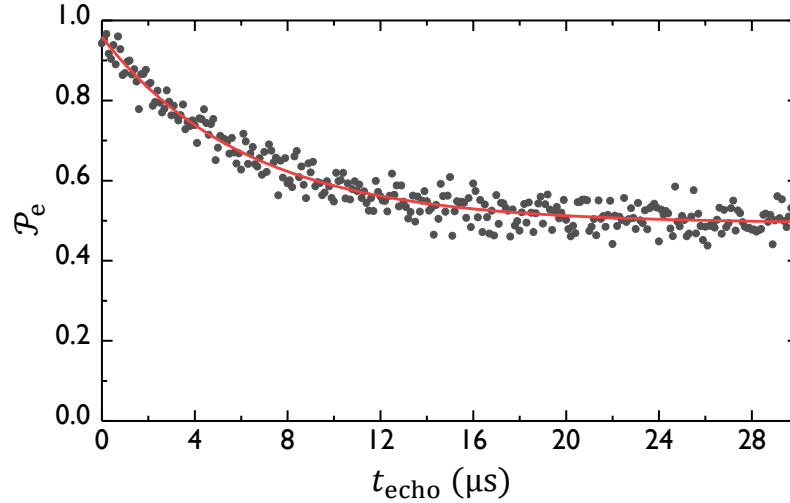


Fig. 5.19 Spin-echo measurement showing probability \mathcal{P}_e to be in the excited state versus time t_{echo} for transmon SPP-v1-Q6 during Measurement Run #7. Data (black points) are overlaid with fit to an exponential decay (red curve) with time constant $6.23 \mu\text{s}$ and offset ≈ 0.5 .

eliminate the effects of unwanted interactions by applying corrective pulses [119].

Note that if the local effects do not vary in time, at least during the timescale of evolution, the ensemble constituents will be refocused just prior to the application of the second $\pi/2$ -pulse. Thus the echo removes effects of inhomogeneous broadening. Of course, this does not remove effects from T_ϕ and T_1 , and the resulting echo decays exponentially. When this technique was applied in optical systems [120], the system itself would emit a light pulse akin to the original excitation, producing an optical “echo” pulse.

Figure 5.19 shows an example of a spin-echo measurement I took on transmon SPP-v1-Q6. By fitting the data to an exponential decay with an offset as in Eq. (5.11), I obtained the T_2 coherence time; this device had a relaxation time of $T_1 = 3.47 \mu\text{s}$ and a coherence time of $T_2 = 6.23 \mu\text{s}$. In this case, the coherence time T_2 was close to

$2T_1 = 6.94 \mu\text{s}$, implying that the dephasing time was much longer than T_1 . In general, for frequency independent loss mechanisms, T_2 is related to T_1 by the relation,

$$\frac{1}{T_2} = \frac{1}{2T_1} + \frac{1}{T_\phi}. \quad (5.13)$$

5.8 Photon Number Splitting

The cQED systems I examined were composed of a cavity as well as one or two transmons. I needed to characterize certain aspects of the cavity as well, as it interacted with the qubits. Here I discuss the coupling of an applied field to the cavity. Unlike the case of the Rabi coupling to a qubit (see [Sec. 5.4](#)), it is not so straightforward to measure this coupling.

In the dispersive limit, at sufficiently low photon numbers, the dressed cavity is a slightly anharmonic system, due to the high-order Kerr nonlinearity arising from the interaction with the transmon [[121](#)]. Thus, a sufficiently strong drive field will yield a coherent state with multiple photons in the cavity, rather than causing coherent

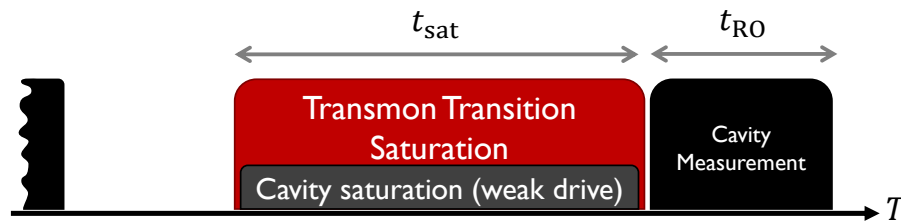


Fig. 5.20 Pulse sequence for photon number splitting. The long pulses are applied to ensure the steady-state of the cavity and the transmon.

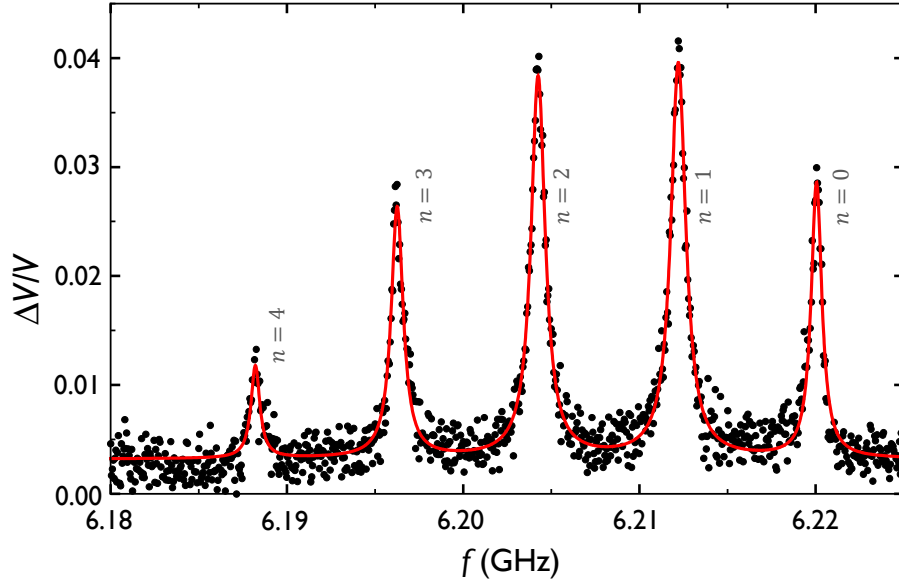


Fig. 5.21 Measurement of photon number splitting spectrum for transmon SPP-v1-Q7 in the cavity 6D during Measurement Run #2. Data (black points) are overlaid with a fit to five Lorentzians (red curve). The drive power at the cavity input was $P_{\text{cav}} \approx -112$ dBm and the calculated mean photon number was $\langle n \rangle \approx 1.6$. The qubit spectroscopic peaks correspond to different cavity photon numbers, as labeled.

oscillations between the two lowest levels. Depending on the intensity of the drive and the decay time of the resonator, the driven cavity will reach a steady coherent state with a photon population following a Poisson distribution [122].

The strength of the coupling of the cavity to the input drive line can be found by measuring the average photon number corresponding to a given drive strength. In my cQED system, I used the transmon as a sensitive detector of the average photon occupation in the cavity; in the low photon number limit, each additional photon in the cavity causes a shift in the qubit frequency an amount 2χ (see Sec. 2.2.3).

Figure 5.20 shows an example where I measured the transition spectrum while applying a weak continuous cavity tone. The cavity photon distribution is “imprinted”

as a series of peaks in the qubit spectrum, with each peak corresponding to the qubit transition with a specific number of photons in the cavity; this technique is known as measuring the photon number splitting spectrum [123]. By extracting the relative heights of the peaks, I determined the average number of photons in the cavity [124], and the strength of the coupling between the input pin and the cavity. I note that this approach only works well if the system is in the strong dispersive regime where $2\chi > \{\kappa, 1/T_2\}$ (κ is the decay rate for the cavity and T_2 is the coherence time for the qubit), and if the qubit and the cavity are driven lightly to ensure that the individual photon number peaks are well-resolved.

5.8.1 Determining the Cavity Coupling to the Input Drive

By measuring the number splitting spectrum as a function of the microwave input drive strength, I obtained the average cavity photon occupation $\langle n \rangle$ versus the drive voltage V_{rms} . Naively, this relationship should be quadratic in the low-power limit, *i.e.* $\langle n \rangle \propto V_{\text{rms}}^2$. It is also possible to restate this relationship in terms of the effective cavity drive strength Ω_{cav} [48, 123, 125],

$$\langle n \rangle = \frac{\Omega_{\text{cav}}^2 Q_{\text{E}}}{2\pi Q_{\text{L}}} \frac{1}{(\kappa/2)^2 + \chi^2}, \quad (5.14)$$

where Q_{L} and Q_{E} are the loaded and external coupling quality factors of the cavity, respectively.

Figure 5.22 shows an example where I measured the photon number splitting

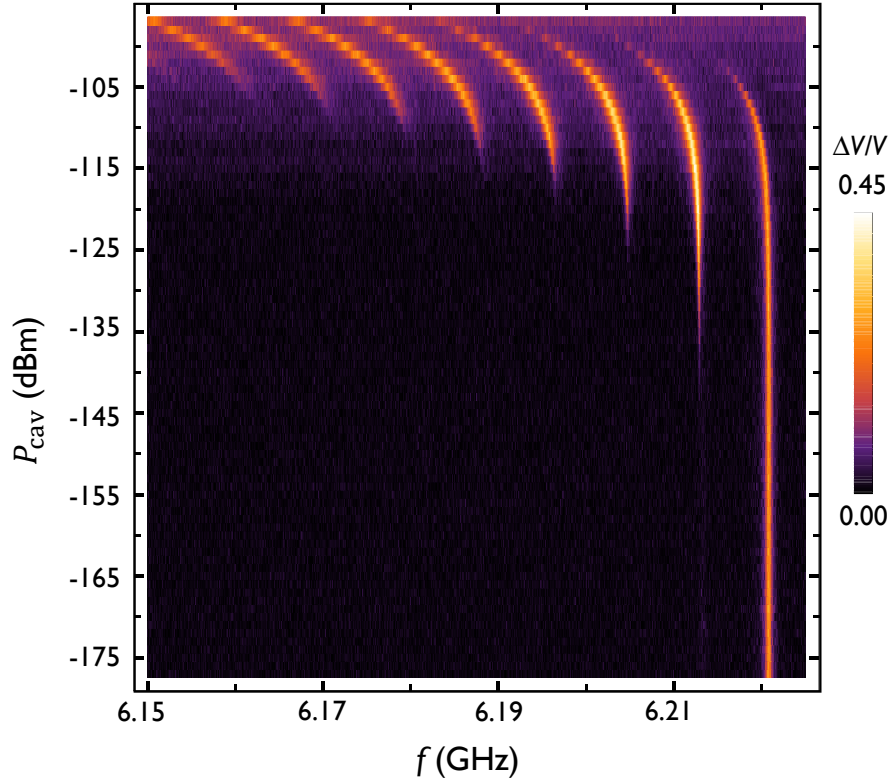


Fig. 5.22 Photon number splitting spectrum versus drive power for transmon SPP-v1-Q7 in the cavity 6D during Measurement Run #2. The transmon spectrum was measured while applying a weak cavity drive at frequency 7.946 83 GHz with different powers P_{cav} .

spectrum versus cavity drive power. At low powers $P_{\text{cav}} < -145$ dBm, only the peak corresponding to zero cavity photons is visible. Above -145 dBm other cavity photon number peaks appear, following a Poisson distribution. For powers $P_{\text{cav}} > -115$ dBm the series of peaks shift to the left, indicating significant Stark shifting. In this case I found $\Omega_{\text{cav}}/2\pi > 3$ MHz.

5.9 Summary of Measured Parameters of the Devices

Table 5.1 gives a summary of the parameters for the devices I fabricated and measured for this dissertation. I determined the input and output quality factors for the cavity (Q_{input} and Q_{output}) by measuring S_{21} , S_{22} , and S_{11} at room temperature. The loaded quality factor of the cavity Q_{loaded} was measured after cooling the cavity to 20 mK. I obtained the cavity lifetime T_{cav} either using a ringdown measurement ($T_{\text{cav}} = T_{\text{ringdown}}/2$) or from the loaded quality factor ($T_{\text{cav}} = Q_{\text{loaded}}/\omega_r$). The charging energy E_C and the Josephson energy E_J of the transmons were extracted from spectroscopic measurements. I used the effective dispersive shift χ_{eff} to calculate the effective qubit-cavity coupling $g_{\text{eff}} = \sqrt{\chi_{\text{eff}}\Delta_{\text{ge}}}$. The Rabi coupling Υ was measured as described in Sec. 5.4.4. The attenuation values at the qubit frequency for the input line were estimated based on S_{21} measurements on the line at room temperature.

All SPP-v1 transmons were fabricated on sapphire substrates. The SPP-v2 transmon was fabricated on a silicon substrated that was not treated with HF. Both cavities 6D and 6G were machined from 6063 Al. Except for the final cooldown in 2017, all other devices listed were packaged in 2015. SPP-v2-Q2 was replaced with SPP-v1-Q7 on June 22, 2015. Subsequent to this repackaging, the two halves of the cavities were not opened during the rest of 2015 and 2016; nevertheless the coupling quality factors were adjusted by simply removing and reattaching modified SMA ports. For the cooldown in 2017, the cavity 6G was opened, machined to have two slots equidistant from the center, and repackaged with both qubits SPP-v1-Q6 and SPP-v1-Q7 inside. The

original center slot was closed off with Indium to ensure boundary integrity.

Table 5.1 Summary of parameters for the devices I fabricated and measured.

Measurement Run	#1	#2	#3	#4	#5	#6	#7
Cooldown Date	5/8/2015	6/22/2015	9/12/2015	9/12/2015	2/25/2016	2/25/2016	9/28/2017
Cavity	6D	6D	6D	6G	6D	6G	6G
Transmon Name	SPP-v2-Q2	SPP-v1-Q7	SPP-v1-Q7	SPP-v1-Q6	SPP-v1-Q7	SPP-v1-Q6	SPP-v1-Q6 SPP-v1-Q7
Q_{output}	350000	309000	207000	3000	207000	3000	3000
Q_{input}	730000	682000	420000	80000	420000	—	80000
Q_{loaded}	42130	69180	119464	2887	124450	1493	2425
f_{bare} (GHz)	7.796813	7.921156	7.9222	7.9222	7.92272	7.92241	7.6804375
$f_{\text{dress}}^{(s)}$ (GHz)	7.8524	7.94683	7.936997	7.9416	7.9430	7.95021	7.7463
$f_{\text{dress}}^{(e)}$ (GHz)	7.8354	7.93887	7.932949	7.9358	7.9373	7.94164	7.732
T_{cav} (μs)	0.86	1.39	2.4	0.058	2.5	0.03	0.1075
f_{ge} (GHz)	6.78133	6.22097	5.52972	5.93986	5.96339	6.33121	6.07135
$f_{\text{gf}/2}$ (GHz)	6.7084	6.12236	5.42422	5.83758	5.862	6.2335	6.6654
$f_{\text{gh}/3}$ (GHz)	6.6304	6.01735	—	5.729	—	6.1295	6.5686
E_C/h (MHz)	146	206	211	204	203	200	180
E_J (GHz)	41	25	19	23	23.4	26.7	31.9
E_J/E_C	280	121	90	112	115	134	177
$\chi_{\text{ge}}/2\pi$ (MHz)	-55.6	-25.7	-14.8	-19.4	-20.3	-27.8	-65.9
$\chi_{\text{ef}}/4\pi$ (MHz)	-47.1	-21.7	-12.8	-16.5	-17.4	-23.5	-58.7
$\chi_{\text{eff}}/2\pi$ (MHz)	-8.5	-3.98	-2.02	-2.9	-2.85	-4.29	-8.35
$g_{\text{ge}}/2\pi$ (MHz)	238	209	188	196	199	210	225
$g_{\text{ef}}/2\pi$ (MHz)	331	287	258	269	275	290	318
$g_{\text{eff}}/2\pi$ (MHz)	95	83	70	76	75	83	74
T_1 (μs)	0.425	50	24	20	18	6.71	3.47
T_2^* (μs)	0.567	9.1	22	20	20	10.5	6.2
T_2' (μs)	0.43	14.4	20	20	15	8.37	4.24
T_2 (μs)	—	—	—	—	25	11.7	6.2
Υ (MHz μV^{-1})	0.29	0.15	0.030	0.21	0.037	2.75	0.32
Attenuation (dB)	—	77	77	83	88	83	90

CHAPTER 6

Fock State Generation using Stimulated Raman

Adiabatic Passage

6.1 Introduction

Quantum states with a well defined number of quanta, or Fock states [126], have many roles in quantum information processing including quantum key distribution [127], quantum memory [128], generation of identical photons for remote entanglement [129] and universal control of quantum elements [130]. Following proposals for generating Fock states in AMO-based cavity QED systems [131, 132], the first experimental demonstration involved exchanging an excitation between a Rydberg atom and a cavity [133].

Fock states were first generated in a circuit quantum electrodynamics (cQED) system by coupling a tunable superconducting qubit to a microwave resonator [134, 135]. In those experiments, the excited state of the superconducting qubit was tuned to be resonant with the resonator and the excitation from the qubit was then transferred to

the resonator by vacuum Rabi oscillations. An advantage of this technique was that the transfer could be performed in a relatively fast time of 25 ns; sufficiently short that dephasing was not an issue. More recently, arbitrary Fock states were generated using selective number dependent arbitrary phase (SNAP) gates on a fixed-frequency qubit-cavity system [130, 136]. The SNAP approach took advantage of a highly coherent qubit-cavity system to generate the desired states in a time of 1 μ s.

STIRAP involves the transfer of population from an initial state $|0\rangle$ to a final state $|2\rangle$ via an intermediate state $|1\rangle$ by applying two Gaussian coherent Raman pulses that overlap in time. The pulse sequence is counter-intuitive, in that the initial pulse is on the $|1\rangle$ to $|2\rangle$ transition, and the second pulse is on the $|0\rangle$ to $|1\rangle$ transition [137, 138]. STIRAP is an interesting technique because it can overcome a forbidden transition (for example $|0\rangle$ to $|2\rangle$ to first order), while never occupying the intermediate state, and is robust against slight variations in the drive parameters [137]. Previous proposals and demonstrations of STIRAP using superconducting quantum devices involved transfer of populations between the three lowest levels of the device [139–141]. Such qutrit levels can have a relatively high anharmonicity and this simplifies the implementation. In contrast, I employed STIRAP to operate on composite cavity-qubit states, a system which has a relatively small anharmonicity. Using a STIRAP protocol with the third excited state of the qubit-cavity system as the intermediate state, I transferred the first excited state population of the qubit to the cavity, and thereby created a single photon Fock state.

In this chapter, I describe the use of a two-photon Stimulated Raman Adiabatic Passage (STIRAP) protocol, to transfer the excitation from a fixed-frequency transmon

qubit to a microwave cavity Fock state in 354 ns. By performing driven coherent manipulations on the generated state, and comparing the results to multi-level simulations, I determined the fidelity for the $n = 1$ Fock state to be $\geq 85\%$, a value similar to other initial demonstrations of Fock states [134–136]. In [Sec. 6.2](#), I describe the device I used, and the experimental setup. [Section 6.3](#) will describe how I modeled the system, and how I implemented the master-equation simulations. In [Sec. 6.4](#), I describe how I extended the process to create the second and third Fock states, with simulated fidelities of 68% and 43%, respectively. These fidelities were limited by the decay rate of the cavity relative to the adiabatic process duration. In [Sec. 6.5](#), I demonstrate how this protocol can be used to create a superposition of Fock states. In [Sec. 6.6](#), I describe reversal of STIRAP. I describe how I generated entanglement between the cavity and the qubit in [Sec. 6.7](#). I will conclude this chapter by summarizing the main results in [Sec. 6.8](#).

6.2 The Device and the Experimental Setup

The cQED system used in my experiment consisted of the transmon SPP-v1-Q7 embedded in the three-dimensional superconducting Al cavity 6D (see [Fig. 6.1\(a\)](#)) [27, 69]. The cavity-transmon system was attached to the mixing chamber of a Leiden Cryogenics CF-450 dilution refrigerator that operated at a temperature of 15 mK. The transmon [27] had a transition frequency of $\omega_q/2\pi = 5.5297$ GHz between the ground and excited state. I fabricated the transmon on a sapphire substrate (see [Chapter 3](#))

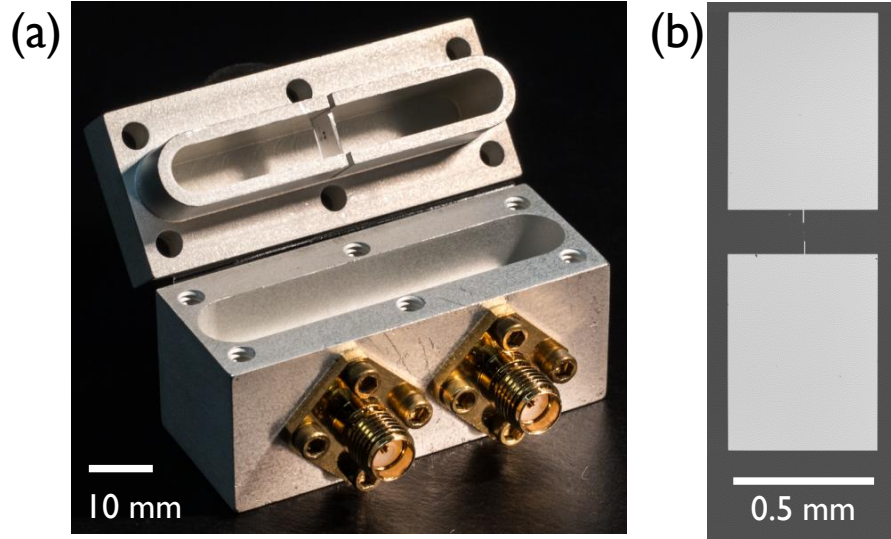


Fig. 6.1 The transmon-cavity system. (a) Photograph of transmon chip in the top of opened 3D Al cavity. (b) Optical micrograph of transmon SPP-v1-Q7 on sapphire chip.

and it had a single Al/AlO_x/Al Josephson junction capacitively shunted by two large 500 μm × 650 μm Al pads which reduced its charging energy (see Fig. 6.1(b)). The large pads also provided coupling with strength $g/2\pi = 69.8$ MHz to the TE₁₀₁ fundamental mode of the cavity with a resonance frequency $\omega_c/2\pi = 7.9350$ GHz. All the results in this chapter were obtained during Measurement Run #3 (see Sec. 5.9).

The input line to the cavity had an attenuation of 77 dB and the output had more than 60 dB of directional isolation at the cavity and qubit frequencies (see Sec. 4.1). To drive the transmon-cavity system, microwaves were delivered to the input port of the cavity with a coupling $Q_{\text{in}} \sim 400,000$ (adjusted and measured at room temperature). The state of the system was interrogated using a high-power cavity transmission measurement that was sensitive to the transmon state [104]. The output port had coupling $Q_{\text{out}} \sim 200,000$ (adjusted and measured at room temperature) and sent the

transmitted microwaves to a low noise HEMT amplifier at 3 K [101]. The output signal was further amplified at room temperature with a low-noise amplifier (see Fig. 4.4). The signal was then mixed down to an intermediate frequency of 10 MHz, digitized and analyzed. The experimental setup is described in detail in Chapter 4 (see Fig. 4.4) and is similar to that described by Novikov *et al.* [142, 143].

The generation of Gaussian pulses was carried out by programming a Tektronix AWG70002A arbitrary waveform generator (AWG). The maximum sampling rate for the instrument was 25 GSa/s with 10 bits of resolution for voltage. The output from the AWG was amplified at room temperature with a Mini-Circuits ZVA-183-S+ amplifier before being sent into the dilution refrigerator.

6.3 Modeling and Characterizing the System

In my setup, the coupling strength $g \sim 70$ MHz is much smaller than the qubit-cavity detuning $\Delta = \omega_c - \omega_q = 2.4$ GHz. In this limit, the undriven qubit-cavity system can be well described by the dispersive Jaynes-Cummings Hamiltonian [50]:

$$\mathcal{H}_{\text{JC}} = \frac{1}{2}\hbar\omega_q\sigma_z + \hbar(\omega_c + \chi\sigma_z)\hat{\mathcal{N}} \quad (6.1)$$

where $\hat{\mathcal{N}}$ is the photon number operator for the cavity, σ_z is the Pauli-Z operator, and $\chi/2\pi = -2.0$ MHz is the effective frequency dispersive shift resulting from the cavity-qubit coupling.

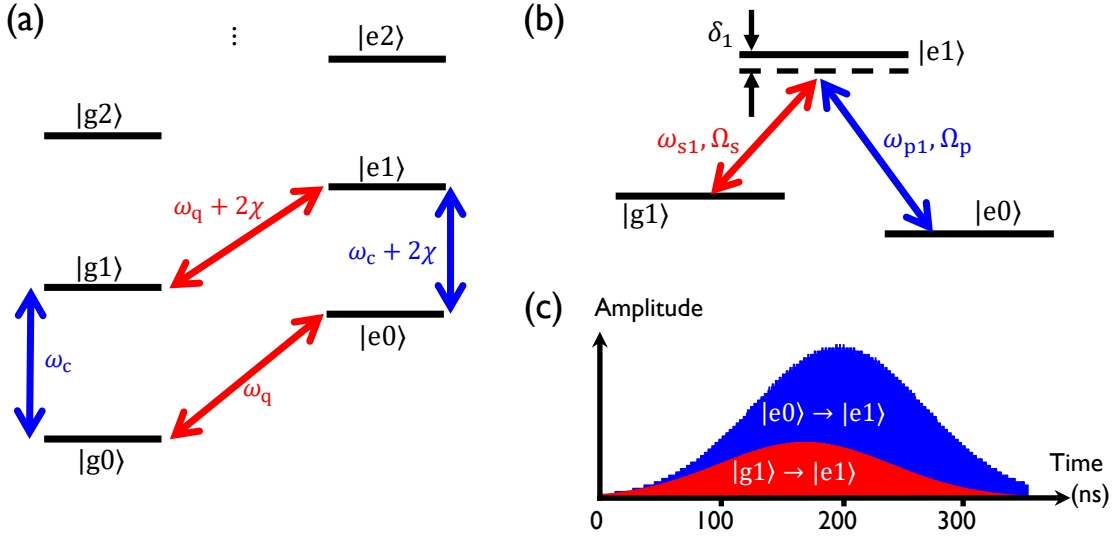


Fig. 6.2 STIRAP in a transmon-cavity system. (a) Level structure (not to scale) for the transmon-cavity system. Letters and numbers within kets denote qubit and cavity photon-like states, respectively. (b) Levels used for the generation of $|g1\rangle$ Fock state with the Stokes (red) and pump (blue) tones with frequencies $\{\omega_{s1}, \omega_{p1}\}$ and drive strengths $\{\Omega_s, \Omega_p\}$, respectively. δ_1 is the common detuning for both drives from $|e1\rangle$. (c) Pulse envelopes for the Stokes (red) and pump (blue) tones.

The Hamiltonian \mathcal{H}_{JC} gives an energy level structure that has two ladders. One ladder is for all states that have the qubit in the ground state $|g\rangle$, while the second ladder is for the excited state $|e\rangle$ (see Fig. 6.2(a)). The rungs of each ladder correspond to a different integer number of cavity photons. My state measurement technique allowed me to find the total probability \mathcal{P}_e to find the system in the $|e\rangle$ ladder, by averaging repeated measurements.

The transmon had a characteristic relaxation time of $T_1 = 24\mu\text{s}$ and a Ramsey decay time $T_2^* = 22\mu\text{s}$. The cavity had a lifetime $\kappa^{-1} = 2.5\mu\text{s}$, set by Q_{out} to allow for relatively fast measurements. I note that my device operated in the strong dispersive regime of circuit QED since $2\chi \gg \left\{ \kappa, \frac{1}{T_1}, \frac{1}{T_2^*} \right\}$ [124].

For my numerical simulations, the master equation for the density matrix ρ was solved in the time domain. The Jaynes-Cummings ladders were truncated to a maximum of 11 levels in the $|g\rangle$ ladder and 10 levels in the $|e\rangle$ ladder. Denoting the cavity and qubit microwave drive strengths $\Omega_c(t)$ and $\Omega_q(t)$, respectively, the drive Hamiltonian can be written as (see [Sec. 2.2.4](#))

$$\mathcal{H}_{\text{int}} = \hbar\Omega_c(t)(a + a^\dagger) + \hbar\Omega_q(t)(|g\rangle\langle e| + |e\rangle\langle g|) \quad (6.2)$$

where a and a^\dagger represent the annihilation and creation operators for the cavity, respectively.

Cavity and qubit dissipation was incorporated through the Lindblad-Kossakowski formalism [[54](#), [55](#)]. The driven system Hamiltonian can then be written as, $\mathcal{H} = \mathcal{H}_{\text{JC}} + \mathcal{H}_{\text{int}}$ and the resulting master equation for the density matrix ρ can be written as,

$$\frac{\partial \rho}{\partial t} = \frac{1}{i\hbar} [\mathcal{H}, \rho] + \sum_j \Gamma_j \left(A_j \rho A_j^\dagger - \frac{1}{2} A_j^\dagger A_j \rho - \frac{1}{2} \rho A_j^\dagger A_j \right). \quad (6.3)$$

Here, the index j runs through the various decoherence channels (cavity relaxation, qubit relaxation, qubit dephasing) and Γ_j represents the decoherence rate for each channel. A_j are the Lindblad operators corresponding to each channel. The qubit and cavity relaxation Lindblad operators can be given in the form $A_{\text{qdec}} = \sigma^-$ and $A_{\text{cdec}} = a$, respectively, and the qubit dephasing can be represented by the Lindblad operator $A_{\text{qdph}} = \sigma_z$.

Fidelity between any two states (for example realized state ϕ and target state ψ) described by density matrices ρ and σ , can be defined as

$$F(\rho, \sigma) = \text{Tr} \sqrt{\sqrt{\rho} \sigma \sqrt{\rho}}. \quad (6.4)$$

The above definition simplifies considerably when one of the states is a pure state (e.g. $|g1\rangle$, or $|g0\rangle + |g2\rangle$) [3]. As I was trying to generate pure states, I instead used

$$\mathcal{F}(\rho, |\psi\rangle) = [F(\rho, |\psi\rangle)]^2 = \langle \psi | \rho | \psi \rangle \quad (6.5)$$

where $|\psi\rangle$ is the target pure state and ρ is the density matrix for the generated state. Equation (6.5) is more intuitive than Eq. (6.4), since it is just the probability of finding the system in state ψ .

6.4 Generating Fock States $n = 1, 2, 3$

The process I used to generate the single-photon Fock state $|g1\rangle$ involved use of the four lowest levels in the system: $|g0\rangle$, $|e0\rangle$, $|g1\rangle$, and $|e1\rangle$ (see Fig. 6.2(a)). After passively cooling the system to the $|g0\rangle$ state, a 32 ns duration $\pi_{g0 \rightarrow e0}$ pulse at the qubit frequency ω_q was sent to add one excitation to the qubit and obtain the state $|e0\rangle$. To transfer population from $|e0\rangle$ to $|g1\rangle$, which is a first order forbidden transition, STIRAP was used via the intermediate level $|e1\rangle$ (Fig. 6.2(b)). In this protocol, I first applied a Stokes tone at frequency $\omega_{s1} = \omega_q + 2\chi - \delta_1$, slightly detuned by an amount

δ_1 from the $|g1\rangle$ to $|e1\rangle$ transition frequency and with a Gaussian envelope for the amplitude. I then applied a slightly delayed Gaussian-shaped pump tone pulse that overlapped with the Stokes pulse. The pump pulse had a frequency $\omega_{p1} = \omega_c + 2\chi - \delta_1$, which included the same detuning δ_1 as the Stokes tone.

For a conventional three-level system undergoing STIRAP, process fidelity does not depend heavily on the detuning from the intermediate level. However, my system has a multi-level transmon coupled to a multi-level cavity. I found that a negative detuning from level $|e1\rangle$ (*i.e.* $-\delta_1 < 0$) was beneficial to minimize leakage to higher levels, and I optimized δ_1 through simulations. The counter-intuitive profile for the Stokes and pump pulses was

$$\Omega(t) = \Omega_s \exp\left[-\frac{(t-t_s)^2}{2\sigma^2}\right] \sin[\omega_{s1}t + \phi_s] + \Omega_p \exp\left[-\frac{(t-t_p)^2}{2\sigma^2}\right] \sin[\omega_{p1}t + \phi_p], \quad (6.6)$$

where Ω_s and Ω_p were the peak amplitudes of the Stokes and pump tones respectively, σ was the width of the Gaussian envelope for both pulses, t_s and t_p were the times when the Stokes and pump envelopes were at their maximum, and ϕ_s and ϕ_p were offset phases in the Stokes and pump carrier tones respectively.

To determine the initial choices for STIRAP parameters, density matrix simulations were performed at the outset of the experiment. I solved the master equation in the laboratory frame, while applying the time dependent STIRAP protocol. Following initial experiments, the model was refined using a total of 11 cavity levels in the $|g\rangle$ -ladder and 10 cavity levels in the $|e\rangle$ -ladder. The programmed waveforms used for

the experiment were used in the numerical simulations (see Table 6.1).

Figure 6.3 shows the measured probabilities \mathcal{P}_e (filled points) of the qubit being in its excited state versus time t during generation of the first, second and third Fock states using the STIRAP protocol. For comparison, results from the simulations are

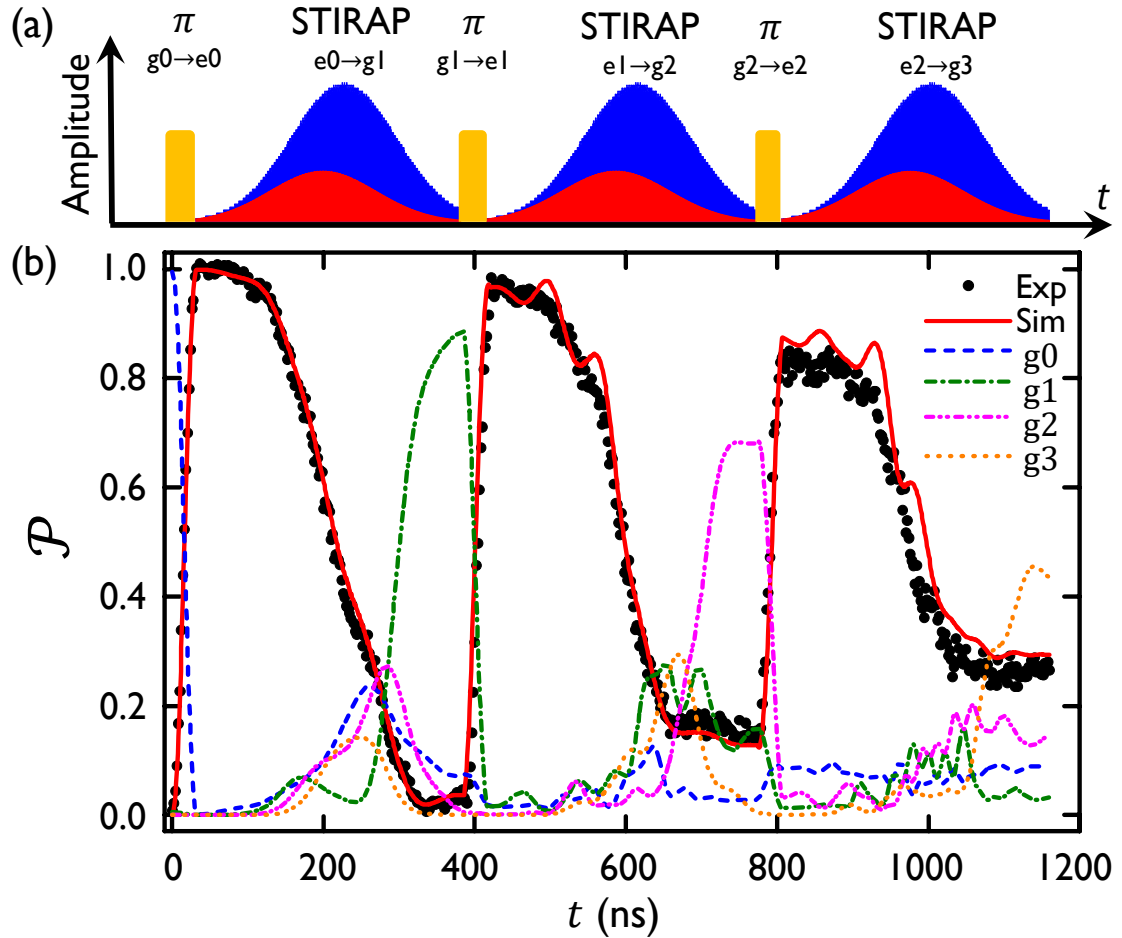


Fig. 6.3 Generation of the first three Fock states. (a) Pulse sequence for generating Fock states $|g_1\rangle$, $|g_2\rangle$ and $|g_3\rangle$. The π -pulses (yellow) transfer $|g_0\rangle \rightarrow |e_0\rangle$, $|g_1\rangle \rightarrow |e_1\rangle$ and $|g_2\rangle \rightarrow |e_2\rangle$. The Stokes (red) and pump (blue) pulses transfer $|e_0\rangle \rightarrow |g_1\rangle$, $|e_1\rangle \rightarrow |g_2\rangle$ and $|e_2\rangle \rightarrow |g_3\rangle$. (b) State probabilities \mathcal{P} versus time t for $|g_1\rangle$, $|g_2\rangle$ and $|g_3\rangle$ Fock state generation protocol shown in (a). Measured data are total qubit excited state populations \mathcal{P}_e (black dots). Solid red curve shows the corresponding \mathcal{P}_e from density matrix simulations. Dashed/dotted curves show simulated evolution of the populations of Fock states $|g_0\rangle$, $|g_1\rangle$, $|g_2\rangle$ and $|g_3\rangle$ corresponding to 0, 1, 2, and 3 photons in the cavity respectively.

Table 6.1 Parameter values used in STIRAP pulses. The drive phases ϕ_{p1} and ϕ_{s1} had no effect on the generation of the Fock states and for simplicity were set to zero.

Parameter	Symbol	Value
Stokes drive strength (qubit-like)	$\Omega_s/2\pi$	9.6 MHz
Pump drive strength (cavity-like)	$\Omega_p/2\pi$	26.2 MHz
Stokes-pump pulse separation	t_{sep}	14 ns
Standard deviation of Gaussian pulses	σ	70.8 ns
Total length of each truncated Gaussian pulse	t_{len}	340 ns
Common detuning for Stokes/pump drives from $ e1\rangle$	δ_1	8.1 MHz
Common detuning for Stokes/pump drives from $ e2\rangle$	δ_2	9.7 MHz
Common detuning for Stokes/pump drives from $ e3\rangle$	δ_3	11.3 MHz
$ g1\rangle \rightarrow e1\rangle$ Stokes frequency	$\omega_{s1}/2\pi$	5.5176 GHz
$ e0\rangle \rightarrow e1\rangle$ Pump frequency	$\omega_{p1}/2\pi$	7.9248 GHz
$ g2\rangle \rightarrow e2\rangle$ Stokes frequency	$\omega_{s2}/2\pi$	5.5119 GHz
$ e1\rangle \rightarrow e2\rangle$ Pump frequency	$\omega_{p2}/2\pi$	7.9233 GHz
$ g3\rangle \rightarrow e3\rangle$ Stokes frequency	$\omega_{s3}/2\pi$	5.5063 GHz
$ e2\rangle \rightarrow e3\rangle$ Pump frequency	$\omega_{p3}/2\pi$	7.9217 GHz

shown as curves. To collect each point at time t in this plot, execution of the protocol was halted at time t , and a high-power cavity pulse applied to destructively measure the probability of the qubit being in the excited state. The protocol was started again from the beginning and repeated 1000 times to obtain the average probability to be in the excited state \mathcal{P}_e . For the first 32 ns, a $\pi_{g0 \rightarrow e0}$ was sent to the device and upon completion $\mathcal{P}_e > 96\%$ (confidence level obtained from evaluating false counts during single shot measurements). After placing the system in $|e0\rangle$, the Stokes and pump STIRAP pulses were sent to the device using the parameters listed in Table 6.1. The total duration to complete STIRAP was 354 ns. Comparing the data to the simulations, I found that the fidelity upon completion was $\mathcal{F}_{g1} = 89\%$, limited by photon leakage out of the cavity.

Due to the relatively small photon anharmonicity and the relatively short lifetime of

photons in the cavity, Wigner tomography [144] could not be performed in my system. Instead, I examined the fidelity of the Fock state by performing Rabi oscillations immediately following the STIRAP protocol (see Appendix B). The Rabi oscillations were performed by driving at both the $|g1\rangle \rightarrow |e1\rangle$ transition frequency $\omega_{g1 \rightarrow e1}$, and at the $|g0\rangle \rightarrow |e0\rangle$ transition frequency ω_q , for a range of drive amplitudes. For small drive amplitudes V_{drive} , the oscillations when driven at ω_q (Fig. 6.4(a)) show a larger Rabi frequency f_{Rabi} and lower \mathcal{P}_e amplitude, consistent with the drive frequency being detuned from the $|g1\rangle \rightarrow |e1\rangle$ transition. Each Rabi oscillation was fit to the sum of two oscillatory functions to extract the frequency f_{Rabi} and the amplitude A_{Rabi} of each component. The amplitude of the resonant component is a metric for the fidelity with which the STIRAP process generated the desired state $|g1\rangle$.

Figure 6.4(b) shows the four extracted Rabi frequencies when the system was driven at the two drive frequencies $\omega_{g1 \rightarrow e1}$ and ω_q . Two of the data sets are linear with drive voltage and extrapolate to a zero Rabi frequency at zero drive voltages, consistent with a resonant drive process. The other pair of Rabi frequencies extrapolates, at small drive voltages, to a frequency of approximately 4 MHz, consistent with a non-resonant process with detuning 2χ (Fig. 6.2(a)). The fidelity of the $|g1\rangle$ Fock state can be determined from the amplitude of the Rabi oscillations, as shown in Fig. 6.4(c). At small drive voltages, the amplitude for the resonant component when driving at $\omega_{g1 \rightarrow e1}$ yielded a fidelity of $\mathcal{F}_{g1} \geq 85\%$.

Following generation of $|g1\rangle$, the second ($|g2\rangle$) and third ($|g3\rangle$) Fock states were produced in a similar manner (see Fig. 6.3). When generating the higher Fock states, I tuned the parameters through simulations, to optimize the fidelity of the desired state

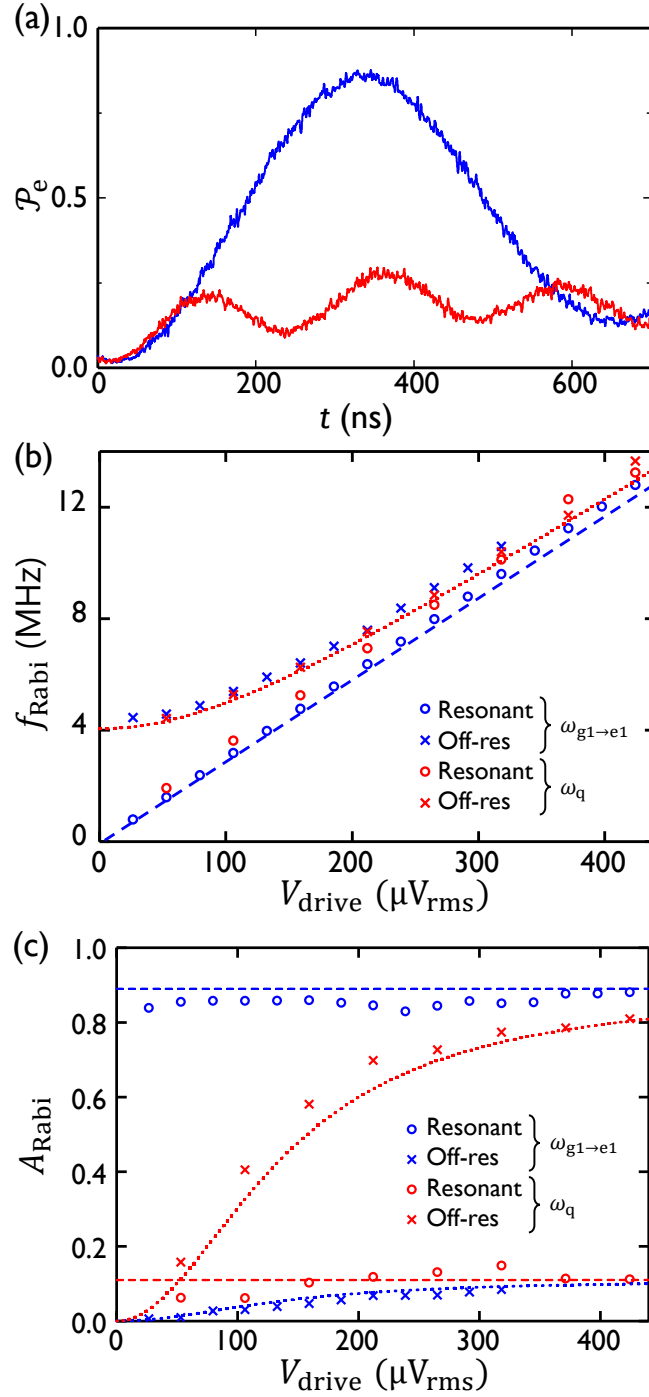


Fig. 6.4 Verification of $|g_1\rangle$ Fock state: (a) Driven Rabi oscillations at $\omega_{g_1 \rightarrow e_1}$ (blue) and ω_q (red) frequencies, at a relatively small drive amplitude of $V_{\text{drive}} = 53 \mu\text{V}_{\text{rms}}$. (b) Extracted Rabi frequencies f_{Rabi} versus drive amplitude V_{drive} following generation of $|g_1\rangle$ through STIRAP. Dashed and dotted lines depict expected frequencies for a two-level system subjected to an on-resonant and 4.04 MHz detuned off-resonant drives, respectively. (c) Extracted Rabi amplitude oscillations. Dashed and dotted lines depict expected behavior for a two-level system after setting up the cavity in a Fock state with $\mathcal{F}_{g_1} = 89\%$.

Table 6.2 Optimized cavity and qubit pulse parameters used in simulating Fock state generation.

Parameter	Symbol	Value
Number of transmon levels	n_q	2
Maximum number of cavity excitations	n_{ex}	10
Non-dressed cavity frequency	$\tilde{\omega}_c/2\pi$	7.93497 GHz
Non-dressed qubit frequency	$\tilde{\omega}_q/2\pi$	5.53175 GHz
Effective cavity-qubit coupling	$g/2\pi$	69.8 MHz
$ g0\rangle \rightarrow e0\rangle$ π -pulse frequency	$\omega_{g0 \rightarrow e0}/2\pi$	5.5297 GHz
$ g1\rangle \rightarrow e1\rangle$ π -pulse frequency	$\omega_{g1 \rightarrow e1}/2\pi$	5.5257 GHz
$ g2\rangle \rightarrow e2\rangle$ π -pulse frequency	$\omega_{g2 \rightarrow e2}/2\pi$	5.5216 GHz
$ g0\rangle \rightarrow e0\rangle$ π -pulse strength	$\Omega_{g0 \rightarrow e0}/2\pi$	17.0 MHz
$ g1\rangle \rightarrow e1\rangle$ π -pulse strength	$\Omega_{g1 \rightarrow e1}/2\pi$	15.4 MHz
$ g2\rangle \rightarrow e2\rangle$ π -pulse strength	$\Omega_{g2 \rightarrow e2}/2\pi$	14.7 MHz
$ g0\rangle \rightarrow e0\rangle$ π -pulse time	$t_{g0 \rightarrow e0}$	32 ns
$ g1\rangle \rightarrow e1\rangle$ π -pulse time	$t_{g1 \rightarrow e1}$	34 ns
$ g2\rangle \rightarrow e2\rangle$ π -pulse time	$t_{g2 \rightarrow e2}$	32 ns

(see Table 6.2 for the general system parameters used in simulations). $|g2\rangle$ was created by adding another excitation to the system: a $\pi_{g1 \rightarrow e1}$ pulse was followed by another STIRAP protocol taking the system to $|g2\rangle$, with a comparison to the simulations yielding a fidelity $\mathcal{F}_{g2} = 68\%$ (see Fig. B.4). A similar process was implemented to generate $|g3\rangle$, with a comparison to the simulations yielding a fidelity $\mathcal{F}_{g3} = 43\%$. As with $|g1\rangle$, simulations revealed that \mathcal{F}_{g2} and \mathcal{F}_{g3} were limited by κ .

For comparison, the red curve in Fig. 6.3 shows the simulated results for the excited state probability using the optimized parameters in Table 6.1 and Table 6.2. Except for some small, fine-scale oscillatory behaviour found in the simulation during the $|g2\rangle$ and $|g3\rangle$ STIRAP protocol, there is good agreement with the experiment. The dashed and dotted curves show the simulation of the expected populations of the

various Fock states in the cavity, which I could not measure directly. The rotating wave approximation was not employed in the simulations, and the 21 level simulation for $|g1\rangle$ generation was also checked against a simulation performed with 51 levels in the two-ladder system, which did not yield significant differences.

I note that Bergmann *et al.* have derived both local and global criteria for adiabatic following in a system, to verify that a system is truly undergoing a STIRAP process [137]. The local adiabaticity criterion addresses the instantaneous non-adiabatic coupling possible with various pulse shapes. As my experiment employed smooth Gaussian pulses, the local adiabaticity criterion was naturally satisfied. The global adiabaticity criterion addresses adiabaticity for the entire process, and for STIRAP is given by

$$\Omega_{\text{eff}}\Delta\tau > 10 \quad (6.7)$$

where $\Omega_{\text{eff}} = \sqrt{\Omega_p^2 + \Omega_s^2}$ is the root-mean-square (rms) Rabi frequency and $\Delta\tau$ is the total overlap time for the two pulses [137]. Using Eq. (6.6) and my parameters for generating $|g1\rangle$, I found $\int \Omega_{\text{eff}} dt \sim 30$, satisfying global adiabaticity Eq. (6.7). The relative insensitivity of the STIRAP protocol to parameter fluctuations was verified through simulations (see Table 6.3). Examining the table, one sees that a $\pm 10\%$ variation in the parameters resulted in significantly smaller reductions in fidelity, with the exception of increase in Ω_p or decrease in δ .

Table 6.3 Sensitivity of process fidelity to STIRAP parameters: Simulated loss of fidelity in $|g1\rangle$ generation due to varying the STIRAP parameters by 10% from the predetermined optimal values.

Process Parameter	Loss of fidelity from parameter adjustment	
	Decrease of 10%	Increase of 10%
Stokes drive strength (Ω_s)	3.2%	6.4%
Pump drive strength (Ω_p)	2.9%	10.3%
Pulse truncate length (t_{len})	1.2%	3.5%
Standard deviation of pulse (σ)	0.4%	5.6%
Separation between pulses (t_{sep})	0.5%	0.5%
Common detuning from $ e1\rangle$ (δ)	16.9%	1.8%
π -pulse length ($t_{g \rightarrow e}$)	2.3%	2.5%

6.5 Generating Fock State Superpositions

STIRAP can also be used to create superpositions of Fock states. To generate a superposition of $|g0\rangle$ and $|g1\rangle$, I replaced the initial $\pi_{g0 \rightarrow e0}$ pulse for the Fock state creation with a 16 ns $(\pi/2)_{g0 \rightarrow e0}$ pulse to create the superposition state $(|g0\rangle + |e0\rangle)/\sqrt{2}$. Next I used the $|e0\rangle \rightarrow |g1\rangle$ STIRAP protocol to coherently transfer the population in $|e0\rangle$ to $|g1\rangle$ (see Fig. 6.5(a)). Following the 370 ns total execution time, I observed $\mathcal{P}_e \approx 0$ and simulations showed that the state was an equal superposition of $|g0\rangle$ and $|g1\rangle$.

During this STIRAP process, I found that \mathcal{P}_e exceeded 0.5 and displayed an oscillatory pattern (see Fig. 6.5(a)). To understand this aspect of the data, I measured the behavior when the phase of each microwave drive was independently varied. I found that the oscillations depended strongly on the phase $\phi_{\pi/2}$ of the initial $\pi/2$ pulse and the phase ϕ_s of the Stokes tone but not the phase ϕ_p of the pump tone (see Fig. 6.6).

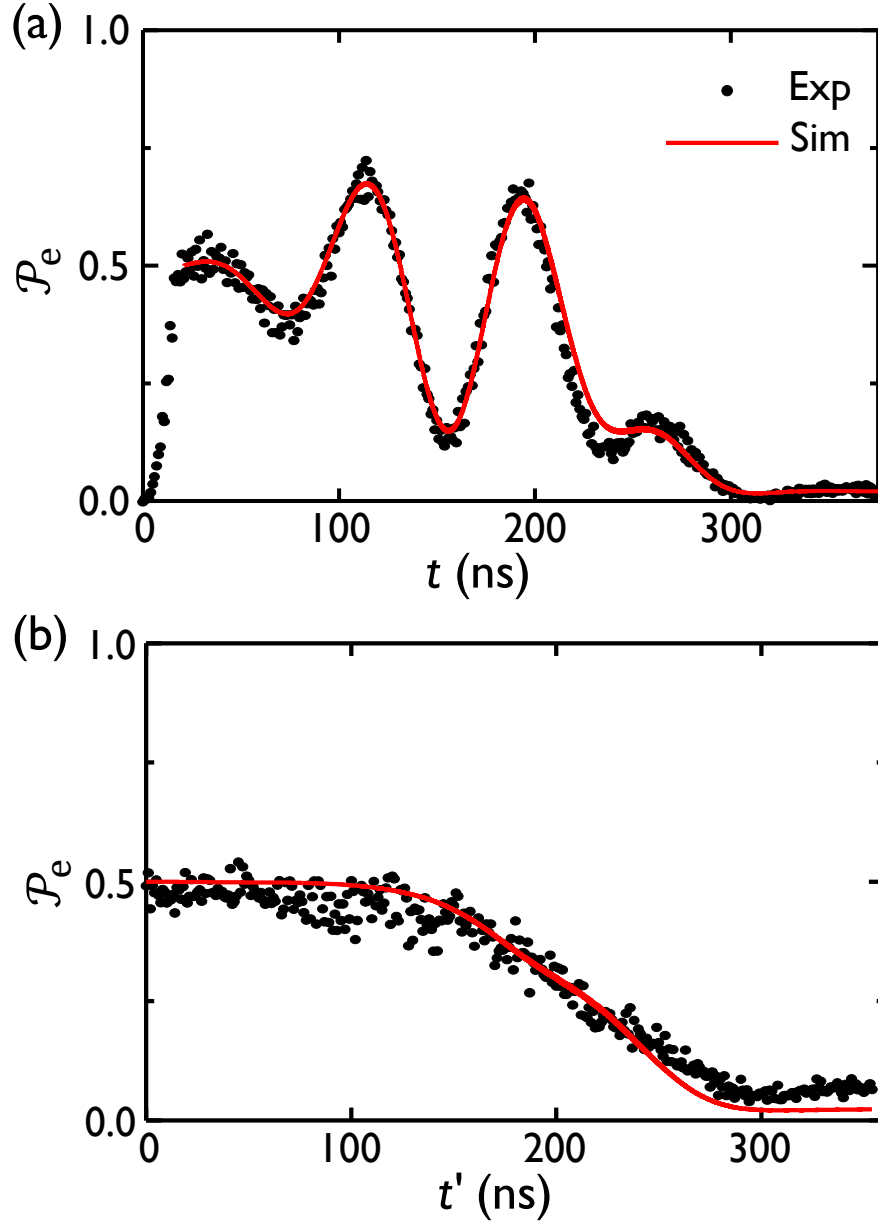


Fig. 6.5 Generation of Fock state superpositions with STIRAP (a) Equal superposition between $|g_0\rangle$ and $|g_1\rangle$ generated using STIRAP after a $\pi/2$ initialization pulse. All phases for the drives and the initialization were set to zero ($\phi_{\pi/2} = \phi_s = \phi_p = 0$). (b) STIRAP performed on the system after driving to a mixed steady state with a $150\ \mu\text{s}$ long pulse at frequency ω_q . $t' = 0$ corresponds to the end of the saturation pulse. Experimental data points (black circles) and simulated pooled populations (solid red curve) are shown.

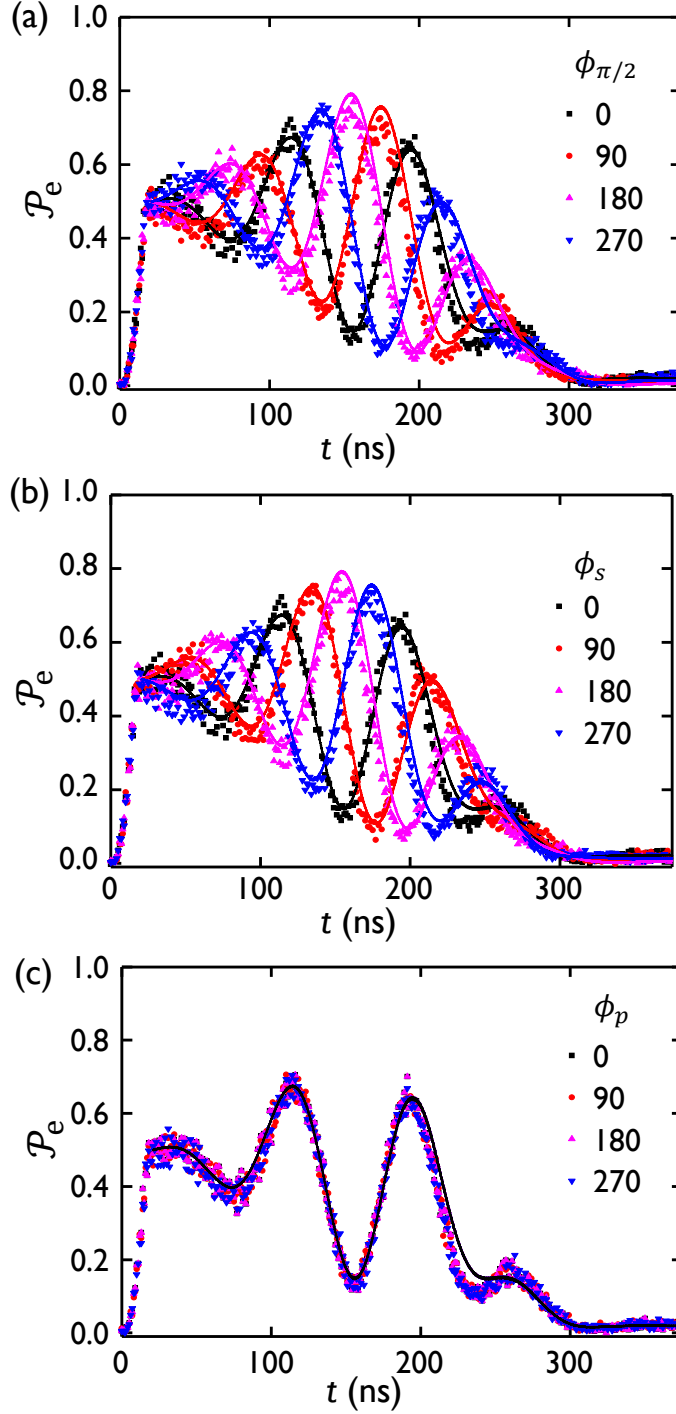


Fig. 6.6 Fock state superpositions' variations with STIRAP phases. Equal superpositions between $|g_0\rangle$ and $|g_1\rangle$ are generated using a $\pi/2$ initialization pulse. (a) The phases ϕ of $\pi/2$ initialization, (b) Stokes and (c) pump pulses were changed while the other phases were held constant at zero. The experimental data points for phases 0° (black), 90° (red), 180° (magenta) and 270° (blue) as well as the respective simulated evolutions of \mathcal{P}_e (solid curves) are shown. The phase of the initialization and Stokes pulses exhibit complementary behavior in modifying the oscillatory features during the generation of $(|g_0\rangle + |g_1\rangle)/\sqrt{2}$. The phase ϕ_p of the pump pulse has no impact on the oscillatory features.

This phase dependence, and the fact that \mathcal{P}_e exceeds 0.5, during execution suggests that the population in $|g0\rangle$ in the initial state plays a pivotal role when turning on the Stokes tone. Comparing the data to the simulations again revealed good agreement (see solid curves in Fig. 6.6). The simulations also implied that the final state was prepared with a fidelity of approximately 93%, limited by the decay rate κ of the cavity.

To further examine the dependence on the initial state, STIRAP was performed after the qubit was driven to a mixed steady-state, removing qubit phase coherence. This resulted in the disappearance of oscillations observed previously (see Fig. 6.5(b)). I inferred that the oscillations were the direct result of coherent interference within the system when undergoing STIRAP. I believe the four lowest levels $|g0\rangle$, $|e0\rangle$, $|g1\rangle$ and $|e1\rangle$ set up a suitable system for observing quantum interference between difference excitation pathways [145], though confirming the source of this interference was beyond the scope of this work. The existence of oscillations during the STIRAP process demonstrates the coherent nature of the behavior as well as the preservation of coherence during execution.

6.6 STIRAP Reversal

I discussed in Sec. 6.4 and Sec. 6.5, the use of STIRAP for the transfer $|e0\rangle \rightarrow |g1\rangle$. The reverse process $|g1\rangle \rightarrow |e0\rangle$ can also be accomplished simply by reversing the order of pulses. When performing the reversal immediately after $|g1\rangle$ Fock state generation, the recovered population is $\approx 80\%$; consistent with the significantly longer time to

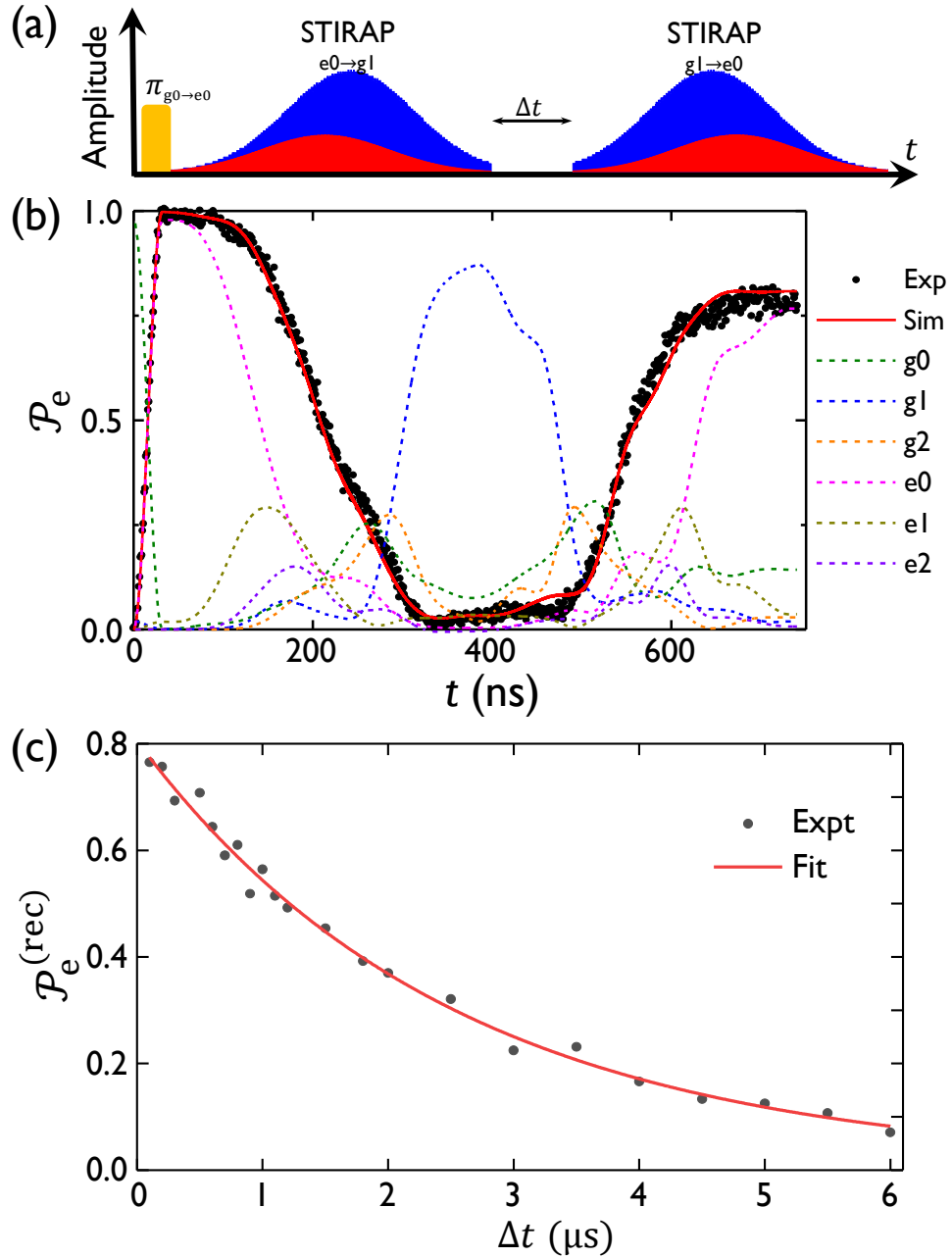


Fig. 6.7 Reverse STIRAP and measurement of cavity decay rate. (a) Pulse sequence to generate $|g1\rangle$ and map back with a time-delay Δt . (b) Data from reversing STIRAP (black points) and simulated evolution (solid red curve) for $\Delta t = 0$. Dashed lines show simulated evolution of lowest Jaynes-Cummings levels. (c) Recovered populations from reversals performed with various Δt time-delays (black points) along with the exponential-decay fit (solid red) with decay constant $\tau = 2.51 \mu s$.

complete this two step process (see Fig. 6.7(a),(b)).

A delay can be introduced prior to the reversal pulses to investigate the $|g1\rangle$ decay which occurs with rate κ . By varying the delay time Δt and plotting versus the recovered population $\mathcal{P}_e^{(\text{rec})}$, I was able to obtain the cavity decay time (see Fig. 6.7(c)). For longer delays, a lower population is available for the reverse mapping, and eventually ($\Delta t = 6\mu\text{s}$) most of the population has decayed to $|g0\rangle$, and there is little population to be transferred back to $|e0\rangle$. Fitting yielded an exponential decay time of $\tau_{\text{cav}} = \kappa^{-1} = 2.51\mu\text{s}$, which was in excellent agreement with independent measurements of cavity lifetime.

6.7 Fractional STIRAP

In the previous sections, STIRAP was employed as a SWAP operation to transfer any population in the excited state of the qubit to the first excited state of the cavity, or vice versa. In contrast, Vitanov *et al.* [146] described a technique by which it was possible to create superpositions of states by performing a partial transfer, which they termed f-STIRAP (fractional STIRAP). They achieved this by allowing the Stokes pulse to precede the pump pulse as in conventional STIRAP, but letting them vanish simultaneously at the end. By adjusting the synchronization time, the superposition components could be adjusted [146].

In my system, I implemented f-STIRAP by decreasing the Stokes and pump ampli-

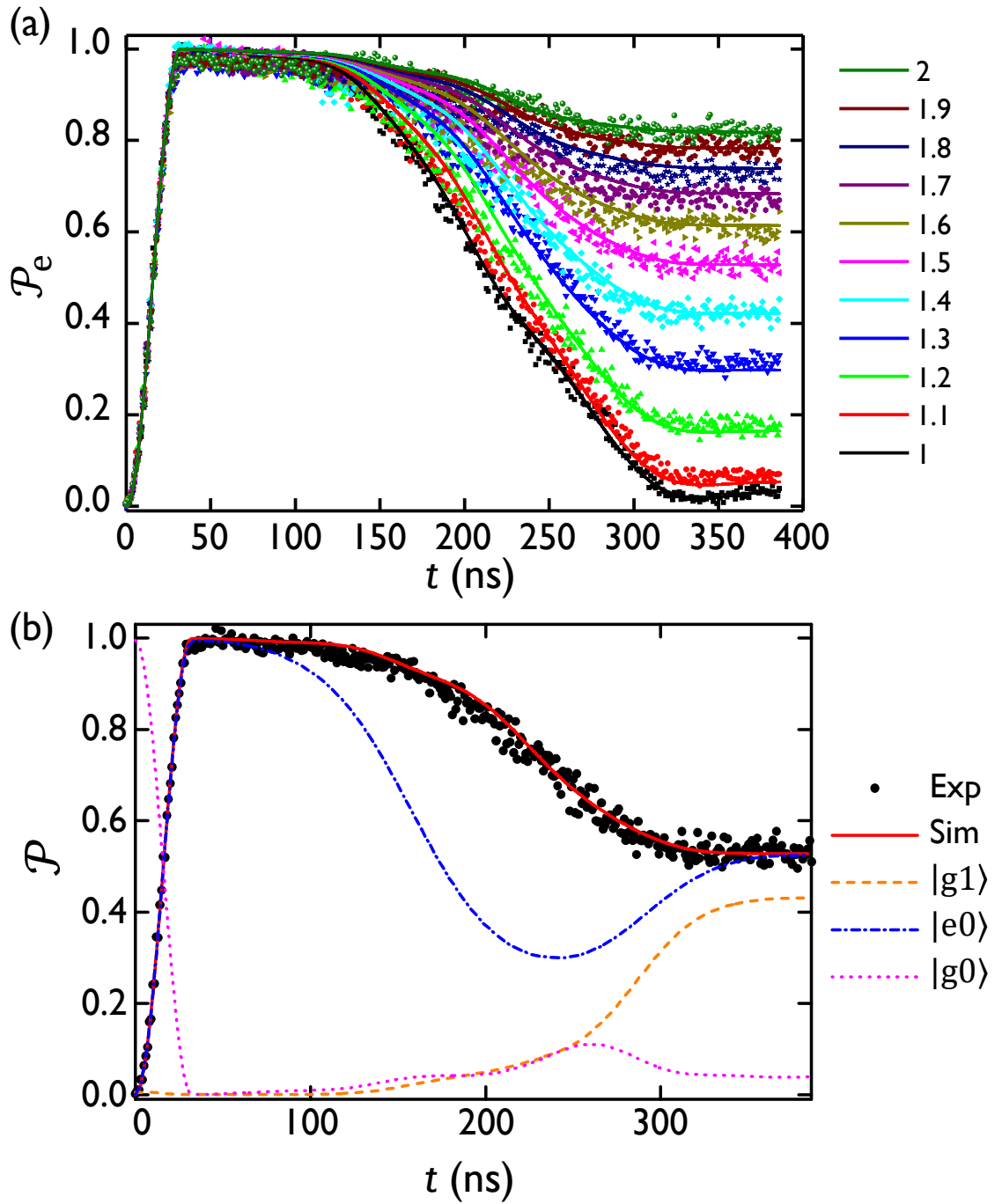


Fig. 6.8 Cavity-qubit entangled state preparation. (a) Plot showing \mathcal{P}_e versus t for different Stokes and pump drive attenuation factors β . The data points and pooled excited populations from simulations (solid curves) with colors corresponding to the value of β are shown. (b) Generation of the coherent superposition between $|g1\rangle$ (orange dashed) and $|e0\rangle$ (blue dash-dotted) occurs for $\beta = 1.5$. Data points (black) and simulated excited population (red curve) are shown.

tudes by the same attenuation factor β from the optimal STIRAP values so that

$$\Omega'_s = \Omega_s / \beta \tag{6.8}$$

$$\Omega'_p = \Omega_p / \beta.$$

By varying β , partial transfers were performed from the qubit to the cavity, as verified by the residual population in the qubit $|e\rangle$ state (see Fig. 6.8(a)). When $\beta = 1.5$, comparing the simulations to the data gave final populations for $|g1\rangle$ and $|e0\rangle$ as 0.43 and 0.52, respectively (see Fig. 6.8(b)). The resultant state was approximately $0.723 |e0\rangle + (0.563 - 0.324i) |g1\rangle$ with a 6% probability for being in other states. This was consistent with the generation of a highly entangled state between the qubit and the cavity.

6.8 Summary

In summary, a STIRAP-based protocol for coherently transferring the population from a superconducting qubit to $n = 1, 2,$ and 3 Fock states in a superconducting microwave cavity was demonstrated. The protocol required $3n$ drives to move the system from the ground state, to the n^{th} Fock state.

Based on my simulations, increasing the lifetime of the cavity by a factor of ten [147] would improve the fidelity for generation of the first Fock state from the present value of 89% to 95%. An increased lifetime would also allow the application of more sophisticated measurement analysis techniques on the generated states [136], which

were not viable in the present system due to the relatively low anharmonicity. Further improvements in the Fock state fidelity would require increasing the width of the STIRAP Gaussian pulses (σ). Alternatively, increasing the dispersive shift χ would enable the use of stronger drives and shorter STIRAP times, as increased anharmonicity reduces leakage to other states. Implementing adiabatic shortcuts [148–150] is another approach which could potentially speed up the transfer process. I note that if the cavity lifetime is much shorter than the qubit lifetime, STIRAP can be used to reset the qubit by transferring population from the $|e\rangle$ ladder to the $|g\rangle$ ladder and using the short cavity lifetime to initialize to $|g0\rangle$.

I note that the STIRAP approach also works in the reverse direction; if the order of the Stokes and probe pulses are reversed, then the population will be transferred from the cavity to the qubit. In fact, I used this technique to measure the lifetime of the first Fock state and found it to be $2.51\ \mu\text{s}$, in good agreement with the decay rate of the cavity. This protocol could be used for single-shot detection of itinerant microwave photons with noise limited only by the fidelity of the qubit readout. Such a high-fidelity single-microwave-photon detector may allow measurements of the Bell state between the qubit and the cavity, including violation of Bell's inequality [151].

CHAPTER 7

A Generalized CNOT Gate

7.1 Introduction

Entanglement is at the core of quantum computing, as can be seen from the requirement that we must be able to do arbitrary single-qubit rotations and an entangling two-qubit gate in order to form a universal quantum gate set [3, 152]. Different types of entangling gates have performance that is facilitated or hindered depending on the computer architecture, and a wide variety of such gates have been examined using trapped ions [11], semiconductor quantum dots [153], and nitrogen-vacancy centers in diamond [154]. For superconducting qubits, entangling gates can be broadly categorized into those based on flux-tunability & parametric control, and all-microwave control [155, 156]. Understanding the trade-offs and performance of gates for quantum computing applications is an active area of research, with scalability, ease of use, gate speed and gate fidelity being important factors in determining the suitability of a gate for a particular quantum system.

In cQED [42] based systems, flux-tunable elements allow fast and efficient gates

at the expense of more control lines and shorter coherence times, mostly attributed to flux-noise and operating the qubits off the sweet spot [157]. Examples of such gates include the dynamically tuned C-Phase gate [158–160], the iSWAP gate [161], and the direct-resonance $\sqrt{\text{iSWAP}}$ gate [162, 163]. Gates utilizing all-microwave controls are slower in general, require fewer control lines but enable longer qubit lifetimes. Examples include the cross-resonance (CR) gate [164, 165], resonator-sideband-induced $\sqrt{\text{iSWAP}}$ gate [166], the microwave-activated C-Phase gate [167], and the resonator-induced-phase (RIP) gate [46, 168]. A major limitation of the CR gate is the requirement of positioning qubit frequencies within a narrow window, which proves cumbersome when scaling to many qubits, due to frequency crowding issues [169]. The CR gate also requires the qubits to be addressed through individual input drive lines, which is a potential limitation. On the other hand, the RIP gate is able to operate with a common qubit drive through a bus cavity and with a large frequency detuning. However, the interaction between the qubits is directly mediated through the cavity and exposes the system to significant losses via the cavity, especially if one wants to use a strongly coupled cavity for high-speed readout.

In this chapter, I present my results from an experimental implementation of an all-microwave generalized CNOT gate, using the technique Speeding up Waveforms by Inducing Phases to Harmful Transitions (SWIPHT) [170, 171]. The SWIPHT gate has a few potential advantages compared to the CR gate, including that the detuning between qubits is not as critical for gate performance, and individual qubit addressability is not required. Furthermore, as the interaction between qubits is indirectly mediated by the cavity, the SWIPHT gate is not as susceptible to decoherence from the cavity as the RIP

gate is. Our cavity was very short-lived by-design to allow a rapid readout, but this had no apparent effect on gate performance, as verified by master equation simulations. As I discuss below, I found that my results were in good agreement with the master equation simulations and that the gate fidelity was primarily limited by the gate time, the lifetime of the qubits, and SPAM errors.

7.2 The Device and the Experimental Setup

7.2.1 Details of the cQED System

The cQED system I used in this experiment consisted of the two transmons SPP-v1-Q6 and SPP-v1-Q7 on separate chips mounted in the single three-dimensional superconducting Al cavity 6G. The device was cooled on the mixing chamber of the Leiden CF-450 dilution refrigerator, nominally to a base temperature of 20 mK [27, 69]. The cavity 6G, which originally only had a single slot in the center of the lid, was modified by machining two slots for the transmons, with each slot being 3 mm equidistant from the center of the lid (see Fig. 7.1). Each transmon had a single Al/AlO_x/Al Josephson junction and two large 500 μm × 650 μm Al pads capacitively shunting the junction. All the results I report in this chapter were obtained during Measurement Run #7.

The transition frequencies between the two lowest levels ($|g\rangle$ and $|e\rangle$) of the transmons were $\omega_L/2\pi = 6.07135$ GHz for qubit L (Q_L), and $\omega_H/2\pi = 6.75427$ GHz for qubit H (Q_H). The direct capacitive coupling between the transmons, combined with

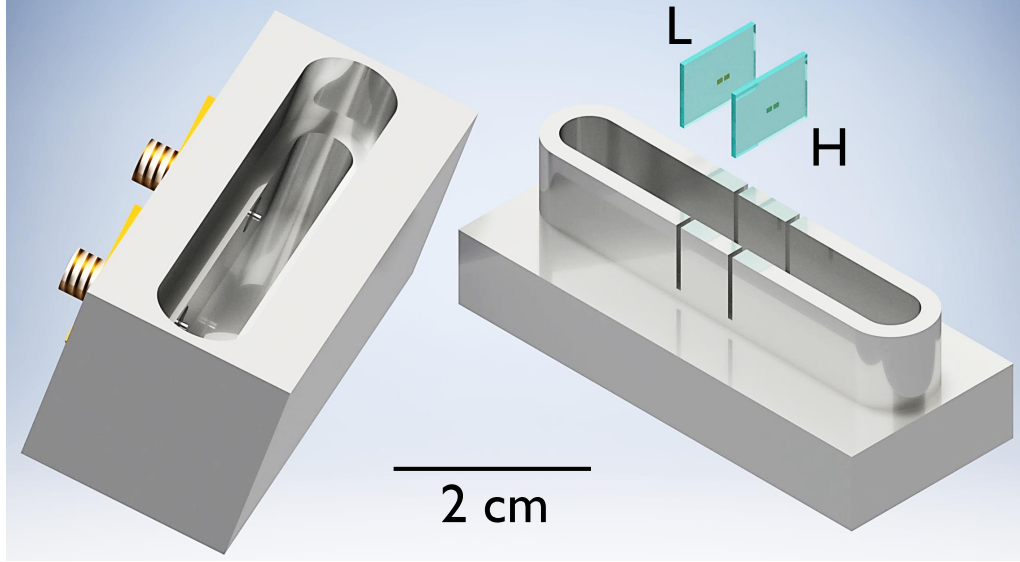


Fig. 7.1 Computer generated model of two transmons and the two sections of the 3D Al cavity.

the indirect coupling through the 7.7463 GHz cavity resonance, resulted in a qubit-qubit dispersive shift [172] of $2\chi_{\text{qq}}/2\pi = -1.04$ MHz. The detailed system parameters are given in Table 7.1. I determined the system parameters such as the bare frequencies of the components, and the couplings between components by diagonalizing the coupled Hamiltonian for the system (see next Section).

7.2.2 The System Hamiltonian

The effective Hamiltonian for the coupled system can be written as,

$$\begin{aligned} \tilde{\mathcal{H}}_0 = \hbar \sum_{j=L,H} \left[\tilde{\omega}_j a_j^\dagger a_j + \frac{E_C^{(j)}}{2} a_j^\dagger a_j (a_j^\dagger a_j - 1) + g_j (a_R^\dagger a_j + a_R a_j^\dagger) \right] \\ + \hbar \tilde{\omega}_R a_R^\dagger a_R + \hbar J (a_L^\dagger a_H + a_L a_H^\dagger), \end{aligned} \quad (7.1)$$

Table 7.1 Device parameters for the two qubits coupled to the cavity. Values were obtained by extracting eigenstates for the Hamiltonian Eq. (7.1) and comparing the resulting transition frequencies to the measured spectrum.

System parameter	Symbol	Value
Bare frequency of transmon L	$\omega_L/2\pi$	6.103 22 GHz
Bare frequency of transmon H	$\omega_H/2\pi$	6.799 43 GHz
Bare frequency of cavity	$\omega_R/2\pi$	7.669 27 GHz
Charging energy of transmon L	$E_C^{(L)}/h$	206.5 MHz
Charging energy of transmon H	$E_C^{(H)}/h$	192.6 MHz
Transmon-transmon direct coupling	$J/2\pi$	14.3 MHz
Cavity-transmon coupling (L)	$g_L/2\pi$	224.6 MHz
Cavity-transmon coupling (H)	$g_H/2\pi$	207.5 MHz
Cavity-transmon dispersive shift (L)	$\chi_L/2\pi$	-3.3 MHz
Cavity-transmon dispersive shift (H)	$\chi_H/2\pi$	-7.2 MHz
Qubit-qubit dispersive shift	$\chi_{qq}/2\pi$	-1.04 MHz
Cavity lifetime	$1/\kappa$	50 ns
Relaxation time of transmon L	T_{1L}	9.0 μ s
Relaxation time of transmon H	T_{1H}	3.5 μ s
Spin-echo time of transmon L	T_{2L}	14.6 μ s
Spin-echo time of transmon H	T_{2H}	6.2 μ s

where a and a^\dagger are the annihilation and creation operators, and the subscripts L, H, or R identifies whether the operation is on Q_L , Q_H , or the resonator state. Since the gates I perform do not involve occupation of excited states of the cavity or transmon levels higher than $|e\rangle$ (*i.e.* $|f\rangle$, $|h\rangle$, \dots), for simplicity, I restrict consideration to the computational two-qubit subspace of the system spanned by $\{|gg\rangle, |ge\rangle, |eg\rangle, |ee\rangle\}$, where the labels within kets represent the states of Q_L and Q_H , respectively. In this case, the undriven system can be described by the Hamiltonian:

$$\mathcal{H}_0 = \frac{\hbar}{2}(\omega_L + \chi_{qq})\sigma_z^{(L)} + \frac{\hbar}{2}(\omega_H + \chi_{qq})\sigma_z^{(H)} + \frac{\hbar\chi_{qq}}{2}\sigma_z^{(L)}\sigma_z^{(H)}, \quad (7.2)$$

where $\sigma_z^{(L)}$ and $\sigma_z^{(H)}$ are the Pauli-Z operators for the qubits L and H, respectively.

The two-qubit system was driven using the SWIPHT protocol (described in [Sec. 7.3](#)), with qubit L as the control, and qubit H as the target [[170](#)]. The drive Hamiltonian can be expressed as:

$$\mathcal{H}_d = \frac{\hbar\Omega(t)}{2} [\sigma_H^- e^{i(\omega_d t + \phi_d)} + \sigma_H^+ e^{-i(\omega_d t + \phi_d)}], \quad (7.3)$$

where $\Omega(t)$ is the envelope of the drive pulse, σ_H^+ is the raising operator for qubit H, σ_H^- is the lowering operator for qubit H, ϕ_d is the drive phase and ω_d is the drive frequency for the gate pulse. The full system Hamiltonian for the two-qubit subspace can then be written as,

$$\mathcal{H} = \mathcal{H}_0 + \mathcal{H}_d. \quad (7.4)$$

7.2.3 Joint Qubit State Readout

Since the two qubits were coupled to a single readout cavity, I had to develop a method to read out the state of both qubits. This was not the standard situation where a single transmon was coupled to a cavity, and the cavity can be probed at its bare frequency with a high-power pulse to destructively measure the qubit state [[104](#)]. For the single qubit case, optimization of the pulse power allows maximum discrimination between the $|g\rangle$ and $|e\rangle$ states of the qubit, and pumping to higher states of the transmon can be used to achieve a higher degree of discrimination [[33](#)]. I

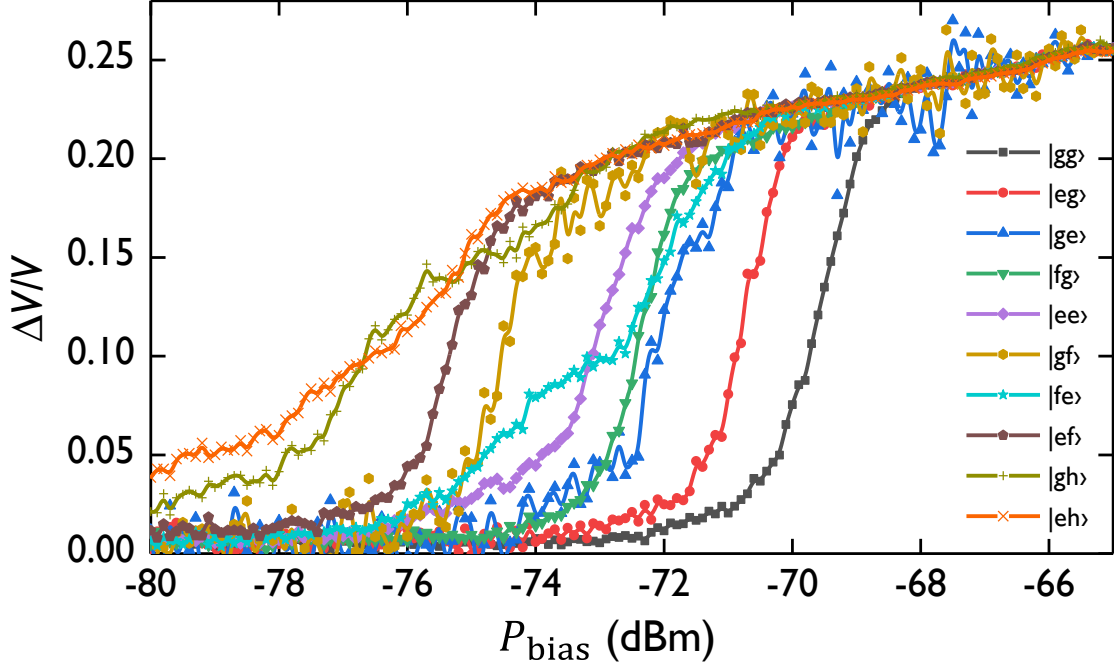


Fig. 7.2 Two-transmon S-curves. Cavity S_{21} measurements of $\Delta V/V$ versus P_{bias} averaged over 1000 shots taken for 10 different two-qubit state initializations.

extended this standard approach to perform joint-state-readout of the two-transmon system by judicious choice of measurement power and mappings to higher transmon levels.

To set up the joint-readout, I first initialized the two-transmon system in each of the nine states $|gg\rangle$, $|eg\rangle$, $|ge\rangle$, $|fg\rangle$, $|ee\rangle$, $|gf\rangle$, $|fe\rangle$, $|ef\rangle$, $|gh\rangle$, $|eh\rangle$. After each state initialization, a $2\mu\text{s}$ long pulse was applied on resonance with the bare cavity frequency, and the resulting transmission $\Delta V/V$ averaged over 1000 shots. I did these measurements as a function of cavity power P_{cav} , to obtain the switching curves $\Delta V/V$ versus P_{cav} for each of the transmon states (see Fig. 7.2).

The vertical dashed lines in Fig. 7.3 show the seven bias powers P_1 – P_7 that I selected for joint qubit-state readout. I chose $|e\rangle \rightarrow |f\rangle$ or $|e\rangle \rightarrow |f\rangle \rightarrow |h\rangle$ mappings based on

their ability to discriminate between the eigenstates $|gg\rangle$, $|ge\rangle$, $|eg\rangle$, and $|ee\rangle$. The bias powers were hand-picked to maximize the amount of information extracted using a minimal number of measurements. For example, at power P_4 , the $|gh\rangle$ and $|eh\rangle$ signals were nearly identical (~ 0.21), and the $|gg\rangle$ and $|eg\rangle$ signals were also close to each other (~ 0.01). Thus, if the excited state of qubit H was mapped $|e\rangle \rightarrow |f\rangle \rightarrow |h\rangle$, P_4 would be an ideal bias point to measure the state of transmon H, irrespective of the state of transmon L. In contrast, if qubit H were only mapped $|e\rangle \rightarrow |f\rangle$, the resulting signals for $|gf\rangle$ and $|ef\rangle$ would be further apart. Similarly, if qubit L was mapped $|e\rangle \rightarrow |f\rangle$, the resulting signal is not as large (0.08–0.12) and provides less contrast (see Fig. 7.3). Furthermore, I preferred to use points on Fig. 7.2 where the curves had smaller slopes, to reduce the uncertainty in measured values. Table 7.2 summarizes the resulting bias points and mappings that I used.

Figure 7.4 shows the joint measurement procedure; after gating operations on the qubits were finished, one or two state maps were applied, followed by a cavity measurement pulse. For a given initial state, the application of a mapping β followed by a measurement pulse at cavity bias power P_β resulted in an average transmission signal

$$\mathcal{M}_\beta = \mathcal{C}_{gg}^{(\beta)} \mathcal{P}_{gg} + \mathcal{C}_{eg}^{(\beta)} \mathcal{P}_{eg} + \mathcal{C}_{ge}^{(\beta)} \mathcal{P}_{ge} + \mathcal{C}_{ee}^{(\beta)} \mathcal{P}_{ee}, \quad (7.5)$$

where \mathcal{P}_{ij} is the probability of finding the system in the state $|ij\rangle$, and $\mathcal{C}_v^{(\beta)}$ is the output when the system is in state v and power P_β is applied (see Eq. (7.6)). To determine the \mathcal{P}_{ij} for an unknown state, I determined the average values of \mathcal{M}_β for $\beta = \{1, \dots, 7\}$ by

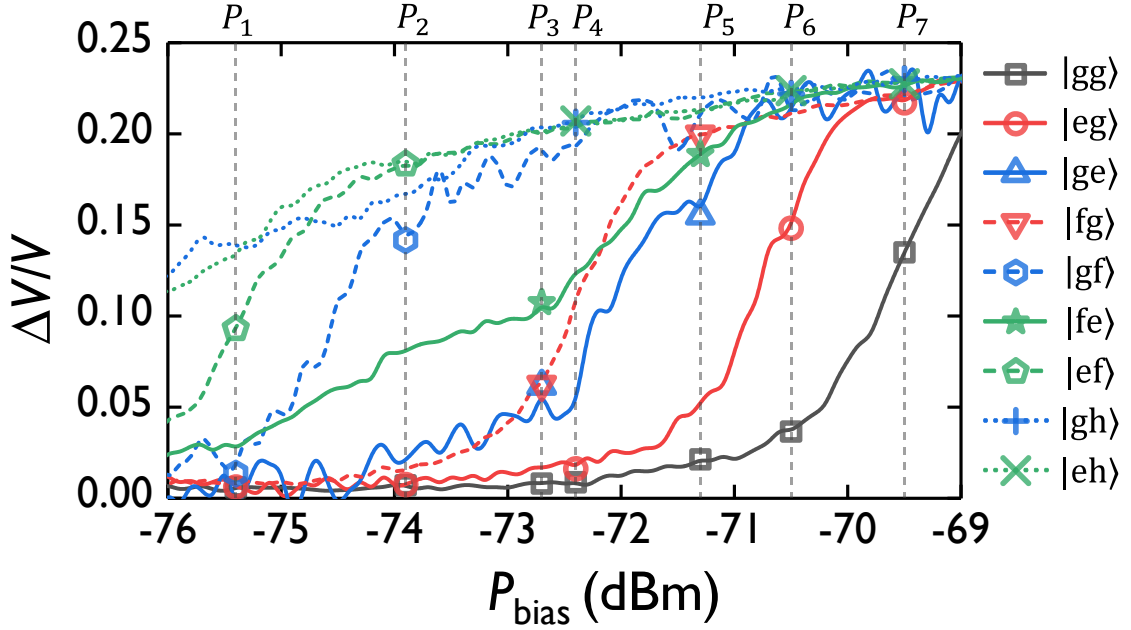


Fig. 7.3 Cavity powers chosen for joint qubit readout. Plot of pulsed cavity transmission measurements $\Delta V/V$, averaged over 1000 shots, versus cavity bias power P_{bias} for different initial two-qubit states. The measurement was performed at the bare cavity frequency $\omega_R/2\pi = 7.680\,438$ GHz. Dashed lines show powers P_1 – P_7 chosen for joint-qubit readout. Each power P_i has four associated symbols, corresponding to the system being prepared in $|gg\rangle$ (black), $|eg\rangle$ (red), $|ge\rangle$ (blue), or $|ee\rangle$ (green), and then mapped to a higher level in some cases (see Table 7.2) before being read out.

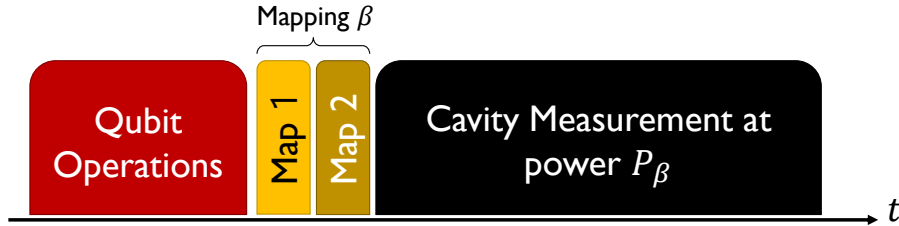


Fig. 7.4 Pulse train for joint qubit readout. The pulses used for the joint qubit readout are depicted. Following qubit manipulation (red), one or two mapping pulses (yellow and gold) are applied, and then the cavity measurement pulse (black) is applied at the corresponding power P_β (as listed in Table 7.2).

completing ~ 1000 repeated preparations, mappings, and measurements of the same state. Finally, to find the best fit values for the probabilities $\{\mathcal{P}_{gg}, \mathcal{P}_{ge}, \mathcal{P}_{eg}, \mathcal{P}_{ee}\}$, χ^2

Table 7.2 Parameters for joint-qubit readout shown in Fig. 7.4. Seven different cavity input bias powers P_β between -75.4 dBm and -69.5 dBm were used for joint qubit measurements. Note that in all cases, the $|e\rangle$ state of transmon L or transmon H was mapped to the $|f\rangle$ or $|h\rangle$ state before applying the cavity readout pulse. Also Map 2 was only used for $\beta = 4, 6,$ and $7,$ to map $|f\rangle \rightarrow |h\rangle$ for Q_H .

β	P_β (dBm)	Map 1		Map 2
		Q_L	Q_H	Q_H
1	-75.4	—	$e \rightarrow f$	—
2	-73.9	—	$e \rightarrow f$	—
3	-72.7	$e \rightarrow f$	—	—
4	-72.4	—	$e \rightarrow f$	$f \rightarrow h$
5	-71.3	$e \rightarrow f$	—	—
6	-70.5	—	$e \rightarrow f$	$f \rightarrow h$
7	-69.5	—	$e \rightarrow f$	$f \rightarrow h$

minimization was performed on Eq. (7.5) as discussed further in Sec. 7.4.

I did separate measurements to determine the calibration data matrix \mathcal{C} and the corresponding error matrix \mathcal{E} for the seven cavity powers P_β , for each of the initialized eigenstates. The $\mathcal{C}_v^{(\beta)}$ values can be directly read off of Fig. 7.3. Expressed as a matrix,

I found:

$$\mathcal{C} = 10^{-2} \begin{pmatrix} 0.554 & 3.69 & 0.724 & 11.6 \\ 0.657 & 16.35 & 0.943 & 19.86 \\ 0.836 & 5.88 & 9.62 & 21.35 \\ 1.05 & 21.40 & 2.13 & 22.46 \\ 2.4 & 18.06 & 21.23 & 23.405 \\ 4.02 & 23.42 & 18.24 & 24.003 \\ 15.06 & 23.959 & 23.44 & 24.367 \end{pmatrix}. \quad (7.6)$$

The corresponding matrix of uncertainties for \mathcal{C} was found to be

$$\mathcal{E} = 10^{-2} \begin{pmatrix} 0.033 & 0.60 & 0.065 & 2.6 \\ 0.052 & 0.92 & 0.099 & 0.25 \\ 0.082 & 0.41 & 1.80 & 0.20 \\ 0.11 & 0.22 & 0.18 & 0.16 \\ 0.2 & 0.51 & 0.24 & 0.086 \\ 0.27 & 0.13 & 0.45 & 0.065 \\ 0.42 & 0.081 & 0.14 & 0.025 \end{pmatrix}. \quad (7.7)$$

I obtained these statistics by repeating the 1000 shot measurements 1000 times, for each of the data points in Fig. 7.3. For each set of 1000 shots, I found the mean value; let $\mathcal{C}_{\nu,j}^{(\beta)}$ be the mean for the j^{th} set. I then found $\mathcal{C}_{\nu}^{(\beta)}$ by averaging together the 1000 values of $\mathcal{C}_{\nu,j}^{(\beta)}$, and took the standard deviation of the $\mathcal{C}_{\nu,j}^{(\beta)}$ to get $\mathcal{E}_{\nu}^{(\beta)}$. Thus $\mathcal{E}_{\nu}^{(\beta)}$ is the uncertainty in $\mathcal{C}_{\nu}^{(\beta)}$.

The expression for \mathcal{M}_{β} given in Eq. (7.5) corresponds to a measurement that returns an average value $\mathcal{C}_{\nu}^{(\beta)}$ when the system is in eigenstate ν and power P_{β} is applied. A more complete model takes into account the noise in the readout electronics and the bifurcating nature of the non-linear readout [104]. In this case, each single-shot measurement is randomly drawn from a distribution that I will assume has the following simple form [173]

$$\frac{dp_{\nu}^{(\beta)}}{d\mathcal{V}} = K \left\{ \frac{(1 - \mathcal{K}_{\nu}^{(\beta)})}{\sigma_{\text{low}}^{(\beta,\nu)} \sqrt{2\pi}} \exp \left[-\frac{(\mathcal{V} - V_{\text{low}}^{(\beta,\nu)})^2}{2(\sigma_{\text{low}}^{(\beta,\nu)})^2} \right] + \frac{(\mathcal{K}_{\nu}^{(\beta)})}{\sigma_{\text{high}}^{(\beta,\nu)} \sqrt{2\pi}} \exp \left[-\frac{(\mathcal{V} - V_{\text{high}}^{(\beta,\nu)})^2}{2(\sigma_{\text{high}}^{(\beta,\nu)})^2} \right] \right\}, \quad (7.8)$$

where $\left(\frac{dp_{\nu}^{(\beta)}}{d\mathcal{V}} \right) d\mathcal{V}$ is the probability of a single-shot measurement producing an output between \mathcal{V} and $\mathcal{V} + \delta\mathcal{V}$, where $\mathcal{V} \equiv \Delta V/V$, and K is a normalizing constant; here

$K = 1$ since $\int \left(\frac{dp}{d\mathcal{V}}\right) d\mathcal{V} = 1$. $\mathcal{K}_\nu^{(\beta)}$ and $(1 - \mathcal{K}_\nu^{(\beta)})$ are probabilities that the cavity bifurcates to the “high” and “low” transmission states when measured, respectively. $V_{\text{low}}^{(\beta, \nu)}$ and $\sigma_{\text{low}}^{(\beta, \nu)}$ are the mean and standard deviation of the cavity signal $\Delta V/V$ when it bifurcates to the “low” transmission state, respectively. $V_{\text{high}}^{(\beta, \nu)}$ and $\sigma_{\text{high}}^{(\beta, \nu)}$ are the mean and standard deviation of the cavity signal $\Delta V/V$ when it bifurcates to the “high” transmission state, respectively. Note that the underlying distributions corresponding to “high” and “low” transmission states are assumed to be normal distributions as one would expect for simple added noise, and all the preceding listed quantities are expressed with the measurement performed at a power P_β with the system prepared in the eigenstate ν . Full analysis of the results using this model of measurement is in progress.

7.3 The SWIPHT Gate

The SWIPHT gate is based on a theoretical method that implements a desired evolution on a driven two-level system [174, 175]. The method provides a general framework to implement a multitude of operations on a two-level system. Economou and Barnes [170] applied this method to a system of two transmons coupled to a single cavity. In particular, they provided an analytical solution to implement a generalized CNOT gate as well as a generalized CZ gate. I used their SWIPHT technique to implement a generalized CNOT gate which I will call the SWIPHT gate.

An interesting feature of Economou and Barnes [170] implementation of the

SWIPHT gate is that the control pulse shape is entirely determined by the qubit-qubit dispersive shift χ_{qq} . The duration of the pulse is

$$\tau_g = \frac{5.87}{2|\chi_{\text{qq}}|}, \quad (7.9)$$

and the pulse shape can be written as

$$\Omega(t) = \frac{\ddot{\gamma}}{\sqrt{\chi_{\text{qq}}^2 - \dot{\gamma}^2}} - 2\sqrt{\chi_{\text{qq}}^2 - \dot{\gamma}^2} \cot(2\gamma), \quad (7.10)$$

where

$$\gamma(t) = 138.9 \left(\frac{t}{\tau_g} \right)^4 \left(1 - \frac{t}{\tau_g} \right)^4 + \frac{\pi}{4}. \quad (7.11)$$

From Eq. (7.9) and Eq. (7.10) it can be shown that the maximum amplitude of the pulse is

$$\Omega_{\text{max}} = 0.887 \times 2|\chi_{\text{qq}}|. \quad (7.12)$$

The SWIPHT gate operates on the principle of applying a π -rotation on a desired transition (bit-flip), and simultaneously applying a 2π -rotation (no bit-flip) on an undesired transition within the computational subspace. The resonator plays a minimal role, allowing the use of a cavity with a strongly coupled output port for a fast qubit readout. The generalized CNOT gate implemented by the SWIPHT gate can be written

as

$$\text{SWIPHT} = \begin{pmatrix} 0 & e^{i\varphi_d} & 0 & 0 \\ e^{-i\varphi_d} & 0 & 0 & 0 \\ 0 & 0 & e^{i\xi} & 0 \\ 0 & 0 & 0 & e^{i\zeta} \end{pmatrix}, \quad (7.13)$$

with $\varphi_d = 0$, $\xi \approx 1.16$ rad, and $\zeta \approx 1.98$ rad (note $\xi + \zeta = \pi$). As with a standard CNOT operation, the target qubit is flipped depending on the control qubit. However, this is a generalized CNOT gate since the control qubit also acquires extra z -rotations (represented by ξ and ζ) due to the non-trivial 2π -rotation imposed on the harmful transition, as discussed next.

The numerical values in Eqs. 7.9 and 7.11 are determined by the boundary conditions for the desired $|gg\rangle \leftrightarrow |ge\rangle$ transition at frequency ω_H to complete a π -rotation, and the undesired $|eg\rangle \leftrightarrow |ee\rangle$ transition at frequency $\omega_H + 2\chi_{qq}$ to complete a 2π -rotation. For our experiment, $\omega_d/2\pi = 6.75427$ GHz, $\Omega_{\max}/2\pi = 913$ kHz, $\tau_g = 907$ ns, and the resulting control pulse envelope is shown in Fig. 7.5. The required SWIPHT pulse was generated using a 25 GSa/s Tektronix AWG70002A arbitrary waveform generator. Since an AWG performs digital signal processing, it has a limited sampling rate and voltage resolution, resulting in minor distortions of the output waveform compared to an ideal waveform.

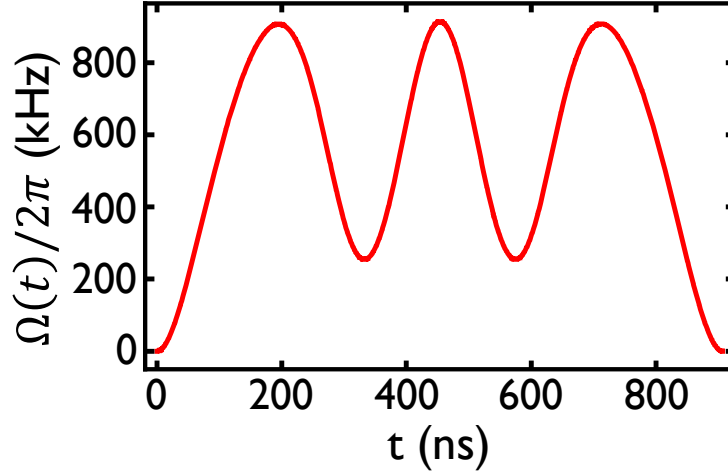


Fig. 7.5 SWIPHT pulse shape $\Omega/2\pi$ versus time t . The analytically derived SWIPHT pulse envelope $\Omega(t)$ used in the experiment has a peak amplitude of $\Omega_{\max} = 913$ kHz and a duration of $\tau_p = 907$ ns.

7.4 Quantum State Tomography

I used the method outlined in [Sec. 7.2.3](#) to determine the diagonal elements (*i.e.* populations) ρ_{ii} of the density matrix. In this section, I discuss how I also obtained the off-diagonal elements (*i.e.* coherences) of the density matrix by using quantum state tomography (QST). This involved applying rotations to the system just prior to measurement [[64](#), [176](#)]. By performing these rotations before measurement, partial information of the state was obtained. The partial information was then used to reconstruct the complete density matrix using a maximum likelihood estimation technique [[63](#)] as described next.

Table 7.3 List of tomographic maps. Overcomplete set of tomographic operations applied prior to the measurement protocol.

Gate name	Tomographic map	Gate name	Tomographic map
G_1	$I \otimes I$	G_{10}	$I \otimes R_x^{-\pi/2}$
G_2	$I \otimes R_x^{\pi/2}$	G_{11}	$I \otimes R_y^{-\pi/2}$
G_3	$I \otimes R_y^{\pi/2}$	G_{12}	$R_x^{-\pi/2} \otimes I$
G_4	$R_x^{\pi/2} \otimes I$	G_{13}	$R_y^{-\pi/2} \otimes I$
G_5	$R_y^{\pi/2} \otimes I$	G_{14}	$R_x^{-\pi/2} \otimes R_x^{-\pi/2}$
G_6	$R_x^{\pi/2} \otimes R_x^{\pi/2}$	G_{15}	$R_x^{-\pi/2} \otimes R_y^{-\pi/2}$
G_7	$R_x^{\pi/2} \otimes R_y^{\pi/2}$	G_{16}	$R_y^{-\pi/2} \otimes R_x^{-\pi/2}$
G_8	$R_y^{\pi/2} \otimes R_x^{\pi/2}$	G_{17}	$R_y^{-\pi/2} \otimes R_y^{-\pi/2}$
G_9	$R_y^{\pi/2} \otimes R_y^{\pi/2}$		

7.4.1 Constructing the Likelihood Function

To determine the density matrix from my tomographic data, I constructed a likelihood function \mathcal{L} that characterized the closeness of the density matrix to the data. To ensure that I extracted a physically meaningful density matrix, even if there were state preparation and measurement (SPAM) errors, I used an explicitly “physical” representation of the density matrix (described in detail in [Sec. 2.4.2](#)), then varied the free parameters in ρ to find the most probable representation of the state of the system [\[63\]](#). In this analysis, I used the 17 tomographic pulse combinations (see [Table 7.3](#)) for each cavity measurement power P_β to get an overcomplete set of measurements $\mathcal{M}_{\beta,\tau}$ [\[64\]](#).

The likelihood function \mathcal{L} is given by

$$\mathcal{L} = \sum_{\tau=1}^{17} \sum_{\beta=1}^7 \frac{\{\mathcal{M}_{\beta,\tau} - \sum_{\nu} [\mathcal{E}_{\nu}^{(\beta)} (G_{\tau} \hat{\rho} G_{\tau}^{\dagger})_{\nu\nu}]\}^2}{\sum_{\nu} [\mathcal{E}_{\nu}^{(\beta)} (G_{\tau} \hat{\rho} G_{\tau}^{\dagger})_{\nu\nu}]^2}, \quad (7.14)$$

where $\hat{\rho}$ is the parameterized, explicitly-physical density matrix [63]. Here τ is the index for applied tomographic gates, β is the index for cavity mapping and measurement power P_{β} , ν is the index for system eigenstates $\{|gg\rangle, |ge\rangle, |eg\rangle, |ee\rangle\}$, and G_{τ} are the tomographic gates used for QST (see Table 7.3). The numerator of \mathcal{L} quantifies the closeness of measured signals $\mathcal{M}_{\beta,\tau}$ to those expected from $\hat{\rho}$. In general the different measurements $\mathcal{M}_{\beta,\tau}$ will have different uncertainties associated with them. Thus, the closeness is weighed by using the estimated square of the uncertainty in $\mathcal{M}_{\beta,\tau}$ in the denominator of \mathcal{L} . By minimizing \mathcal{L} with respect to the 16 free parameters in $\hat{\rho}$ (see Appendix D), the most probable physical density matrix ρ was extracted.

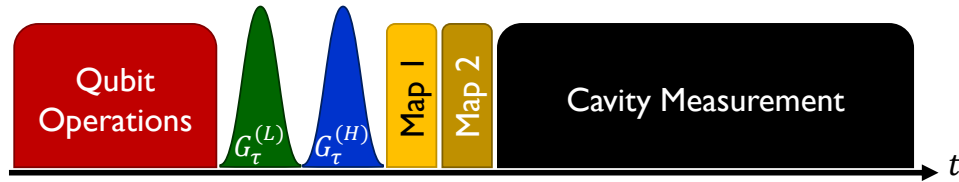


Fig. 7.6 Pulse train used during QST. Following qubit manipulation (red), tomographic pulses $G_{\tau}^{(L)}$ on qubit L (green) and $G_{\tau}^{(H)}$ on qubit H (blue) were applied. As in Fig. 7.4, up to two mapping pulses (yellow and gold) were then applied and finally the cavity measurement pulse (black) was applied.

7.4.2 QST During SWIPHT Evolution

To verify that the system was evolving properly during the SWIPHT gate, the SWIPHT pulse was started at $t = 0$, but stopped at times $n \delta t < \tau_g$ for $n = 0$ to $n = 181$, and $\delta t = 5$ ns; QST was performed for each timestep. For the measurements, I first initialized the system in the desired state ($|gg\rangle$, $|ge\rangle$, $|eg\rangle$, or $|ee\rangle$), applied the part of the SWIPHT pulse from time $t = 0$ to $n \delta t$, applied tomographic pulses $G_\tau^{(L)}$ and $G_\tau^{(H)}$, and finally performed a measurement (see Fig. 7.6). At each 5 ns timestep, this process was repeated for each of the seven cavity powers P_β for 1000 single-shot averages, to obtain $\mathcal{M}_{\beta,\tau}$.

The points in Fig. 7.7 show the measured probabilities (\mathcal{P}_{gg} , \mathcal{P}_{ge} , \mathcal{P}_{eg} , and \mathcal{P}_{ee}) versus t , with the system initialized in the $|gg\rangle$ state (Fig. 7.7(a)) and in the $|ge\rangle$ state (Fig. 7.7(b)). The curves in Fig. 7.7 show reasonably good agreement between the data and master equation simulations (as discussed below), provided I include a drive phase $\phi_d = 245^\circ$. Note that when qubit L is not excited, e.g. $|gg\rangle$, a bit-flip operation takes place and when qubit L is excited, e.g. $|eg\rangle$, the bit-flip operation is suppressed. I note that the maximum eigenstate population at the end of the operations is not 100%, and the master equation simulations suggest that most of this loss can be attributed to qubit relaxation.

The master equation simulations only included the relaxation rates of the two qubits, since the devices were mostly T_1 limited. The example code for QST in Appendix D show the procedure for the full SWIPHT pulse length. For the case of simulating the evolutions in Fig. 7.7, I executed the program and extracted the density matrix for all

times $t < 908$ ns.

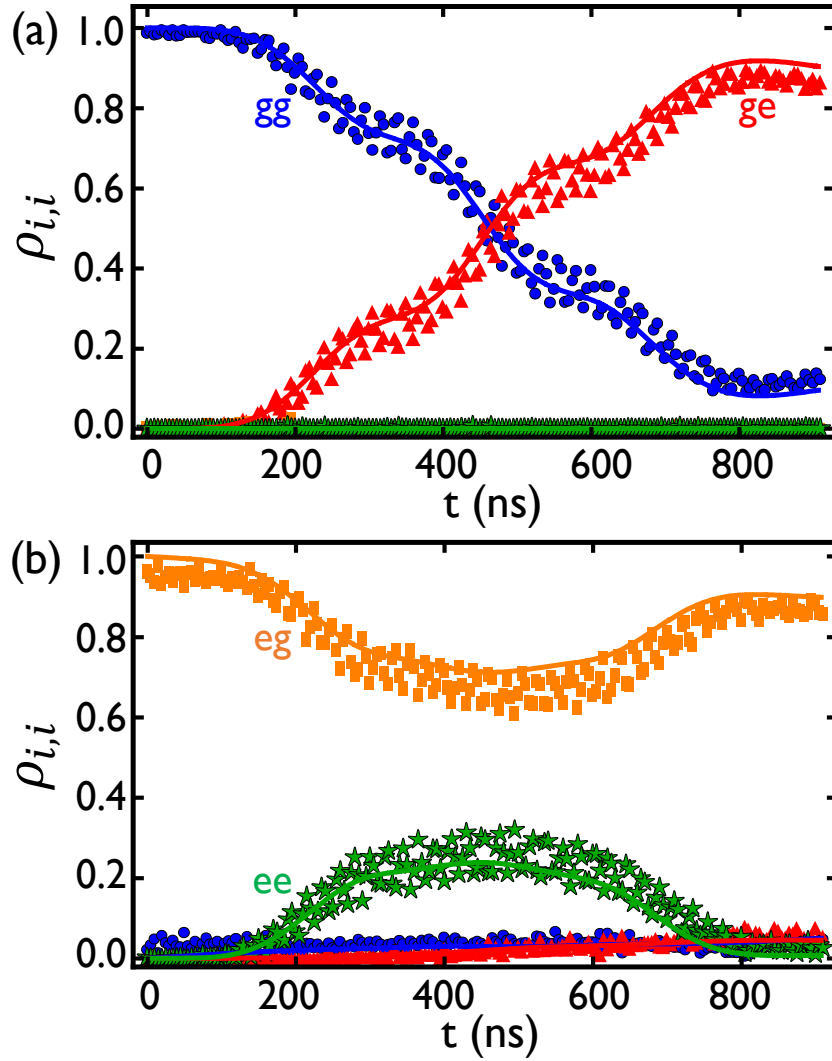


Fig. 7.7 (a) Evolution of populations during partial SWIPHT gate lasting time t , after initializing the system in state $|gg\rangle$ and then performing QST. Discrete points are experimental data and the solid curves are obtained using master equation simulations of the two-qubit system. This data was obtained with a SWIPHT drive phase $\phi_d = 245^\circ$. (b) Corresponding population evolution during partial SWIPHT pulse lasting time t , when system was prepared in state $|eg\rangle$.

7.4.3 Verification of Coherence and Phase Control

To verify that the phase φ_d of the SWIPHT gate (see Eq. (7.13)) is set by the phase of the drive, I varied ϕ_d of the drive from -2π rad to $+2\pi$ rad while generating a Bell state between the two qubits. To do this, I initialized qubit L in one of four superposition states $(R_{x,y}^{\pm\pi/2} \otimes I)|gg\rangle$, where I is the identity operator, and R is the rotation operator on qubit L with a given axis (x or y) and phase ($\pm\pi/2$). I then applied, the SWIPHT gate and performed QST. Since the initial state was an equal superposition of the control qubit's $|g\rangle$ and $|e\rangle$ states, applying the generalized CNOT gate generated a Bell state between the two qubits. Figure 7.8 shows the resulting dependence of the off-diagonal term $\rho_{ge,eg}$ in the density matrix versus ϕ_d . The plots showed a clear oscillating pattern with a period 2π in ϕ_d , an average amplitude of 0.41. The master equation simulations

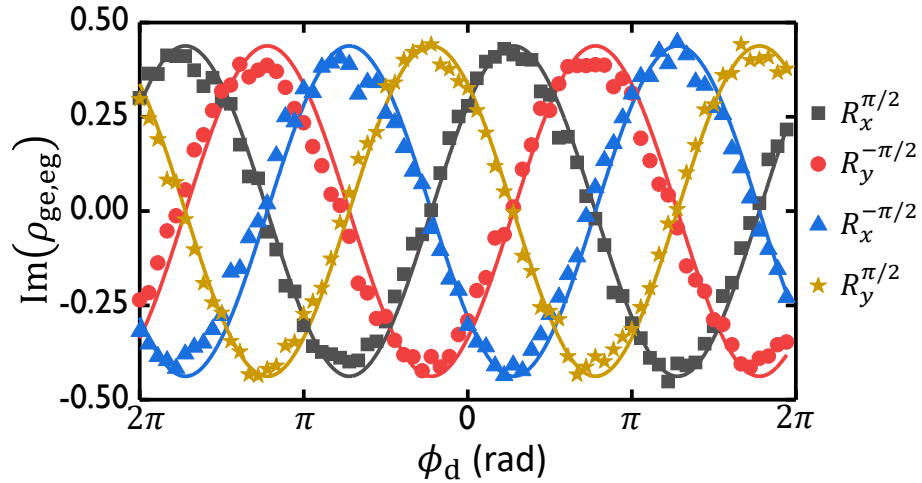


Fig. 7.8 Plot of $\text{Im}(\rho_{ge,eg})$ versus the phase ϕ_d of the SWIPHT pulse, for four different initial superposition states of qubit L $(R_{x,y}^{\pm\pi/2} \otimes I)|gg\rangle$. Points are from QST measurements and the solid curves are from master equation simulations of ρ with a fixed added phase offset of 245° .

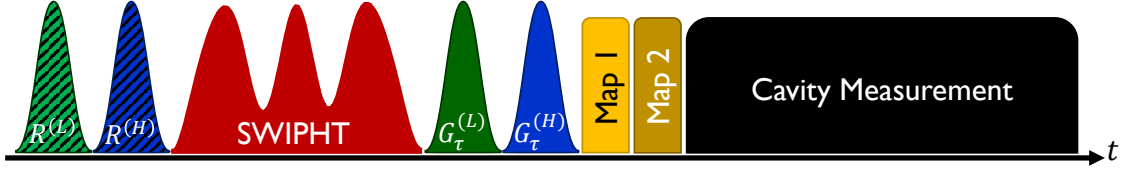


Fig. 7.9 Pulse train for QPT. The two qubits were initialized in one of the states given by $\{I, R_x^\pi, R_{x,y}^{\pm\pi/2}\}^{\otimes 2} |gg\rangle$ (green and blue striped pulses for qubit L and qubit H, respectively). The SWIPHT gate was then applied (red), followed by the tomographic pulses (green and blue solid pulses), mappings to higher levels (yellow and gold), and the measurement pulse (black).

of $\rho_{ge,eg}$ (curves) show good agreement with data, provided I include a phase offset of 245° . This offset is likely due to the phase shift along the heavily-attenuated > 2 m long input line.

7.5 Quantum Process Tomography

To provide a more complete characterization of the SWIPHT gate, I also performed quantum process tomography (QPT) [67, 177]. The essential idea of QPT is to prepare a complete set of initial states and then to perform QST on all the resulting states to quantify the performance of the gate. I adopted the method discussed in O'Brien *et al.* [67], in which a χ -matrix is used to characterize a quantum gate. An equivalent method for characterizing quantum processes using the Pauli transfer matrix has been discussed by Chow *et al.* [177].

Similar to QST, I needed to ensure that the χ -matrix I extracted from my measurements was not un-physical. I used the 16 two-qubit Pauli operators $\{\hat{A}_m\} = \{\hat{I}\hat{I}, \hat{I}\hat{X}, \hat{I}\hat{Y}, \hat{I}\hat{Z}, \hat{X}\hat{I}, \hat{X}\hat{X}, \hat{X}\hat{Y}, \hat{X}\hat{Z}, \hat{Y}\hat{I}, \hat{Y}\hat{X}, \hat{Y}\hat{Y}, \hat{Y}\hat{Z}, \hat{Z}\hat{I}, \hat{Z}\hat{X}, \hat{Z}\hat{Y}, \hat{Z}\hat{Z}\}$ as a basis, where the index

$i = 1, \dots, 16$ denotes the operator number. χ was then a 16×16 matrix. Now, I can write an ideal CNOT gate as

$$\text{CNOT} = \frac{1}{2} \hat{I}\hat{I} + \frac{1}{2} \hat{I}\hat{X} - \frac{1}{2} \hat{Z}\hat{I} + \frac{1}{2} \hat{Z}\hat{X}. \quad (7.15)$$

Similarly the SWIPHT operation can be written as

$$\text{SWIPHT} = i0.4577 \hat{I}\hat{I} + \frac{1}{2} \hat{I}\hat{X} - i0.4577 \hat{Z}\hat{I} + \frac{1}{2} \hat{Z}\hat{X} + 0.2012 \hat{I}\hat{Z} - 0.2012 \hat{Z}\hat{Z}, \quad (7.16)$$

where contributions to the norm smaller than 10^{-4} have been neglected in the real components of the coefficients for $\hat{I}\hat{I}$ and $\hat{Z}\hat{I}$, and the imaginary components of the coefficients for $\hat{I}\hat{Z}$ and $\hat{Z}\hat{Z}$. The resulting χ -matrix has 36 non-zero elements, 20 of which are real and 16 which are imaginary. The visual representation of the χ -matrix can serve as a gate diagnostic tool, with discrepancies between ideal and experimental χ -matrices providing insight into sources of systematic errors and possible remedies [3].

To ensure that χ represents a trace-preserving process, the constraint $\sum_{mn} \chi_{mn} \hat{A}_n^\dagger \hat{A}_m = I$ must be met [67]. To enforce this constraint, I introduced a Lagrange multiplier λ and a cost function:

$$\Xi = \sum_{i,j=1}^{16} \left\{ [\text{Re}(\mathcal{X}_{ij}) - I_{ij}]^2 + [\text{Im}(\mathcal{X}_{ij})]^2 \right\}, \quad (7.17)$$

where $\mathcal{X} = \sum_{mn} \chi_{mn} \hat{A}_n^\dagger \hat{A}_m$. I then defined a likelihood function

$$\tilde{\mathcal{L}} = \sum_{\sigma=1}^{36} \sum_{\tau=1}^{17} \sum_{\beta=1}^7 \frac{\left\{ \mathcal{M}_{\beta,\tau}^{(\sigma)} - \sum_{\nu} [\mathcal{E}_{\nu}^{(\beta)} (G_{\tau} \rho_{\text{out}}^{(\sigma)} G_{\tau}^{\dagger})_{\nu\nu}] \right\}^2}{\sum_{\nu} [\mathcal{E}_{\nu}^{(\beta)} (G_{\tau} \rho_{\text{out}}^{(\sigma)} G_{\tau}^{\dagger})_{\nu\nu}]^2} + \lambda \Xi, \quad (7.18)$$

where σ is an index for the overcomplete set of 36 initial states given by $\{I, R_x^{\pi}, R_{x,y}^{\pm\pi/2}\}^{\otimes 2} |gg\rangle$ (see Fig. 7.9). In this expression, $\rho_{\text{out}}^{(\sigma)}$ denotes an explicitly physical output density matrix for a given initial state obtained using the χ -matrix as,

$$\rho_{\text{out}}^{(\sigma)} = \sum_{m,n=1}^{16} \chi_{mn} \hat{A}_m \rho_{\text{in}}^{(\sigma)} \hat{A}_n^{\dagger}, \quad (7.19)$$

where $\rho_{\text{in}}^{(\sigma)}$ is the density matrix corresponding to the initial state index σ .

Minimizing $\tilde{\mathcal{L}}$ with respect to each complex quantity χ_{mn} and λ yields $\tilde{\chi}$, the maximum-likelihood estimate for the χ -matrix that describes the underlying process. Figure 7.10(a) shows $\tilde{\chi}$ I extracted from the measurements of the SWIPHT gate. Figure 7.10(b) and Fig. 7.10(c) show, respectively, the χ -matrices I obtained from master equation simulations of the SWIPHT gate incorporating decoherence (χ_{sim}), and the ideal decoherence-free case (χ_{SW}). The effects of decoherence can be seen by comparing χ_{sim} to the ideal χ_{SW} ; for example all the non-zero components in χ_{SW} are slightly smaller in magnitude in χ_{sim} . The presence of some additional non-zero components in $\tilde{\chi}$ and χ_{sim} , that do not occur in χ_{SW} , indicate the presence of coherent errors [16]. For example, the real part of $\tilde{\chi}$ and χ_{sim} have non-zero contributions from (II, IX) and (IX, II) , while the contributions vanish in the ideal χ_{SW} . In addition, by comparing $\tilde{\chi}$ with χ_{sim} , I infer that additional coherent z -rotations are present in $\tilde{\chi}$. I note that I

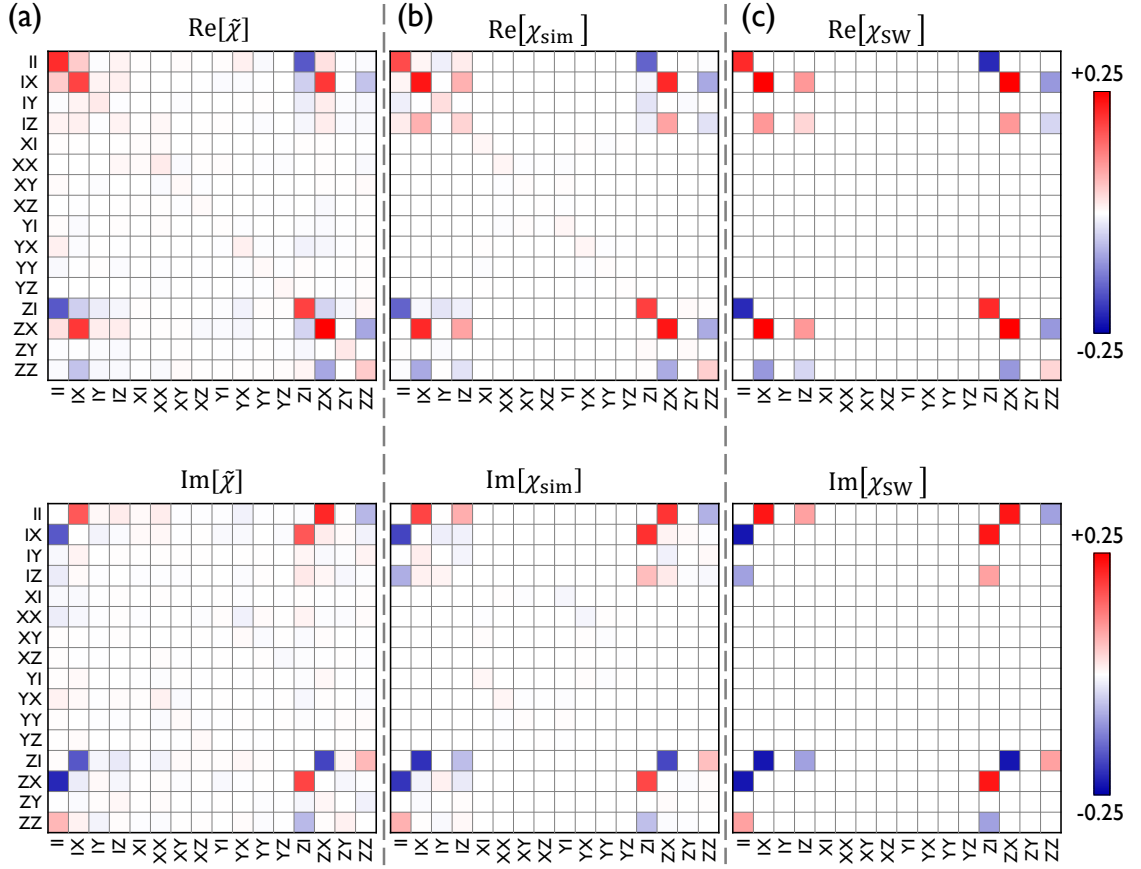


Fig. 7.10 Process matrices from QPT. Real and imaginary parts of experimental ($\tilde{\chi}$), simulated (χ_{sim}) and ideal (χ_{sw}) process matrices for the SWIPHT operation with qubit L as the control. The maximum theoretical magnitude for any element is 0.25.

also observed extra z -rotations using QPT on single qubit gates (see [Appendix E](#)).

To compare the extracted $\tilde{\chi}$ to the expected χ_{sw} from the ideal decoherence-free SWIPHT operation, I computed the process fidelity

$$\mathcal{F}_p = \text{Tr}(\tilde{\chi} \chi_{\text{sw}}), \quad (7.20)$$

Table 7.4 Gate times τ_{gate} and measured QPT performance metrics \mathcal{F}_p , \mathcal{F}_g , and $\overline{\text{Tr}(\rho^2)}$ for several gates. For the four SWIPHT gates at the bottom of the table, the subscript denotes the control qubit, and the superscript denotes the phase ϕ_d of the drive.

Gate	τ_{gate} (ns)	\mathcal{F}_p	\mathcal{F}_g	$\overline{\text{Tr}(\rho^2)}$
$I \otimes I$	0	0.94	0.95	0.97
$I \otimes R_x^\pi$	37	0.93	0.94	0.97
$I \otimes R_y^\pi$	37	0.91	0.93	0.95
$I \otimes R_x^{\pi/2}$	37	0.91	0.93	0.96
$I \otimes R_y^{\pi/2}$	37	0.90	0.92	0.95
$I \otimes R_x^{-\pi/2}$	37	0.90	0.92	0.96
$I \otimes R_y^{-\pi/2}$	37	0.90	0.92	0.95
$R_x^\pi \otimes I$	72	0.89	0.92	0.95
$R_y^\pi \otimes I$	72	0.87	0.90	0.93
$R_x^{\pi/2} \otimes I$	72	0.86	0.89	0.93
$R_y^{\pi/2} \otimes I$	72	0.85	0.88	0.93
$R_x^{-\pi/2} \otimes I$	72	0.82	0.85	0.94
$R_y^{-\pi/2} \otimes I$	72	0.84	0.88	0.95
SWIPHT _L ⁰	907	0.76	0.81	0.72
SWIPHT _H ⁰	907	0.75	0.80	0.73
SWIPHT _L ^{49π/36}	907	0.77	0.82	0.72
SWIPHT _H ^{7π/12}	907	0.77	0.82	0.74

and the mean gate fidelity

$$\mathcal{F}_g = \frac{\mathcal{F}_p d + 1}{d + 1}, \quad (7.21)$$

where $d = 4$ is the dimensionality of the two-qubit system [67, 178, 179]. I found that $\mathcal{F}_p = 0.76$, $\mathcal{F}_g = 0.81$, and the average purity of the gate $\overline{\text{Tr}(\rho^2)} = [d \text{Tr}(\tilde{\chi}^2) + 1]/(d + 1) = 0.72$ [67]. Average purity is a metric for the degree of mixture introduced by a gate and indicates how much the process was affected by incoherent errors [178].

To understand if the SWIPHT gate was significantly limited by decoherence in the

qubits, I performed QPT for master equation simulations; *i.e.* I performed QPT on a complete set of simulated results (see [Appendix D](#)). Since the simulated results only possessed relatively small numerical errors from the limited precision of the numerical calculation, I ignored the denominator of the first term in [Eq. \(7.18\)](#) during the minimization to calculate the simulated process matrix χ_{sim} . I observed that the SWIPHT performance metrics from the simulations were $\mathcal{F}_p = 0.84$, $\mathcal{F}_g = 0.87$, and $\overline{\text{Tr}(\rho^2)} = 0.77$. These were significantly better (5%) than the experimental results, but otherwise showed reasonable agreement with the experiment, and revealed that the main reason for infidelity as relaxation in the qubits.

To understand why the SWIPHT gate gave somewhat lower fidelity than found in the simulation, I also performed QPT on other gates, including three simple variations on the SWIPHT gate (see [Table 7.4](#) and [Appendix E](#)). All the single qubit gates had relatively high purity due to fast gate times, while all the SWIPHT gates showed lower purity, in part due to qubit relaxation during the longer gate times. Of particular note was the $I \otimes I$ gate, which I set up to be a zero-length operation undergoing QPT. For this simple null gate, I found $\mathcal{F}_g = 0.95$, supporting that there were $\sim 5\%$ errors introduced due to SPAM during QPT. I note that the $I \otimes I$ operation had the highest performing metrics, compared to all other gates (see [Table 7.4](#)).

7.6 Summary

In this chapter, I discussed my results on the SWIPHT gate, a generalized CNOT operation between two fixed-frequency transmon qubits [170, 171]. Four different implementations of SWIPHT yielded gate fidelities $\mathcal{F}_g \simeq 80 - 82\%$, similar to initial demonstrations of other all-microwave gates [165, 167, 180]. Overall, I found good agreement between the data and master equation simulations that incorporated decoherence. In the presence of decoherence, the maximum theoretical gate fidelity was $\mathcal{F}_g = 86\%$, while experimental fidelities were about 5% lower, likely due to SPAM. The relatively rapid decay of the cavity with a lifetime $1/\kappa = 50$ ns, directly affected the qubit lifetimes due to the Purcell effect, but otherwise had a minimal impact on the fidelity of the SWIPHT gate.

As described by Deng *et al.* [171], the gate time τ_g could be significantly reduced by using qubits with $|g\rangle \leftrightarrow |e\rangle$ frequencies that were closer together, similar to the situation for CR gates [164, 165]. I should also emphasize that all the gate fidelities I reported were obtained through QPT, and not corrected for state preparation and measurement (SPAM) associated errors. Detection and measurement of the two-qubit states was performed using a joint-readout technique, which could be further optimized, or superseded by a more efficient dispersive readout [64]. I also note that the single-qubit gate fidelities (see Table 7.4) could have been improved by derivative pulse-shaping techniques [181], and this would have possibly given overall higher SWIPHT fidelities, as process tomography is sensitive to SPAM errors in the

state initialization and tomography pulses. Finally, I found that adjusting the drive phase allowed excellent control of the phase of the target qubit, and that the phase accumulation on the control qubit could be corrected through single qubit rotations.

CHAPTER 8

Conclusion

8.1 Summary of Main Results

In this dissertation, I described my research on superconducting qubits. This work included the design, fabrication, characterization, measurement and simulation of transmons and cavities. All of the major results I presented were taken using the two transmons SPP-v1-Q6 and SPP-v1-Q7, and the two cavities 6D and 6G. Depending on the set of parameters I needed, the couplings to the cavities were modified between different measurement runs. When not using the devices, I stored them in a dry-box. Nevertheless, there were also some run-to-run variations and variations in the transmons due to aging, which I had little control over.

8.1.1 Fock State Generation

In [Chapter 6](#), I described my work on generating Fock states in a superconducting microwave cavity. I used the STIRAP (Stimulated Raman Adiabatic Passage) technique,

to generate the Fock states by transferring an excitation from the transmon to the cavity. I was able to perform this transfer successively to generate Fock states up to $n = 3$. The results showed good agreement with master-equation simulations I performed using MATLAB (see [Appendix C](#)).

To confirm that the correct states were being generated, Wigner tomography [[144](#)] would have been the method of choice. However, given the relatively short lifetime of our cavity ($\kappa^{-1} = 2.4\mu\text{s}$), and the relatively short anharmonicity in the cavity, performing Wigner tomography would have been challenging. Instead, I verified the generation of the Fock states by performing Rabi oscillations on the states generated by STIRAP. This was sensitive enough to reveal the change in cavity frequency due to the dispersive shift. I was also able to generate superpositions between cavity Fock states, as well as Bell states involving the transmon and the cavity.

8.1.2 A Generalized CNOT Gate

In [Chapter 7](#), I presented my results on implementing a generalized CNOT gate using the SWIPHT (Speeding up Waveforms by Inducing Phases to Harmful Transitions) technique. I repackaged two qubits, which I had measured previously into a single cavity that I had modified to hold two chips. The output coupling Q of the cavity was set low ($Q_{\text{output}} \sim 3000$) to obtain a fast readout time. I initially expected this setup to only serve as a test-bed for me to learn how to characterize two qubits, and develop two-qubit control and measurement techniques. To my surprise, the results I obtained far exceeded my expectations.

One of the major issues I faced was reading out the qubit states. The qubits had transition frequencies that were relatively close to the cavity frequency, and the coupling g of each qubit to the cavity was not too different from the single-qubit cases I had worked with previously. I found that the high-power-readout (see [Sec. 5.2.2](#)) worked well for the readout of individual qubit readout for the individual qubit Q_H . However, to read out both qubits efficiently I had to develop a least-squares joint-state-detection-method, which involved measuring at multiple cavity powers and mapping the qubit states to higher transmon levels.

The results from the SWIPHT experiment showed good agreement with the master-equation simulations I performed using Mathematica. To fully characterize the SWIPHT gates, I used quantum process tomography with maximum-likelihood-estimation. The construction and numerical search for the minimum of the likelihood function, which contained 257 parameters and 4284 individual terms, proved difficult using Mathematica. I therefore apportioned the likelihood function for the 36 initial states, used MATLAB to generate those 36 components in parallel, and finally imported the grand likelihood function function into Mathematica for numerical minimization. With this approach, I was able to complete QPT characterization of gates in a timely manner.

8.2 Possible Improvements

8.2.1 Improving Fock State Generation

The major limitation in my experiment to generate Fock states was the lifetime of the cavity. Having a longer lifetime would have resulted in higher fidelities, as well as improved detection and verification methods. As I discussed in [Chapter 6](#), I set the cavity quality factor to ensure a reasonably fast readout time ($\sim 3 \mu\text{s}$). Unfortunately, this relatively short time was detrimental to the STIRAP transfer of the excitation; the photons suffered significant loss since they were stored in the same cavity that I used to read out the qubit state.

One way to improve the process would be to use two cavities — a storage cavity for storing the generated Fock states and a measurement cavity for reading out the transmon state. Two possible geometries for such an approach have been discussed by Reagor *et al.* [[147](#)] and Axline *et al.* [[182](#)]. In both cases, they used a high-quality-factor seamless cylindrical cavity as the storage cavity, while the readout cavity was another 3D cavity or 2D resonator, respectively.

Having a larger qubit-cavity dispersive shift would also facilitate a faster operation time; the STIRAP pulses were limited in Rabi drive strength by the limited anharmonicity. For the parameters of my device, more intense pulses would have resulted in unwanted excitations into other cavity states. By increasing the coupling of the qubit to the cavity, or decreasing the qubit-cavity detuning, a larger qubit-cavity dispersive shift would be generated. This allows the use of stronger drives with shorter durations.

8.2.2 Improving the SWIPHT gate

There are many possible avenues for improving the generalized CNOT gate that I implemented using the SWIPHT technique. As I discussed in [Chapter 7](#), a major limiting factor in the gate time was the small qubit-qubit dispersive shift χ_{qq} . This quantity can be increased by reducing the qubit-qubit detuning, and also by having the $|g\rangle \leftrightarrow |e\rangle$ of one qubit close in frequency to the $|e\rangle \leftrightarrow |f\rangle$ transition of the second qubit [[171](#)]. However, having a higher χ_{qq} would significantly affect the operation of single-qubit gates, since this is a fixed coupling term. It would then be necessary to implement special techniques to perform single-qubit gates [[183](#)], or engineer a SWIPHT-like pulse to perform identical operations on both transitions.

I should note, that the technique introduced by Economou and Barnes [[170](#)] is fairly general, and applies to any two transitions which are close in frequency. Thus, the exact mechanism which lifts the degeneracy between the two close transitions is irrelevant. When the degeneracy is lifted, it is possible to appropriately address the system using SWIPHT to execute a CNOT gate. The speed and performance in SWIPHT however seems to come at the cost of the simplicity of single-qubit gates. Examination of the trade-offs of different parameter choices would be an interesting topic for further investigation.

APPENDIX A

Experimental Determination of Quality Factors for a Bandpass Cavity

A.1 Modeling the Cavity

A bandpass cavity having two ports can be modeled using a simplified lumped element circuit. This allows for analytical expressions that can be used to extract the scattering parameters (S-parameters).

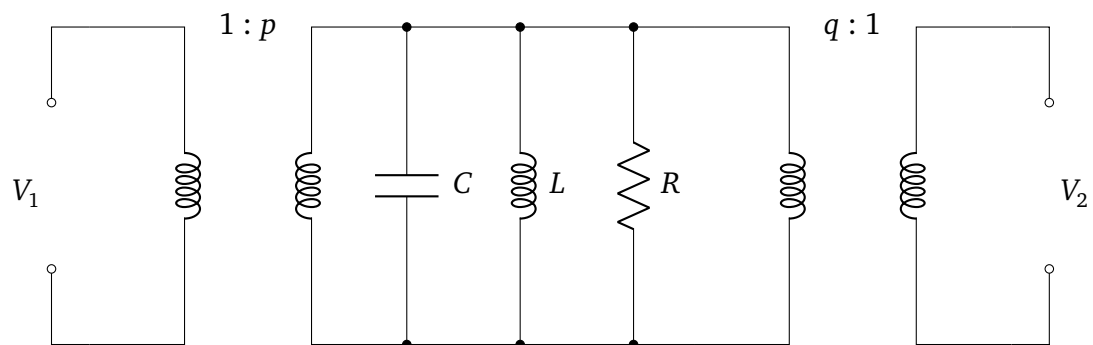


Fig. A.1 Simplified effective circuit model for a bandpass resonator.

I used inductive coupling in Fig. A.1 to model the input and output coupling from the transmission lines to the cavity. This simplifies the analysis considerably. L , C , R are the effective inductance, capacitance and resistance of the fundamental mode of the cavity. G_0 is the characteristic admittance of the transmission lines. p and q represent the ratios of the turns of the input and output transformers, respectively.

The internal, input, output, loaded, and external quality factors can be defined respectively as [184]

$$Q_0 = R \sqrt{\frac{C}{L}} = \frac{R}{\omega_0 L} \quad (\text{A.1})$$

$$Q_{\text{in}} = \frac{p^2}{G_0} \sqrt{\frac{C}{L}} = \frac{p^2}{\omega_0 L G_0} \quad (\text{A.2})$$

$$Q_{\text{out}} = \frac{q^2}{G_0} \sqrt{\frac{C}{L}} = \frac{q^2}{\omega_0 L G_0} \quad (\text{A.3})$$

$$\frac{1}{Q_L} = \frac{1}{Q_0} + \frac{1}{Q_{\text{in}}} + \frac{1}{Q_{\text{out}}} \quad (\text{A.4})$$

$$\frac{1}{Q_E} = \frac{1}{Q_{\text{in}}} + \frac{1}{Q_{\text{out}}}. \quad (\text{A.5})$$

A.2 ABCD Matrix Analysis for the Model

ABCD matrices are a convenient method to model circuits with many different components [103]. The ABCD matrices for the circuit in Fig. A.1 are, from left to right,

$$\mathbf{K} = \begin{bmatrix} \frac{1}{p} & 0 \\ 0 & p \end{bmatrix}, \mathbf{M} = \begin{bmatrix} 1 & 0 \\ \frac{1}{R} & 1 \end{bmatrix}, \mathbf{N} = \begin{bmatrix} 1 & 0 \\ \frac{1}{i\omega L} & 1 \end{bmatrix}, \mathbf{P} = \begin{bmatrix} 1 & 0 \\ i\omega C & 1 \end{bmatrix}, \mathbf{Q} = \begin{bmatrix} q & 0 \\ 0 & \frac{1}{q} \end{bmatrix}.$$

The total ABCD matrix for the complete circuit is obtained by multiplying the matrices for individual components, preserving the order, and one finds:

$$\mathbf{U} = \mathbf{K} \cdot \mathbf{M} \cdot \mathbf{N} \cdot \mathbf{P} \cdot \mathbf{Q} = \begin{bmatrix} \frac{q}{p} & 0 \\ pq \left(\frac{1}{R} - \frac{i}{L\omega} + iC\omega \right) & \frac{p}{q} \end{bmatrix}.$$

A.3 Obtaining the S-parameters

The S-parameters can be found from the ABCD matrix [103] using the following relations:

$$\begin{aligned} S_{11} &= \frac{A + BG_0 - \frac{C}{G_0} - D}{A + BG_0 + \frac{C}{G_0} + D} = -1 + \frac{2 \left(\frac{Q_L}{Q_{in}} \right)}{1 + i \frac{Q_L}{\omega\omega_0} (\omega^2 - \omega_0^2)} \\ &= -1 - \frac{2iQ_0Q_{out}\omega\omega_0}{Q_0Q_{in}Q_{out}(\omega^2 - \omega_0^2) - i(Q_{in}Q_{out} + Q_0Q_{out} + Q_0Q_{in})\omega\omega_0} \end{aligned} \quad (\text{A.6})$$

$$\begin{aligned} S_{22} &= \frac{-A + BG_0 - \frac{C}{G_0} + D}{A + BG_0 + \frac{C}{G_0} + D} = -1 + \frac{2 \left(\frac{Q_L}{Q_{out}} \right)}{1 + i \frac{Q_L}{\omega\omega_0} (\omega^2 - \omega_0^2)} \\ &= -1 - \frac{2iQ_0Q_{in}\omega\omega_0}{Q_0Q_{in}Q_{out}(\omega^2 - \omega_0^2) - i(Q_{in}Q_{out} + Q_0Q_{out} + Q_0Q_{in})\omega\omega_0} \end{aligned} \quad (\text{A.7})$$

$$\begin{aligned} S_{21} &= \frac{2}{A + BG_0 + \frac{C}{G_0} + D} = \frac{2 \left(\frac{Q_L}{\sqrt{Q_{in}Q_{out}}} \right)}{1 + i \frac{Q_L}{\omega\omega_0} (\omega^2 - \omega_0^2)} \\ &= \frac{2Q_0\omega\omega_0\sqrt{Q_{in}Q_{out}}}{(Q_{in}Q_{out} + Q_0Q_{out} + Q_0Q_{in})\omega\omega_0 + iQ_0Q_{in}Q_{out}(\omega^2 - \omega_0^2)}. \end{aligned} \quad (\text{A.8})$$

In obtaining the above expressions, I have made the following substitutions and simplified to eliminate the variables p , q , L , C , R and G_0 .

$$R = \omega_0 L Q_0$$

$$C = \frac{1}{\omega_0^2 L}$$

$$p = \sqrt{\omega_0 L G_0 Q_{\text{in}}}$$

$$q = \sqrt{\omega_0 L G_0 Q_{\text{out}}}$$

A.4 Approximations for Calculation of Quality Factors

A.4.1 $Q_{\text{out}} = Q_{\text{in}} = 2Q_E$

With the assumption $Q_{\text{out}} = Q_{\text{in}} = 2Q_E$, I obtain the following formula for S_{21} (Eq. (A.8))

$$S_{21} = \frac{\left(\frac{Q_L}{Q_E}\right)}{1 + i \frac{Q_L}{\omega \omega_0} (\omega^2 - \omega_0^2)}. \quad (\text{A.9})$$

This reduces to the following simplified formula under the approximation $\omega \approx \omega_0 + \Delta$,

$$S_{21} = \frac{\left(\frac{Q_L}{Q_E}\right)}{1 + 2i Q_L \frac{\omega - \omega_0}{\omega_0}}. \quad (\text{A.10})$$

A.4.2 $\omega = \omega_0$

For the case $\omega = \omega_0$, the formulas for the S-parameters are considerably simplified allowing for back of the envelope calculations of Q_{in} and Q_{out} . One finds:

$$S_{11}^{(\omega=\omega_0)} = \frac{2Q_L}{Q_{\text{in}}} - 1 \quad (\text{A.11})$$

$$S_{22}^{(\omega=\omega_0)} = \frac{2Q_L}{Q_{\text{out}}} - 1 \quad (\text{A.12})$$

$$S_{21}^{(\omega=\omega_0)} = \frac{2Q_L}{\sqrt{Q_{\text{in}}Q_{\text{out}}}}. \quad (\text{A.13})$$

APPENDIX B

Rabi Oscillations after FSG

Rabi oscillations were performed immediately after $|g1\rangle$ and $|g2\rangle$ generation. The amplitude and frequency of the resulting oscillations allowed me to verify that the correct state was generated. I compare the resulting oscillations to master equation simulations, and observe good agreement.

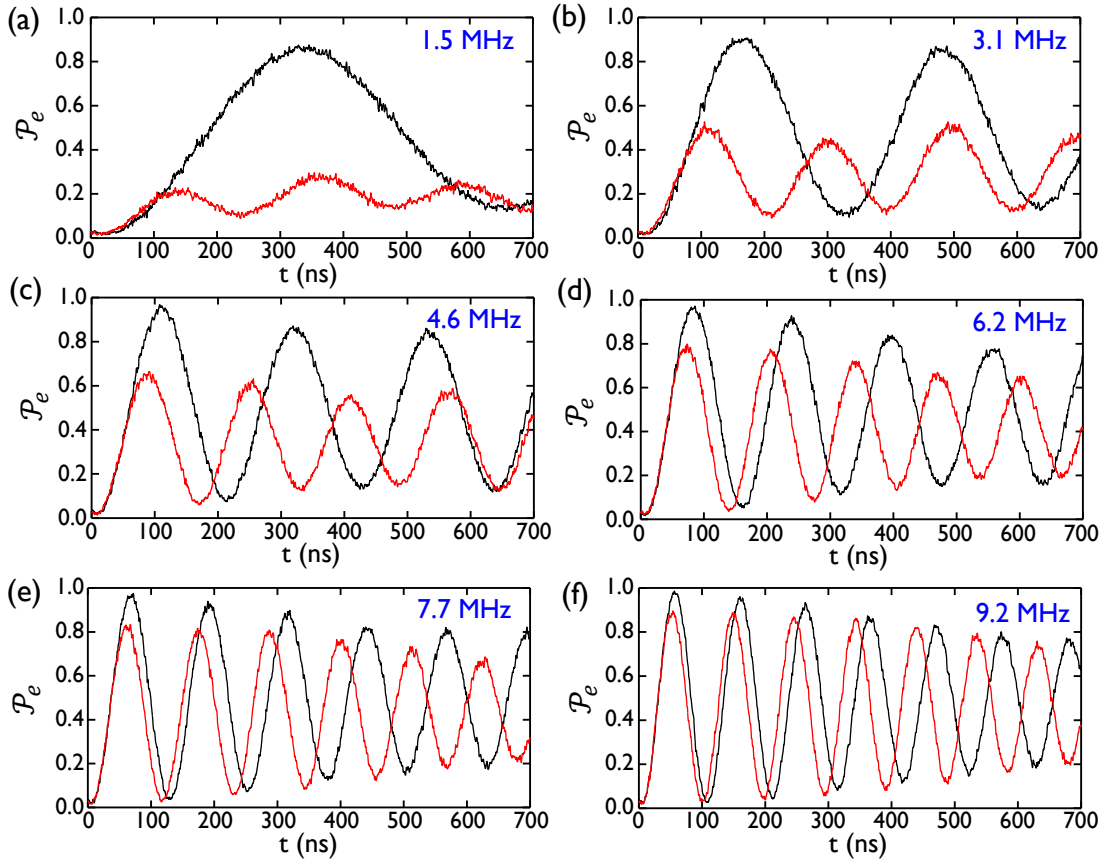


Fig. B.1 Rabi oscillations performed after $|g_1\rangle$ generation. Immediately following $|g_1\rangle$ generation, Rabi oscillations were performed with microwave drives of frequency ω_q and $\omega_{g_1 \rightarrow e_1}$. Different drive amplitudes were used, resulting in resonant oscillations when driven at $\omega_{g_1 \rightarrow e_1}$ (black) and off-resonant oscillations when driven at ω_q (red) as expected. The oscillations from driving at $\omega_{g_1 \rightarrow e_1}$ can be easily distinguished from higher-frequency and lower-amplitude oscillations produced by driving at ω_q . The nominal strengths for the Rabi drives are (a) 1.5 MHz (b) 3.1 MHz (c) 4.6 MHz (d) 6.2 MHz (e) 7.7 MHz and (f) 9.2 MHz.

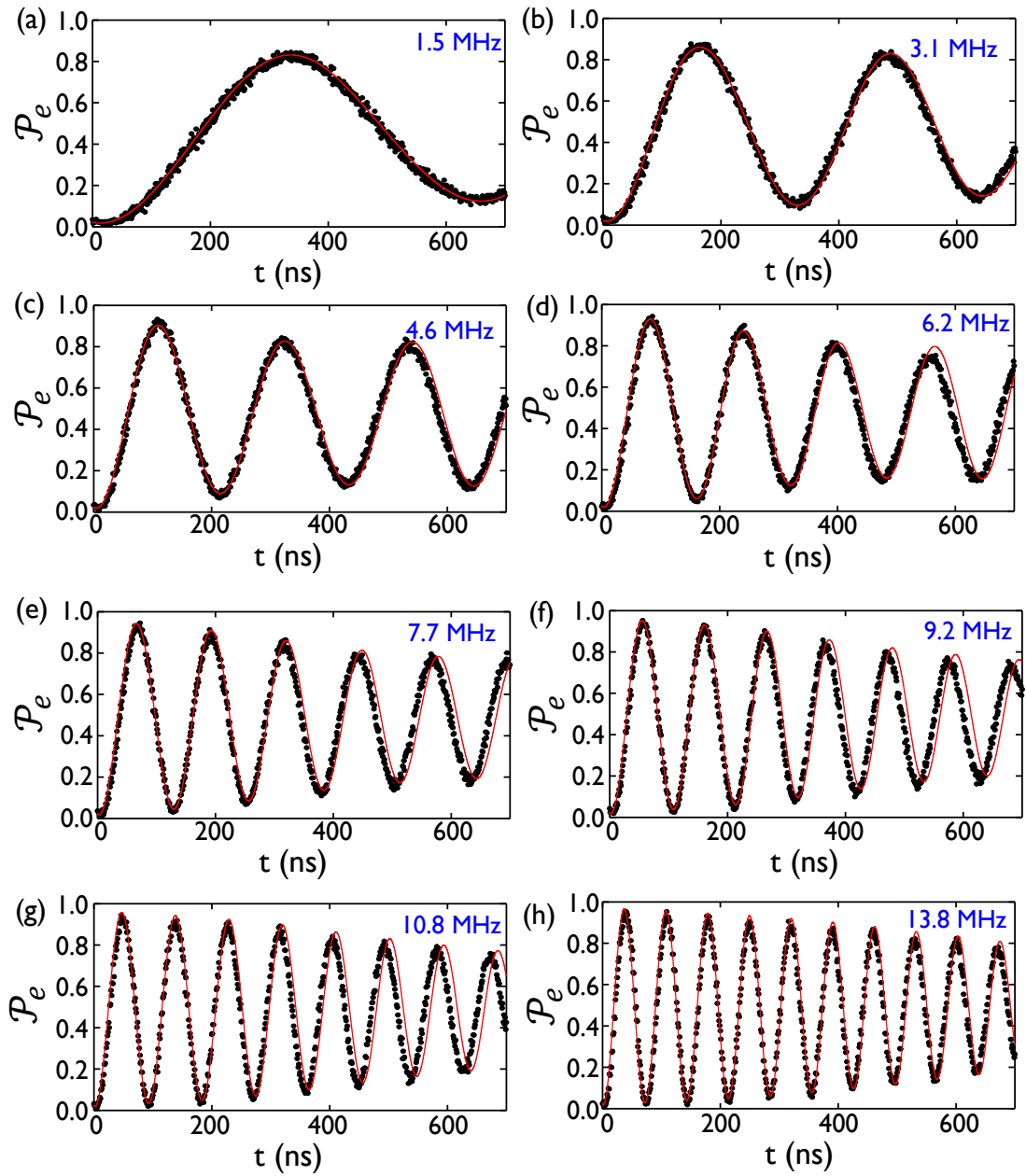


Fig. B.2 Rabi oscillations performed after $|g_1\rangle$ generation under $\omega_{g_1 \rightarrow e_1}$ drive. Data (black points) are overlaid with simulated evolution (solid red). Examination of these curves reveals that the oscillations contain components at two different frequencies: a majority corresponding to resonant Rabi oscillations and a minority component at the off-resonant Rabi frequency. The nominal strengths for the Rabi drives are (a) 1.5 MHz (b) 3.1 MHz (c) 4.6 MHz (d) 6.2 MHz (e) 7.7 MHz (f) 9.2 MHz (g) 10.8 MHz (h) 13.8 MHz.

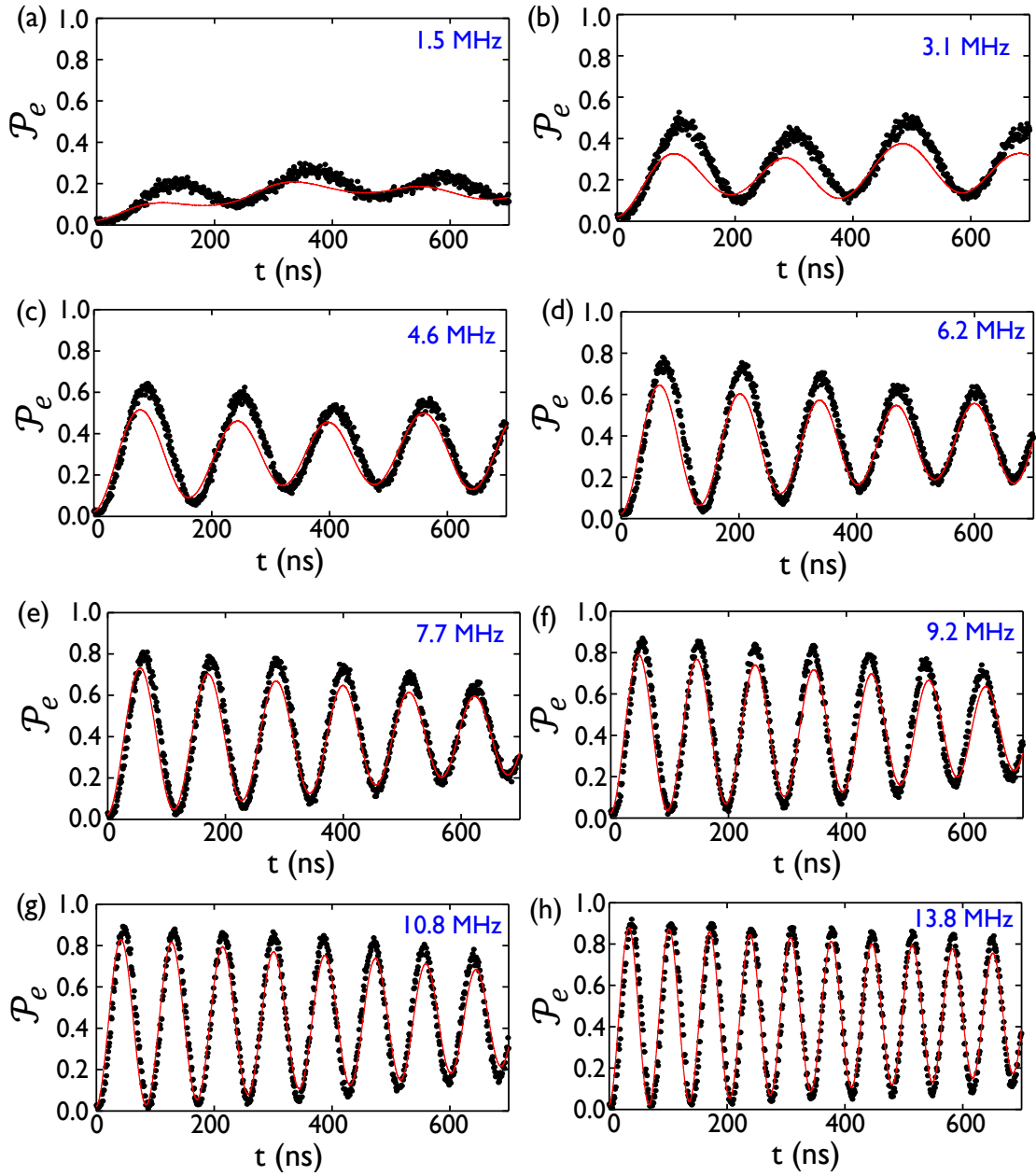


Fig. B.3 Rabi oscillations performed after $|g_1\rangle$ generation under ω_q drive. Data black points) are overlaid with simulated evolution (solid red). Examination of these curves reveals that the oscillations contain components at two different frequencies: a majority corresponding to resonant Rabi oscillations and a minority component at the off-resonant Rabi frequency. The nominal strengths for the Rabi drives are (a) 1.5 MHz (b) 3.1 MHz (c) 4.6 MHz (d) 6.2 MHz (e) 7.7 MHz (f) 9.2 MHz (g) 10.8 MHz (h) 13.8 MHz.

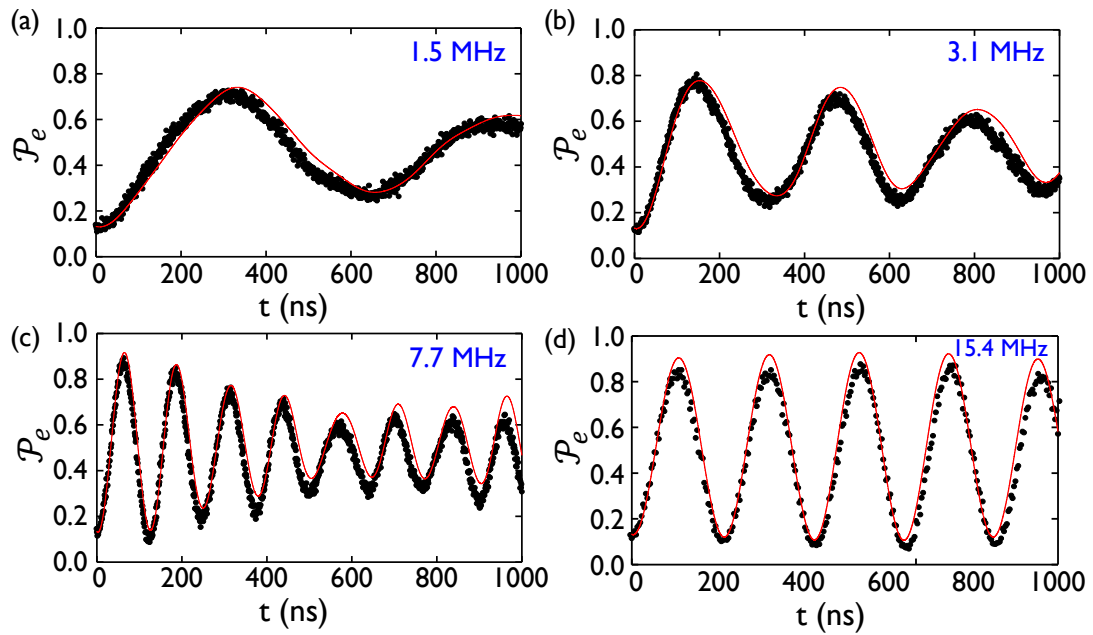


Fig. B.4 Rabi oscillations performed after $|g_2\rangle$ generation under $\omega_{g_2 \rightarrow e_2}$ drive. Following $|g_2\rangle$ generation, a limited number of Rabi oscillations were performed at various drive strengths to verify the generated state. Data from experiments (black points) are overlaid with simulated evolution (solid red). The nominal strengths for the Rabi drives are (a) 1.5 MHz (b) 3.1 MHz (c) 7.7 MHz and (d) 15.4 MHz.

APPENDIX C

MATLAB Code for STIRAP Master Equation Simulations

C.1 The Main Program for Simulating FSG upto $n = 3$

```
1 clear all;
2
3 %% System Parameters
4
5 ncav = 25;      % number of cavity levels
6 ntot = 2*ncav + 1; % total number of levels
7 pi2= 2*pi;
8 wC = pi2*7.934971E9;
9 wQ = pi2*5.5317455E9;
10 g = pi2*69.8E6;
11
12 piAmp = pi2/(59E-9); %59 seemed without any interference
13 piAmp2 = pi2/(65E-9); %65 seemed without any interference
14 piAmp3 = pi2/(65E-9); %65 seemed without any interference
15 rabiAmp = 0*pi2/(60E-9);
16
17 qubAmp = pi2*9.6E6;
18 cavAmp= pi2*26.2E6;
19 driveAmp=cavAmp;
20 a=qubAmp/cavAmp;
21
22 pulseLength = 340.01E-9;
23 stDevFraction = 4.8;
24 pulseSeparation = 14E-9;
25
26 delta1 = pi2*8.1E6; % detuning
27 delta2 = pi2*9.7E6;
28 delta3 = pi2*11.3E6;
29
30 piLength= 32.01E-9;
31 piLength2= 34.01E-9;
```

```

32 piLength3= 32.01E-9;
33 rabiLength= 0*500.01E-9;
34
35 tRed = pulseLength/2 + piLength;           % center of first pulse
36 tBlue = tRed + pulseSeparation; % center of second pulse
37
38 tmax = pulseLength + pulseSeparation + piLength;
39 tmax2 = pulseLength + pulseSeparation + piLength2;
40 tmax3 = pulseLength + pulseSeparation + piLength3;
41
42 stDev = pulseLength/stDevFraction;         % st.dev of pulses
43 timeStep = 40E-12;
44 finalTime = tmax+tmax2+tmax3 + rabiLength;
45
46 Qdec = 1/(24E-6);           % Qubit Decay rate
47 Cdec = 1/(2.5E-6);         % Cavity Decay rate
48 Qdph = 1/(41E-6);         % Qubit Dephasing Rate
49
50 %% The Bare Hamiltonian
51
52 H0 = zeros(ntot);
53
54 for i = 1:ncav
55     H0(2*i+1,2*i+1)=i*wC;
56     H0(2*i,2*i)=(i-1)*wC+wQ;
57
58     H0(2*i,2*i+1)=sqrt(i)*g;
59     H0(2*i+1,2*i)=sqrt(i)*g;
60 end
61
62 %Obtaining the drive frequencies
63
64 [e_vecs, e_vals] = eig(H0);
65
66 wg0xe0 = e_vals(2,2);
67 wg1xe1 = (e_vals(4,4)-e_vals(3,3));
68 wg2xe2 = (e_vals(6,6)-e_vals(5,5));
69 wg3xe3 = (e_vals(8,8)-e_vals(7,7));
70
71 wRed = (e_vals(4,4)-e_vals(3,3)-delta1);
72 wBlue = (e_vals(4,4)-e_vals(2,2)-delta1);
73 wRed2 = (e_vals(6,6)-e_vals(5,5)-delta2);
74 wBlue2 = (e_vals(6,6)-e_vals(4,4)-delta2);
75 wRed3 = (e_vals(8,8)-e_vals(7,7)-delta3);
76 wBlue3 = (e_vals(8,8)-e_vals(6,6)-delta3);
77
78 H0=e_vals;
79
80 %% Dissipation (Defining Jump Operators)
81
82 Aqub = zeros(ntot);
83 Acav = zeros(ntot);
84 Adph = zeros(ntot);
85

```

```

86 for i = 1:ncav
87     Aqub(2*i-1,2*i) = 1;
88     Acav(2*i-1,2*i+1) = sqrt(i);
89     %   Acav(2*i+1,2*i-1) = sqrt(0.04*i);
90     Adph(2*i-1, 2*i-1) = 1;
91     Adph(2*i, 2*i) = -1;
92 end
93
94 for i = 1:ncav-1
95     Acav(2*i,2*i+2) = sqrt(i);
96     %   Acav(2*i+2,2*i) = sqrt(0.04*i);
97 end
98
99 AcAc = 0.5*(Acav)'*Acav;
100 AqAq = 0.5*(Aqub)'*Aqub;
101 AdAd = 0.5*(Adph)'*Adph;
102
103 %% Initial state for solving the differential equations
104
105 initConditions = zeros(ntot^2,1);
106 initConditions(1)=0.995;
107 initConditions(ntot*2+3)=0.005;
108
109 %% Bare Driving Matrix
110
111 V = zeros(ntot,ntot);
112 for i = 1:ncav
113     V(2*i-1,2*i) = 1;
114     V(2*i,2*i-1) = 1;
115     V(2*i-1,2*i+1) = sqrt(i);
116     V(2*i+1,2*i-1) = sqrt(i);
117 end
118
119 for i = 1:ncav-1
120     V(2*i,2*i+2) = sqrt(i);
121     V(2*i+2,2*i) = sqrt(i);
122 end
123
124 %% Complete Hamiltonian and creating the set of differential equations
125
126 tspan = 0:0.04E-9:finalTime;
127 [tspanM, tspanN] = size(tspan);
128
129 [T, R] = ode45(@(t,rho)myode_Dph_FullPulses_FS3_rabis(t, rho, H0, V, piAmp, piAmp2,
    piAmp3, rabiAmp, qubAmp, cavAmp, Acav, AcAc, Aqub, AqAq, Adph, AdAd, Cdec, Qdec,
    Qdph, piLength, piLength2, piLength3, rabiLength, tRed, tBlue, tmax, tmax2,
    tmax3, stDev, wRed, wBlue, wRed2, wBlue2, wRed3, wBlue3, wg0xe0, wg1xe1, wg2xe2,
    wg3xe3), tspan, transpose(initConditions));
130
131 %% Plotting the obtained data
132
133 %converting output data to reals
134 RR = real(R);
135 II=imag(R);

```

```

136
137 g0Data = RR(:,1);
138 e0Data = RR(:,ntot+2);
139 g1Data = RR(:,ntot*2+3);
140 e1Data = RR(:,ntot*3+4);
141 g2Data = RR(:,ntot*4+5);
142 e2Data = RR(:,ntot*5+6);
143 g3Data = RR(:,ntot*6+7);
144 e3Data = RR(:,ntot*7+8);
145 eData = RR(:,ntot+2)+RR(:,ntot*3+4)+RR(:,ntot*5+6)+RR(:,ntot*7+8)+RR(:,ntot*9+10)+RR
      (:,ntot*11+12);
146
147 eData = RR(:,ntot+2)+RR(:,ntot*3+4)+RR(:,ntot*5+6)+RR(:,ntot*7+8)+RR(:,ntot*9+10)+RR
      (:,ntot*11+12)+RR(:,ntot*13+14)+RR(:,ntot*15+16);
148 diagonalelements = RR(:,[1,ntot+2,2*ntot+3,3*ntot+4,4*ntot+5,5*ntot+6,6*ntot+7,7*
      ntot+8,8*ntot+9,9*ntot+10,10*ntot+11,11*ntot+12,12*ntot+13,13*ntot+14,14*ntot
      +15,15*ntot+16,16*ntot+17,17*ntot+18,18*ntot+19]);
149 diagonalFullelements = RR(:,[1,ntot+2,2*ntot+3,3*ntot+4,4*ntot+5,5*ntot+6,6*ntot
      +7,7*ntot+8,8*ntot+9,9*ntot+10,10*ntot+11,11*ntot+12,12*ntot+13,13*ntot+14,14*
      ntot+15,15*ntot+16,16*ntot+17,17*ntot+18,18*ntot+19,...
150      19*ntot+20,20*ntot+21,21*ntot+22,22*ntot+23,23*ntot+24,24*ntot+25,25*ntot+26,26*
      ntot+27,27*ntot+28,28*ntot+29,29*ntot+30,30*ntot+31,31*ntot+32,32*ntot
      +33,33*ntot+34]);
151
152 figure();
153 plot(T,g0Data, T,e0Data, T,g1Data, T,e1Data,T,g2Data, T,e2Data, 'LineWidth',2);
154 legend('g0','e0','g1','e1','g2','e2');
155 xlabel('Evolution time (s)');
156 ylabel('Population');
157
158 figure();
159 plot(T,eData, 'LineWidth',2);
160 legend('e');
161 xlabel('Evolution time (s)');
162 ylabel('Population');
163
164 % dlmwrite('rr.csv',RR)
165 % dlmwrite('ii.csv',II)
166
167 % dlmwrite('g0.csv',g0Data)
168 % dlmwrite('e0.csv',e0Data)
169 % dlmwrite('e1.csv',e1Data)
170 % dlmwrite('g1.csv',g1Data)
171 % dlmwrite('e2.csv',e2Data)
172 % dlmwrite('g2.csv',g2Data)
173 % dlmwrite('e3.csv',e3Data)
174 % dlmwrite('g3.csv',g3Data)
175 % dlmwrite('e.csv',eData)
176 % dlmwrite('t.csv',T)
177 % dlmwrite('diagonals.csv',diagonalelements)
178 % dlmwrite('diagonalsFull.csv',diagonalFullelements)

```

C.2 Subprogram for the Lindblad Master Equation

```

1 %% Creating the Gaussian Pulses
2
3 function drhodt = myode_Dph_FullPulses_FS3_rabis(t, rho, H0, V, piAmp, piAmp2,
4     piAmp3, rabiAmp, QdriveAmp, CdriveAmp, Acav, AcAc, Aqub, AqAq, Adph, AdAd, Cdec,
5     Qdec, Qdph, piLength, piLength2, piLength3, rabiLength, tRed, tBlue, tmax,
6     tmax2, tmax3, stDev, wRed, wBlue, wRed2, wBlue2, wRed3, wBlue3, wg0xe0, wg1xe1,
7     wg2xe2, wg3xe3)
8
9 %% Dissipation Operators
10
11 rho = reshape (rho, size(H0));
12
13 % forcing a first operation to set the size of rho
14 Acavrho = Acav*rho;
15 Aqubrho = Aqub*rho;
16 Adphrho = Adph*rho;
17
18 Lcav = Acavrho*Acav' - AcAc*rho - rho*AcAc;
19 Lqub = Aqubrho*Aqub' - AqAq*rho - rho*AqAq;
20 Ldph = Adphrho*Adph' - AdAd*rho - rho*AdAd;
21
22 %% Drive Matrix
23
24 pSep = tBlue - tRed;
25
26 tnow=floor(t/40E-12)*40E-12;
27
28 piPulse1 = heaviside(piLength-tnow).*sin(wg0xe0*tnow);
29 qubPulse1 = heaviside((tnow-piLength).*(tmax-pSep-tnow)).*round(exp(-(tnow-tRed)
30     .^2/(2*stDev.^2)).*sin(wRed*tnow-piLength)*0.58/0.0009765625)*0.0009765625/0.58;
31 cavPulse1 = heaviside((tnow-piLength-pSep).*(tmax-tnow)).*round(exp(-(tnow-tBlue)
32     .^2/(2*stDev.^2)).*sin(wBlue*tnow-piLength-pSep)*0.0455/0.0009765625)
33     *0.0009765625/0.0455;
34
35 piPulse2 = heaviside((tnow-tmax).*(tmax+piLength2-tnow)).*sin(wg1xe1*tnow-tmax);
36 qubPulse2 = heaviside((tnow-piLength2-tmax).*(tmax+tmax2-pSep -tnow)).*round(exp(-(
37     tnow-tRed-tmax).^2/(2*stDev.^2)).*sin(wRed2*tnow-tmax-piLength2)
38     *0.58/0.0009765625)*0.0009765625/0.58;
39 cavPulse2 = heaviside((tnow-piLength2-tmax-pSep).*(tmax+tmax2 -tnow)).*round(exp(-(
40     tnow-tBlue-tmax).^2/(2*stDev.^2)).*sin(wBlue2*tnow-tmax-piLength2-pSep)
41     *0.0455/0.0009765625)*0.0009765625/0.0455;
42
43 piPulse3 = heaviside((tnow-tmax-tmax2).*(tmax+tmax2+piLength3-tnow)).*sin(wg2xe2*
44     tnow-tmax-tmax2);
45 qubPulse3 = heaviside((tnow-piLength3-tmax-tmax2).*(tmax+tmax2+tmax3-pSep -tnow)).*
46     round(exp(-(tnow-tRed-tmax-tmax2).^2/(2*stDev.^2)).*sin(wRed3*tnow-tmax-tmax2-
47     piLength3)*0.58/0.0009765625)*0.0009765625/0.58;
48 cavPulse3 = heaviside((tnow-piLength3-tmax-tmax2-pSep).*(tmax+tmax2+tmax3 -tnow)).*
49     round(exp(-(tnow-tBlue-tmax-tmax2).^2/(2*stDev.^2)).*sin(wBlue3*tnow-tmax-tmax2-
50     piLength3-pSep)*0.0455/0.0009765625)*0.0009765625/0.0455;
51

```

C.2. SUBPROGRAM FOR THE LINDBLAD MASTER EQUATION

```
36 rabiPulse = heaviside((tnow-tmax-tmax2-tmax3).*(tmax+tmax2+tmax3 + rabiLength -tnow)
37 ).*sin(wg3xe3*tnow);
38 pulses = piAmp*piPulse1 + QdriveAmp*qubPulse1 + CdriveAmp*cavPulse1 + piAmp2*
39 piPulse2 + QdriveAmp*qubPulse2 + CdriveAmp*cavPulse2 + piAmp3*piPulse3 +
40 QdriveAmp*qubPulse3 + CdriveAmp*cavPulse3 + rabiAmp*rabiPulse;
41 V = pulses*V;
42 Htot = H0+V;
43 %% Final output Density matrix
44
45 drhodt = (Qdph/2)*Ldph + Cdec*Lcav + Qdec*Lqub + lj*rho*Htot - lj*Htot*rho;
46 drhodt=drhodt(:);
```

APPENDIX D

Code for Quantum Tomography

D.1 Mathematica Program for Performing Quantum State Tomography

Preparation-----

```
ClearAll["`*"]; Clear["Global`*"]; ClearSystemCache[]; $HistoryLength = 0;
SetDirectory[NotebookDirectory[]];
ket2dm[M_] := M.M†;
$Assumptions = {t1 ∈ Reals, t2 ∈ Reals, t3 ∈ Reals, t4 ∈ Reals, t5 ∈ Reals, t6 ∈ Reals, t7 ∈ Reals,
  t8 ∈ Reals, t9 ∈ Reals, t10 ∈ Reals, t11 ∈ Reals, t12 ∈ Reals, t13 ∈ Reals, t14 ∈ Reals, t15 ∈ Reals,
  t16 ∈ Reals};
```

Importing Data-----

```
cavBiases = {14.6, 16.1, 17.3, 17.6, 18.7, 19.5, 20.5};
dataSets = {allData146, allData161, allData173, allData176, allData187, allData195, allData205};
dataSets =
  Import /@
    ("SWIPHT_LAmp=0.495_HAmp=0.000_cPwr=" <> ToString[NumberForm[#, {4, 2}]] <>
      "dBm_LAngle=0deg_HAngle=0deg.dat" & /@ cavBiases);
For[i = 1, i <= Length[dataSets], i++, dataSets[[i]] = dataSets[[i, 1 ;; 17]]];
{allData146, allData161, allData173, allData176, allData187, allData195, allData205} = dataSets;

S146 = allData146[[All, 2]]; S161 = allData161[[All, 2]];
S173 = allData173[[All, 2]]; S176 = allData176[[All, 2]];
S187 = allData187[[All, 2]]; S195 = allData195[[All, 2]];
S205 = allData205[[All, 2]];
```

Calibration values-----

```
(*The following set of equations contains the weights from S-curves used during MLE*)
{b0MLE, a0MLE} = CoefficientArrays[{
  0.00554 * gg + 0.00724 * eg + 0.0369 * ge + 0.116 * ee == S146,
  0.00657 * gg + 0.00943 * eg + 0.1635 * ge + 0.1986 * ee == S161,
  0.00836 * gg + 0.0962 * eg + 0.0588 * ge + 0.2135 * ee == S173,
  0.0105 * gg + 0.02129 * eg + 0.2140 * ge + 0.2246 * ee == S176,
  0.0240 * gg + 0.2123 * eg + 0.1806 * ge + 0.23405 * ee == S187,
  0.0402 * gg + 0.1824 * eg + 0.2342 * ge + 0.24003 * ee == S195,
  0.1506 * gg + 0.2344 * eg + 0.23959 * ge + 0.24367 * ee == S205},
  {gg, ge, eg, ee}];

(*The following set of equations will contain the errors associated with each of the measurements*)
{b0Errors, a0Errors} = CoefficientArrays[{
  0.00033 * gg + 0.00065 * eg + 0.0060 * ge + 0.026 * ee == 0,
  0.00052 * gg + 0.00099 * eg + 0.0092 * ge + 0.0025 * ee == 0,
  0.00082 * gg + 0.018 * eg + 0.0041 * ge + 0.0020 * ee == 0,
  0.0011 * gg + 0.0018 * eg + 0.0022 * ge + 0.0016 * ee == 0,
  0.0020 * gg + 0.0024 * eg + 0.0051 * ge + 0.00086 * ee == 0,
  0.0027 * gg + 0.0045 * eg + 0.0013 * ge + 0.00065 * ee == 0,
  0.0042 * gg + 0.0014 * eg + 0.00081 * ge + 0.00025 * ee == 0},
  {gg, ge, eg, ee}];
```

System Parameters-----

```
Ee = 2 π 6.75427; (*target qubit frequency*)
δ = 2 π 0.00103; (*qubit-qubit shift*)
ε = 2 π 6.07135 -  $\frac{\delta}{2}$ ;
ωp = Ee; (*Drive frequency*)
Γ1 = 1 / 3500; Γ2 = 1 / 9030; (*target and control qubit decay rates*)
A = 138.9; Δ = δ;
τp =  $\frac{5.87}{\text{Abs}[\Delta]}$ ; (*Length of SWIPT pulse*)
```

Gate Definitions-----

```
θ = π / 2; θ1 = -π / 2;
identity = IdentityMatrix[2];
sigmax = {{0, 1}, {1, 0}}; sigmay = {{0, -I}, {I, 0}}; sigmaz = {{1, 0}, {0, -1}};
id = ArrayFlatten[identity⊗identity];
sx = ArrayFlatten[sigmax⊗identity]; sy = ArrayFlatten[sigmay⊗identity];
sz = ArrayFlatten[sigmaz⊗identity];
tx = ArrayFlatten[identity⊗sigmax]; ty = ArrayFlatten[identity⊗sigmay];
tz = ArrayFlatten[identity⊗sigmaz];
sx2 = Cos[θ / 2] id - I Sin[θ / 2] sx; sy2 = Cos[θ / 2] id - I Sin[θ / 2] sy;
sz2 = Cos[θ / 2] id - I Sin[θ / 2] sz;
tx2 = Cos[θ / 2] id - I Sin[θ / 2] tx; ty2 = Cos[θ / 2] id - I Sin[θ / 2] ty;
tz2 = Cos[θ / 2] id - I Sin[θ / 2] tz;
snx2 = Cos[θ1 / 2] id - I Sin[θ1 / 2] sx;
sny2 = Cos[θ1 / 2] id - I Sin[θ1 / 2] sy;
tnx2 = Cos[θ1 / 2] id - I Sin[θ1 / 2] tx;
tny2 = Cos[θ1 / 2] id - I Sin[θ1 / 2] ty;
```


Initial Conditions-----

$\xi = (245 - 0)$ Degree; (*Adjustment phase for the SWIPHT pulse*)

$$\text{initialState} = \text{N@Flatten@ket2dm} \left[\text{sx2.} \begin{pmatrix} 1 \\ 0 \\ 0 \\ 0 \end{pmatrix} \right];$$

Initial Definitions-----

$$H0 = \begin{pmatrix} 0 & 0 & 0 & 0 \\ 0 & Ee & 0 & 0 \\ 0 & 0 & \frac{\delta}{2} + \epsilon & 0 \\ 0 & 0 & 0 & Ee - \frac{\delta}{2} + \epsilon \end{pmatrix};$$

$$H0RWA = \begin{pmatrix} 0 & 0 & 0 & 0 \\ 0 & \omega p & 0 & 0 \\ 0 & 0 & \omega p & 0 \\ 0 & 0 & 0 & 2 \omega p \end{pmatrix};$$

$$V = \begin{pmatrix} 0 & \Omega[t] e^{i(\omega p t + \xi)} & 0 & 0 \\ \Omega[t] e^{-i(\omega p t + \xi)} & 0 & 0 & 0 \\ 0 & 0 & 0 & \Omega[t] e^{i(\omega p t + \xi)} \\ 0 & 0 & \Omega[t] e^{-i(\omega p t + \xi)} & 0 \end{pmatrix};$$

(Htot = H0 + V) // MatrixForm;

(U = MatrixExp[I H0 t]) // MatrixForm;

(Hrot = Chop@FullSimplify[U.Htot.Inverse[U] + ID[U, t].Inverse[U]]) // MatrixForm;

$$\rho = \begin{pmatrix} \rho_{0x0}[t] & \rho_{0x1}[t] & \rho_{0x2}[t] & \rho_{0x3}[t] \\ \rho_{1x0}[t] & \rho_{1x1}[t] & \rho_{1x2}[t] & \rho_{1x3}[t] \\ \rho_{2x0}[t] & \rho_{2x1}[t] & \rho_{2x2}[t] & \rho_{2x3}[t] \\ \rho_{3x0}[t] & \rho_{3x1}[t] & \rho_{3x2}[t] & \rho_{3x3}[t] \end{pmatrix};$$

assume = Flatten[\rho /. t -> 0];

For[i = 1, i ≤ Length[assume], i++,

 assume[[i]] = ToExpression[ToString[assume[[i]] <> "==" <> ToString@initialState[[i]]];]

$\mathcal{D}[A_ , \rho_] := A . \rho . A^H - \frac{1}{2} A^H . A . \rho - \frac{1}{2} \rho . A^H . A;$ (*Lindblad operator definition*)

(*Creating the jump operators*)

$$Aq1 = \begin{pmatrix} 0 & 1 & 0 & 0 \\ 0 & 0 & 0 & 0 \\ 0 & 0 & 0 & 1 \\ 0 & 0 & 0 & 0 \end{pmatrix}; \quad Aq2 = \begin{pmatrix} 0 & 0 & 1 & 0 \\ 0 & 0 & 0 & 1 \\ 0 & 0 & 0 & 0 \\ 0 & 0 & 0 & 0 \end{pmatrix};$$

Creating the SWIPHT Pulses-----

$$xx[t_] = \left(A \left(\frac{t}{\tau p} \right)^4 \left(1 - \frac{t}{\tau p} \right)^4 + \frac{\pi}{4} \right);$$

$$\Omega[t_] = \left(\frac{\mathcal{D}[xx[t], \{t, 2\}]}{2 \sqrt{\frac{\Delta^2}{4} - \mathcal{D}[xx[t], t]^2}} - \sqrt{\frac{\Delta^2}{4} - \mathcal{D}[xx[t], t]^2} \cot[2 xx[t]] \right);$$

$$\text{maxRabiDrive} = \frac{\Omega[\tau p / 2]}{2 \pi} * 10^6;$$

The complete Hamiltonian-----

```
equationsR = (I * (ρ.Hrot - Hrot.ρ)) + Γ1 * D[Aq1, ρ] + Γ2 * D[Aq2, ρ];
equationsL = D[ρ, t];
```

Solving the system of equations-----

```
solutions = NDSolve[Join[Flatten[Table[equationsL[[i, j]] = equationsR[[i, j]], {i, 1, 4}, {j, 1, 4}]],
  assume], Flatten[ρ], {t, 0, tp}, MaxSteps -> Infinity];
thyρ = Chop[{ρ /. solutions} /. t -> tp][[1, 1, All]];
thyPlotMatrix = Partition[Join[Riffle[Flatten[thyρ], 0, 5], {0, 0, 0, 0, 0, 0}], 5];
F = (Tr[MatrixPower[MatrixPower[thyρ, 0.5].expρ.MatrixPower[thyρ, 0.5], 0.5]])^2;
```

Maximum Likelihood Estimation-----

$$T = \begin{pmatrix} t1 & 0 & 0 & 0 \\ t5 + I t6 & t2 & 0 & 0 \\ t11 + I t12 & t7 + I t8 & t3 & 0 \\ t15 + I t16 & t13 + I t14 & t9 + I t10 & t4 \end{pmatrix};$$

```
ρp = FullSimplify@ $\frac{T^H.T}{\text{Tr}[T^H.T]}$ ;
(* List of gates = II, IY, YI, IX, XI, XX, YY, YX, XY *)
tomoMeasures[i_] := Transpose@{
  ρp[[i, i]],
  (ty2.ρp.ty2^H)[[i, i]], (sy2.ρp.sy2^H)[[i, i]],
  (tx2.ρp.tx2^H)[[i, i]], (sx2.ρp.sx2^H)[[i, i]],
  (sx2.tx2.ρp.tx2^H.sx2^H)[[i, i]], (sy2.ty2.ρp.ty2^H.sy2^H)[[i, i]],
  (sy2.tx2.ρp.tx2^H.sy2^H)[[i, i]], (sx2.ty2.ρp.ty2^H.sx2^H)[[i, i]],
  (tny2.ρp.tny2^H)[[i, i]], (sny2.ρp.sny2^H)[[i, i]],
  (tnx2.ρp.tnx2^H)[[i, i]], (snx2.ρp.snx2^H)[[i, i]],
  (snx2.tnx2.ρp.tnx2^H.snx2^H)[[i, i]], (sny2.tny2.ρp.tny2^H.sny2^H)[[i, i]],
  (sny2.tnx2.ρp.tnx2^H.sny2^H)[[i, i]], (snx2.tny2.ρp.tny2^H.snx2^H)[[i, i]]};
likelihood = 0;
For[k = 1, k <= Length[cavBiases], k++,
  sumForAGivenBias = Sum[a0MLE[[k, j]] * tomoMeasures[j], {j, 1, 4}];
  differenceForAGivenBias = sumForAGivenBias - dataSets[[k, All, 2]];

  measurementError = Sum[(a0Errors[[k, j]] * a0MLE[[k, j]] * tomoMeasures[j])^2, {j, 1, 4}];

  likelihood +=  $\frac{\text{differenceForAGivenBias}^2}{\text{measurementError}}$ ];
likelihood = Total@Flatten@likelihood;
noiseTriangle =
  (
    RandomReal[{-1, 1}]      0      0      0
    RandomComplex[{-1, 1}]  RandomReal[{-1, 1}]      0      0
    RandomComplex[{-1, 1}]  RandomComplex[{-1, 1}]  RandomReal[{-1, 1}]  0
    RandomComplex[{-1, 1}]  RandomComplex[{-1, 1}]  RandomComplex[{-1, 1}]  RandomReal[{-1, 1}]
  );
(noise =  $\frac{1}{1000}$  FullSimplify@ $\frac{\text{noiseTriangle}^H.\text{noiseTriangle}}{\text{Tr}[\text{noiseTriangle}^H.\text{noiseTriangle}]}$ ) // MatrixForm;
(guess = thyρ) // MatrixForm;
cleanSample = guess + noise;
```

Constructing the Initialization for the T - Matrix-----

```

level1Minors = Map[Reverse, Minors[cleanSample], {0, 1}];
level2Minors = Map[Reverse, Minors[cleanSample, 2], {0, 1}];
TInitializingData = {
  {If[Det[cleanSample] ≠ 0,  $\sqrt{\frac{\text{Det}[\text{cleanSample}]}{\text{level1Minors}[[1, 1]]}}$ , 0], 0, 0, 0},
  {If[level1Minors[[1, 2]] ≠ 0,  $\frac{\text{level1Minors}[[1, 2]]}{\sqrt{\text{level1Minors}[[1, 1]] \text{level2Minors}[[1, 1]]}}$ , 0],
  If[level1Minors[[1, 1]] ≠ 0,  $\sqrt{\frac{\text{level1Minors}[[1, 1]]}{\text{level2Minors}[[1, 1]]}}$ , 0], 0, 0},
  {If[level2Minors[[1, 4]] ≠ 0,  $\frac{\text{level2Minors}[[1, 4]]}{\sqrt{\text{cleanSample}[[4, 4]] \text{level2Minors}[[1, 1]]}}$ , 0],
  If[level2Minors[[1, 2]] ≠ 0,  $\frac{\text{level2Minors}[[1, 2]]}{\sqrt{\text{cleanSample}[[4, 4]] \text{level2Minors}[[1, 1]]}}$ , 0],
  If[level2Minors[[1, 1]] ≠ 0,  $\sqrt{\frac{\text{level2Minors}[[1, 1]]}{\text{cleanSample}[[4, 4]]}}$ , 0], 0},
  {If[cleanSample[[4, 1]] ≠ 0,  $\frac{\text{cleanSample}[[4, 1]]}{\sqrt{\text{cleanSample}[[4, 4]]}}$ , 0], If[cleanSample[[4, 2]] ≠ 0,  $\frac{\text{cleanSample}[[4, 2]]}{\sqrt{\text{cleanSample}[[4, 4]]}}$ , 0],
  If[cleanSample[[4, 3]] ≠ 0,  $\frac{\text{cleanSample}[[4, 3]]}{\sqrt{\text{cleanSample}[[4, 4]]}}$ , 0],  $\sqrt{\text{cleanSample}[[4, 4]]}}$ };
TInitializingData = Chop[TInitializingData - I * DiagonalMatrix[Im@Diagonal[TInitializingData]]];
 $\frac{\text{TInitializingData}^n \cdot \text{TInitializingData}}{\text{Tr}[\text{TInitializingData}^n \cdot \text{TInitializingData}]}$  // MatrixForm;

```

Results of MLE-----

```

initializeParameters =
  Union[Partition[Riffle[FullSimplify@Re@Flatten[T], FullSimplify@Re@Flatten[TInitializingData]], 2],
  Partition[Riffle[FullSimplify@Im@Flatten[T], FullSimplify@Im@Flatten[TInitializingData]], 2]] [[
  2 ;; -1]];
sol = FindMinimum[likelihood, initializeParameters, MaxIterations → Infinity];
(sss = pp /. sol[[2]]) // MatrixForm; expρ = sss;
 $\mathcal{F} = (\text{Tr}[\text{MatrixPower}[\text{MatrixPower}[\text{thy}\rho, 0.5] \cdot \text{exp}\rho \cdot \text{MatrixPower}[\text{thy}\rho, 0.5], 0.5]])^2$ ;

```

Experimental matrix and Result from Master - equation Simulations-----

```

thyPlotMatrix = Partition[Join[Riffle[Flatten[thyρ], 0, 5], {0, 0, 0, 0, 0, 0}], 5];
expPlotMatrix = Partition[Join[Riffle[Flatten[expρ], 0, 5], {0, 0, 0, 0, 0, 0}], 5];
colorTheme = "Rainbow"; plotHeightRange = {-0.6, 0.6};
thyPlot = ListPlot3D[Re@thyPlotMatrix, InterpolationOrder → 0, Mesh → None, Filling → Axis,
  ImageSize → 500, PlotRange → plotHeightRange, ColorFunction → ColorData[{colorTheme, plotHeightRange}],
  ColorFunctionScaling → False];
expPlot = ListPlot3D[Re@expPlotMatrix, InterpolationOrder → 0, Mesh → None, Filling → Axis, ImageSize → 500,
  PlotRange → plotHeightRange, ColorFunction → ColorData[{colorTheme, plotHeightRange}],
  ColorFunctionScaling → False];
thyPlotIm = ListPlot3D[Im@thyPlotMatrix, InterpolationOrder → 0, Mesh → None, Filling → Axis,
  ImageSize → 500, PlotRange → plotHeightRange, ColorFunction → ColorData[{colorTheme, plotHeightRange}],
  ColorFunctionScaling → False];
expPlotIm = ListPlot3D[Im@expPlotMatrix, InterpolationOrder → 0, Mesh → None, Filling → Axis,
  ImageSize → 500, PlotRange → plotHeightRange, ColorFunction → ColorData[{colorTheme, plotHeightRange}],
  ColorFunctionScaling → False];
Show[GraphicsGrid[{{thyPlot, expPlot, thyPlotIm, expPlotIm, BarLegend[{colorTheme, plotHeightRange]}]}],
  ImageSize → 2500];

```

Ideal SWIPT Results-----

```

equationsRPerfect = (I * (ρ.Hrot - Hrot.ρ));
solutionsPerfect =
  NDSolve[Join[Flatten[Table[equationsL[[i, j]] = equationsRPerfect[[i, j]], {i, 1, 4}, {j, 1, 4}]],
    assume], Flatten[ρ], {t, 0, τp}, MaxSteps → Infinity];
perfectρ = Chop[({ρ /. solutionsPerfect} /. t → τp)[[1, 1, All]]];
perfectF = (Tr[MatrixPower[MatrixPower[perfectρ, 0.5].expρ.MatrixPower[perfectρ, 0.5], 0.5]])^2;
(perfectPlotMatrix = Partition[Join[Riffle[Flatten[perfectρ], 0, 5], {0, 0, 0, 0, 0, 0}], 5]) // MatrixForm;
perfectPlotRe = ListPlot3D[Re@perfectPlotMatrix, InterpolationOrder → 0, Mesh → None,
  Filling → Axis, ImageSize → 500, PlotRange → plotHeightRange,
  ColorFunction → ColorData[{colorTheme, plotHeightRange}], ColorFunctionScaling → False];
perfectPlotIm = ListPlot3D[Im@perfectPlotMatrix, InterpolationOrder → 0, Mesh → None,
  Filling → Axis, ImageSize → 500, PlotRange → plotHeightRange,
  ColorFunction → ColorData[{colorTheme, plotHeightRange}], ColorFunctionScaling → False];
Show[GraphicsGrid[{{perfectPlotRe, perfectPlotIm}}, ImageSize → 1000];

```

Generalized CNOT Results-----

```

ξ = (245) Degree; L1 = (113.67) Degree; L2 = (66.21) Degree;
cnotphase = 
$$\begin{pmatrix} 0 & E^{i\xi} & 0 & 0 \\ E^{-i\xi} & 0 & 0 & 0 \\ 0 & 0 & E^{iL2} & 0 \\ 0 & 0 & 0 & E^{iL1} \end{pmatrix}; \text{cnot}\rho = \text{ket2dm}[\text{cnotphase.sx2.} \begin{pmatrix} 1 \\ 0 \\ 0 \\ 0 \end{pmatrix}];$$

cnotF = (Tr[MatrixPower[MatrixPower[cnotρ, 0.5].expρ.MatrixPower[cnotρ, 0.5], 0.5]])^2;
cnotperfectF = (Tr[MatrixPower[MatrixPower[cnotρ, 0.5].perfectρ.MatrixPower[cnotρ, 0.5], 0.5]])^2;
TrDistance = 0.5 * Tr[MatrixPower[(cnotρ - perfectρ) . (cnotρ - perfectρ), 0.5]];
N@ (cnotPlotMatrix = Partition[Join[Riffle[Flatten[cnotρ], 0, 5], {0, 0, 0, 0, 0, 0}], 5]) // MatrixForm;
cnotPlotRe = ListPlot3D[Re@cnotPlotMatrix, InterpolationOrder → 0, Mesh → None, Filling → Axis,
  ImageSize → 500, PlotRange → plotHeightRange, ColorFunction → ColorData[{colorTheme, plotHeightRange}],
  ColorFunctionScaling → False];
cnotPlotIm = ListPlot3D[Im@cnotPlotMatrix, InterpolationOrder → 0, Mesh → None, Filling → Axis,
  ImageSize → 500, PlotRange → plotHeightRange, ColorFunction → ColorData[{colorTheme, plotHeightRange}],
  ColorFunctionScaling → False];
Show[GraphicsGrid[{{cnotPlotRe, cnotPlotIm}}, ImageSize → 1000];

```

D.2 MATLAB Programs for Constructing the Likelihood Function

D.2.1 MATLAB Function to Import the Raw Data Files

```

1 function VarName2 = importfile(filename, startRow, endRow)
2 %% Initialize variables.
3 delimiter = '\t';
4 if nargin<=2
5     startRow = 1;
6     endRow = 17;
7 end
8 %% Format string for each line of text:
9 formatSpec = '%*s%f%*s%*s%*s%[^\\n\\r]';
10
11 %% Open the text file.
12 fileID = fopen(filename,'r');
13 %% Read columns of data according to format string.
14 dataArray = textscan(fileID, formatSpec, endRow(1)-startRow(1)+1, 'Delimiter',
15     delimiter, 'HeaderLines', startRow(1)-1, 'ReturnOnError', false);
16 for block=2:length(startRow)
17     frewind(fileID);
18     dataArrayBlock = textscan(fileID, formatSpec, endRow(block)-startRow(block)+1, '
19     Delimiter', delimiter, 'HeaderLines', startRow(block)-1, 'ReturnOnError',
20     false);
21     dataArray{1} = [dataArray{1};dataArrayBlock{1}];
22 end
23 %% Close the text file.
24 fclose(fileID);
25 %% Allocate imported array to column variable names
26 VarName2 = dataArray{:, 1};

```

D.2.2 MATLAB Function to Obtain the Density Matrix of a Ket

```

1 function f = ket2dm(vec)
2
3 resultingDM = vec * ctranspose(vec);
4
5 if size(vec) ==[4 1]
6     f = vec * ctranspose(vec);
7 else if size(vec) ==[1 4]
8     f = ctranspose(vec) * vec;
9     end
10 end

```

D.2.3 MATLAB Function to Construct a Single Term of the Likelihood Function

```

1 function f = mle_multiLoad (loadVars)
2
3 %loadVars = [1, 0, 0, 0, 0]; % for testing purposes
4
5 %% Tomography Gate Definitions
6
7 theta = pi()/2;
8
9 sigma0 = eye(2);
10 sigmax = [0 1; 1 0];
11 sigmay = [0 -1j; 1j 0];
12 sigmaz = [1 0; 0 -1];
13
14 id = kron(sigma0, sigma0);
15 sx = kron(sigmax, sigma0);
16 sy = kron(sigmay, sigma0);
17 sz = kron(sigmaz, sigma0);
18
19 tx = kron(sigma0, sigmax);
20 ty = kron(sigma0, sigmay);
21 tz = kron(sigma0, sigmaz);
22
23 sx2 = cos(theta/2) * id - 1j*sin(theta/2) * sx;
24 sy2 = cos(theta/2) * id - 1j*sin(theta/2) * sy;
25 tx2 = cos(theta/2) * id - 1j*sin(theta/2) * tx;
26 ty2 = cos(theta/2) * id - 1j*sin(theta/2) * ty;
27
28 thetaN = -pi()/2;
29
30 snx2 = cos(thetaN/2) * id - 1j*sin(thetaN/2) * sx;
31 sny2 = cos(thetaN/2) * id - 1j*sin(thetaN/2) * sy;
32 tnx2 = cos(thetaN/2) * id - 1j*sin(thetaN/2) * tx;
33 tny2 = cos(thetaN/2) * id - 1j*sin(thetaN/2) * ty;
34
35 %% Tomography Gate Definitions
36
37 initialStates = cell(1,36);
38
39 initialStates{1} = id*id;
40 initialStates{2} = id*sx;
41 initialStates{3} = id*sx2;
42 initialStates{4} = id*sy2;
43 initialStates{5} = id*snx2;
44 initialStates{6} = id*sny2;
45 initialStates{7} = tx*id;
46 initialStates{8} = tx*sx;
47 initialStates{9} = tx*sx2;
48 initialStates{10} = tx*sy2;
49 initialStates{11} = tx*snx2;
50 initialStates{12} = tx*sny2;

```

```

51 initialStates{13} = tx2*id;
52 initialStates{14} = tx2*sx;
53 initialStates{15} = tx2*sx2;
54 initialStates{16} = tx2*sy2;
55 initialStates{17} = tx2*srx2;
56 initialStates{18} = tx2*sry2;
57 initialStates{19} = ty2*id;
58 initialStates{20} = ty2*sx;
59 initialStates{21} = ty2*sx2;
60 initialStates{22} = ty2*sy2;
61 initialStates{23} = ty2*srx2;
62 initialStates{24} = ty2*sry2;
63 initialStates{25} = tnx2*id;
64 initialStates{26} = tnx2*sx;
65 initialStates{27} = tnx2*sx2;
66 initialStates{28} = tnx2*sy2;
67 initialStates{29} = tnx2*srx2;
68 initialStates{30} = tnx2*sry2;
69 initialStates{31} = tny2*id;
70 initialStates{32} = tny2*sx;
71 initialStates{33} = tny2*sx2;
72 initialStates{34} = tny2*sy2;
73 initialStates{35} = tny2*srx2;
74 initialStates{36} = tny2*sry2;
75
76 %% QPT Basis Operators Definitions
77
78 qptG = kron(sigma0, sigma0);
79 qptG(:, :, 2) = kron(sigma0, sigmax);
80 qptG(:, :, 3) = kron(sigma0, sigmay);
81 qptG(:, :, 4) = kron(sigma0, sigmaz);
82
83 qptG(:, :, 5) = kron(sigmax, sigma0);
84 qptG(:, :, 6) = kron(sigmax, sigmax);
85 qptG(:, :, 7) = kron(sigmax, sigmay);
86 qptG(:, :, 8) = kron(sigmax, sigmaz);
87
88 qptG(:, :, 9) = kron(sigmay, sigma0);
89 qptG(:, :, 10) = kron(sigmay, sigmax);
90 qptG(:, :, 11) = kron(sigmay, sigmay);
91 qptG(:, :, 12) = kron(sigmay, sigmaz);
92
93 qptG(:, :, 13) = kron(sigmaz, sigma0);
94 qptG(:, :, 14) = kron(sigmaz, sigmax);
95 qptG(:, :, 15) = kron(sigmaz, sigmay);
96 qptG(:, :, 16) = kron(sigmaz, sigmaz);
97
98 %% Import files
99
100 cavBiases = [14.6, 16.1, 17.3, 17.6, 18.7, 19.5, 20.5];
101 nBiases = length(cavBiases);
102
103 startRow = 1;
104 endRow = 17;

```

```

105 myData = cell(1,nBiases);
106
107 for fileNum = 1:nBiases
108     fileName = sprintf('SWIPHT_LAmp=%.3f_HAmp=%.3f_cPwr=%.2fdBm_LAngle=%ddeg_HAngle
                        =%ddeg.dat',loadVars(2), loadVars(3), cavBiases(fileNum), loadVars(4),
                        loadVars(5));
109     myData{fileNum} = importfile(fileName,startRow,endRow);
110 end
111
112 initialGate = initialStates{int8(loadVars(1))};
113 filename2 = sprintf('outputMLE%d.txt',loadVars(1));
114
115 %% Calibration Data
116
117 % calibData = [0.00554372, 0.00656907, 0.00836246, 0.0104682, 0.0240326, 0.0402416,
                0.150597;
118 %     0.036941, 0.163517, 0.0588138, 0.214049, 0.180645, 0.234204, 0.239586;
119 %     0.00723601, 0.0094296, 0.0961728, 0.0212939, 0.212308, 0.182376, 0.234367;
120 %     0.116254, 0.198568, 0.2135, 0.224613, 0.234051, 0.240033, 0.243667];
121 %
122 % calibErrors = [0.000329402, 0.000525341, 0.000825815, 0.00108812, 0.00201983,
                 0.00268108, 0.00422894;
123 %     0.00603975, 0.00921869, 0.00413449, 0.00225383, 0.00506191, 0.00131298,
                 0.000811017;
124 %     0.00065282, 0.000993634, 0.0177775, 0.00182644, 0.00243249, 0.00447199,
                 0.00135528;
125 %     0.0257651, 0.00252809, 0.00197846, 0.00155931, 0.000863653, 0.000648532,
                 0.000252292];
126
127 calibData = [0.00554, 0.00657, 0.00836, 0.0105, 0.0240, 0.0402, 0.1506;
              0.0369, 0.1635, 0.0588, 0.2140, 0.1806, 0.2342, 0.23959;
              0.00724, 0.00943, 0.0962, 0.02129, 0.2123, 0.1824, 0.2344;
              0.116, 0.1986, 0.2135, 0.2246, 0.23405, 0.24003, 0.24367];
130
131
132 calibErrors = [0.00033, 0.00052, 0.00082, 0.0011, 0.0020, 0.0027, 0.0042;
                0.0060, 0.0092, 0.0041, 0.0022, 0.0051, 0.0013, 0.00081;
                0.00065, 0.00099, 0.018, 0.0018, 0.0024, 0.0045, 0.0014;
                0.026, 0.0025, 0.0020, 0.0016, 0.00086, 0.00065, 0.00025];
135
136
137 %% Define the Chi Matrix
138
139 % for r2017b processing
140 % T1 = sym('t', [16 16], 'real'); % creating the real portion
141 % T2 = sym('s', [16 16], 'real'); % creating the imag portion
142
143 T1 = sym('t', [16 16]); % creating the real portion
144 T2 = sym('s', [16 16]); % creating the imag portion
145 T1 = sym(T1, 'real');
146 T2 = sym(T2, 'real');
147
148
149 T3 = diag(diag(T2)); % removing the imag portion from diagonal
150 T = triu(T1 + 1j*T2 - 1j*T3); % final T matrix
151

```



```

152 Chi = ctranspose(T)*T;
153
154 %% MLE function construction
155
156 rho_p = 0;
157 for m = 1:16
158     for n = 1:16
159         rho_p = rho_p + (Chi(m,n) * qptG(:,:,m) * ket2dm(initialGate * [1 0 0 0]') *
160             qptG(:,:,n));
161     end
162 end
163
164 tomoMeasures{1} = rho_p;
165 tomoMeasures{2} = (ty2*rho_p*ty2');
166 tomoMeasures{3} = (sy2*rho_p*sy2');
167 tomoMeasures{4} = (tx2*rho_p*tx2');
168 tomoMeasures{5} = (sx2*rho_p*sx2');
169 tomoMeasures{6} = (sx2*tx2*rho_p*tx2'*sx2');
170 tomoMeasures{7} = (sy2*ty2*rho_p*ty2'*sy2');
171 tomoMeasures{8} = (sy2*tx2*rho_p*tx2'*sy2');
172 tomoMeasures{9} = (sx2*ty2*rho_p*ty2'*sx2');
173 tomoMeasures{10} = (tny2*rho_p*tny2');
174 tomoMeasures{11} = (sny2*rho_p*sny2');
175 tomoMeasures{12} = (tnx2*rho_p*tnx2');
176 tomoMeasures{13} = (snx2*rho_p*snx2');
177 tomoMeasures{14} = (snx2*tnx2*rho_p*tnx2'*snx2');
178 tomoMeasures{15} = (sny2*tny2*rho_p*tny2'*sny2');
179 tomoMeasures{16} = (sny2*tnx2*rho_p*tnx2'*sny2');
180 tomoMeasures{17} = (snx2*tny2*rho_p*tny2'*snx2');
181
182 %% Simplifying all the diagonal components for easier processing later
183
184 for tomoMap=1:17
185     for pop=1:4
186         tomoMeasures{tomoMap}(pop,pop) = simplify(tomoMeasures{tomoMap}(pop,pop));
187     end
188 end
189
190 %% Likelihood construction
191
192 likelihood = 0;
193 for bias=1:nBiases
194     differenceForABias = 0;
195     for tomoMap=1:17
196         sumForABias = 0;
197         measurementError = 0;
198         for pop=1:4
199             sumForABias = sumForABias + (calibData(pop,bias) * tomoMeasures{tomoMap}
200                 (pop,pop));
201             measurementError = measurementError + ((calibErrors(pop,bias) *
202                 tomoMeasures{tomoMap}(pop,pop))^2);
203         end
204     end
205     %dataTable = table2array(myData{bias}); % for R2014b processing
206     dataTable = myData{bias};

```

```
203         differenceForABias = differenceForABias + (sumForABias - dataTable(tomoMap))  
                ^2 / measurementError;  
204     end  
205     likelihood = likelihood + differenceForABias;  
206 end  
207  
208 %% Saving the Data for Likelihood function  
209  
210 if (exist(filename2))  
211     delete(filename2);  
212 end  
213  
214 f_sym2 = fopen(filename2, 'wt');  
215 fprintf(f_sym2, '%s', char((likelihood)));  
216 fclose(f_sym2);  
217  
218 f = int16(loadVars(1));
```

D.2.4 MATLAB Program for Parallel Construction of All the Terms of the Likelihood Function

```
1  clc
2  clear all;
3
4  grandTable = [ 1, 0, 0, 0, 0
5                 2, 1, 0, 0, 0
6                 3, 0.495, 0, 0, 0
7                 4, 0.495, 0, -90,0
8                 5, 0.495, 0, 180,0
9                 6, 0.495, 0, 90, 0
10                7, 0, 0.635, 0, 0
11                8, 1, 0.635, 0, 0
12                9, 0.495, 0.635, 0, 0
13                10, 0.495, 0.635, -90,0
14                11, 0.495, 0.635, 180,0
15                12, 0.495, 0.635, 90, 0
16                13, 0, 0.316, 0, 0
17                14, 1, 0.316, 0, 0
18                15, 0.495, 0.316, 0, 0
19                16, 0.495, 0.316, -90,0
20                17, 0.495, 0.316, 180,0
21                18, 0.495, 0.316, 90, 0
22                19, 0, 0.316, 0, -90
23                20, 1, 0.316, 0, -90
24                21, 0.495, 0.316, 0, -90
25                22, 0.495, 0.316, -90,-90
26                23, 0.495, 0.316, 180,-90
27                24, 0.495, 0.316, 90, -90
28                25, 0, 0.316, 0, 180
29                26, 1, 0.316, 0, 180
30                27, 0.495, 0.316, 0, 180
31                28, 0.495, 0.316, -90,180
32                29, 0.495, 0.316, 180,180
33                30, 0.495, 0.316, 90, 180
34                31, 0, 0.316, 0, 90
35                32, 1, 0.316, 0, 90
36                33, 0.495, 0.316, 0, 90
37                34, 0.495, 0.316, -90,90
38                35, 0.495, 0.316, 180,90
39                36, 0.495, 0.316, 90, 90];
40
41  parfor tomos=1:36
42      mle_multiLoad(grandTable(tomos,:));
43  end
```

D.2.5 MATLAB Program to Construct the Expression for the Completeness Relation

```

1 %% Tomography Gate Definitions
2
3 theta = pi()/2;
4
5 sigma0 = eye(2);
6 sigmax = [0 1; 1 0];
7 sigmay = [0 -1j; 1j 0];
8 sigmaz = [1 0; 0 -1];
9
10 id = kron(sigma0, sigma0);
11 sx = kron(sigmax, sigma0);
12 sy = kron(sigmay, sigma0);
13 sz = kron(sigmaz, sigma0);
14
15 tx = kron(sigma0, sigmax);
16 ty = kron(sigma0, sigmay);
17 tz = kron(sigma0, sigmaz);
18
19 sx2 = cos(theta/2) * id - 1j*sin(theta/2) * sx;
20 sy2 = cos(theta/2) * id - 1j*sin(theta/2) * sy;
21 tx2 = cos(theta/2) * id - 1j*sin(theta/2) * tx;
22 ty2 = cos(theta/2) * id - 1j*sin(theta/2) * ty;
23
24 thetaN = -pi()/2;
25
26 snx2 = cos(thetaN/2) * id - 1j*sin(thetaN/2) * sx;
27 sny2 = cos(thetaN/2) * id - 1j*sin(thetaN/2) * sy;
28 tnx2 = cos(thetaN/2) * id - 1j*sin(thetaN/2) * tx;
29 tny2 = cos(thetaN/2) * id - 1j*sin(thetaN/2) * ty;
30
31 %% Tomography Gate Definitions
32
33 initialStates = cell(1,16);
34
35 initialStates{1} = id*id;
36 initialStates{2} = id*sx;
37 initialStates{3} = id*sx2;
38 initialStates{4} = id*sy2;
39 initialStates{5} = tx*id;
40 initialStates{6} = tx*sx;
41 initialStates{7} = tx*sx2;
42 initialStates{8} = tx*sy2;
43 initialStates{9} = tx2*id;
44 initialStates{10} = tx2*sx;
45 initialStates{11} = tx2*sx2;
46 initialStates{12} = tx2*sy2;
47 initialStates{13} = ty2*id;
48 initialStates{14} = ty2*sx;
49 initialStates{15} = ty2*sx2;
50 initialStates{16} = ty2*sy2;

```

```

51
52 %% QPT Basis Operators Definitions
53
54 qptG = kron(sigma0, sigma0);
55 qptG(:, :, 2) = kron(sigma0, sigmax);
56 qptG(:, :, 3) = kron(sigma0, sigmay);
57 qptG(:, :, 4) = kron(sigma0, sigmaz);
58
59 qptG(:, :, 5) = kron(sigmax, sigma0);
60 qptG(:, :, 6) = kron(sigmax, sigmax);
61 qptG(:, :, 7) = kron(sigmax, sigmay);
62 qptG(:, :, 8) = kron(sigmax, sigmaz);
63
64 qptG(:, :, 9) = kron(sigmay, sigma0);
65 qptG(:, :, 10) = kron(sigmay, sigmax);
66 qptG(:, :, 11) = kron(sigmay, sigmay);
67 qptG(:, :, 12) = kron(sigmay, sigmaz);
68
69 qptG(:, :, 13) = kron(sigmaz, sigma0);
70 qptG(:, :, 14) = kron(sigmaz, sigmax);
71 qptG(:, :, 15) = kron(sigmaz, sigmay);
72 qptG(:, :, 16) = kron(sigmaz, sigmaz);
73
74 %% Define the Chi Matrix
75
76 % for r2017b processing
77 T1 = sym('t', [16 16], 'real'); % creating the real portion
78 T2 = sym('s', [16 16], 'real'); % creating the imag portion
79
80 % T1 = sym('t', [16 16]); % creating the real portion
81 % T2 = sym('s', [16 16]); % creating the imag portion
82 % T1 = sym(T1, 'real');
83 % T2 = sym(T2, 'real');
84
85
86 T3 = diag(diag(T2)); % removing the imag portion from diagonal
87 T = triu(T1 + 1j*T2 - 1j*T3); % final T matrix
88
89 Chi = ctranspose(T)*T;
90
91 %% Completeness relation with Lagrange multiplier
92
93 constructedIdentity = 0 * eye(4);
94 finalLagrange = 0;
95
96 id4 = eye(4);
97
98 for m=1:16
99     for n=1:16
100         constructedIdentity = constructedIdentity + Chi(m,n) * qptG(:, :, m) * qptG
            (:, :, n);
101     end
102 end
103

```

```
104 for m=1:4
105     for n=1:4
106         finalLagrange = finalLagrange + (real(constructedIdentity(m,n)) - id4(m,n))
            ^2 + (imag(constructedIdentity(m,n)))^2;
107     end
108 end
109
110 lag = finalLagrange;
111
112 %% Saving the Data for Lagrange Multiplier function
113
114 filename1 = 'outputCorrectedLagrange_Manual.txt';
115 if (exist(filename1))
116     delete(filename1);
117 end
118
119 f_sym1 = fopen(filename1, 'wt');
120 fprintf(f_sym1, '%s', char((lag)));
121 fclose(f_sym1);
```

D.3 Mathematica Program to Perform Quantum State Tomography

This program reads the files generated from the previous MATLAB code and performs the maximum likelihood estimation.

Preparation-----

```
ClearAll["`*"]; Clear["Global`*"]; ClearSystemCache[]; $HistoryLength = 0;
SetDirectory[NotebookDirectory[]];
ket2dm[M_] := M.M†;
$Assumptions =
  Union[Flatten@Table[ToExpression["t" <> ToString[i] <> "x" <> ToString[j]] ∈ Reals, {i, 16}, {j, 16}],
    Flatten@Table[ToExpression["s" <> ToString[i] <> "x" <> ToString[j]] ∈ Reals, {i, 16}, {j, 16}],
    {λ ∈ Reals}];
StartingLambdaValue = 1;
NumberOfInitialStatesToFit = 36;
```

Gate Definitions-----

```
θ = π / 2; θ1 = -π / 2;
identity = IdentityMatrix[2];
sigmax = {{0, 1}, {1, 0}}; sigmay = {{0, -I}, {I, 0}}; sigmaz = {{1, 0}, {0, -1}};
id = ArrayFlatten[identity⊗identity];
sx = ArrayFlatten[sigmax⊗identity]; sy = ArrayFlatten[sigmay⊗identity];
sz = ArrayFlatten[sigmaz⊗identity];
tx = ArrayFlatten[identity⊗sigmax]; ty = ArrayFlatten[identity⊗sigmay];
tz = ArrayFlatten[identity⊗sigmaz];
sx2 = Cos[θ / 2] id - I Sin[θ / 2] sx; sy2 = Cos[θ / 2] id - I Sin[θ / 2] sy;
sz2 = Cos[θ / 2] id - I Sin[θ / 2] sz;
tx2 = Cos[θ / 2] id - I Sin[θ / 2] tx; ty2 = Cos[θ / 2] id - I Sin[θ / 2] ty;
tz2 = Cos[θ / 2] id - I Sin[θ / 2] tz;
snx2 = Cos[θ1 / 2] id - I Sin[θ1 / 2] sx; sny2 = Cos[θ1 / 2] id - I Sin[θ1 / 2] sy;
tnx2 = Cos[θ1 / 2] id - I Sin[θ1 / 2] tx; tny2 = Cos[θ1 / 2] id - I Sin[θ1 / 2] ty;
ξ = (0) Degree; λ1 = (113.67) Degree; λ2 = (66.21) Degree;
```

$$\text{cnotHFq} = \begin{pmatrix} 0 & E^{I\xi} & 0 & 0 \\ E^{-I\xi} & 0 & 0 & 0 \\ 0 & 0 & E^{I\lambda_2} & 0 \\ 0 & 0 & 0 & E^{I\lambda_1} \end{pmatrix};$$

QPT Gate Definitions-----

```

g[1] = ArrayFlatten[identity@identity];
g[2] = ArrayFlatten[identity@sigmax];
g[3] = ArrayFlatten[identity@sigmay];
g[4] = ArrayFlatten[identity@sigmaz];
g[5] = ArrayFlatten[sigmax@identity];
g[6] = ArrayFlatten[sigmax@sigmax];
g[7] = ArrayFlatten[sigmax@sigmay];
g[8] = ArrayFlatten[sigmax@sigmaz];
g[9] = ArrayFlatten[sigmay@identity];
g[10] = ArrayFlatten[sigmay@sigmax];
g[11] = ArrayFlatten[sigmay@sigmay];
g[12] = ArrayFlatten[sigmay@sigmaz];
g[13] = ArrayFlatten[sigmaz@identity];
g[14] = ArrayFlatten[sigmaz@sigmax];
g[15] = ArrayFlatten[sigmaz@sigmay];
g[16] = ArrayFlatten[sigmaz@sigmaz];

```

X Matrix definitions-----

```

(T = Table[
  If[j > i,
    ToExpression["t" <> ToString[i] <> "x" <> ToString[j]] +
    I * ToExpression["s" <> ToString[i] <> "x" <> ToString[j]],
    If[j == i,
      ToExpression["t" <> ToString[i] <> "x" <> ToString[j]],
      0]
  ], {i, 16}, {j, 16}] // MatrixForm;
X = Simplify[T.T];
numberOfOptimizeParameters = Length@Variables@X;

```

Long Expressions from MATLAB-----

```

replacementRules = {"_" -> "x", "i" -> "I", "\\\r\\n" -> "", "ans" -> "", "=" -> ""};
lag = ToExpression@StringReplace[Import["outputCorrectedLagrange_Manual.txt"], replacementRules];
mleTable = Table[p, {p, 1, NumberOfInitialStatesToFit}];
mleTable = ParallelTable[
  ToExpression["mle" <> ToString[i] <> "=N@ToExpression@StringReplace[Import[\"outputMLE\" <>
    ToString[i] <> ".txt\"], {\"_\" -> \"x\", \"i\" -> \"I\"}];"];
  ToExpression["mle" <> ToString[i]], {i, 1, NumberOfInitialStatesToFit}];

```


D.3. MATHEMATICA PROGRAM TO PERFORM QUANTUM STATE TOMOGRAPHY

Previous Solution from Solving with fixed error values

```
solFromFixedErrors = {s10x11 -> -3.180632401243754`^-6, s10x12 -> 1.5717033020302681`^-6, s10x13 -> -1.985864803342644`^-6,
s10x14 -> -8.70597476376936`^-6, s10x15 -> -7.015277546201579`^-6, s10x16 -> 8.03579007129929`^-6, s11x12 -> 7.902315010450201`^-7,
s11x13 -> -2.313010267819399`^-6, s11x14 -> 3.5523334486568762`^-6, s11x15 -> 8.559337298326189`^-6, s11x16 -> -8.424292815519581`^-7,
s12x13 -> -4.8659487769431544`^-6, s12x14 -> 6.744456083265854`^-6, s12x15 -> -1.8090534596306031`^-6,
s12x16 -> 0.000012517691801958891, s13x14 -> 2.3635897371426607`^-6, s13x15 -> -2.4085192457268895`^-6,
s13x16 -> -5.358615401493727`^-6, s14x15 -> 3.21281320875445`^-8, s14x16 -> 6.176667949931038`^-7, s15x16 -> -1.1756970713920815`^-7,
s1x10 -> -0.030386382899817507, s1x11 -> -0.0072859559104510915, s1x12 -> -0.004099443802838109, s1x13 -> -0.011048153937148477,
s1x14 -> 0.46848713252793117, s1x15 -> 0.00434478213768275, s1x16 -> -0.15813881802845414, s1x2 -> 0.3597941547787879,
s1x3 -> 0.018112562315437734, s1x4 -> 0.04064076815966765, s1x5 -> 0.01388032343903583, s1x6 -> 0.04088597361073039,
s1x7 -> -0.007279327188886423, s1x8 -> -0.002630058905841912, s1x9 -> -0.010554993141885162, s2x10 -> 0.047072265752757615,
s2x11 -> -0.01439299853769621, s2x12 -> -0.014416816140697791, s2x13 -> 0.17106348373601338, s2x14 -> -0.00679399846284322,
s2x15 -> 0.013868449667682865, s2x16 -> -0.011671106718647913, s2x3 -> -0.07835065692790183, s2x4 -> 0.009492694609180622,
s2x5 -> 0.04589415876152599, s2x6 -> 0.023973365947912717, s2x7 -> -0.0014945263090628865, s2x8 -> 0.010783047518953032,
s2x9 -> 0.02393144144235894, s3x10 -> -0.01659570028058219, s3x11 -> 0.009623437284876881, s3x12 -> -0.008096676064083135,
s3x13 -> 0.007853438543292832, s3x14 -> -0.06994323748948496, s3x15 -> -0.03859156639756375, s3x16 -> 0.08372978810262696,
s3x4 -> 0.045817995890217386, s3x5 -> 0.019726938193452028, s3x6 -> 0.07400512093971533, s3x7 -> 0.0058917882368699085,
s3x8 -> 0.0062418834034440665, s3x9 -> 0.0292523781455762, s4x10 -> 0.003650003599150931, s4x11 -> 0.016124051502015995,
s4x12 -> -0.0097928366498484818, s4x13 -> 0.07696600830171209, s4x14 -> -0.031685314323363016, s4x15 -> -0.11978139139931596,
s4x16 -> 0.013156354911674729, s4x5 -> -0.0038321011787662666, s4x6 -> 0.003921021954274655, s4x7 -> -0.0366800014774593,
s4x8 -> 0.009679911598268797, s4x9 -> 0.00789992439062912, s5x10 -> -0.004989231572985889, s5x11 -> -0.031078287066359952,
s5x12 -> 0.022897284233992288, s5x13 -> 0.05687117264400936, s5x14 -> -0.049921380623654615, s5x15 -> -0.014000568851073355,
s5x16 -> 0.03191537657598426, s5x6 -> 0.008136186694297928, s5x7 -> -0.010190310638605246, s5x8 -> 0.011589805816033269,
s5x9 -> 0.007102305213028081, s6x10 -> -0.06493538423658389, s6x11 -> 0.04084058142850362, s6x12 -> 0.013914650621046649,
s6x13 -> 0.00969464839575685, s6x14 -> 0.026695843480954946, s6x15 -> -0.007297326450360799, s6x16 -> -0.02855182026280955,
s6x7 -> 0.008365689351621242, s6x8 -> -0.0265219648049484138, s6x9 -> 0.004373350963886727, s7x10 -> 0.049889365686499404,
s7x11 -> 0.00502335156934873, s7x12 -> -0.00015761184198197426, s7x13 -> -0.02474734922446878, s7x14 -> 0.013456484881530523,
s7x15 -> -0.023812043608892514, s7x16 -> 0.008326784975590636, s7x8 -> -0.059332796334306063, s7x9 -> -0.02777009339373244,
s8x10 -> 0.00001509930476478091, s8x11 -> 8.743438381268404`^-6, s8x12 -> 0.000014306766041176888, s8x13 -> -0.00003955182782154372,
s8x14 -> 0.00004701977550031877, s8x15 -> 0.00001961016422254961, s8x16 -> 0.00003073421420383619, s8x9 -> -0.000012979393306402807,
s9x10 -> 8.724721411402268`^-7, s9x11 -> -6.453967804318006`^-7, s9x12 -> 8.55797575058384`^-6, s9x13 -> 0.0000229597596375431,
s9x14 -> -0.000017811635537823194, s9x15 -> -6.36366049221097`^-7, s9x16 -> 0.000046748762690409574, t10x10 -> 0.000010051222168127104,
t10x11 -> 2.3601730769493393`^-6, t10x12 -> -1.0826560104012013`^-6, t10x13 -> -4.463281160986165`^-6, t10x14 -> 8.879996243868553`^-6,
t10x15 -> -9.83637335546199`^-6, t10x16 -> 5.407587280696072`^-6, t11x11 -> 2.263493305603312`^-6, t11x12 -> -1.5804094220319702`^-6,
t11x13 -> -1.2177923919132947`^-6, t11x14 -> 0.00001204947082487085, t11x15 -> 5.374892523770293`^-6, t11x16 -> -3.1301225173929968`^-6,
t12x12 -> 8.758157176503663`^-7, t12x13 -> -0.000016025647392165917, t12x14 -> 1.833102899755931`^-6, t12x15 -> 3.620001672544921`^-6,
t12x16 -> 0.000012625663202869616, t13x13 -> -5.89258311365452`^-6, t13x14 -> 9.321430061639383`^-7, t13x15 -> 3.179539239060188`^-6,
t13x16 -> 4.0794119310035225`^-7, t14x14 -> -3.059086620535822`^-7, t14x15 -> -1.6180377822754913`^-7,
t14x16 -> -3.830668080826245`^-7, t15x15 -> -2.267751061044066`^-7, t15x16 -> 1.165434280170037`^-7, t16x16 -> -7.130681387741039`^-7,
t1x1 -> 0.452006784424777, t1x10 -> 0.032855610932619454, t1x11 -> 0.010491355614836374, t1x12 -> 0.00045780779338405496,
t1x13 -> -0.36065219804740467, t1x14 -> 0.06149111164588601, t1x15 -> -0.0033441877550340012, t1x16 -> -0.013781046439125692,
t1x2 -> 0.11189259581340696, t1x3 -> -0.007611132384967747, t1x4 -> 0.027667875974598015, t1x5 -> 0.006068817874611381,
t1x6 -> 0.0018307333453984216, t1x7 -> 0.004551101301021993, t1x8 -> 0.0030938487777466216, t1x9 -> 0.005878491037874447,
t2x10 -> 0.01655143083742064, t2x11 -> 0.01689134955311564, t2x12 -> 0.0013655463564095206, t2x13 -> -0.004910606062156438,
t2x14 -> 0.09963853941653038, t2x15 -> -0.013968755489482738, t2x16 -> -0.008277819649521755, t2x2 -> 0.20675291589002223,
t2x3 -> 0.024473623276398213, t2x4 -> -0.012984785348195116, t2x5 -> -0.019475995891286565, t2x6 -> 0.08761131192286652,
t2x7 -> 0.011862473470855514, t2x8 -> -0.006027646200330583, t2x9 -> -0.018396572935144292, t3x10 -> 0.05181036942555026,
t3x11 -> 0.0010005967379380358, t3x12 -> -0.009332895400415223, t3x13 -> -0.06314978247310223, t3x14 -> 0.032292925910217304,
t3x15 -> -0.027926927427953368, t3x16 -> -0.04568204057542694, t3x3 -> -0.1140933551891964, t3x4 -> -0.007839043659532157,
t3x5 -> 0.022117301328291778, t3x6 -> 0.032497847366940835, t3x7 -> -0.019254072066010267, t3x8 -> 0.01950189048439056,
t3x9 -> -0.009631503580975004, t4x10 -> 0.02728274109325494, t4x11 -> -0.03567138147318772, t4x12 -> 0.006327640570940986,
t4x13 -> -0.003768407685949619, t4x14 -> 0.032941280052333086, t4x15 -> -0.05410110051569517, t4x16 -> -0.04932832767311707,
t4x4 -> 0.08978999085438892, t4x5 -> 0.0008695001721608258, t4x6 -> 0.030178141075760594, t4x7 -> -0.004144349805012477,
t4x8 -> 0.01295463593375814, t4x9 -> 0.013517207422038454, t5x10 -> 0.010419683741640172, t5x11 -> -0.020515952677066875,
t5x12 -> 0.0193284572963544, t5x13 -> 0.03124446885900001, t5x14 -> 0.027421864497525646, t5x15 -> -0.04402571560068402,
t5x16 -> -0.05070910411928882, t5x5 -> -0.03085005976258049, t5x6 -> -0.02774509473577938, t5x7 -> 0.029677969270593615,
t5x8 -> -0.014384801668604244, t5x9 -> -0.004830618674772696, t6x10 -> 0.013610600244055132, t6x11 -> 0.003664718025693527,
t6x12 -> -0.02126080655221568, t6x13 -> -0.027782183617720523, t6x14 -> -0.031457351788257336, t6x15 -> -0.02945779274621918,
t6x16 -> -0.0908492543365194, t6x6 -> 0.05682234758918807, t6x7 -> -0.0470978338208259, t6x8 -> -0.0013043977933188211,
t6x9 -> 0.01076874702783084093, t7x10 -> 0.01851152092767361, t7x11 -> 0.021378990386469274, t7x12 -> -0.06721680342679641,
t7x13 -> -0.017096589855427804, t7x14 -> 0.004120644311313835, t7x15 -> 0.013939069731345476, t7x16 -> -0.0329688211008503,
t7x7 -> 0.02487272203204345, t7x8 -> 0.011099412971450593, t7x9 -> 0.010134326719652989, t8x10 -> -0.000015929311418535354,
t8x11 -> 3.05612291251834`^-6, t8x12 -> 0.000020017801952870493, t8x13 -> 0.00002438499618030268, t8x14 -> -0.000017782381445035978,
t8x15 -> 0.00004959725896256022, t8x16 -> 0.000025047550843188218, t8x8 -> -0.000017740229131132805, t8x9 -> -5.254137747332628`^-6,
t9x10 -> -6.135359972472073`^-6, t9x11 -> -1.377578988281224`^-6, t9x12 -> 2.4299661311338643`^-6, t9x13 -> 0.00004299742909713805,
t9x14 -> -9.822767043607417`^-7, t9x15 -> -0.000025568992419941192, t9x16 -> -0.0000311654251224982, t9x9 -> 3.387685695808347`^-6,
λ -> 2.239146262972046`};
```

Sum of Operators and Finding the correct Initialization-----

```

decompositionOSR =
NSolve[
  cnotHFq == (a[1] g[1] + a[2] g[2] + a[3] g[3] + a[4] g[4] + a[5] g[5] + a[6] g[6] + a[7] g[7] +
    a[8] g[8] + a[9] g[9] + a[10] g[10] + a[11] g[11] + a[12] g[12] + a[13] g[13] + a[14] g[14] +
    a[15] g[15] + a[16] g[16]), {a[1], a[2], a[3], a[4], a[5], a[6], a[7], a[8], a[9], a[10],
    a[11], a[12], a[13], a[14], a[15], a[16]}}];
OSRCoefficients =
Transpose@
  ({a[1], a[2], a[3], a[4], a[5], a[6], a[7], a[8], a[9], a[10], a[11], a[12], a[13], a[14],
    a[15], a[16]} /. decompositionOSR);
decomposedOperator = OSRCoefficients;
(IdealX = decomposedOperator.decomposedOperator");

χInitializingData = Chop@CholeskyDecomposition@(X /. solFromFixedErrors);
initializeParameters =
  Union[Partition[Riffle[FullSimplify@Re@Flatten[T], FullSimplify@Re@Flatten[χInitializingData]], 2],
    Partition[Riffle[FullSimplify@Im@Flatten[T], FullSimplify@Im@Flatten[χInitializingData]], 2]] [[
    -numberOfOptimizeParameters ;; -1]];
fullInitializeParameters = Union[initializeParameters, {{λ, StartingLambdaValue}}];
ReplaceRulesForInitializeParameters =
  Flatten@
    ToExpression@StringReplace[StringReplace[ToString@initializeParameters,
      {"", {" " → ";"}, {" " → "->"}, {";" → ""}]];

```

MLE Initialization-----

```
MLECombined = N[λ2 * lag + Total@mleTable];
```

Performing MLE-----

```

startTime = AbsoluteTime[];
Block[{c = 0},
  {sol = FindMinimum[Re@MLECombined, fullInitializeParameters, MaxIterations → 4000,
    StepMonitor => If[Mod[c, 100] == 0,
      Print["step = " <> ToString[c++] <> ", value = " <> ToString[
        Re@MLECombined
        -----
        1000
      ]],
      c++];
  ]],
  c}];
Print["time elapsed = " <> ToString[AbsoluteTime[] - startTime]];
NotebookSave[];

```

D.4 Mathematica Program to Generate the Simulation Data for QPT

```

ClearAll["`*"]; Clear["Global`*"]; ClearSystemCache[]; $HistoryLength = 0;
SetDirectory[NotebookDirectory[]];
ParallelEvaluate[
  $Assumptions = {t1 ∈ Reals, t2 ∈ Reals, t3 ∈ Reals, t4 ∈ Reals, t5 ∈ Reals, t6 ∈ Reals, t7 ∈ Reals, t8 ∈ Reals, t9 ∈ Reals,
    t10 ∈ Reals, t11 ∈ Reals, t12 ∈ Reals, t13 ∈ Reals, t14 ∈ Reals, t15 ∈ Reals, t16 ∈ Reals};];

ParallelDo[
  ket2dm[M_] := M.M^M;
  listOfInitializations =
    Flatten@{{"id.id"}, {"id.sx"}, {"id.sx2"}, {"id.sy2"}, {"tx.id"}, {"tx.sx"}, {"tx.sx2"}, {"tx.sy2"}, {"tx2.id"},
      {"tx2.sx"}, {"tx2.sx2"}, {"tx2.sy2"}, {"ty2.id"}, {"ty2.sx"}, {"ty2.sx2"}, {"ty2.sy2"}};
  identity = IdentityMatrix[2]; sigmax = {{0, 1}, {1, 0}}; sigmay = {{0, -1}, {1, 0}}; sigmaz = {{1, 0}, {0, -1}};
  θ = π/2; θ1 = -π/2; id = ArrayFlatten[identity@identity];
  sx = ArrayFlatten[sigmax@identity]; sy = ArrayFlatten[sigmay@identity]; sz = ArrayFlatten[sigmaz@identity];
  tx = ArrayFlatten[identity@sigmax]; ty = ArrayFlatten[identity@sigmay]; tz = ArrayFlatten[identity@sigmaz];
  sx2 = Cos[θ/2] id - I Sin[θ/2] sx; sy2 = Cos[θ/2] id - I Sin[θ/2] sy; sz2 = Cos[θ/2] id - I Sin[θ/2] sz;
  tx2 = Cos[θ/2] id - I Sin[θ/2] tx; ty2 = Cos[θ/2] id - I Sin[θ/2] ty; tz2 = Cos[θ/2] id - I Sin[θ/2] tz;
  snx2 = Cos[θ1/2] id - I Sin[θ1/2] sx; sny2 = Cos[θ1/2] id - I Sin[θ1/2] sy;
  tnx2 = Cos[θ1/2] id - I Sin[θ1/2] tx; tny2 = Cos[θ1/2] id - I Sin[θ1/2] ty;
  initialState = N@Flatten@ket2dm[ToExpression@({listOfInitializations[[initialStIndex]]} . {{1}, {0}, {0}, {0}})];
  H0 = {{0, 0, 0, 0}, {0, Ee, 0, 0}, {0, 0, δ/2 + ε, 0}, {0, 0, 0, Ee - δ/2 + ε}};
  V = {{0, e^(i(ε+τω)) Ω[t], 0, 0}, {e^(-i(ε+τω)) Ω[t], 0, 0, 0}, {0, 0, 0, e^(i(ε+τω)) Ω[t]}, {0, 0, 0, e^(-i(ε+τω)) Ω[t]}};
  (Htot = H0 + V) // MatrixForm; (U = MatrixExp[I H0 t]) // MatrixForm;
  (Hrot = Chop@FullSimplify[U.Htot.Inverse[U] + I D[U, t].Inverse[U]]) // MatrixForm;
  ρ = {{ρ0x0[t], ρ0x1[t], ρ0x2[t], ρ0x3[t]}, {ρ1x0[t], ρ1x1[t], ρ1x2[t], ρ1x3[t]}, {ρ2x0[t], ρ2x1[t], ρ2x2[t], ρ2x3[t]},
    {ρ3x0[t], ρ3x1[t], ρ3x2[t], ρ3x3[t]}};
  assume = Flatten[ρ /. t → 0];
  For[assumeIndex = 1, assumeIndex ≤ Length[assume], assumeIndex++, assume[[assumeIndex]] = ToExpression[
    ToString[assume[[assumeIndex]]] <> "==" <> ToString@initialState[[assumeIndex]]];];
  D[A_, ρ_] := A.ρ.A^H - 1/2 A^H.A.ρ - 1/2 ρ.A^H.A; (*Lindblad operator definition*)
  Aq1 = {{0, 1, 0, 0}, {0, 0, 0, 0}, {0, 0, 0, 1}, {0, 0, 0, 0}};
  Aq2 = {{0, 0, 1, 0}, {0, 0, 0, 1}, {0, 0, 0, 0}, {0, 0, 0, 0}}; (*Creating the jump operators*)
  xx[t_] = (A (t/τp)^4 (1 - t/τp)^4 + π/4); Ω[t_] = 
$$\left( \frac{D[xx[t], \{t, 2\}]}{2\sqrt{\frac{\Delta^2}{4} - D[xx[t], t]^2}} - \sqrt{\frac{\Delta^2}{4} - D[xx[t], t]^2} \cot[2xx[t]] \right);$$

  ξ = (θ - 0) Degree; (*Adjustment phase for the SWIPHT pulse*)
  Ee = 2π6.75427; (*target qubit frequency*) δ = 2π0.00103; (*qubit-qubit shift*) ε = 2π6.07135 - δ/2;
  r1 = 1/3400; r2 = 1/9030; (*qubits' decay rate*)
  A = 138.9; Δ = δ;
  ωp = Ee; (*Drive frequency*)
  τp = 5.87/Abs[Δ]; (*Length of SWIPHT pulse*)
  equationsR = (I * (ρ.Hrot - Hrot.ρ)) + r1 * D[Aq1, ρ] + r2 * D[Aq2, ρ]; equationsL = D[ρ, t];
  solutions = NDSolve[Join[Flatten[Table[equationsL[[i, j]] = equationsR[[i, j]], {i, 1, 4}, {j, 1, 4}]], assume],
    Flatten[ρ], {t, 0, τp}, MaxSteps → Infinity];
  thyp = Chop[({ρ /. solutions} /. t → τp)[[1, 1, All]]];
  {initialStIndex, listOfInitializations[[initialStIndex]], thyp};
  Export[ToString@initialStIndex <> ".dat", thyp];
, {initialStIndex, 1, 16}]

```

APPENDIX E

QPT Process Matrices for Implementing SWIPHT

E.1 QPT Process Matrices for SWIPHT Gates

The figures below show real and imaginary parts of χ -matrices obtained from the experiment, master-equation simulations and decoherence-free ideal gates when implementing the SWIPHT protocol. The plots include results for qubit Q_H or Q_L as the control and two values of ϕ_d . The maximum theoretical magnitude for any element is 0.25.

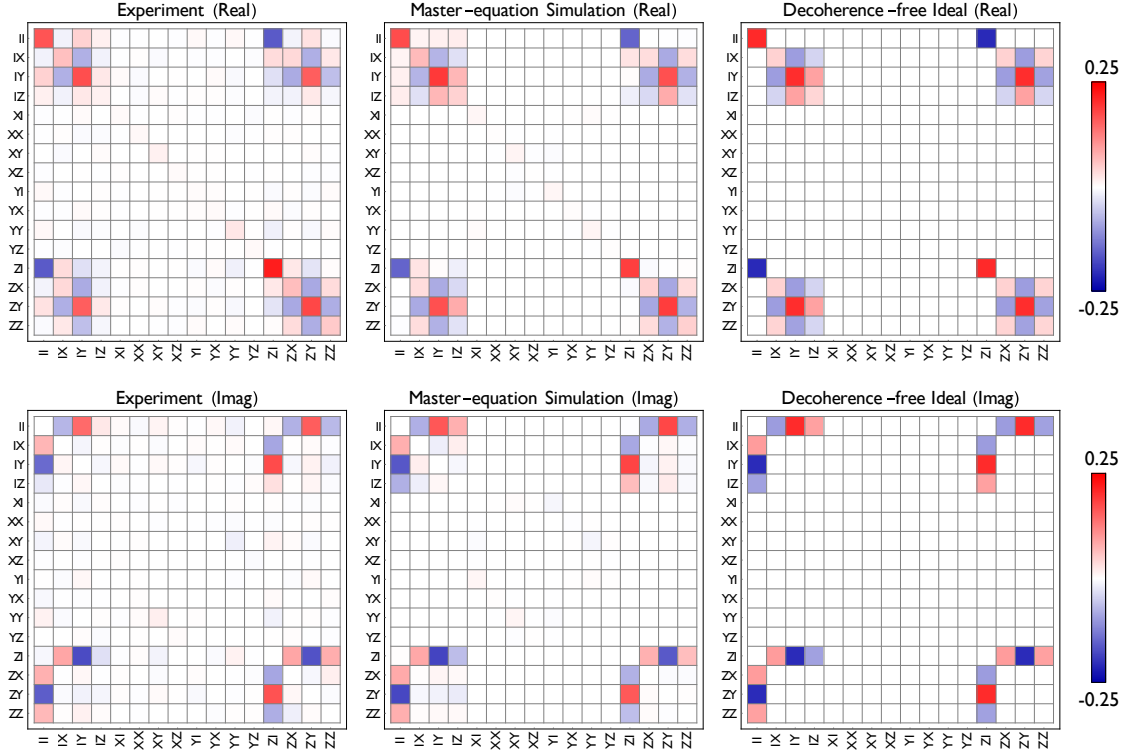


Fig. E.1 χ -matrix for $\text{SWIPT}_L^{49\pi/36}$. Qubit L is the control and $\phi_d = 49\pi/36$.

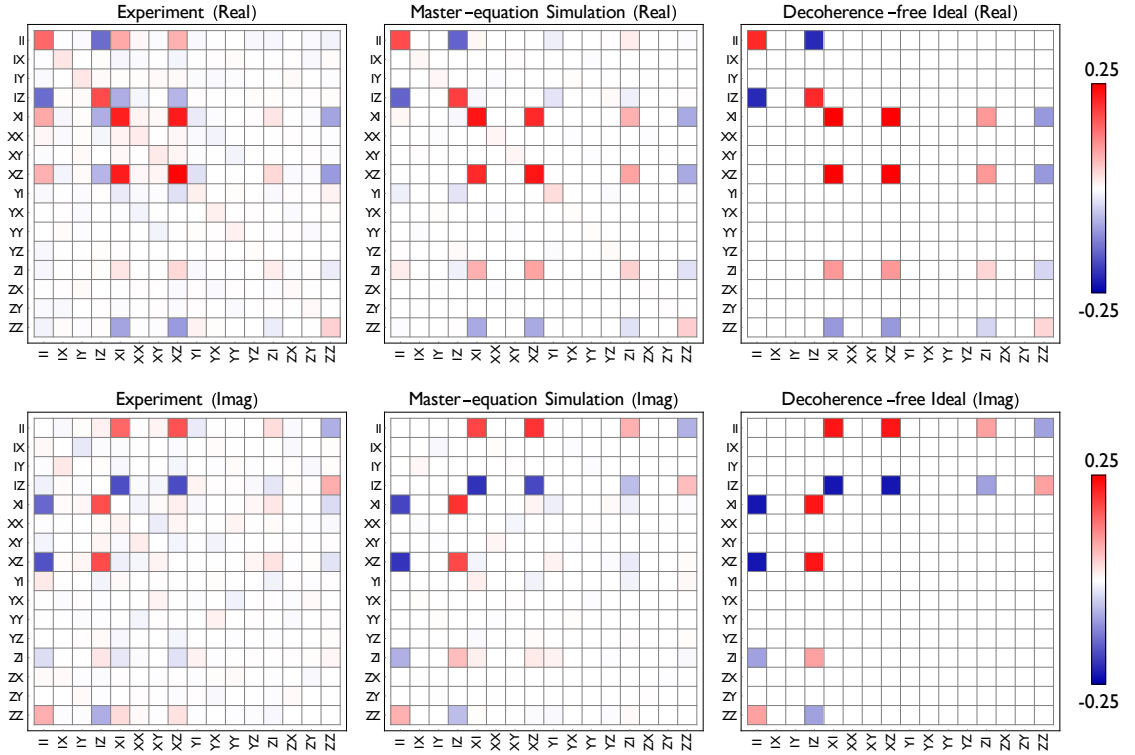


Fig. E.2 χ -matrix for SWIPT_H^0 . Qubit H is the control and $\phi_d = 0$.

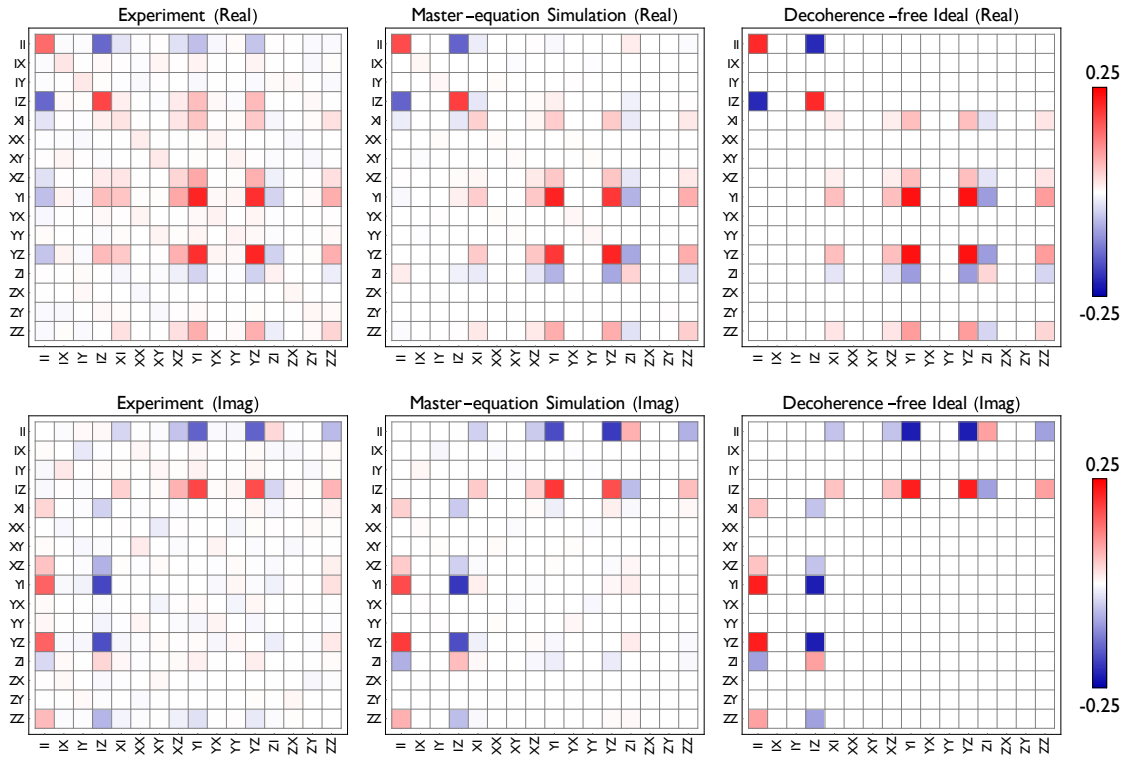


Fig. E.3 χ -matrix for $\text{SWIPT}_H^{7\pi/12}$. Qubit H is the control and $\phi_d = 7\pi/12$.

E.2 QPT Process Matrices for Single-Qubit Gates

In the figures below, I show the real and imaginary parts of χ -matrices obtained from the experiment for single-qubit gates. In each case, I also show the χ -matrices for the and decoherence-free ideal gates for comparison. The maximum theoretical magnitude for any element is 1.0 for R^π gates and 0.5 for $R^{\pi/2}$ gates.

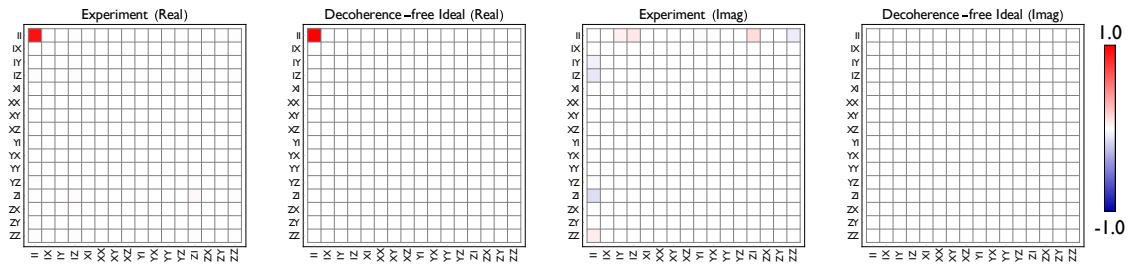


Fig. E.4 χ -matrix for $I \otimes I$.

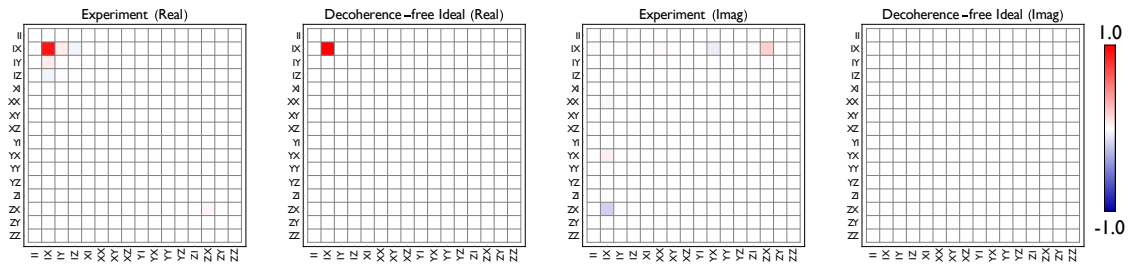


Fig. E.5 χ -matrix for $I \otimes R_x^\pi$.

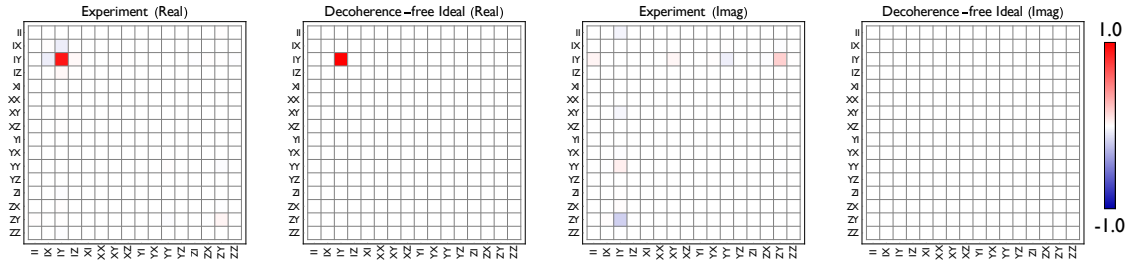


Fig. E.6 χ -matrix for $I \otimes R_y^\pi$.

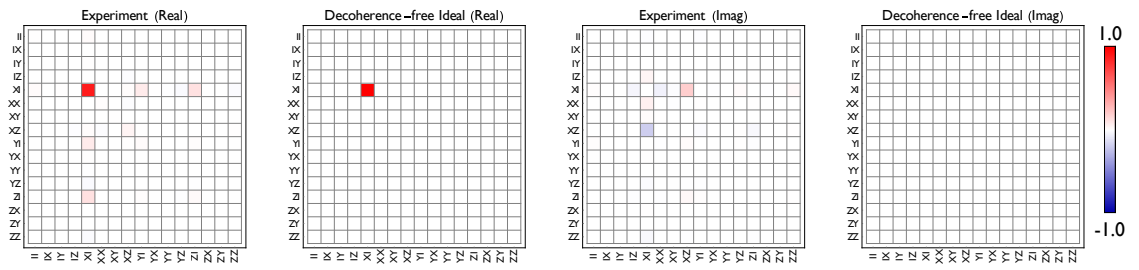


Fig. E.7 χ -matrix for $R_x^\pi \otimes I$.

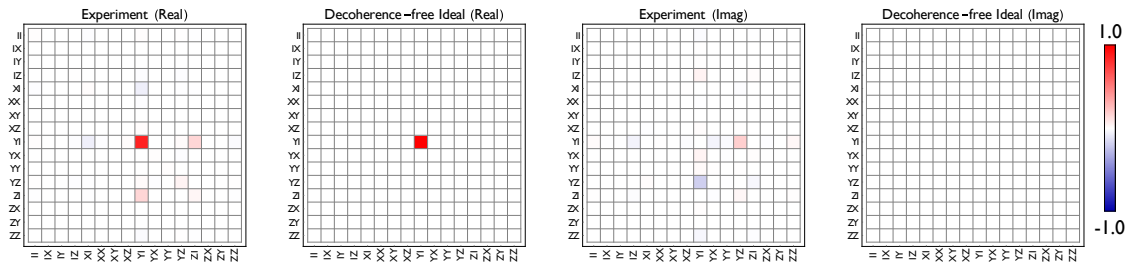


Fig. E.8 χ -matrix for $R_y^\pi \otimes I$.

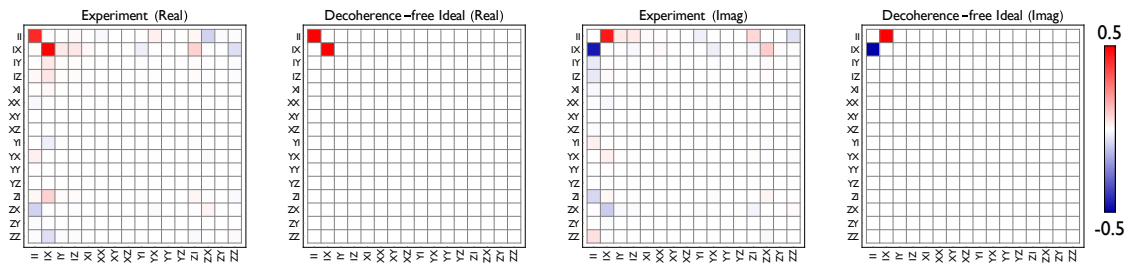


Fig. E.9 χ -matrix for $I \otimes R_x^{\pi/2}$.

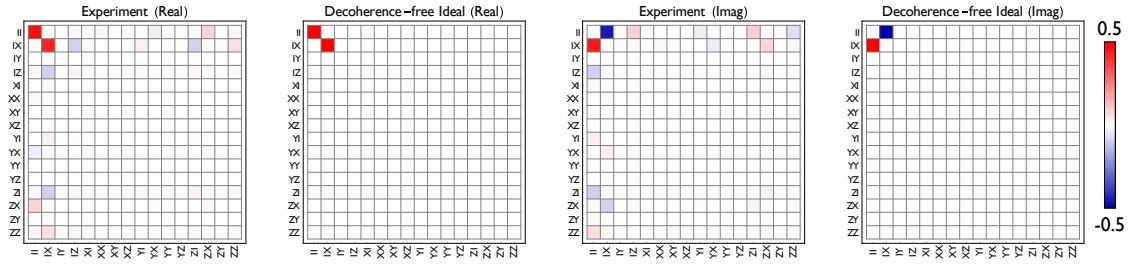


Fig. E.10 χ -matrix for $I \otimes R_x^{-\pi/2}$.

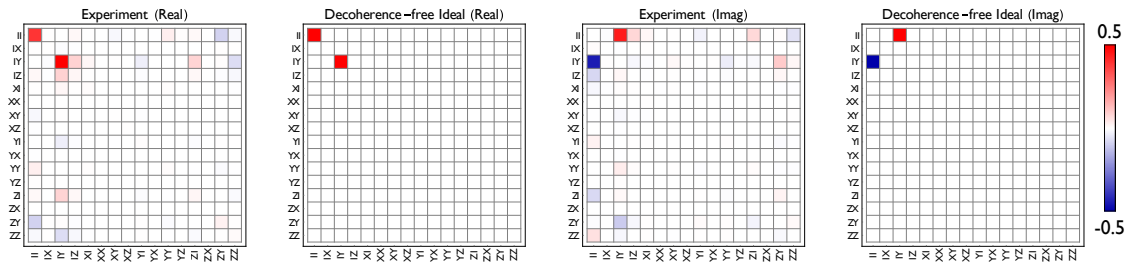


Fig. E.11 χ -matrix for $I \otimes R_y^{\pi/2}$.

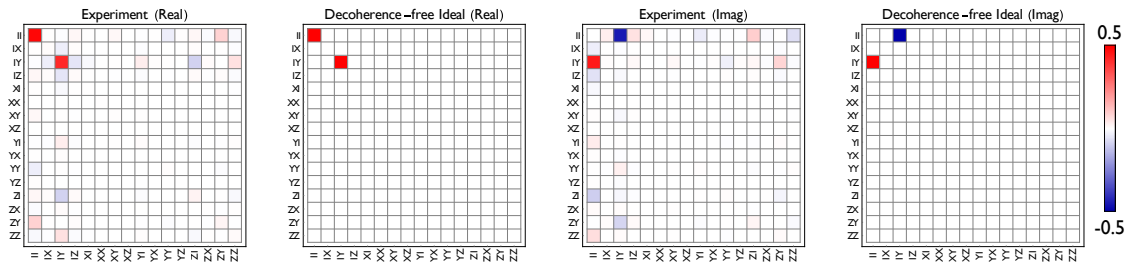


Fig. E.12 χ -matrix for $I \otimes R_y^{-\pi/2}$.

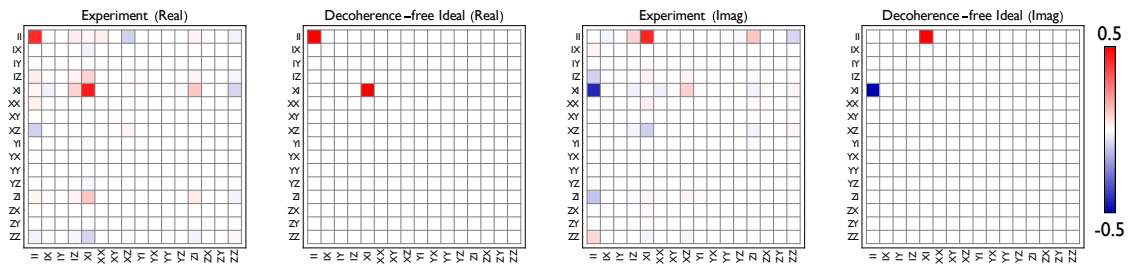


Fig. E.13 χ -matrix for $R_x^{\pi/2} \otimes I$.

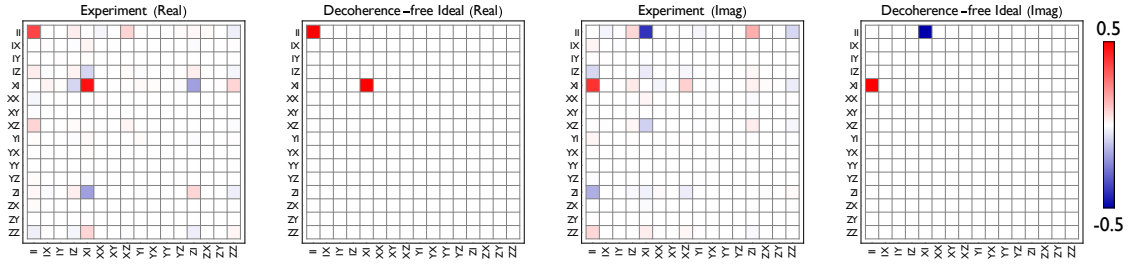


Fig. E.14 χ -matrix for $R_x^{-\pi/2} \otimes I$.

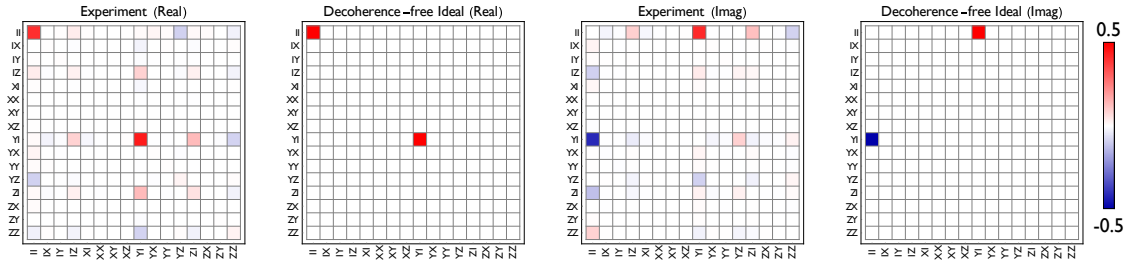


Fig. E.15 χ -matrix for $R_y^{\pi/2} \otimes I$.

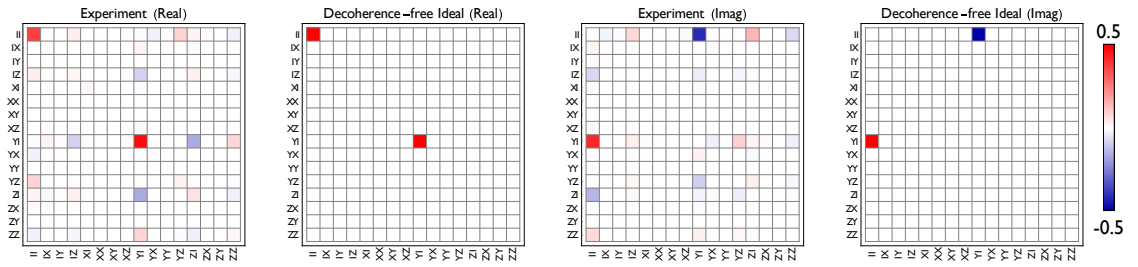


Fig. E.16 χ -matrix for $R_y^{-\pi/2} \otimes I$.

Bibliography

- [1] A. Church, “An Unsolvable Problem of Elementary Number Theory,” *Am. J. Math.* **58**, 345 (1936).
- [2] A. M. Turing, “On Computable Numbers, with an Application to the Entscheidungsproblem,” *Proc. London Math. Soc.* **s2-42**, 230 (1937).
- [3] M. A. Nielsen and I. L. Chuang, *Quantum Computation and Quantum Information*, 10th ed. (Cambridge University Press, 2010).
- [4] D. Deutsch, “Quantum theory, the Church–Turing principle and the universal quantum computer,” *Proc. R. Soc. London, Ser. A* **400**, 97 (1985).
- [5] R. P. Feynman, “Simulating physics with computers,” *Int. J. Theor. Phys.* **21**, 467 (1982).
- [6] P. A. Benioff, “Quantum mechanical Hamiltonian models of discrete processes that erase their own histories: Application to Turing machines,” *Int. J. Theor. Phys.* **21**, 177 (1982).
- [7] D. Z. Albert, “On quantum-mechanical automata,” *Phys. Lett. A* **98**, 249 (1983).
- [8] P. W. Shor, “Algorithms for quantum computation: discrete logarithms and factoring,” in *Proceedings 35th annual symposium on foundations of computer science* (Nov. 1994), pp. 124–134.
- [9] D. P. DiVincenzo, “The Physical Implementation of Quantum Computation,” *Fortschr. Phys.* **48**, 771 (2000).
- [10] M. Brune, F. Schmidt-Kaler, A. Maali, J. Dreyer, E. Hagle, J. M. Raimond, and S. Haroche, “Quantum Rabi Oscillation: A Direct Test of Field Quantization in a Cavity,” *Phys. Rev. Lett.* **76**, 1800 (1996).
- [11] C. Monroe, D. M. Meekhof, B. E. King, W. M. Itano, and D. J. Wineland, “Demonstration of a Fundamental Quantum Logic Gate,” *Phys. Rev. Lett.* **75**, 4714 (1995).
- [12] J. A. Jones and M. Mosca, “Implementation of a quantum algorithm on a nuclear magnetic resonance quantum computer,” *J. Chem. Phys.* **109**, 1648 (1998).
- [13] A. Imamoglu, D. D. Awschalom, G. Burkard, D. P. DiVincenzo, D. Loss, M. Sherwin, and A. Small, “Quantum Information Processing Using Quantum Dot Spins and Cavity QED,” *Phys. Rev. Lett.* **83**, 4204 (1999).
- [14] Y. Nakamura, Y. A. Pashkin, and J. S. Tsai, “Coherent control of macroscopic quantum states in a single-Cooper-pair box,” *Nature* **398**, 786 (1999).

- [15] P. W. Shor, “Fault-tolerant Quantum Computation,” in *Proceedings of the 37th Annual Symposium on Foundations of Computer Science*, FOCS ’96 (1996), pp. 56–65.
- [16] P. Kaye, R. Laflamme, and M. Mosca, *An Introduction to Quantum Computing* (Oxford University Press, 2007).
- [17] R. F. Voss and R. A. Webb, “Macroscopic Quantum Tunneling in 1- μm Nb Josephson Junctions,” *Phys. Rev. Lett.* **47**, 265 (1981).
- [18] M. H. Devoret, J. M. Martinis, and J. Clarke, “Measurements of Macroscopic Quantum Tunneling out of the Zero-Voltage State of a Current-Biased Josephson Junction,” *Phys. Rev. Lett.* **55**, 1908 (1985).
- [19] J. M. Martinis, M. H. Devoret, and J. Clarke, “Energy-Level Quantization in the Zero-Voltage State of a Current-Biased Josephson Junction,” *Phys. Rev. Lett.* **55**, 1543 (1985).
- [20] T. A. Fulton, P. L. Gammel, D. J. Bishop, L. N. Dunkleberger, and G. J. Dolan, “Observation of combined Josephson and charging effects in small tunnel junction circuits,” *Phys. Rev. Lett.* **63**, 1307 (1989).
- [21] M. Büttiker, “Zero-current persistent potential drop across small-capacitance Josephson junctions,” *Phys. Rev. B* **36**, 3548 (1987).
- [22] C. D. Tesche, “Can a noninvasive measurement of magnetic flux be performed with superconducting circuits?” *Phys. Rev. Lett.* **64**, 2358 (1990).
- [23] R. Rouse, S. Han, and J. E. Lukens, “Observation of Resonant Tunneling between Macroscopically Distinct Quantum Levels,” *Phys. Rev. Lett.* **75**, 1614 (1995).
- [24] V. Bouchiat, D. Vion, P. Joyez, D. Esteve, and M. H. Devoret, “Quantum coherence with a single Cooper pair,” *Physica Scripta* **1998**, 165 (1998).
- [25] F. C. Wellstood, C. Urbina, and J. Clarke, “Low frequency noise in dc superconducting quantum interference devices below 1 K,” *Appl. Phys. Lett.* **50**, 772 (1987).
- [26] W. D. Oliver, “Superconducting Qubits,” in *Quantum Information Processing: Lecture Notes of the 44th IFF Spring School 2013*, edited by D. P. DiVincenzo (Forschungszentrum Jülich, 2013) Chap. A4.
- [27] J. Koch *et al.*, “Charge-insensitive qubit design derived from the Cooper pair box,” *Phys. Rev. A* **76**, 042319 (2007).
- [28] IBM, *IBM Q Experience*, <https://quantumexperience.ng.bluemix.net/qx/devices> (visited on 06/23/2018).
- [29] C. Vu, *IBM Announces Advances to IBM Quantum Systems & Ecosystem*, <https://www-03.ibm.com/press/us/en/pressrelease/53374.wss> (visited on 06/23/2018).
- [30] J. Kelly, *A Preview of Bristlecone, Google’s New Quantum Processor*, <https://ai.googleblog.com/2018/03/a-preview-of-bristlecone-googles-new.html> (visited on 06/23/2018).

- [31] Intel, *Quantum Computing – 49-Qubit Processor*, <https://newsroom.intel.com/press-kits/quantum-computing/> (visited on 06/23/2018).
- [32] S. Boixo *et al.*, “Characterizing quantum supremacy in near-term devices,” *Nat. Phys.* **14**, 595 (2018).
- [33] S. P. Premaratne, F. C. Wellstood, and B. S. Palmer, “Microwave photon Fock state generation by stimulated Raman adiabatic passage,” *Nat. Commun.* **8**, 14148 (2017).
- [34] M. Tinkham, *Introduction to Superconductivity*, 2nd ed. (Dover Publications Inc., 1996).
- [35] B. D. Josephson, “Possible new effects in superconductive tunnelling,” *Phys. Lett.* **1**, 251 (1962).
- [36] L. N. Cooper, “Bound Electron Pairs in a Degenerate Fermi Gas,” *Phys. Rev.* **104**, 1189 (1956).
- [37] B. D. Josephson, “The discovery of tunnelling supercurrents,” *Rev. Mod. Phys.* **46**, 251 (1974).
- [38] A. Cottet, “Implementation of a quantum bit in a superconducting circuit,” PhD dissertation (University of Paris VI, 2002).
- [39] S. Haroche and J.-M. Raimond, *Exploring the quantum: atoms, cavities, and photons*, 1st ed., Oxford Graduate Texts (Oxford University Press, USA, 2006).
- [40] S. Haroche, “Nobel Lecture: Controlling photons in a box and exploring the quantum to classical boundary,” *Rev. Mod. Phys.* **85**, 1083 (2013).
- [41] J. M. Raimond, M. Brune, and S. Haroche, “Manipulating quantum entanglement with atoms and photons in a cavity,” *Rev. Mod. Phys.* **73**, 565 (2001).
- [42] A. Blais, R.-S. Huang, A. Wallraff, S. M. Girvin, and R. J. Schoelkopf, “Cavity quantum electrodynamics for superconducting electrical circuits: An architecture for quantum computation,” *Phys. Rev. A* **69**, 062320 (2004).
- [43] A. Wallraff *et al.*, “Strong coupling of a single photon to a superconducting qubit using circuit quantum electrodynamics,” *Nature* **431**, 162 (2004).
- [44] R. J. Schoelkopf and S. M. Girvin, “Wiring up quantum systems,” *Nature* **451**, 664 (2008).
- [45] P. K. Day, H. G. LeDuc, B. A. Mazin, A. Vayonakis, and J. Zmuidzinas, “A broadband superconducting detector suitable for use in large arrays,” *Nature* **425**, 817 (2003).
- [46] H. Paik *et al.*, “Experimental Demonstration of a Resonator-Induced Phase Gate in a Multiqubit Circuit-QED System,” *Phys. Rev. Lett.* **117**, 250502 (2016).
- [47] J. J. Sakurai and J. Napolitano, *Modern Quantum Mechanics*, 2nd ed. (Pearson Education Inc., 2011).
- [48] B. Suri, “Transmon Qubits Coupled to Superconducting Lumped Element Resonators,” PhD dissertation (University of Maryland, 2015).

- [49] L. S. Bishop, “Circuit Quantum Electrodynamics,” PhD dissertation (Yale University, May 2010).
- [50] E. T. Jaynes and F. W. Cummings, “Comparison of quantum and semiclassical radiation theories with application to the beam maser,” *Proc. IEEE* **51**, 89 (1963).
- [51] D. I. Schuster, “Circuit Quantum Electrodynamics,” PhD dissertation (Yale University, 2007).
- [52] D. A. Steck, *Quantum and Atom Optics*, revision 0.12.0, (May 2017) <http://steck.us/teaching>.
- [53] P. Meystre and M. Sargent III, *Elements of Quantum Optics*, 3rd ed. (Springer-Verlag Berlin Heidelberg, 1999).
- [54] G. Lindblad, “On the generators of quantum dynamical semigroups,” *Comm. Math. Phys.* **48**, 119 (1976).
- [55] A. Kossakowski, “On quantum statistical mechanics of non-Hamiltonian systems,” *Rep. Math. Phys.* **3**, 247 (1972).
- [56] A. A. Clerk and D. W. Utami, “Using a qubit to measure photon-number statistics of a driven thermal oscillator,” *Phys. Rev. A* **75**, 042302 (2007).
- [57] J.-H. Yeh, J. LeFebvre, S. Premaratne, F. C. Wellstood, and B. S. Palmer, “Microwave attenuators for use with quantum devices below 100 mK,” *J. Appl. Phys.* **121**, 224501 (2017).
- [58] W. Band and J. L. Park, “The empirical determination of quantum states,” *Foun. Phys.* **1**, 133 (1970).
- [59] V. Bužek, R. Derka, G. Adam, and P. Knight, “Reconstruction of Quantum States of Spin Systems: From Quantum Bayesian Inference to Quantum Tomography,” *Ann. Phys.* **266**, 454 (1998).
- [60] Y.-x. Liu, L. F. Wei, and F. Nori, “Tomographic measurements on superconducting qubit states,” *Phys. Rev. B* **72**, 014547 (2005).
- [61] J. B. Altepeter, D. F. James, and P. G. Kwiat, “Qubit Quantum State Tomography,” in *Quantum State Estimation (Lecture Notes in Physics)*, edited by M. Paris and J. Řeháček (Springer, 2010) Chap. 4.
- [62] Z. Hradil, J. Řeháček, J. Fiurášek, and M. Ježek, “Maximum-Likelihood Methods in Quantum Mechanics,” in *Quantum State Estimation (Lecture Notes in Physics)*, edited by M. Paris and J. Řeháček (Springer, 2010) Chap. 3.
- [63] D. F. V. James, P. G. Kwiat, W. J. Munro, and A. G. White, “Measurement of qubits,” *Phys. Rev. A* **64**, 052312 (2001).
- [64] J. M. Chow *et al.*, “Detecting highly entangled states with a joint qubit readout,” *Phys. Rev. A* **81**, 062325 (2010).
- [65] U. Fano, “Description of States in Quantum Mechanics by Density Matrix and Operator Techniques,” *Rev. Mod. Phys.* **29**, 74 (1957).

- [66] G. M. D’Ariano, L. Maccone, and M. G. A. Paris, “Quorum of observables for universal quantum estimation,” *J. Phys. A: Math. Gen.* **34**, 93 (2001).
- [67] J. L. O’Brien, G. J. Pryde, A. Gilchrist, D. F. V. James, N. K. Langford, T. C. Ralph, and A. G. White, “Quantum Process Tomography of a Controlled-NOT Gate,” *Phys. Rev. Lett.* **93**, 080502 (2004).
- [68] M. Göppl *et al.*, “Coplanar waveguide resonators for circuit quantum electrodynamics,” *J. Appl. Phys.* **104**, 113904 (2008).
- [69] H. Paik *et al.*, “Observation of High Coherence in Josephson Junction Qubits Measured in a Three-Dimensional Circuit QED Architecture,” *Phys. Rev. Lett.* **107**, 240501 (2011).
- [70] A. Megrant *et al.*, “Planar superconducting resonators with internal quality factors above one million,” *Appl. Phys. Lett.* **100**, 113510 (2012).
- [71] A. Dunsworth *et al.*, “Characterization and reduction of capacitive loss induced by sub-micron Josephson junction fabrication in superconducting qubits,” *Appl. Phys. Lett.* **111**, 022601 (2017).
- [72] S. Novikov, “Raman Coherence Effects in a Superconducting Jaynes-Cummings System,” PhD dissertation (University of Maryland, 2015).
- [73] C. Wang *et al.*, “Surface participation and dielectric loss in superconducting qubits,” *Applied Physics Letters* **107**, 162601 (2015).
- [74] A. A. Houck *et al.*, “Controlling the Spontaneous Emission of a Superconducting Transmon Qubit,” *Phys. Rev. Lett.* **101**, 080502 (2008).
- [75] ANSYS, *3D Electromagnetic Field Simulator for RF and Wireless Design*, <https://www.ansys.com/products/electronics/ansys-hfss> (visited on 05/31/2018).
- [76] S. E. Nigg *et al.*, “Black-Box Superconducting Circuit Quantization,” *Phys. Rev. Lett.* **108**, 240502 (2012).
- [77] F. Deppe, S. Saito, H. Tanaka, and H. Takayanagi, “Determination of the capacitance of nm scale Josephson junctions,” *J. Appl. Phys.* **95**, 2607 (2004).
- [78] F. Solgun, D. W. Abraham, and D. P. DiVincenzo, “Blackbox quantization of superconducting circuits using exact impedance synthesis,” *Phys. Rev. B* **90**, 134504 (2014).
- [79] Kyocera Global, *Sapphire Technical Data*, <https://global.kyocera.com/prdct/fc/list/material/sapphire/sapphire.html> (visited on 05/31/2018).
- [80] MicroChem, *NANO PMMA and Copolymer*, http://microchem.com/pdf/PMMA_Data_Sheet.pdf (visited on 05/31/2018).
- [81] Zeon, *ZEP520A ; High Performance Positive EB Resist*, http://www.zeon.co.jp/business_e/enterprise/imagelec/zep520A.html (visited on 05/31/2018).
- [82] Rohm and Haas Electronic Materials, *Microposit FSC Series Surface Coating*, http://docs.capitolscientific.com/manufacture/dow_electronic_materials/datasheets/FSC-M-Surface_Coating.pdf (visited on 06/01/2018).

- [83] Dicing Blade Technology, *Hubbed Resinoid Blades*, <http://www.dicing-blades.com/custom-blades/> (visited on 06/01/2018).
- [84] Disco, *Automatic Dicing Saw DAD3220/3230/3430*, <http://www.discousa.com/eg/products/catalog/pdf/dad3220.pdf> (visited on 06/01/2018).
- [85] G. J. Dolan, "Offset masks for lift-off photoprocessing," *Appl. Phys. Lett.* **31**, 337 (1977).
- [86] FUJIFILM, *Developers*, http://www.fujifilmusa.com/products/semiconductor_materials/photoresist-ancillaries/developers/index.html#overview (visited on 06/01/2018).
- [87] Avantor, *Amyl Acetate (Mixed Isomers), Purified*, <https://www.avantorinc.com/commerce/product.aspx?id=2147510412> (visited on 06/01/2018).
- [88] V. Ambegaokar and A. Baratoff, "Tunneling Between Superconductors," *Phys. Rev. Lett.* **10**, 486 (1963).
- [89] D. H. Douglass and R. Meservey, "Energy Gap Measurements by Tunneling Between Superconducting Films. I. Temperature Dependence," *Phys. Rev.* **135**, A19 (1964).
- [90] P. N. Chubov, V. V. Eremenko, and Y. A. Pilipenko, "Dependence of the Critical Temperature and Energy Gap on the Thickness of Superconducting Aluminum Films," *Sov. J. Exp. Theor. Phys.* **28**, 389 (1969).
- [91] O. A. E. Cherney and J. Shewchun, "Enhancement of superconductivity in thin aluminium films," *Can. J. Phys.* **47**, 1101 (1969).
- [92] R. Meservey and P. M. Tedrow, "Properties of Very Thin Aluminum Films," *J. Appl. Phys.* **42**, 51 (1971).
- [93] R. B. Pettit and J. Silcox, "Film structure and enhanced superconductivity in evaporated aluminum films," *Phys. Rev. B* **13**, 2865 (1976).
- [94] N. A. Court, A. J. Ferguson, and R. G. Clark, "Energy gap measurement of nanostructured aluminium thin films for single Cooper-pair devices," *Supercond. Sci. Tech.* **21**, 015013 (2008).
- [95] M. H. Devoret, A. Wallraff, and J. M. Martinis, *Superconducting Qubits: A Short Review*, (2004) <https://arxiv.org/abs/cond-mat/0411174>.
- [96] P. Das, R. B. de Ouboter, and K. W. Taconis, "A Realization of a London-Clarke-Mendoza Type Refrigerator," in *Low Temperature Physics LT9*, edited by J. G. Daunt, D. O. Edwards, F. J. Milford, and M. Yaqub (1965), pp. 1253–1255.
- [97] A. T.A. M. de Waele, "Basic Operation of Cryocoolers and Related Thermal Machines," *J. Low Temp. Phys.* **164**, 179 (2011).
- [98] Leiden Cryogenics, *Cryogen Free CF-CS50*, <http://www.leiden-cryogenics.com/products/cryogen-free/cf-cs50> (visited on 05/06/2018).
- [99] D. I. Schuster *et al.*, "ac Stark Shift and Dephasing of a Superconducting Qubit Strongly Coupled to a Cavity Field," *Phys. Rev. Lett.* **94**, 123602 (2005).

- [100] A. P. Sears *et al.*, “Photon shot noise dephasing in the strong-dispersive limit of circuit QED,” *Phys. Rev. B* **86**, 180504 (2012).
- [101] Cosmic Microwave Technology, Inc., *CIT412*, <http://cosmicmicrowavetechnology.com/index.php/cryogenic-low-noise-amplifiers/cit412-cryogenic-low-noise-broadband-amplifier/> (visited on 06/08/2018).
- [102] Amuneal, *Magnetic Shielding Materials*, <http://www.amuneal.com/magnetic-shielding/magnetic-shielding-materials> (visited on 06/08/2018).
- [103] D. Pozar, *Microwave Engineering*, 3rd (John Wiley and Sons Inc., 2005).
- [104] M. D. Reed, L. DiCarlo, B. R. Johnson, L. Sun, D. I. Schuster, L. Frunzio, and R. J. Schoelkopf, “High-Fidelity Readout in Circuit Quantum Electrodynamics Using the Jaynes-Cummings Nonlinearity,” *Phys. Rev. Lett.* **105**, 173601 (2010).
- [105] R. Schreier and H. Shibata, in *Advances in Analog and RF IC Design for Wireless Communication Systems*, edited by G. Manganaro and D. Leenaerts, 1st ed. (Elsevier Inc., 2013) Chap. 8.
- [106] RF Wireless World, *Heterodyne receiver vs Homodyne receiver*, <http://www.rfwireless-world.com/Terminology/heterodyne-receiver-versus-homodyne-receiver.html> (visited on 05/08/2018).
- [107] Microwaves101, *Superheterodyne Receivers*, <https://www.microwaves101.com/encyclopedias/superheterodyne-receivers> (visited on 05/08/2018).
- [108] V. A. Kotelnikov, “On the transmission capacity of the ‘ether’ and of cables in electrical communications,” in *Proc. first All-Union Conf. Technological Reconstruction of the Commun. Sector and Low-Current Eng.* (1933).
- [109] H. Nyquist, “Certain Topics in Telegraph Transmission Theory,” *Trans. Am. Inst. Electr. Eng.* **47**, 617 (1928).
- [110] C. E. Shannon, “Communication in the Presence of Noise,” *Proc. IRE* **37**, 10 (1949).
- [111] Keysight Technologies, *The ABC’s of Arbitrary Waveform Generation*, <https://literature.cdn.keysight.com/litweb/pdf/5989-4138EN.pdf> (visited on 05/08/2018).
- [112] L3 Narda-Miteq, *Model: AMF-3F-04000800-07-10P*, <https://nardamiteq.com/viewmodel.php?model=AMF-3F-04000800-07-10P> (visited on 06/08/2018).
- [113] T. K. Mavrogordatos *et al.*, “Simultaneous Bistability of a Qubit and Resonator in Circuit Quantum Electrodynamics,” *Phys. Rev. Lett.* **118**, 040402 (2017).
- [114] L. Allen and J. H. Eberly, *Optical resonance and two-level atoms* (John Wiley & Sons Inc., 1975).
- [115] M. L. Citron, H. R. Gray, C. W. Gabel, and C. R. Stroud, “Experimental study of power broadening in a two-level atom,” *Phys. Rev. A* **16**, 1507 (1977).
- [116] I. I. Rabi, “Space Quantization in a Gyating Magnetic Field,” *Phys. Rev.* **51**, 652 (1937).

- [117] N. F. Ramsey, “A Molecular Beam Resonance Method with Separated Oscillating Fields,” *Phys. Rev.* **78**, 695 (1950).
- [118] E. L. Hahn, “Spin Echoes,” *Phys. Rev.* **80**, 580 (1950).
- [119] S. Sheldon, E. Magesan, J. M. Chow, and J. M. Gambetta, “Procedure for systematically tuning up cross-talk in the cross-resonance gate,” *Phys. Rev. A* **93**, 060302 (2016).
- [120] I. D. Abella, N. A. Kurnit, and S. R. Hartmann, “Photon Echoes,” *Phys. Rev.* **141**, 391 (1966).
- [121] G. Kirchmair *et al.*, “Observation of quantum state collapse and revival due to the single-photon Kerr effect,” *Nature* **495**, 205 (2013).
- [122] W. H. Louisell, *Quantum Statistical Properties of Radiation* (John Wiley & Sons Inc., 1973).
- [123] J. Gambetta *et al.*, “Qubit-photon interactions in a cavity: Measurement-induced dephasing and number splitting,” *Phys. Rev. A* **74**, 042318 (2006).
- [124] D. I. Schuster *et al.*, “Resolving photon number states in a superconducting circuit,” *Nature* **445**, 515 (2007).
- [125] B. Suri *et al.*, “Observation of Autler-Townes effect in a dispersively dressed Jaynes-Cummings system,” *New J. Phys.* **15**, 125007 (2013).
- [126] V. Fock, “Konfigurationsraum und zweite Quantelung,” *Z. Physik* **75**, 622 (1932).
- [127] C. Bennett and G. Brassard, “Quantum cryptography: Public key distribution and coin tossing,” in Proc. IEEE International Conference on Computers, Systems and Signal Processing (1984), pp. 175–179.
- [128] C. Liu, Z. Dutton, C. H. Behroozi, and L. V. Hau, “Observation of coherent optical information storage in an atomic medium using halted light pulses,” *Nature* **409**, 490 (2001).
- [129] A. Narla *et al.*, “Robust Concurrent Remote Entanglement Between Two Superconducting Qubits,” *Phys. Rev. X* **6**, 031036 (2016).
- [130] S. Krastanov *et al.*, “Universal control of an oscillator with dispersive coupling to a qubit,” *Phys. Rev. A* **92**, 040303 (2015).
- [131] A. S. Parkins, P. Marte, P. Zoller, and H. J. Kimble, “Synthesis of arbitrary quantum states via adiabatic transfer of Zeeman coherence,” *Phys. Rev. Lett.* **71**, 3095 (1993).
- [132] A. S. Parkins, P. Marte, P. Zoller, O. Carnal, and H. J. Kimble, “Quantum-state mapping between multilevel atoms and cavity light fields,” *Phys. Rev. A* **51**, 1578 (1995).
- [133] M. Hennrich, T. Legero, A. Kuhn, and G. Rempe, “Vacuum-Stimulated Raman Scattering Based on Adiabatic Passage in a High-Finesse Optical Cavity,” *Phys. Rev. Lett.* **85**, 4872 (2000).

- [134] M. Hofheinz *et al.*, “Generation of Fock states in a superconducting quantum circuit,” *Nature* **454**, 310 (2008).
- [135] M. Hofheinz *et al.*, “Synthesizing arbitrary quantum states in a superconducting resonator,” *Nature* **459**, 546 (2009).
- [136] R. W. Heeres *et al.*, “Cavity State Manipulation Using Photon-Number Selective Phase Gates,” *Phys. Rev. Lett.* **115**, 137002 (2015).
- [137] K. Bergmann, H. Theuer, and B. W. Shore, “Coherent population transfer among quantum states of atoms and molecules,” *Rev. Mod. Phys.* **70**, 1003 (1998).
- [138] N. Vitanov, M. Fleischhauer, B. Shore, and K. Bergmann, in *Advances In Atomic, Molecular, and Optical Physics*, Vol. 46, edited by B. Bederson and H. Walther (Academic Press, 2001) Chap. 2.
- [139] K. S. Kumar, A. Vepsäläinen, S. Danilin, and G. S. Paraoanu, “Stimulated Raman adiabatic passage in a three-level superconducting circuit,” *Nat. Commun.* **7**, 10628 (2016).
- [140] H. K. Xu *et al.*, “Coherent population transfer between uncoupled or weakly coupled states in ladder-type superconducting qutrits,” *Nat. Commun.* **7**, 11018 (2016).
- [141] P. G. Di Stefano, E. Paladino, T. J. Pope, and G. Falci, “Coherent manipulation of noise-protected superconducting artificial atoms in the Lambda scheme,” *Phys. Rev. A* **93**, 051801 (2016).
- [142] S. Novikov, T. Sweeney, J. E. Robinson, S. P. Premaratne, B. Suri, F. C. Wellstood, and B. S. Palmer, “Raman coherence in a circuit quantum electrodynamics lambda system,” *Nat. Phys.* **12**, 75 (2016).
- [143] S. Novikov, J. E. Robinson, Z. K. Keane, B. Suri, F. C. Wellstood, and B. S. Palmer, “Autler-Townes splitting in a three-dimensional transmon superconducting qubit,” *Phys. Rev. B* **88**, 060503 (2013).
- [144] V. Bužek, in *Quantum State Estimation*, Vol. 649, edited by M. Paris and J. Řeháček (Springer-Verlag Berlin Heidelberg, 2004) Chap. 6, pp. 223–229.
- [145] P. B. Chapple, K. G. H. Baldwin, and H.-A. Bachor, “Interference between competing quantum-mechanical pathways for four-wave mixing,” *J. Opt. Soc. Am. B* **6**, 180 (1989).
- [146] N. V. Vitanov, K. A. Suominen, and B. W. Shore, “Creation of coherent atomic superpositions by fractional stimulated Raman adiabatic passage,” *J. Phys. B: At. Mol. Opt. Phys.* **32**, 4535 (1999).
- [147] M. Reagor *et al.*, “Quantum memory with millisecond coherence in circuit QED,” *Phys. Rev. B* **94**, 014506 (2016).
- [148] E. Torrontegui *et al.*, in *Advances in Atomic, Molecular, and Optical Physics*, Vol. 62, edited by E. Arimondo, P. R. Berman, and C. C. Lin (Academic Press, 2013) Chap. 2, pp. 117–169.

- [149] Y.-X. Du *et al.*, “Experimental realization of stimulated Raman shortcut-to-adiabatic passage with cold atoms,” [Nat. Commun. 7, 12479 \(2016\)](#).
- [150] B. B. Zhou *et al.*, “Accelerated quantum control using superadiabatic dynamics in a solid-state lambda system,” [Nat. Phys. 13, 330 \(2016\)](#).
- [151] J. F. Clauser, M. A. Horne, A. Shimony, and R. A. Holt, “Proposed Experiment to Test Local Hidden-Variable Theories,” [Phys. Rev. Lett. 23, 880 \(1969\)](#).
- [152] A. Barenco *et al.*, “Elementary gates for quantum computation,” [Phys. Rev. A 52, 3457 \(1995\)](#).
- [153] D. M. Zajac, A. J. Sigillito, M. Russ, F. Borjans, J. M. Taylor, G. Burkard, and J. R. Petta, “Resonantly driven CNOT gate for electron spins,” [Science 359, 439 \(2018\)](#).
- [154] H.-R. Wei and G. Lu Long, “Hybrid quantum gates between flying photon and diamond nitrogen-vacancy centers assisted by optical microcavities,” [Sci. Rep. 5, 12918 \(2015\)](#).
- [155] J. M. Gambetta, J. M. Chow, and M. Steffen, “Building logical qubits in a superconducting quantum computing system,” [npj Quantum Inf. 3, 2 \(2017\)](#).
- [156] M. Reagor *et al.*, “Demonstration of universal parametric entangling gates on a multi-qubit lattice,” [Sci. Adv. 4 \(2018\)](#).
- [157] R. Barends *et al.*, “Coherent Josephson Qubit Suitable for Scalable Quantum Integrated Circuits,” [Phys. Rev. Lett. 111, 080502 \(2013\)](#).
- [158] F. W. Strauch, P. R. Johnson, A. J. Dragt, C. J. Lobb, J. R. Anderson, and F. C. Wellstood, “Quantum Logic Gates for Coupled Superconducting Phase Qubits,” [Phys. Rev. Lett. 91, 167005 \(2003\)](#).
- [159] R. Barends *et al.*, “Superconducting quantum circuits at the surface code threshold for fault tolerance,” [Nature 508, 500 \(2014\)](#).
- [160] L DiCarlo *et al.*, “Demonstration of two-qubit algorithms with a superconducting quantum processor,” [Nature 460, 240 \(2009\)](#).
- [161] R. McDermott *et al.*, “Simultaneous State Measurement of Coupled Josephson Phase Qubits,” [Science 307, 1299 \(2005\)](#).
- [162] R. C. Bialczak *et al.*, “Quantum process tomography of a universal entangling gate implemented with Josephson phase qubits,” [Nat. Phys. 6, 409 \(2010\)](#).
- [163] A. Dewes *et al.*, “Characterization of a Two-Transmon Processor with Individual Single-Shot Qubit Readout,” [Phys. Rev. Lett. 108, 057002 \(2012\)](#).
- [164] C. Rigetti and M. Devoret, “Fully microwave-tunable universal gates in superconducting qubits with linear couplings and fixed transition frequencies,” [Phys. Rev. B 81, 134507 \(2010\)](#).
- [165] J. M. Chow *et al.*, “Simple All-Microwave Entangling Gate for Fixed-Frequency Superconducting Qubits,” [Phys. Rev. Lett. 107, 080502 \(2011\)](#).

- [166] P. J. Leek *et al.*, “Using sideband transitions for two-qubit operations in superconducting circuits,” *Phys. Rev. B* **79**, 180511 (2009).
- [167] J. M. Chow, J. M. Gambetta, A. W. Cross, S. T. Merkel, C. Rigetti, and M. Steffen, “Microwave-activated conditional-phase gate for superconducting qubits,” *New J. Phys.* **15**, 115012 (2013).
- [168] A. W. Cross and J. M. Gambetta, “Optimized pulse shapes for a resonator-induced phase gate,” *Phys. Rev. A* **91**, 032325 (2015).
- [169] R. Schutjens, F. A. Dagga, D. J. Egger, and F. K. Wilhelm, “Single-qubit gates in frequency-crowded transmon systems,” *Phys. Rev. A* **88**, 052330 (2013).
- [170] S. E. Economou and E. Barnes, “Analytical approach to swift nonleaky entangling gates in superconducting qubits,” *Phys. Rev. B* **91**, 161405 (2015).
- [171] X.-H. Deng, E. Barnes, and S. E. Economou, “Robustness of error-suppressing entangling gates in cavity-coupled transmon qubits,” *Phys. Rev. B* **96**, 035441 (2017).
- [172] J. Majer *et al.*, “Coupling superconducting qubits via a cavity bus,” *Nature* **449**, 443 (2007).
- [173] F. C. Wellstood, “Estimating the uncertainty in joint state switching measurements of qubits,” unpublished, 2018.
- [174] E. Barnes and S. Das Sarma, “Analytically Solvable Driven Time-Dependent Two-Level Quantum Systems,” *Phys. Rev. Lett.* **109**, 060401 (2012).
- [175] E. Barnes, “Analytically solvable two-level quantum systems and Landau-Zener interferometry,” *Phys. Rev. A* **88**, 013818 (2013).
- [176] S. Filipp *et al.*, “Two-Qubit State Tomography Using a Joint Dispersive Readout,” *Phys. Rev. Lett.* **102**, 200402 (2009).
- [177] J. M. Chow *et al.*, “Universal Quantum Gate Set Approaching Fault-Tolerant Thresholds with Superconducting Qubits,” *Phys. Rev. Lett.* **109**, 060501 (2012).
- [178] A. Gilchrist, N. K. Langford, and M. A. Nielsen, “Distance measures to compare real and ideal quantum processes,” *Phys. Rev. A* **71**, 062310 (2005).
- [179] M. A. Nielsen, “A simple formula for the average gate fidelity of a quantum dynamical operation,” *Phys. Lett. A* **303**, 249 (2002).
- [180] S. Poletto *et al.*, “Entanglement of Two Superconducting Qubits in a Waveguide Cavity via Monochromatic Two-Photon Excitation,” *Phys. Rev. Lett.* **109**, 240505 (2012).
- [181] F. Motzoi, J. M. Gambetta, P. Rebentrost, and F. K. Wilhelm, “Simple Pulses for Elimination of Leakage in Weakly Nonlinear Qubits,” *Phys. Rev. Lett.* **103**, 110501 (2009).
- [182] C. Axline *et al.*, “An architecture for integrating planar and 3d cqed devices,” *Appl. Phys. Lett.* **109**, 042601 (2016).

- [183] H. S. Ku *et al.*, “Single qubit operations using microwave hyperbolic secant pulses,” [Phys. Rev. A **96**, 042339 \(2017\)](#).
- [184] H. Padamsee, J. Knobloch, and T. Hays, *RF Superconductivity for Accelerators*, 1st (John Wiley and Sons Inc., 1998).